

**Conductivity, structure and
bioconjugation of
gold-polythiophene hybrid nanoparticles
for printed electronics**

Dissertation
zur Erlangung des Grades
des Doktors der Naturwissenschaften
der Naturwissenschaftlich-Technischen Fakultät
der Universität des Saarlandes

von

Indra Backes

Angefertigt am
INM – Leibniz–Institut für Neue Materialien

Saarbrücken, 2024

Tag des Kolloquiums: 05.06.2025

Dekan: Prof. Dr.-Ing. Dirk Bähre

Berichterstatter: Prof. Dr. Tobias Kraus

Prof. Dr. Guido Kickelbick

Akad. Mitglied: Dr. Andreas Rammo

Vorsitz: Prof. Dr. Andreas Speicher

Dedicated to my family

*for their support, encouragement, inspiration, patience
and love*

*“Nothing in life is to be feared, it is only to be understood. Now is the time
to understand more, so that we may fear less.”*

- Marie Curie -

Acknowledgements

First and foremost, I would like to thank my ‘Doktorvater’ *Prof. Dr. Tobias Kraus* for giving me the opportunity to do my research and write my thesis in his renowned group at INM–Leibniz Institute for New Materials. He was an excellent mentor during the last years, who guided and supervised me through this work. I am thankful for all the fruitful discussions with him and that he always gave the right hints, when I was stuck in a scientific dead end. I also appreciate his patience during numerous revisions of this work and his valuable feedback, that helped me to get to the point, especially in writing this thesis. I am grateful that I had the chance to work under his guidance and for all the faith he put in me and my research. Furthermore, I thank *Prof. Dr. Guido Kickelbick* for reviewing my thesis and becoming the second referee.

Many thanks go to *Jun.-Prof. Dr. Lola González-García*, my scientific mentor and friend, who always had an open ear for all my scientific and personal problems. I am not only thankful for her scientific support, but also for all the fun, laughter and Spanish temperament she brought to the lab. I enjoyed our coffee breaks and the unforgettable football matches we watched together. I am grateful for her encouragement during the last years.

I would like to give special thanks to *Andrea Pyttlik* for her friendship. I am thankful for all the long evenings and weekends we spent together in the lab. I really appreciate the hours and hours of discussions about science and life, as well as our memorable trip to Lisbon. Without her help and enthusiasm, research would have been much harder. I would also like to thank *Michael Klos*, my former student, who became a real friend. I am grateful for all his experimental support, especially in the field of filtration. It was a pleasure to work with him and I am thankful for all his input that helped me to improve my research. Many thanks also go to *Anna Molitor* and *Juraj Drzic*, who were the best office mates ever and became friends. I really appreciate the working atmosphere in our office with all the fun, laughter, good vibes and sporty challenges we had together.

In general, I want to thank all the members of the structure formation group, who created an amazing working atmosphere and without whose support this thesis would not have been possible: *Dr. Roman Buchheit, Lukas Engel, Dr. Simon Bettscheider, Dr. Louis Weber, Dr. Long Zhang, Dr. Ioannis Kanelidis, Dr. Aljosha-Rakim Jochem, Dr. Dominik Gerstner, Dr. Peng Zhang, Dr. Manuel Oliva-Ramírez, Dr. Albenc Nexha, Dr. Björn Kuttich, Dr. Bart-Jan Niebuur, Selim Basaran, David van Impelen and Anika Kleemann.*

Specials thanks go to *Dr. Thomas Kister*, who has an amazing particle competence to fix every broken machine, often by using epoxy glue. He also helped to solve many experimental problems with his huge knowledge about nanoparticle synthesis and he was a great motivator with immense enthusiasm. I am also thankful for many useful scientific discussions with *Dr. David Doblas-Jiménez*, who always helped with his outstanding knowledge in data analysis. I would also like to thank the engineer of the structure formation group *Robert Strahl*. He gave me much technical support, especially in the field of inkjet printing. I am thankful for his tips and tricks regarding the handling and maintenance of the inkjet printer.

A big thank you to *Dr. Andreas Hegetschweiler*, who helped me to start the project about biofunctionalizable gold nanoparticles. He gave much support in the early stage of the project and paved the way for the patent application. I appreciate the help of *Dr. Thibaut Thai*, who has comprehensive knowledge about gold nanorods, especially about their biofunctionality. He gave the right hints to achieve the breakthrough in the bioconjugation of gold nanoparticles.

Many thanks also go to *Dr. Beate Reiser*, who started the research on gold-polythiophene hybrid nanoparticles. Without her preliminary work, this thesis would not have been feasible. She always supported me with her experience and knowledge, even after she left the structure formation group. I would further like to thank *Dr. Johannes Maurer*, my former supervisor during my master thesis in the structure formation group. He was a great mentor, providing much positive energy and he sparked my interest in nanoscience.

I am grateful for the help of *Dr. Alberto Escudero*, who realized the upscaling of the gold nanoparticle synthesis. Special thanks go to *Anja Colbus* and *Maria Rodríguez-Jiménez* for their great experimental support in the synthesis of gold nanocrystals. Special thanks

also go to the secretary of the structure formation group *Gabriele Koster*. I appreciate her assistance in many administrative and organizational issues, as well as her sunny disposition and encouraging words.

I would like to show my gratitude to all the colleagues at INM–Leibniz Institute for New Materials for their support during my PhD thesis. Particularly, I thank *Dr. Marcus Koch* for his help in SEM and TEM analysis of nanoparticles and *Robert Drumm*, who always gave assistance in identifying and installing the right characterization equipment and for his experimental and theoretical support in thermogravimetric analysis.

Finally, I owe my deepest gratitude to my beloved family. Words cannot describe the gratitude I owe to *my parents*, who taught me to never give up and who supported me every day of my life. I am incredibly grateful for their patience, faith and selfless love. I thank *Dennis* with all my heart for his loving support and his constant encouragement. I am extremely grateful, that he showed patience and understanding for long lab days, even on weekends, and that he always makes me laugh and feel happy.

Statement on contributions

The ideas of the projects were mainly developed in collaboration between the author of the thesis and her supervisors Prof. Dr. Tobias Kraus and Jun.-Prof. Dr. Lola González-García. Parts of the presented results in chapter 3.1 have been previously published (Backes *et al.* Molecular origin of electrical conductivity in gold–polythiophene hybrid particle films. *J. Phys. Chem. Lett.* 11, 10538–10547 (2020)) in collaboration with Prof. Dr. Karin Jacobs, Dr. Frank Müller and Dr. Anne Holtsch from the Experimental Physics and Center for Biophysics of Saarland University. Furthermore, data concerning biofunctionalizable gold–polythiophene hybrid nanoparticles presented in chapters 3.3 and 3.4 have already been partially incorporated into the patent application *Conductive functionalizable nanocomposites* (DE102019135645A1).

All experiments and data analysis including the creation of the figures/tables were conducted by the author using the cited literature with the following exceptions:

- **Synthesis and purification of AuNPs/AuNRs**

Aqueous synthesis and purification of CTAB-stabilized AuNPs and AuNRs on the lab scale (up to 2 L) were performed by Indra Backes and Michael Klos (INM–Leibniz Institute for New Materials, Saarbrücken, Germany). Large-scale synthesis (10 L) and purification of CTAB-stabilized AuNPs and AuNRs were conducted by Anja Colbus (INM–Leibniz Institute for New Materials, Saarbrücken, Germany) and María Rodríguez Jiménez (INM–Leibniz Institute for New Materials, Saarbrücken, Germany).

- **Ligand exchange with various polythiophenes**

Surface modification of as-synthesized AuNPs and AuNRs with diverse polythiophene ligands and the appropriate purification were carried out by Indra Backes and Michael Klos (INM–Leibniz Institute for New Materials, Saarbrücken, Germany).

- **TEM and SEM analysis**

Sample preparation for TEM and SEM characterization was carried out by Indra Backes. SEMs and TEMs were recorded by Dr. Marcus Koch (INM–Leibniz Institute for New Materials, Saarbrücken, Germany).

- **TGA characterization**

Sample preparation for TGA analysis was conducted by Indra Backes. TGA measurements were performed by Robert Drumm (INM–Leibniz Institute for New Materials, Saarbrücken, Germany) and Indra Backes.

- **XPS, STM and STS characterization**

All XPS data were recorded, analyzed and composed into figures/tables by Dr. Frank Müller (Experimental Physics and Center for Biophysics, Saarland University, Saarbrücken, Germany). STM imaging with corresponding data analysis and the translation of data into figures/tables were performed by Dr. Frank Müller (Experimental Physics and Center for Biophysics, Saarland University, Saarbrücken, Germany) and Dr. Anne Holtsch (Experimental Physics and Center for Biophysics, Saarland University, Saarbrücken, Germany). STS results were collected, interpreted and illustrated in figures/tables by Dr. Anne Holtsch (Experimental Physics and Center for Biophysics, Saarland University, Saarbrücken, Germany).

- **Synthesis of polymer PFS-Na**

The synthesis and purification of the polythiophene derivative PFS-Na was implemented by Dr. Lewis Cowen from the group of Associate Prof. Dr. Bob Schroeder (University College London, UK).

- **Inkjet printing**

Inkjet printing for the production of amperometric biosensors using commercial silver nanoparticle inks and various inks containing different gold-polythiophene hybrid nanoparticles was conducted by Robert Strahl (INM–Leibniz Institute for New Materials, Saarbrücken, Germany) and Indra Backes.

- **Cell experiments**

Cell culturing, cell growth of fibroblasts and neurospheres, as well as the staining and imaging of these cells by fluorescence microscopy were carried out by Dr. Aleeza Farrukh and Dr. Shifang Zhao from the Dynamic Biomaterials group of Prof. Dr. Aránzazu del Campo (INM-Leibniz Institute for New Materials, Saarbrücken, Germany).

Abstract

Printing techniques enable the large-scale and cost-effective production of modern electronic devices such as photovoltaics, displays and thin-film transistors. One main challenge in the fabrication of printed electronics is the formulation of printable nanoparticle inks.

This thesis deals with gold-polythiophene nanoparticles, that form a new electrically conductive hybrid material. Unlike commercial metal nanoparticle inks, these hybrids become conductive immediately after printing without post-treatment. Interactions between the gold nanoparticles and the polymers strongly affect the electrical properties of these hybrids. This work shows which molecular arrangements of the polythiophene chains in the ligand shell and which energy level alignment between the electronic structure of the polymer with those of gold are beneficial for charge transport in hybrid films. Functional groups in the conductive polymer shell of the hybrid materials enable molecular interactions with biological molecules. Biofunctionalizable hybrid gold nanoparticles with carboxylated polythiophene ligands were introduced in this thesis. Layers composed of these hybrids were used as platforms for cell growth and colloidal inks containing these hybrid nanoparticles were applied to produce biosensors for electrochemical glucose monitoring by inkjet printing.

Zusammenfassung

Druckverfahren ermöglichen großflächige und kosteneffiziente Produktion von moderner Elektronik wie Photovoltaik, Displays und Dünnschichttransistoren. Eine primäre Herausforderung bei der Herstellung gedruckter Elektronik ist die Formulierung von druckbaren Nanopartikel-Tinten.

Diese Arbeit befasst sich mit Gold-Polythiophen Nanopartikeln, die ein neuartiges elektrisch leitfähiges Hybridmaterial bilden. Anders als kommerzielle Metall-Nanopartikel-Tinten werden diese Hybridmaterialien nach dem Druckprozess ohne Nachbehandlung sofort leitfähig. Wechselwirkungen zwischen den Gold-Nanopartikeln und den Polymeren beeinflussen stark die elektrischen Eigenschaften dieser Hybridmaterialien. Diese Arbeit zeigt auf welche molekulare Anordnung der Polymerketten in der Ligandenhülle sowie welche energetische Übereinstimmung der elektronischen Struktur des Polymers mit der von Gold vorteilhaft für den Ladungstransport in hybriden Filmen sind. Funktionelle Gruppen in der leitfähigen Polymerhülle der Hybridmaterialien ermöglichen Wechselwirkungen mit biologischen Molekülen. Biologisch funktionalisierbare hybride Goldnanopartikel mit carboxylierten Polythiophen-Liganden wurden in dieser Arbeit eingeführt. Schichten bestehend aus diesen Hybridmaterialien wurden als Substrate für Zellwachstum verwendet und kolloidale Tinten, welche diese hybriden Nanopartikel enthielten, wurden eingesetzt, um Biosensoren für elektrochemische Glukosemessung mittels Tintenstrahldruck zu produzieren.

Table of contents

Acknowledgements	I
Statement on contributions.....	V
Abstract	IX
Zusammenfassung	XI
List of abbreviations.....	XVII
List of symbols	XXIII
1. Motivation.....	1
2. Gold-polythiophene hybrid nanomaterials: Theory and state of the art.....	7
2.1 Gold nanomaterials.....	7
2.1.1 Synthesis of aqueous spherical gold nanoparticles (AuNPs).....	7
2.1.2 Synthesis of aqueous anisotropic gold nanorods (AuNRs)	10
2.1.3 Electrical properties of conductive nanoparticle films	14
2.1.4 Energy level alignment at metal-organic interfaces	20
2.2 Conductive polythiophenes.....	24
2.2.1 Synthesis and internal structure of conductive polymers	25
2.2.2 Electrical properties of conductive polymers	28
2.2.3 Molecular assembly of polythiophenes on planar inorganic substrates.....	33
2.2.4 Molecular assembly of polythiophenes on nanomaterials.....	36
2.3 Hybrid materials	38
2.3.1 Definition and classification of hybrid materials.....	38
2.3.2 Synthesis routes for nanoparticle-polymer hybrid materials	43
2.3.3 Bioconjugation as a method for hybrid material production	47
2.3.4 Applications of conductive nanoparticle-polymer hybrid materials.....	49
3. Results	56
3.1 Molecular origin of electrical conductivity in gold-polythiophene hybrid nanoparticles	56
3.1.1 Structural and colloidal analysis of gold-PTEBS hybrid nanocrystals.....	57
3.1.2 Electrical conductivity of gold-PTEBS hybrid nanocrystal films	62
3.1.3 Characterization of ligand binding in gold-PTEBS hybrids by Raman spectroscopy	66

3.1.4	Spectroscopic characterization of the molecular polymer orientation in gold-PTEBS hybrid nanocrystals	70
3.1.5	Origin of molecular PTEBS configurations on different gold nanocrystals	79
3.1.6	Summary	81
3.2	Tailored ligands for improved electrical conductivity in gold-polythiophene hybrid nanoparticles.....	83
3.2.1	Structural and UV-vis spectroscopic analysis of gold-PFS-Na hybrid nanoparticles.....	86
3.2.2	Colloidal analysis of gold-PFS-Na hybrid nanoparticles	89
3.2.3	Characterization of ligand binding in gold-PFS-Na hybrids by Raman spectroscopy	93
3.2.4	Electrical conductivity of gold-PFS-Na hybrid nanoparticle films	97
3.2.5	Summary	102
3.3	Analysis of biofunctionalizable gold-polythiophene hybrid nanoparticles	104
3.3.1	Structural analysis of biofunctionalizable gold-polythiophene hybrid nanoparticles.....	106
3.3.2	Colloidal analysis of biofunctionalizable gold-polythiophene hybrid nanoparticles.....	107
3.3.3	Characterization of ligand binding in gold-P3KHT hybrids by Raman spectroscopy.....	118
3.3.4	Electrical conductivity of gold-P3KHT hybrid nanoparticle films.....	121
3.3.5	Summary	124
3.4	Bioconjugation of gold-polythiophene hybrid nanoparticles	125
3.4.1	Colloidal analysis of bioconjugated gold-P3KHT hybrid nanoparticles	127
3.4.2	Structural analysis of bioconjugated gold-P3KHT hybrid nanoparticles	132
3.4.3	Characterization of bioconjugation in gold-P3KHT hybrids by Raman spectroscopy.....	134
3.4.4	Electrical conductivity of bioconjugated gold-P3KHT hybrid nanoparticle films	136
3.4.5	Enzymatic activity of bioconjugated gold-P3KHT hybrid nanoparticles	140
3.4.6	Electrochemical glucose sensing using bioconjugated gold-P3KHT hybrids	150
3.4.7	Cell growth supporting features of bioconjugated gold-P3KHT hybrid nanoparticles	162
3.4.8	Summary	169
4.	Conclusion.....	173
5.	Outlook.....	177
6.	Experimental part and characterization.....	181
6.1	Materials	181
6.2	Experimental procedures	184
6.2.1	Synthesis of gold nanocrystals	184
6.2.2	Surface modification of gold nanocrystals with conductive polythiophene ligands.....	186
6.2.3	Bioconjugation of biofunctionalizable gold-polythiophene hybrid nanoparticles.....	191
6.2.4	Deposition of hybrid layers by drop-casting	194

6.2.5	Inkjet printing of amperometric biosensors.....	195
6.2.6	Plasma treatments.....	198
6.2.7	Preparation of colorimetric bioassays for glucose detection	198
6.2.8	Preparation of gold-polythiophene hybrid platforms for cell growth.....	201
6.2.9	Cell experiments.....	204
6.3	Characterization methods	206
6.3.1	Transmission electron microscopy (TEM).....	206
6.3.2	Scanning electron microscopy (SEM).....	207
6.3.3	Optical microscopy.....	207
6.3.4	Fluorescence microscopy	208
6.3.5	3D Confocal microscopy.....	208
6.3.6	Raman spectroscopy.....	210
6.3.7	X-ray photoelectron spectroscopy (XPS)	212
6.3.8	Scanning tunneling microscopy (STM) and spectroscopy (STS).....	212
6.3.9	Zeta potential measurements	213
6.3.10	Dynamic light scattering (DLS)	213
6.3.11	UV-vis spectroscopy	214
6.3.12	Electrical characterization	215
6.3.13	Thermogravimetric analysis (TGA)	216
6.3.14	Density measurements.....	216
6.3.15	Electrochemical characterization of inkjet-printed amperometric biosensors	217
	Appendix	221
A	Thermogravimetric analysis of gold-polythiophene hybrid nanoparticles	221
B	Thickness determination of hybrid gold-polythiophene films.....	224
C	Characterization of agglomerated gold-polythiophene hybrid nanoparticles by DLS	226
D	Colorimetric glucose bioassays containing gold-polythiophene hybrid nanoparticles.....	227
E	Inkjet printing of amperometric biosensors for electrochemical glucose detection	232
	Bibliography.....	235
	Publication list	294

List of abbreviations

2D	Two-dimensional
3D	Three-dimensional
AA	Ascorbic acid
AAO	Anodic aluminum oxide
ABTS	2,2'-Azino-bis(3-ethylbenzothiazoline-6-sulfonic acid) diammonium salt
Ag	Silver
AgBr	Silver bromide
AgNO₃	Silver nitrate
AgNP(s)	Silver nanoparticle(s)
AgNW(s)	Silver nanowire(s)
Al₂O₃	Aluminum oxide
Ar	Argon
Au	Gold
AuNP(s)	Gold nanoparticle(s)
AuNR(s)	Gold nanorod(s)
BSA	Bovine serum albumin
CA	Citric acid
CaP	Calcium phosphate
CdS	Cadmium sulfide
CdSe	Cadmium selenide
CE(s)	Counter electrode(s)
CNC(s)	Cellulose nanocrystal(s)
CNP(s)	Carbon nanoparticle(s)
CNT(s)	Carbon nanotube(s)
COOH/COO⁻ groups	Carboxyl/carboxylate groups
CP(s)	Conductive polymer(s)
CTAB	Cetyltrimethylammonium bromide
Cu	Copper
CuNP(s)	Copper nanoparticle(s)
DAPI	4',6-Diamidino-2-phenylindole
DFT	Density functional theory

DGME	Diethylene glycol monomethyl ether
Diamine linker	4,7,10-Trioxa-1,13-tridecanediamine
DLS	Dynamic light scattering
DOD	Drop-on-demand
Dpi	Dots per inch
e.g.	For example
EA	Electron affinity
EDAC	1-Ethyl-3-(3-dimethylaminopropyl)carbodiimide hydrochloride
EDC	1-Ethyl-3-(3-dimethylaminopropyl)carbodiimide
EDC/S-NHS_{high}	High concentration (2.00 vol%) of EDC/Sulfo-NHS reagent
EDC/S-NHS_{low}	Low concentration (0.75 vol%) of EDC/Sulfo-NHS reagent
EFGs	Epidermal Growth Factors
EHD	Electrohydrodynamic
EML	Emissive layer
FBS	Fetal bovine serum
Fcc	Face centered cubic
Fe₃O₄	Iron oxide
FETs	Field-effect transistors
Fruc	D-fructose
FWHM	Full width at half maximum
GIWAXD	Grazing incidence wide-angle X-ray diffraction
GIXRD	Grazing incidence X-ray diffraction
Gluc	D-Glucose
GOx	Glucose oxidase
H₂	Hydrogen
H₂O₂	Hydrogen peroxide
H₂SO₄	Sulfuric acid
H₃PO₄	Phosphoric acid
HAuCl₄	Chloroauric acid
HCl	Hydrochloric acid
HOMO	Highest occupied molecular orbital
HRP	Horseradish peroxidase
HTL(s)	Hole transport layer(s)

ICP-MS	Inductively Coupled Plasma Mass Spectrometry
ICT	Integer Charge-Transfer
IDIS	Induced Density of Interface States
IE	Ionization energy
IPES	Inverse photoemission spectroscopy
IPN(s)	Interpenetrating network(s)
ITO	Indium tin oxide
KH₂PO₄	Potassium dihydrogen phosphate
Lac	Lactose
LEDs	Light-emitting devices/diodes
LOD(s)	Limit(s) of detection(s)
LSPR	Longitudinal surface plasmon resonance
LUMO	Lowest unoccupied molecular orbital
Mal	D-maltose monohydrate
MES	2-(N-morpholino)ethanesulfonic acid
MWCNT(s)	Multiwalled carbon nanotube(s)
N₂	Nitrogen
Na₂HPO₄·2H₂O	Disodium hydrogen phosphate dihydrate
NaBH₄	Sodium borohydride
NaCl	Sodium chloride
NaOH	Sodium hydroxide
NaOL	Sodium oleate
NHS	<i>N</i> -Hydroxysuccinimide
NIL	Nanoimprint lithography
NIR	Near-infrared
NPCs	Neural progenitor cells
O₂	Oxygen
OA	Oxalic acid
OFET(s)	Organic field-effect transistor(s)
OLED(s)	Organic light-emitting diode(s)
OPV(s)	Organic photovoltaic(s)
P3BT	Poly-(3-butylthiophene-2,5-diyl)
P3DDT	Poly(3-dodecylthiophene-2,5-diyl)

P3DT	Poly(3-decylthiophene-2,5-diyl)
P3HT	Poly(3-hexylthiophene-2,5-diyl)
P3KBT	Poly[3-(potassium-4-butanoate)thiophene-2,5-diyl]
P3KHepT	Poly[3-(potassium-7-heptanoate)thiophene-2,5-diyl]
P3KHT	Poly[3-(potassium-6-hexanoate)thiophene-2,5-diyl]
P3KPT	Poly[3-(potassium-5-pentanoate)thiophene-2,5-diyl]
P3OT	Poly(3-octylthiophene-2,5-diyl)
PANI	Polyaniline
PBS	Phosphate-buffered saline
PC	Polycarbonate
PDI	Polydispersity index
PDMS	Polydimethylsiloxane
PEDOT	Poly(3,4-ethylenedioxythiophene)
PEDOT:PSS	Poly(3,4-ethylenedioxythiophene) polystyrene sulfonate
PEG	Polyethylene glycol
PEG-NH₂	<i>O</i> -(2-Aminoethyl)- <i>O'</i> -methylpolyethylene glycol/ aminated PEG
PES	Polyethersulfone
PET	Polyethylene terephthalate
PFA	Paraformaldehyde
Ph	Polythiophene
PLA	Polylactic acid
PMMA	Poly(methyl methacrylate)
PNIPAM	Poly(<i>N</i> -isopropylacrylamide)
PPy	Polypyrrole
PS	Polystyrene
PSS	Sodium polystyrene sulfonate
Pt	Platinum
PTEBS	Poly[2-(3-thienyl)-ethyloxy-4-butylsulfonate]
PU	Polyurethane
PVA	Poly(vinyl alcohol)
PVP	Polyvinylpyrrolidone
R2R	Roll-to-roll
RE(s)	Reference electrode(s)

RFID	Radio frequency identification
rGOx	Reduced graphene oxide
Rpm	Revolutions per minute
RuO₂	Ruthenium oxide
SAM(s)	Self-assembled monolayer(s)
SEM	Scanning electron microscopy
SEMs	Scanning electron micrographs
SERS	Surface-enhanced Raman spectroscopy
Si	Silicon
SiO₂	Silica
SO₃⁻	Sulfonate groups
SPR	Surface plasmon resonance
STM	Scanning tunneling microscopy
STS	Scanning tunneling spectroscopy
Suc	D-sucrose
Sulfo-NHS/S-NHS	<i>N</i> -Hydroxysulfosuccinimide/ <i>N</i> -Hydroxysulfosuccinimide sodium salt
TCB	1,3,5-Trichlorobenzene
TCs	Transparent conductor(s)
TEM	Transmission electron microscopy
TEMs	Transmission electron micrographs
TGA	Thermogravimetric analysis
TRITC-phalloidin	Tetramethylrhodamine B isothiocyanate-phalloidin
Tween 20	Polyoxyethylene-20-sorbitan monolaurate
Tween 40	Polyoxyethylene-40-sorbitan monopalmitate
Tween 60	Polyoxyethylene-60-sorbitan monostearate
Tween 80	Polyoxyethylene-80-sorbitan monooleate
UA	Uric acid
UDP	Underpotential deposition
UHV	Ultra-high vacuum
UPS	Ultraviolet photoelectron spectroscopy
Ur	Urea
UV-vis	Ultraviolet-visible
WE(s)	Working electrode(s)

XPS	X-ray photoelectron spectroscopy
XRD	X-ray diffraction
ZnO	Zinc oxide

List of symbols

T_g	Glass transition temperature
ρ	(Material/Electrical) resistivity
c	Concentration
c_{LOD}	Concentration at the limit of detection (LOD)
β_n	Conductance decay constant
R_c	Contact resistance
t	Critical exponent
I	Current
I - V curve	Current-voltage curve
D	Diameter
σ	Electrical conductivity
E_{HOMO}	Energetic position of HOMO
E_{LUMO}	Energetic position of LUMO
$E_{\text{HOMO-LUMO}}$	Energy difference between HOMO and LUMO
E_F	Fermi level
V_f	Film fill-factor
T_0	Hopping temperature
d_h	Hydrodynamic diameter
Φ_B^e	Injection barrier for electrons
Φ_B^h	Injection barrier for holes
Z	Inverse Ohnesorge number
l	Length of hybrid films
v_{max}	Maximal reaction velocity
K_m	Michaelis-Menten constant
M_w	Molecular weight
$E_{\text{ICT-}}$	Negative integer charge-transfer state
Φ_c	Percolation threshold
ϵ_r	Permittivity
l_p	Persistence length
$E_{\text{ICT+}}$	Positive integer charge-transfer state
σ_0	Pre-exponential factor

K	Proportionality factor
n	Refractive index
R	Resistance
Δ	Shift of vacuum level E_{vac}
S	Slope of calibration curve
E_{T}	Solvent polarity
S_{BL}	Standard deviation of the blank
$[S]$	Substrate concentration
T	Temperature
t	Thickness of hybrid films
E_{vac}	Vacuum level
η	Viscosity
V	Voltage
Φ	Volume fraction
w	Width of hybrid films
Φ_{m}	Work function
ζ	Zeta potential

1. Motivation

The term ‘printed electronics’ refers to electronic devices fabricated by diverse printing technologies.^{1–3} During the past decade, printed electronics have gained much attention. In 2017 the global market volume of printed electronics was \$14.0 billion and is predicted to increase with an annual growth rate of 13.6% reaching a global volume of \$26.6 billion by 2022.^{3,4} Printing techniques that have been applied and optimized to produce printed electronics include inkjet, screen, gravure, flexographic and electrodynamic printing.^{2–4} Conventional electronics are fabricated by photolithography, vacuum deposition methods (e.g. sputtering or chemical vapor deposition) and electroless plating. These techniques require complicated multi-step production processes, high-cost equipment and often the usage of environmentally harmful chemicals.^{1–5} In contrast, printing techniques allow the low-cost production of printed electronics with high throughput, scalability and rapid processing.^{2–4} Inkjet printing is particularly attractive, since it is versatile, allows the direct writing of complex patterns, produces minimal waste, enables easy changes of the printed design using computer-controlled translation and causes minimal contamination as a non-contact printing technique.^{6–8}

There are multiple application fields of printed electronics that include basic electronic structures such as flexible circuits,⁹ sensors,^{10–12} field-effect transistors (FETs)^{13,14} and radio frequency identification (RFID) antennas.^{15,16} Printed electronics can also be used in more complex applications including optoelectronics such as light-emitting devices (LEDs),^{17,18} displays¹⁹ and solar cells.^{20,21} Additionally, printed electronics are used in devices for energy storage such as batteries^{22,23} and super-capacitors.^{24,25} Current market drivers in printed electronics are flexible electronics on paper, polymer or textile substrates, which are bendable, twistable and foldable.^{3–5} Such devices are difficult to produce by conventional photolithography and vacuum deposition methods, since they are mostly limited to rigid substrates. Furthermore, printed electronics have been fabricated successfully on non-planar surfaces, enabling their usage in robotics,²⁶ aerospace²⁷ and biomedical applications.²⁸

One important aspect in the fabrication of printed electronics is the development of suitable conductive inks.^{1,29,30} In general, printable inks consist of several components. A conductive material is usually dispersed in a liquid medium (aqueous or organic solvent) and additionally various additives (surfactants, binders, etc.) can be added.^{1,29,30} The composition of the ink determines its physical properties such as surface tension, viscosity or wettability. These features have a strong impact on the quality of the printed product, since they affect the drop size, the formation of satellite drops, the drop placement accuracy and the wetting of the substrate.^{29–31} Nanomaterials are frequently used as conductive components in inks for printed electronics. In particular, inks for inkjet printing can benefit from the small dimensions of nanoobjects. Nozzle clogging during drop jetting should be avoided in inkjet printing. Thus, smaller particles are more advantageous. The dimensions of the conductive component should be less than 0.1–0.01 of the diameter of the printing nozzle.¹ For inkjet printing, studies revealed an optimal mean size of nanoparticles in the range of 30–50 nm.^{1,32}

The choice of conductive components strongly depends on the required properties of the printed product such as electrical conductivity, optical properties (e.g. transparency), flexibility (resistance against bending, folding or twisting) and the adhesion to the substrate.¹ Different types of conductive nanomaterials are used in inks for printed electronics including graphene,^{33–35} carbon nanotubes^{36–38} and metallic nanoparticles.^{1,2,29} Inks can also contain conductive polymers^{10,39–41} or combinations of the different conductive materials.^{42–44} Metallic nanoparticle inks are most commonly used for printed electronics, since they offer superior conductivity and stability. Additionally, metals possess an excellent biocompatibility.⁴⁵ Silver and gold nanoparticles with spherical^{46–49} or wire shape^{50,51} are often used to formulate suitable inks for printed electronics.

Printing electronics with metallic nanoparticle inks usually requires a post-printing treatment.^{1–3,5,29} After printing and solvent evaporation, stabilizing agents (ligands) and other non-volatile organic components (surfactants, binders, etc.) of the inks remain between the metallic nanoparticles, creating insulating barriers. These barriers limit the electrical conductivity and impede the formation of continuous conductive pathways due to metal contacts, reducing electrical conductivity. Thus, a post-treatment is required to remove the insulating organic components by decomposition, desorption or evaporation.

This is usually achieved by a sintering step. Sintering describes a process of welding metallic nanoparticles without fully melting them.^{1,29} Neck formation between adjacent nanoparticles during sintering leads to the formation of continuous percolating pathways.^{1,2,29} Conventionally, sintering is performed by a thermal heating step. The high surface-to-volume ratio of nanoparticles increases the self-diffusion of metallic atoms, which result in lower melting temperatures of metallic nanoparticles compared to bulk metals.^{52,53} Hence, thermal sintering can already be achieved at temperatures of 200 °C to 350 °C.^{1,5} These temperatures are still too high for many flexible substrates such as paper and common polymers with low glass transition temperatures T_g (polyethylene and polycarbonate). Thermal sintering can only be applied to rigid non-temperature-sensitive substrates (e.g. glass or silicon) or to more expensive polymer foils (polyimides) with higher T_g .⁶

The production of flexible electronics requires the development of alternative sintering methods that allow the post-treatment at milder conditions.^{1-3,5,29} Sintering without damaging the underlying substrate can be achieved by photonic⁵⁴⁻⁵⁶, plasma,⁵⁷⁻⁵⁹ microwave,⁶⁰⁻⁶² electrical⁶³⁻⁶⁵ and chemical sintering.⁶⁶⁻⁶⁸ Although the newly developed sintering methods are compatible with flexible substrates, the required post-treatments still complicate the fabrication process of printed electronics. Obviating sintering steps would shorten and simplify the production process, resulting in reduced manufacturing costs of printed electronics. Therefore, it is still attractive to develop printable metallic nanoparticle inks, which do not require any sintering after printing.

Reiser and co-workers introduced a new type of sinter-free metal-organic nanocrystals based on metallic gold nanocrystals functionalized with electrically conductive polythiophene ligands.⁶⁹ These hybrid nanocrystals possessed high electrical conductivity after deposition ($1497 \text{ S}\cdot\text{cm}^{-1}$) without further post-treatment.⁶⁹ However, little is known on the origin of the electrical conductivity in these gold-polythiophene hybrid nanocrystals. Interactions between the metal cores and the surrounding ligand shell are the main factors affecting the electrical features of hybrid nanocrystals. The design of new nanomaterials with tailored electrical properties, which match the requirements of diverse electronic applications, requires a deeper knowledge about these metal-ligand interactions. Thus, one goal of this work was to gain more information about the gold-

polythiophene interactions using spectroscopic methods and to correlate these interactions to the electrical properties of the resulting gold-polythiophene hybrid nanocrystals.

Gold-polythiophene interactions can also influence the molecular orientation of the polythiophene chains in the ligand shell of the hybrid nanocrystals. Since in polythiophenes charge transport preferentially occurs along the conjugated polymer backbone and the π - π stacking direction,⁷⁰⁻⁷⁴ the molecular configuration of the polythiophene ligands can have a crucial impact on the overall electrical properties of gold-polythiophene hybrid nanoparticles. Much research was done on how polythiophenes arrange on planar surfaces⁷⁴⁻⁷⁶ and in nano-confined spaces (e.g. produced by nanoimprinting).⁷⁷⁻⁸⁰ However, there were almost no studies about the arrangement of polythiophenes on inorganic nanocrystals.^{81,82} Therefore, I investigated the molecular arrangement of polythiophene chains in the ligand shell of gold-polythiophene hybrid nanoparticles (chapter 3.1). I further analyzed how the orientation of the polymer ligands can be affected by the dimensions (size and shape) of the nanocrystals and examined whether the molecular orientation of the polythiophenes had an impact on the electrical properties of the hybrid nanoparticles.

The ligand-metal interactions in gold-polythiophene hybrid nanoparticles are affected by the energy level alignment of the individual components at the metal/organic interfaces.⁸³⁻⁸⁶ Effective charge transport between the polymer ligand shell and the gold cores across the metal/organic interfaces will only occur if the energetic position of the ligand's molecular orbitals (HOMO, highest occupied molecular orbital and LUMO, lowest unoccupied molecular orbital) match the Fermi level E_F of the metal. Modern optoelectronic devices, such as organic photovoltaics or organic light-emitting diodes, contain organic and inorganic layers. The energy level alignment at these inorganic/organic interfaces are crucial for the device performance and many strategies were developed to tailor the energy level alignment in order to improve the efficiency of the optoelectronics.⁸⁷⁻⁹¹ Most studies on energy level alignment address planar inorganic/organic interfaces and little is known about the energetic adjustment at highly curved inorganic/organic interfaces, which are common in hybrid nanocrystals. Chapter 3.2 deals with the effect of energy level alignment at gold-polythiophene interfaces. I

functionalized gold nanoparticles by various polythiophene ligands that differ in the energetic structure of their molecular orbitals. I attributed observed differences in the electrical properties of the distinct gold-polythiophene hybrid nanoparticles to variations in the energy level alignment between gold cores and ligands. My work can help to gain a better understanding of the energetic adjustment at interfaces of inorganic/organic nanoparticles, which could open up new possibilities in the design of modern optoelectronic devices with enhanced output.

The organic nature of the polythiophene ligand shell enables the addition of further features to the gold-polythiophene hybrid nanocrystals beyond electrical conductivity by introducing organic functional groups such as amine, carboxyl, ester or aromatic groups in the polymer side chains of the polythiophenes. Based on this principle, I developed biofunctionalizable gold-polythiophene hybrid nanoparticles by introducing functional carboxyl/carboxylate groups in the polythiophene ligand shell, which facilitate a covalent attachment of biomolecules to the hybrid nanoparticles (chapters 3.3 and 3.4). These biofunctionalizable gold-polythiophene hybrid nanocrystals offer new opportunities in the growing field of printed flexible and even wearable electronics for biomedical applications,^{92–95} including biofuel cells^{96–98} and biosensors which monitor the vital signs (e.g. body temperature or pulse rate), biomarkers in body fluids (e.g. saliva, tears and sweat) or environmental parameters.^{99–103}

The production of biomedical printed electronics often requires bioactive inks that contain conductive materials and biomolecules such as proteins, enzymes, antibodies or nucleic acids.¹⁰⁴ Commercial state-of-the art metal nanoparticle inks provide high electrical conductivity, but usually do not possess intrinsic biological functionalities. Thus, bioactive printed electronics can only be produced from commercial nanoparticle inks by immobilizing diverse biomolecules on the printed structures after completing the printing process. This additional process step can be avoided by using the biofunctionalizable gold-polythiophene hybrid nanoparticles presented in chapters 3.3 and 3.4. This type of hybrid nanoparticles allows covalent bonding of biomolecules (before and after printing), extending the durability of the nanoparticles' bioactivity compared to commercial metal nanoparticle inks, where biomolecules can only be physisorbed. Furthermore, the sinter-free nature of the gold-polythiophene hybrid

nanocrystals is beneficial for biomolecules, which are temperature-sensitive and would decompose under the harsh sintering conditions of commercial metal nanoparticle inks.

Research on bioactive inks just started and there is still much optimization potential. One main challenge in the development of bioactive inks is the preservation of the biomolecules' activity, since some components of the ink can lead to irreversible unfolding of the biomolecules, which is often accompanied by a loss in activity.^{104,105} The results presented in chapter 3.4 demonstrate that enzymes, which have been covalently linked to the biofunctionalizable gold-polythiophene hybrid nanoparticles, maintained their enzymatic activity. Furthermore, the hybrid nanoparticles remained electrically conductive upon covalent attachment of biomolecules and the bioconjugated gold-polythiophene hybrids were printable without the addition of another host material such as a polymer.

Until today, research on printable bioactive inks mainly focused on inks containing various proteins or enzymes.^{106–108} Biofunctionalizable gold-polythiophene hybrid nanoparticles can help to broaden the field of bioactive inks due to the nature of the carboxyl/carboxylate groups present in the polythiophene ligand shell, which covalently interact with a large variety of biomolecules (e.g. proteins, enzymes, oligonucleotides, DNA, antibodies and growth factors). The unique combination of high electrical conductivity and bioactivity of gold-polythiophene hybrid nanocrystals can meet the demands of new high-performance printed and wearable devices for human healthcare and medical diagnostics.

2. Gold-polythiophene hybrid nanomaterials: Theory and state of the art

2.1 Gold nanomaterials

Gold nanocrystals are the metallic cores of the gold-polythiophene hybrids developed in this work. Knowledge about the characteristics of gold nanomaterials enables the identification of differences and parallels between these materials and the new type of gold-polythiophene hybrid nanocrystals. Hence, this chapter gives an overview about the fundamentals of the synthesis and the electrical properties of gold nanomaterials.

I prepared water-soluble sinter-free gold-polythiophene hybrid nanocrystals in this work by functionalizing different types of aqueous gold nanocrystals with various conductive polythiophene ligands. Many different synthesis methods for the preparation of gold nanomaterials are reported in literature. The main principles of aqueous synthesis routes for the production of spherical gold nanoparticles (AuNPs) and gold nanorods (AuNRs) are given in the upcoming sections 2.1.1 and 2.1.2. Electrical properties of gold nanocrystal films are mainly determined by metal-organic interfaces and the features of these interfaces, which I discussed in section 2.1.3. These metal-organic interfaces are further affected by an energetic match between the electronic structure of the metal and the organic compound. Principles of this energy level alignment, which also influences the electrical properties of gold-polythiophene nanocrystals layers, are described in section 2.1.4.

2.1.1 Synthesis of aqueous spherical gold nanoparticles (AuNPs)

The wet chemical synthesis of gold nanoparticles (AuNPs) by reduction processes require the appropriate choice of gold precursors, reducing and capping agents. The usage of suitable capping agents is important for colloidal stability of the AuNPs. Diverse routes for the synthesis of AuNPs have been published.^{109–111}

Turkevich already achieved the breakthrough in the synthesis of aqueous AuNPs in 1951.¹¹² In the Turkevich method, citrate-capped AuNPs are obtained by the reduction of chloroauric acid (HAuCl_4) with the mild reducing agent trisodium citrate in boiling water (Figure 2-1).

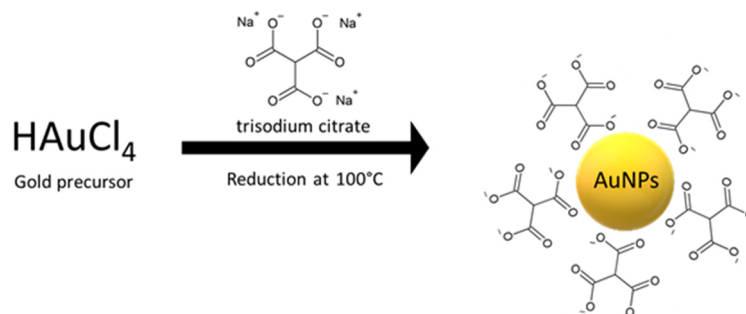


Figure 2-1: Synthesis of AuNPs based on the Turkevich method. Trisodium citrate acts simultaneously as reducing and capping agent.

In the Turkevich synthesis, trisodium citrate acts as both, reducing and stabilizing agent. Frens improved the Turkevich method by controlling the ratio between gold (Au) and reducing agent trisodium citrate.¹¹³ With the Turkevich-Frens approach, (quasi)-spherical AuNPs with diameters in the range of 10-150 nm can be synthesized. Small AuNPs (10-20 nm) produced by the Frens technique are monodisperse with relatively narrow polydispersity (10-15%). However, with increasing particle diameter the polydispersity also increases. AuNPs with diameters above 20 nm produced by the Frens method are polydisperse, highly faceted and quasi-spherical.¹¹³

Larger monodisperse quasi-spherical AuNPs can be obtained by a seed-mediated growth process. This process allows excellent shape- and size-control in the synthesis of nanoparticles. It usually consists of two steps. First, small spherical AuNPs referred as seeds are synthesized. These seed are added in the second step to a growth solution containing the gold precursor, reducing and stabilizing agents. The second growth step requires mild reducing agents to suppress new particle nucleation. Perrault *et al.* used hydroquinone as an adequate reducing agent, since it is only able to reduce Au (I) to Au(0) in the presence of gold nanoparticles.¹¹⁴ This ensures that only heterogeneous nucleation on the surfaces of the seed particles occur leading to successive growth of large gold nanoparticles (diameter up to 200 nm).¹¹⁴

In addition to mild reducing agents such as trisodium citrate, hydroquinone and ascorbic acid, strong reducing agents like sodium borohydride (NaBH_4) have been used in the synthesis of aqueous AuNPs. Small citrate-stabilized AuNPs (6 nm) can be produced by replacing trisodium citrate with NaBH_4 as reducing agent.¹¹⁴ Based on its strong reduction potential, NaBH_4 is able to reduce Au(III) to Au(0) at much lower temperatures compared to mild reducing agents (Figure 2-2). Sodium borohydride is often used to synthesize small seeds in the first step of a seed-mediated growth procedure. For example, El-Sayed and co-workers produced seed particles capped by cetyltrimethylammonium bromide (CTAB) with dimensions below 4 nm already at 30 °C. The surfactant CTAB is a common stabilizing agent that can direct the synthesis of aqueous gold nanoparticles with various shapes as discussed in section 2.1.2.¹¹⁵ Using seed-mediated growth, spherical CTAB-functionalized AuNPs in the range of 10 to 200 nm can be synthesized.^{116,117} Besides small molecules (trisodium citrate or CTAB) polymers can also be utilized as capping agents for aqueous AuNPs. Common water-soluble polymers used to stabilize AuNPs are polyvinylpyrrolidone (PVP)¹¹⁸ and poly(vinyl alcohol) (PVA).¹¹⁹ Polymers such as PVP can simultaneously act as capping and reducing agents.

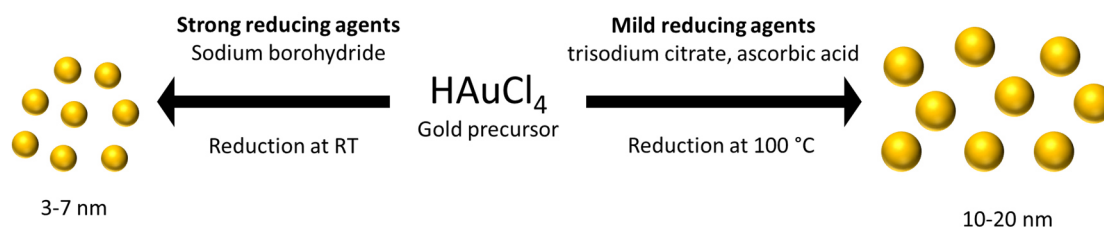


Figure 2-2: Influence of the reduction agent on the particle size and the synthesis temperature in the fabrication of aqueous AuNPs.

The synthesis in non-polar organic solvents yield only small particles (<10 nm). Mostly thiol- or amine-terminated molecules are used as stabilizing agents.^{120,121} In 1994, Brust and Schiffrin first published a two-phase method yielding monodisperse thiolate-capped AuNPs, which are stable in many organic solvents.¹²¹ Until today, the Brust-Schiffrin method and its modifications are common routes for the synthesis of AuNPs in non-polar media.

2.1.2 Synthesis of aqueous anisotropic gold nanorods (AuNRs)

The most established protocol for the synthesis of aqueous gold nanorods (AuNRs) with high monodispersity and good size and shape control is a seed-mediated route. Small seed particles are formed under conditions favoring rapid nucleation. Subsequently, these seeds are further grown to AuNRs in a slow growth step under mild reducing conditions. Different parameters such as type of seeds, surfactants, addition of silver ions, temperature or pH, can influence the size, morphology and yield of the synthesized AuNRs.

The classical surfactant employed in AuNRs synthesis is CTAB. Cationic surfactants (e.g. CTAB) are able to form cylindrical micellar structures. The original idea implied that these surfactant micelles lend the AuNRs colloidal stability and act as “soft templates” to direct the anisotropic growth of spherical seeds to AuNRs.^{122,123} Further studies showed that AuNRs are surrounded by a CTAB bilayer.^{124,125} In the inner layer, the CTAB molecules adsorb to the gold surface by the trimethylammonium headgroups, while in the outer layer these polar headgroups face the solvent to achieve water solubility. Both layers are connected by van der Waals interactions between adjacent surfactant chains.

The trimethylammonium headgroup of CTAB seems to be crucial for the successful synthesis of AuNRs. Variation of the trimethylammonium headgroup leads to the formation of spherical particles instead of AuNRs.¹¹⁵ The trimethylammonium headgroup preferentially binds to the high-energy side facets of the AuNRs, blocking these facets for further growth.^{124,125} The stronger attachment of CTAB to the side facets guides the anisotropic growth of the gold nanorods. While the structure of the surfactant headgroup is important for the growth of AuNRs, the exact chain length of the surfactant has minor influence.¹²⁴ However, the carbon tail should be long enough to promote colloidal stability.¹²⁴ Experimental studies revealed the importance of the surfactant’s counter ion. Attempts to replace the bromine ion of CTAB by other halides in the synthesis of monodisperse AuNRs failed. The existence of bromine ions in the reaction solution appears essential for the symmetry breaking process to form anisotropic nanorods out of isotropic spherical seeds.^{126,127} Tetrachloroauric acid HAuCl_4 is the most common gold precursor in the synthesis of aqueous AuNRs. Based on the ligand field theory, the

complexation strength for Au(III) is stronger for bromine ions than chlorine ions.¹²⁸ During the synthesis of gold nanorods, the chlorine ions of AuCl_4^- are immediately replaced by bromine ligands of the CTAB surfactant as depicted in equation 2-1.



The ligand exchange of chlorine by bromine ions results in a color change of the growth solution from yellow to orange.¹²⁸ The groups of Murphy and Jin reported that bromide ions adsorb on the surface of the growing AuNRs.^{129,130} This was further supported by mass spectroscopy, Raman spectroscopy and X-ray photoelectron spectroscopy (XPS), which identified Au-Br species in the final AuNRs.^{131–133} Additionally, the cationic surfactant CTAB also forms complexes with the gold precursor (AuBr_4^- -CTAB⁺).^{128,134} Both, the ligand exchange and the complex formation lower the redox potential of the gold precursor.¹³⁵ This affects the choice of the right reducing agent in the final growth step. Strong reducing agents such as sodium borohydride (NaBH_4) are required for the production of small seed particles. In contrast, the growth of AuNRs is performed under mild reducing conditions using weak reductants. The most widely used mild reducing agent for the synthesis of gold nanorods is ascorbic acid.^{136,137} At pH values below 9, ascorbic acid is not able to reduce the gold precursor to elemental gold.¹²⁸ This prevents the secondary nucleation in the growth solution. The complete reduction of the gold salt by ascorbic acid is only possible in the presence of the seed particles acting as nuclei in the growth solution.

In the growth solution with HAuCl_4 and CTAB, the gold precursor is reduced to Au(I) after the addition of ascorbic acid (see equation 2-2). Due to the reduction of Au(III) to Au(I), the growth solution turns colorless.



In the second reduction step seed particles are added to the growth solution, which act as catalyst for the reduction of Au(I) to Au(0). The reduction only takes place at the electron-rich surface of the seed particles.^{128,138} Two different mechanisms for the final reduction step are discussed in literature: (1) the formation of elemental gold occurs by a

disproportionation reaction according to equation 2-3, resulting in Au(0) and Au(III).^{128,138}



The oxidized species Au(III) is directly reduced to Au(I) again by the remaining reducing agent in the growth solution. (2) *in-situ* reduction of Au(I) by the Au(0) surface of the seeds (see equation 2-4).^{117,139} The Au(0) surface of the seeds extracts electrons from the reductant to catalyze the reduction step.



The seed particles are essential for the reduction and influence the morphology of the synthesized AuNRs. Murphy and co-workers established the first synthesis route for AuNRs based on citrate-capped seeds.^{123,140} These seed particles with diameters of 3 nm to 4 nm possessed twinned structures.^{123,141} Citrate-stabilized seeds are used in a silver-free synthesis resulting in pentatwinned gold nanorods. The tips of these AuNRs consists of {111} facets, while the sides of the AuNRs are terminated by {100} facets.¹⁴⁰ Complex purification processes are required to remove byproducts, since the shape yield of pentatwinned AuNRs is low (< 30%).

In contrast, shape yields above 90% can be achieved by the aqueous synthesis of single-crystalline AuNRs.^{115,128} This method was first established by Nikoobakht and El-Sayed in 2003.¹¹⁵ They used seeds which were functionalized by CTAB. These seed particles are single crystals with diameters below 2 nm.^{115,141} The tips of single-crystalline AuNRs are enclosed by {111} and {100} facets, while some lateral facets are composed of the highly energetic {110} planes, which are not present in pentatwinned AuNRs.^{142,143} While pentatwinned AuNRs possess larger dimensions and higher aspect ratios, the synthesized single-crystalline AuNRs are usually smaller and their aspect ratios are lower. The longitudinal mode of the surface plasmon resonance (SPR) is located in the near-infrared (NIR) region for pentatwinned AuNRs. The position of the longitudinal SPR peak of single-crystalline AuNRs can be adjusted from the visible to the NIR range by carefully controlling their size due to extensive process control.¹²⁸

The successful synthesis of single-crystalline AuNRs requires CTAB-capped seed particles and the presence of silver ions in the growth solution. Silver nitrate AgNO_3 is usually added during the synthesis. The exact role of silver ions in the synthesis of aqueous AuNRs is not clear yet. Different mechanisms are discussed in literature. One is silver underpotential deposition (UPD) on specific gold facets.^{126,141,144,145} UPD describes the reduction of a noble metal at potentials above its Nernst potential.¹²³ The seed particles drain electrons from the reducing agent and become cathodically polarized.¹²³ This allows the UPD of silver ions even under the acid conditions ($\text{pH} \approx 3$) of the growth solution.^{123,146} The UPD shift increases with the coordination number of the adsorbed silver ions,¹²³ so that the reduction of Ag(I) to Ag(0) occurs preferentially on the lateral $\{110\}$. The formation of Ag monolayers on these facets hinders crystal growth along these crystal planes. As a result, the $\{100\}$ and $\{111\}$ facets grow faster, resulting in anisotropic growth along the $[100]$ direction.¹²³ Another proposed mechanism assumes the blocking of specific facets by AgBr- or cetyltrimethylammonium- Br-Ag^+ complexes.^{133,144,146} These complexes adsorb to the lateral facets and hinder gold addition to these crystal planes. Similar to the UPD, the capping of the side facets leads to anisotropic growth of AuNRs.

The incorporation of 2% to 9% silver into gold nanorods was proved by XPS, surface-enhanced Raman spectroscopy (SERS) and inductively coupled plasma mass spectrometry (ICP-MS).^{132,147} While the presence of silver ions is crucial for the synthesis of single-crystalline AuNRs, these ions inhibit the formation of pentatwinned AuNRs. Therefore, the latter are usually synthesized under silver-free conditions. Figure 2-3 gives an overview about the general requirements for the synthesis of single-crystalline and pentatwinned AuNRs.

New strategies in the aqueous synthesis of AuNRs include the use of additives such as aromatic and aliphatic molecules or inorganic cations and anions.¹²⁸ Most popular is the use of a second surfactant in addition to CTAB. The introduction of salicylic acid or sodium oleate to the growth solution overcomes the limitations of the classical CTAB route.^{148–150} These additives allow a good control of the size and monodispersity of the produced AuNRs. Binary surfactant mixtures enable the synthesis of AuNRs over a larger range of dimensions with tunable longitudinal surface plasmon resonances. The

additional surfactants also improve the reproducibility of the gold nanorod synthesis. The second surfactant can interact with CTAB molecules, leading to its incorporation to the CTAB bilayer.¹⁴⁹ This affects the interactions between CTAB and the growing AuNRs and further stabilizes the cylindrical structure of the CTAB micelles.^{148,149}

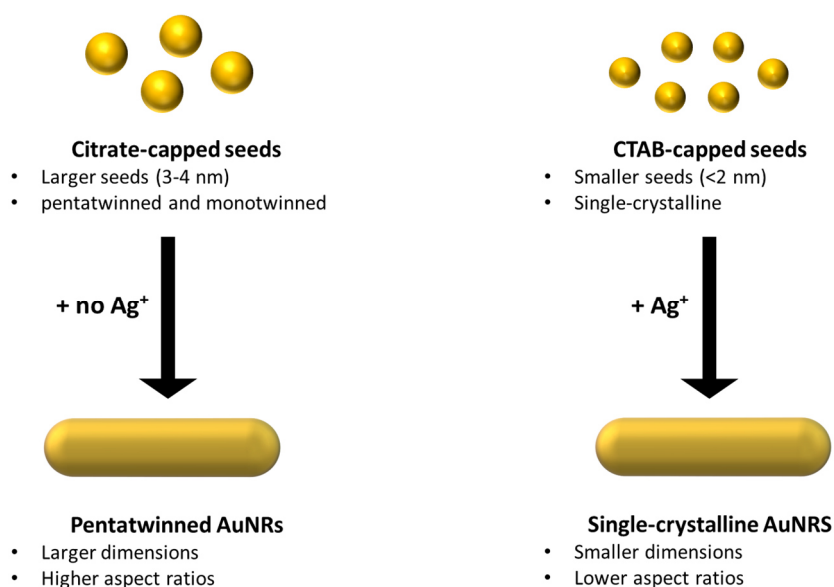


Figure 2-3: Differences in the synthesis of pentatwinned and single-crystalline AuNRs.

Besides the seed-mediated growth, AuNRs can also be synthesized by electrochemical^{151,152} and photochemical methods^{153,154} or by the “hard” template technique, in which AuNRs are prepared by the deposition of gold inside the pores of nanoporous alumina or polycarbonate (PC).^{155–159}

2.1.3 Electrical properties of conductive nanoparticle films

Films made of various gold nanocrystals are less conductive than bulk gold (Table 2-1), which possesses an electrical conductivity σ of $4.2 \cdot 10^5$ S/cm (electrical resistivity ρ of $2.35 \cdot 10^{-6}$ $\Omega \cdot \text{cm}$).¹⁶⁰ The conductivity in nanocrystals films is reduced by stronger electron scattering than in the bulk material.^{161–163} Since nanoparticles are often smaller than the mean free path of electrons, elastic and inelastic scattering occurs in nanocrystal layers, which decreases the electrical conductivity.^{161,163}

Table 2-1: Electrical conductivities of films composed of various gold nanocrystals stabilized by different organic ligands. Conductivities of systems marked with * were determined after sintering of the layers. Table partially adapted from [164].

Type of gold nanocrystal	Ligand	Conductivity [S/cm]
AuNPs(*) ¹⁶⁵	oleylamine	$3.1 \cdot 10^5$
AuNPs(*) ¹⁶⁶	1-butanethiol	1497
AuNPs ¹⁶⁷	citrate	4545.5
AuNPs ¹⁶⁸	citrate	2227.2
AuNPs ¹⁶⁹	chalcogenide ligand $\text{Na}_4\text{Sn}_2\text{S}_6$	>1000
AuNPs ¹⁷⁰	4-nitrophenol	750
AuNPs ¹⁷⁰	thiophenol	100
AuNPs ¹⁷⁰	4-methoxythiophenol	1
AuNPs ¹⁶⁷	mercaptopropionic acid	0.625
AuNPs ¹⁶⁷	tris(4,6-dimethyl-3-sulfonatophenyl)phosphine trisodium salt hydrate	0.333
AuNPs ¹⁷¹	1,3-propanedithiol	$0.103, 2.89 \cdot 10^{-2}$
AuNPs ^{172,173}	1,6-hexanedithiol	$4.2 \cdot 10^{-2}, 3.73 \cdot 10^{-2}$
AuNPs ¹⁷¹	1,5-pentanedithiol	$2.26 \cdot 10^{-2}, 6.84 \cdot 10^{-3}$
AuNPs ¹⁶⁷	bis(p-sulfonatophenyl)phenylphosphine dihydrate dipotassium	$7.5 \cdot 10^{-3}$
AuNPs ¹⁷¹⁻¹⁷⁴	1,9-nonanedithiol	$2.06 \cdot 10^{-3}, 1.5 \cdot 10^{-3}, 3.38 \cdot 10^{-4}, 3.32 \cdot 10^{-4}$
AuNPs ^{175,176}	terthiophene derivatives	$1 \cdot 10^{-3}, 2 \cdot 10^{-4}, 4.8 \cdot 10^{-8}$
AuNPs ¹⁷¹⁻¹⁷⁴	1,8-octanedithiol	$7.93 \cdot 10^{-4}, 6.38 \cdot 10^{-4}$
AuNPs ¹⁷¹	1,10-decanedithiol	$3.12 \cdot 10^{-4}, 2.10 \cdot 10^{-4}$
AuNPs ^{172,173}	1,12-dodecandithiol	$2.30 \cdot 10^{-4}, 4.1 \cdot 10^{-5}$
AuNPs ¹⁷²	1,16-hexadecanedithiol	$4.81 \cdot 10^{-5}$
AuNPs ¹⁷⁷	6-(3-thienyl)hexanethiol	$2.0 \cdot 10^{-5}$
AuNPs ¹⁶⁷	11-mercaptopundecanoic acid	$4.5 \cdot 10^{-6}$
AuNPs ¹⁷⁵	thiolated pyrrole derivatives	$3 \cdot 10^{-7}$
AuNPs ¹⁷⁷	12-(3-thienyl)-dodecanethiol	$7.8 \cdot 10^{-8}$
AuNRs ⁶⁹	PTEBS	1429

There are significant differences in the detected electrical conductivities of various gold nanoparticle films (Table 2-1). Nonetheless, two trends can be identified in electrical conductivities of AuNPs layers. First, sintered films possess higher conductivities than non-sintered ones and second, the electrical properties of gold nanocrystals depend on the stabilizing organic ligands. According to Table 2-1, ligands containing unsaturated groups (e.g. aromatic motifs) enhance the electrical conductivity of AuNPs over those of saturated ligands. One special example in Table 2-1 are the AuNRs stabilized by PTEBS.

Their excellent electrical conductivity is based on their sinter-free nature comparable to the gold-polythiophene nanocrystals introduced in this work.

Sintering and the choice of ligand affect the inter-particle contacts between adjacent AuNPs, which are important, since charge transport in nanoparticle films require the formation of a percolating conductive network.¹⁷⁸ Classic percolation theory^{179,180} predicts different regimes for films consisting of randomly oriented nanocrystals that form a 3D network:^{161,181}

- (a) Insulating region: the nanocrystals are not in contact and conduction can only occur via tunneling processes.
- (b) Transition region: transition from insulation to bulk region at a critical volume fraction of nanocrystals, the percolation threshold Φ_c , conducting paths are formed throughout the whole film along which charge transport occurs.
- (c) Bulk region: many nanoparticles are in contact with each other forming continuous pathways for charge carriers throughout the entire film. In this regime metallic conduction comparable to continuous metal films occurs.

The conductivity of nanoparticle films close to the percolation threshold scales with a characteristic power law given in equation 2-5:^{182–184}

$$\sigma \propto \sigma_0 \cdot (\Phi - \Phi_c)^t \quad (2-5)$$

Where σ is the conductivity of the nanocrystal film and σ_0 a pre-exponential factor that depends on the conductivity of the nanocrystals, their contact resistance and network topology.^{185,186} The volume fraction is given by Φ , while Φ_c defines the percolation threshold. The critical exponent t describes the connectivity of nanocrystals¹⁸⁶ and is about 2 for random 3D networks, while in 2D networks the critical exponent t is reduced to about 1.33.^{179,180,186}

Simulations predict a percolation threshold Φ_c of 18-20 vol% for randomly packed hard spheres^{187,188} and of about 29 vol% for randomly packed overlapping (soft) spheres in a 3D network.^{189–191} Computational studies revealed that the theoretical threshold Φ_c of randomly packed spheres can be slightly lowered by the introduction of polydispersity,^{192,193} since smaller spheres can fill in the voids of the network formed by

the large spheres. Theoretical models further showed that the percolation threshold Φ_c is inversely proportional to the aspect ratio (ratio between length L and width w) of anisotropic nanocrystals.^{194,195} Thinner and longer nanocrystals such as nanowires or nanorods can significantly decrease the percolation threshold Φ_c .¹⁸²

Percolating nanocrystal films resemble three-dimensional infinite resistor networks, in which the collective resistance is directly proportional to the individual (uniform) resistivity of each resistor.^{196,197} The contact resistance R_c at nanoparticle junctions dominates the overall resistance of the nanoparticle films.^{198–203} High contact resistances R_c can be attributed to poor contacts between the particles (e.g. due to insulating ligands), or small contact areas at the particle junctions.¹⁸³ Strategies to improve the electrical conductivity of nanocrystal films often include methods to reduce the contact resistance between the individual particles. Computational and experimental studies showed that the overall conductivity for films consisting of carbon nanotubes scale linearly with the number density of junctions, while it is inversely proportional to the contact resistance as (equation 2-6).^{204,205}

$$\sigma = \frac{K \cdot V_f^2}{R_c \cdot D} \quad (2-6)$$

In equation 2-6, σ is the conductivity of the nanotube film, K is a proportionality factor, V_f is the film fill-factor, D is the diameter of the nanotube bundles and R_c is the contact resistance.²⁰⁴ Equation 2-6 clearly shows that lowering the contact resistance R_c directly enhances the overall conductivity.

One strategy to lower the contact resistance R_c is reducing the number of contacts in a given area fraction.²⁰³ This can be obtained by replacing spherical nanoparticles with anisotropic nanocrystals and by increasing the aspect ratio of nanowires.²⁰⁶ Experiments revealed that silver nanowire (AgNW) networks (high aspect ratio structures) are more electrically conductive, due to the reduced amount of contacts than films prepared from spherical silver nanoparticles (AgNPs).²⁰³ Further increase in the electrical conductivity of AgNWs films was observed by enhancing the length of the AgNWs.^{203,207}

Another way to lower the contact resistance R_c is based on increasing the contact areas between adjacent nanocrystals. This can be done by welding,^{198,201,208} mechanical pressing^{202,209} and sintering.^{203,210,211} Sintering can be conducted by a classical thermal annealing treatment at evaluated temperatures ($>200^\circ\text{C}$) after film deposition.^{203,210,211} Alternative sintering methods have been developed, which can be performed at lower temperatures and even ambient conditions. Such new sintering methods of nanocrystal films include microwave^{60,61,212}, plasma^{59,213} or chemical treatments.^{67,214,215} Nanocrystals can also be sintered by applying a current^{64,65} or by irradiation with intensive light.^{216–218} Metal atoms diffuse to the contact area at the particle-particle junctions in the sintering process, leading the particles to merge (necking).^{203,210,211} This process improves the contact between the nanocrystals and enhances the contact area, which lowers the contact resistance R_c and enhances the overall electrical conductivity in the nanocrystal films.^{203,210,211} The increase in contact area between nanocrystals upon sintering is mostly accompanied by decomposition of the ligand molecules present at the particle junctions and the choice of ligands can influence the sintering behavior of the nanocrystal films. For example, Gupta *et al.* showed that the sintering temperature of AuNPs stabilized by alkanethiols can be decreased from about 200°C to below 160°C by decreasing the number of carbon atoms in the alkane chain of the ligand from eight (1-octanethiol) to four (1-butanethiol).^{166,164}

Percolation theory predicts that nanoparticle films become conductive upon the formation of percolating networks. Charge transport in non-sintered nanocrystal films is limited and metallic conduction is often not obtained even if percolation is achieved due to the organic ligands present at the nanocrystals' interfaces. These ligands are important for the synthesis and the colloidal stability of nanocrystals (section 2.1.1 and 2.1.2), but they act as insulating barriers inhibiting direct contact between adjacent metallic nanoparticles. This increases the contact resistance R_c at the interfaces and reduces the overall electrical conductivity of the nanocrystal films. The most prominent charge transport mechanisms in non-sintered nanoparticle films are tunneling and hopping. For example, Murray and co-workers detected electrical conductivity based on electron tunneling in films made of alkanethiol-functionalized gold nanoparticles or gold clusters.^{161,219,220} They further showed that the conductivity σ at various temperatures exponentially depends on the

number of carbon atoms n of the alkanethiol ligands. This relation is illustrated in equation 2-7, where β_n is the conductance decay constant, which determines the distance over which charge is transported by tunneling.^{161,219,220}

$$\sigma \propto \exp(-\beta_n \cdot n) \quad (2-7)$$

The dimensions of the alkanethiol ligands determine inter-particle spacing. Equation 2-7 reveals that with increasing distance between gold nanoparticles due to longer ligands the tunneling rate is decreased. Charge transport properties in non-sintered nanoparticle films can be improved by lowering conductance decay constants β_n of the ligands. Higher electrical conductivities and smaller conductance decay constants β_n in AuNPs films were achieved by replacing the saturated alkanethiol ligands with alkanedithiols¹⁷² or unsaturated π -conjugated ligands (alkene- or arenethiols).^{172,161,221,222}

Unsaturated π -conjugated ligands are beneficial for the electrical properties of nanoparticle films. While saturated ligands (e.g. alkanethiols) have a large gap between their highest occupied molecular orbital (HOMO) and lowest unoccupied molecular orbital (LUMO), the HOMO-LUMO gap of unsaturated π -conjugated ligands is much smaller.²²³ For example, the energy difference between the HOMO and LUMO $E_{\text{HOMO-LUMO}}$ is only 4 eV for the phenyl ring, while it is about 8 eV for alkyl chains.²²⁴ Additionally, the HOMO level of unsaturated π -conjugated ligands is often closer to the Fermi level of metal nanoparticles.²²³ Both effects cause better energy level alignment at the metal-ligand interfaces, which facilitates charge transfer in nanocrystal films. I will further focus on the energy level alignment between the metal nanoparticles and the surrounding organic ligands in section 2.1.4.

Tunneling in non-sintered nanocrystal films only occurs over short distances (in alkane ligands 2-3 nm).²²³ Charge transport over longer distances happens by hopping,²²³ where in electron hopping electrons move from an occupied state of the metal to an unoccupied state (molecular orbital) of the organic ligand or vice versa.¹⁶¹ Charge transport by hopping in organic ligands is based on hopping of charge carriers (electrons or holes) from one state to the other along the molecule.²²³ Due to the smaller HOMO-LUMO gap and the better energy level alignment at the metal-organic interface, unsaturated ligands enable both, tunneling and hopping, while charge transport processes in saturated ligands

is restricted to tunneling. Tunneling is the most dominant charge transport mechanism for small unsaturated π -conjugated molecules.²²³ With increasing length of the unsaturated π -conjugated molecules tunneling is replaced by long-range hopping processes.²²³ Charge transport along the long polymer chains of the unsaturated polythiophene ligands used in this work should occur via hopping and depends on the intrinsic electrical conductivity of the polythiophene.

The following chapters show that films made of gold-polythiophene hybrid nanocrystals are electrically conductive after deposition without post-treatment. I will illustrate that the contact resistance R_c in these hybrid layers between the nanocrystals is influenced by the molecular assembly of the polythiophene chains in the ligand shell (chapter 3.1). Furthermore, I will demonstrate that polythiophene ligands align energetically well with gold nanoparticles (chapter 3.2) and that tailoring the molecular structure of the polythiophene ligands can further improve the energy level alignment at the gold-polythiophene interfaces, increasing the electrical conductance in hybrid nanoparticle films.

2.1.4 Energy level alignment at metal-organic interfaces

The energetic match of the metal's Fermi level E_F with the HOMO and LUMO of organic compounds sets the efficiency of the charge carrier transfer between organic ligands and metallic nanoparticles. This energy level alignment and the resulting injection barriers for charge carriers (electrons and holes) were already addressed in many reviews.^{83–86} Therefore, I will briefly summarize the principles of energy level alignment and charge carrier transfer.

In a metal the Fermi level E_F represents the boundary between unoccupied and occupied states.²²⁵ The Fermi level can be determined by measuring the work function Φ_m . This positive quantity describes the energy gap between the Fermi level E_F and the vacuum level E_{vac} .^{83,85,225} The work function Φ_m and the position of the Fermi level can be determined experimentally, e.g. by ultraviolet photoelectron spectroscopy (UPS). The exact work function Φ_m of metal surfaces strongly depends on the crystallographic

orientation, the purity and the processing method.²²⁵ Reported work functions Φ_m of clean gold surfaces vary between 5.1 eV and 5.47 eV.^{226–228}

Charge transport between the metal and the organic ligand can depend on electron affinity (EA) and ionization energy (IE) of the ligands, which are set by the HOMO and LUMO levels. The ionization energy is a positive quantity defined as the energy difference between the HOMO of the ligand and the vacuum level E_{vac} , while the energy difference between the vacuum level E_{vac} and the LUMO of the ligand determines the EA (positive quantity) as illustrated in Figure 2-4. Electrons will flow from the metal nanoparticle to the surrounding ligand shell if the metal's work function is larger than the ionization energy of the ligand. This is the case when the LUMO of the ligand lies below the Fermi level of the metal ($E_F > E_{LUMO}$).⁸⁶ Conversely, electrons flow from the organic ligand to the metal core, if the electron affinity of the ligand is larger than the metal's work function. In this case, the HOMO of the ligand lies above the Fermi level of the metal ($E_F < E_{HOMO}$). If no external potential is applied, there will be no charge transfer between the metal nanoparticle and the surrounding ligand shell if the Fermi level of the metal is located between the HOMO and the LUMO of the ligands.

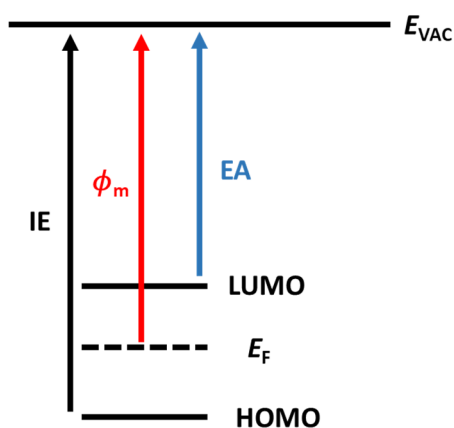


Figure 2-4: Definitions of work function Φ_m , ionization energy IE and electron affinity EA for an organic semiconductor. E_{vac} defines the vacuum level.

The injection barriers for charge carriers (electrons and holes) across the metal-organic interfaces are determined by the following equations.^{83,85,86}

$$\Phi_B^e = \Phi_m - EA \quad (2-8)$$

$$\Phi_B^h = IE - \Phi_m \quad (2-9)$$

Φ_B^e : injection barrier for electrons

Φ_B^h : injection barrier for holes

Φ_m : work function of the metal

EA: electron affinity of the organic compound

IE: ionization energy of organic compound

Charge transfer processes between metallic nanocrystals and organic ligand shells can be described by the Integer Charge-Transfer (ICT) model.^{83–86} Figure 2-5a illustrates a case where the metal's Fermi level lies below the energetic position of the HOMO (E_{HOMO}). Electrons will flow spontaneously from the organic ligands to the metallic nanocrystals. The polymer ligands become positively and the metallic nanocrystals negatively charged. This creates a dipole at the metal-organic interface which lowers the vacuum level E_{vac} by the amount Δ as depicted in Figure 2-5a. The dipole will grow until the HOMO level of the polythiophene ligand aligns with the metal's Fermi level ($E_F = E_{\text{HOMO}}$) in equilibrium.

Electrons will spontaneously flow from the metal nanoparticles to the surrounding organic ligands if the energetic position of the ligand's LUMO (E_{LUMO}) lies below the metal's Fermi level (Figure 2-5c). The metal nanoparticles become positively and the organic ligands negatively charged. This creates a dipole at the metal-organic interfaces, which increases the vacuum level E_{vac} (Figure 2-5c). The dipole will grow until an equilibrium is reached when the LUMO level of the organic ligand aligns with the metal's Fermi level ($E_F = E_{\text{LUMO}}$). The alignment of the metal's Fermi level with the HOMO or LUMO of the organic compound is called Fermi-level pinning (Figure 2-5a and c).^{84,86} If the Fermi level of the metal lies between the E_{HOMO} and E_{LUMO} level of the organic ligand, no charge is transferred if no external potential is applied. This phenomenon is referred as vacuum level alignment and it is depicted in Figure 2-5b.⁸⁴

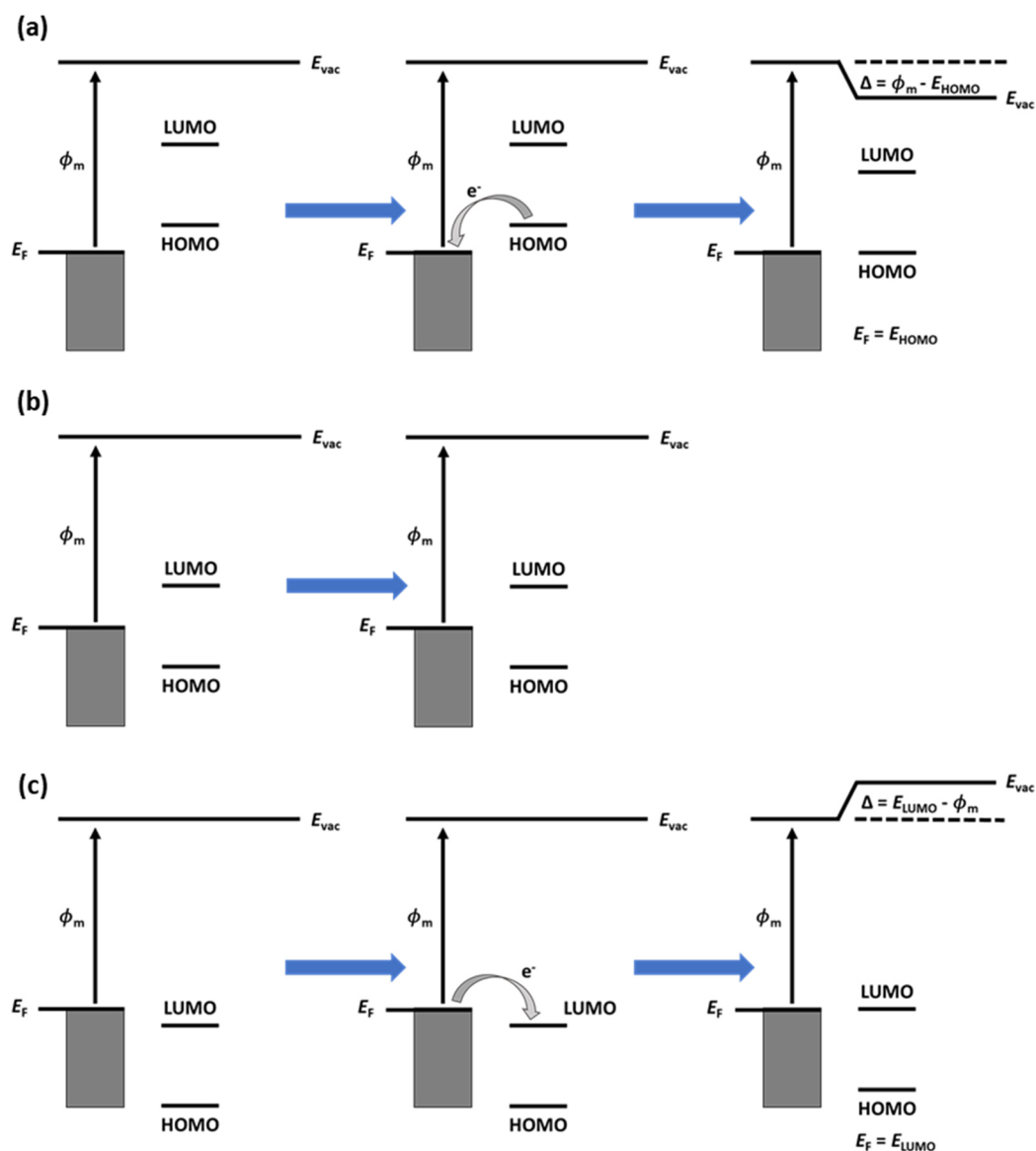


Figure 2-5: Schematic illustration of energy level alignment at the metal-organic interface when (a) $\Phi_m > E_{HOMO}$ (Fermi level pinning to HOMO level E_{HOMO}), (b) $E_{LUMO} > \Phi_m > E_{HOMO}$ (vacuum level alignment) and (c) $\Phi_m < E_{LUMO}$ (Fermi level pinning to LUMO level E_{LUMO}). Electron flow between metal and organic compound creates a dipole, which causes a shift Δ of the vacuum level E_{vac} . Figure adapted from [84,86].

The ICT model applies for systems with negligible hybridization between the metal wave functions and the molecular orbitals of the organic parts. In general, no hybridization occurs if metal-organic interfaces are created under ambient conditions e.g. by casting or printing of polymers on metal substrates.^{84,86} For stronger interactions with hybridization, the much more complex Induced Density of Interface States (IDIS) model has to be used

in order to describe charge transfer between the metal and the organic components. Due to the expected strong interactions between the gold nanocrystals and the polythiophene ligands, the IDIS model would provide a precise picture of the energetic situation at the gold-polythiophene interfaces. However, IDIS modelling requires complex computational simulations. Although the ICT model is less precise than the IDIS method for systems with hybridization, it can still provide an approximated picture and identify trends in the charge transfer at metal-organic interfaces. For reasons of simplicity, I applied the ICT model in this work to quantify differences in the energy level alignment between gold nanocrystals and various polythiophene ligands possessing different energetic structures of their molecular orbitals (HOMOs and LUMOs) and I correlated this energetic match with the overall electrical properties of the diverse gold-polythiophene nanoparticles.

2.2 Conductive polythiophenes

Polythiophenes, a class of conductive polymers (CPs), are the ligands of the gold-polythiophene hybrid nanocrystals introduced in this work. Literature reports strong bonds between sulfur species and gold (Au-thiolate bond strength is 167-184 kJ·mol⁻¹ and Au-S bond dissociation energy is 418 kJ·mol⁻¹).²²⁹⁻²³¹ Hence, sulfur-containing polythiophenes are promising ligand materials for gold nanoparticles, yielding stable hybrid materials. The resulting features of these hybrids are not only determined by the gold cores, but also by the polymer ligand shells. This chapter gives a detailed overview about the characteristics of CPs, focusing especially on polythiophenes.

Section 2.2.1 surveys various synthesis routes of CPs. A good understanding of electrical conductivity in conductive polymers is crucial to distinguish how gold-polythiophene interactions can affect the electrical properties of the hybrid materials. Section 2.2.2 explains the principles of charge transport in conductive polymers. One important factor affecting the electrical features of polythiophenes is their molecular arrangement, since highest electrical conductivity occurs along their conjugated polymer backbone and the π - π stacking direction.⁷⁰⁻⁷⁴ Sections 2.2.3 and 2.2.4 summarize the current state of the art

in the molecular assembly of polythiophenes on planar inorganic substrates and nanomaterials.

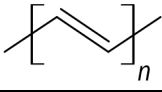
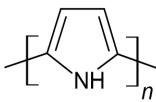
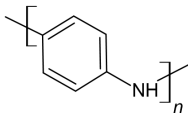
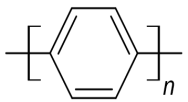
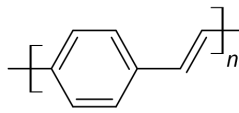
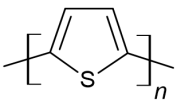
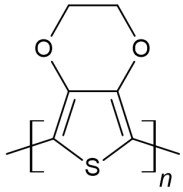
2.2.1 Synthesis and internal structure of conductive polymers

Shirakawa *et al.* found in 1977, that polyacetylene becomes electrically conductive upon doping with oxidizing and reducing agents.²³² This discovery marks the beginning of conductive polymers (CPs), that combine the high electrical and thermal conductivity of metals with the scalable synthesis routes and the variability in processing of polymers. Since Heeger, MacDiarmid and Shirakawa were awarded the Nobel Prize for their development of new CPs in 2000,^{233,234} CPs gained interest in industry and research. The structures and the electrical properties of some conventional CPs are shown in Table 2-2.^{235–239} They are unsaturated and have a conjugated backbone system. Besides strong σ -bonds, CPs possess π -bonds that determine their electrical conductivity.²³⁹ Adjacent π -orbitals lead to delocalized charge carriers along the polymer backbone.²³⁴

Polythiophenes (Phs) combine good chemical and environmental stability with electrical conductivity and their simple processability by solution techniques including different types of printing (inkjet or screen printing).^{240–242} Due to the conjugated backbones, polythiophenes are relatively stiff and sterically hindered. The persistence length l_p defines the flexibility of polymers.²⁴³ It is approximately 3 nm for polythiophenes,^{243–245} which is longer than the l_p of classical polymers such as polyethylene ($l_p=0.7$ nm)²⁴³ or polyisoprene ($l_p=0.43$ nm).²⁴⁵ This high rigidity facilitates dense packing of polythiophene chains, which supports intra- and inter-molecular charge carrier transport (section 2.2.3).⁷⁴ The extended π -systems lead to strong π - π -stacking interactions between individual polythiophene chains.²⁴⁶ Stacking of the regioregular poly(3-hexylthiophene-2,5-diyl) (P3HT), the most popular and best-studied polythiophene, is illustrated in Figure 2-6. The π - π stacking distance of P3HT chains is approximately 0.38 nm.^{247–249} Additional stacking along the alkyl side chain direction in P3HT films is called lamellar stacking. Based on the stacking interactions, P3HT crystallizes in an orthorhombic cell (Figure 2-6): $1.60 \text{ nm} \leq a \leq 1.68 \text{ nm}$, $0.76 \text{ nm} \leq b \leq 0.78 \text{ nm}$, $0.77 \text{ nm} \leq c \leq 0.78 \text{ nm}$.^{250,251}

The cell parameter b is twice the π - π stacking distance. Ordering guided by stacking interactions is important for inter- and intra-chain charge transport.

Table 2-2: Structure and highest achieved electrical conductivity values of common conductive polymers. The given conductivities are for polymers in their doped (not native) form. The data are based on [237,239,252,253].

Polymer	Structure	Conductivity [S/cm]
Polyacetylene		$10^3\text{--}1.7\cdot 10^5$
Polypyrrole (PPy)		$10^2\text{--}7.5\cdot 10^3$
Polyaniline (PANI)		30–200
Poly(p-phenylene)		$10^2\text{--}10^3$
Poly(p-phenylenevinylene)		$3\cdot 10^3\text{--}5\cdot 10^3$
Polythiophene (Ph)		$10\text{--}10^3$
Poly(3,4-ethylenedioxythiophene) (PEDOT)		0.4–400

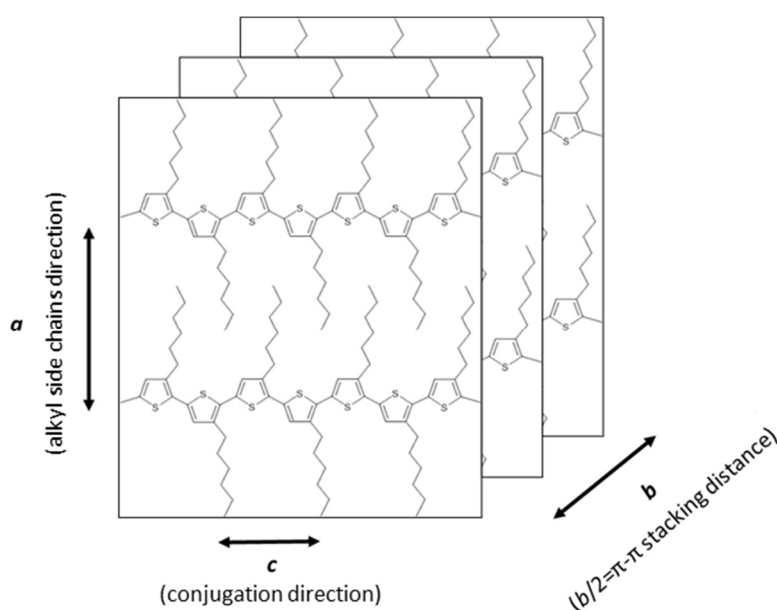


Figure 2-6: Stacking arrangement of P3HT chains. The parameters a , b and c define the orthorhombic unit cell of crystallized P3HT. The π - π -stacking distance is $b/2$.

The synthesis of CPs can be done by chemical or electrochemical methods. Both routes work under oxidative conditions,^{254–257} causing *in-situ* doping of the polymers during synthesis. Doping is crucial to obtain highly conductive CPs (section 2.2.2). Chemical synthesis is performed in a suitable solvent containing the monomer and an oxidizing agent (e.g. ferric chloride, ammonium persulfate). Usually, chemical routes lead to the formation of polymer solutions, polymer powder or thick polymer films. Chemical methods allow the large-scale polymerization of CPs, making these routes ideal for commercial bulk production²³⁹ In electrochemical synthesis the monomer is oxidized by applying an electrical current and the polymer chains deposit on the electrode as thin films (down to 20 nm).^{254,257,258} Electrochemical synthesis is limited to monomers, that can be oxidized by applying an electrical potential.²⁵⁸ Most CPs, including PPy, PANI and polythiophenes, can be synthesized by electrochemical and chemical methods.

CPs such as PANI and PPy are single polymers, while poly(3,4-ethylenedioxythiophene) polystyrene sulfonate (PEDOT:PSS) is a blend, consisting of the conductive polymer PEDOT and the water-soluble sodium polystyrene sulfonate (PSS), which is a polyelectrolyte. Due to its high electrical conductivity and excellent environmental stability, PEDOT:PSS is the most widely used conductive polymer in different

application fields.^{259–262} In this polymer blend, the negatively charged PSS acts simultaneously as doping agent and dispersant.^{263,264} PEDOT is considered insoluble in water. PSS can surround the PEDOT chains in aqueous solution, leading to a stable PEDOT:PSS dispersion, containing nanometer-sized polymer particles.²⁶³

2.2.2 Electrical properties of conductive polymers

Overlapping of π -orbitals in conductive polymers leads to a band structure similar to that present in inorganic semiconductors. The lower edge of the conduction band is assigned to the lowest unoccupied molecular orbital (LUMO), while the upper edge of the valance band is attributed to the highest occupied molecular orbital (HOMO) of the polymer. The energetic HOMO-LUMO difference defines the bandgap of the CPs. A characteristic parameter describing the degree of charge carrier delocalization is the conjugation length. This length scale refers to the point where adding extra monomer units does not alter the electronic structure of the polymer any more. With increasing conjugation length, the carrier mobility and with this the internal conductivity increase.

Inter- and intra-chain hopping processes dominate charge carrier transport in CP films.²⁴⁷ The molecular arrangement has a strong impact on these hopping mechanisms and the intrinsic electrical properties of the polymers.^{265,266} Carrier hopping is a thermally activated process. The temperature dependence of the conductivity can be described in terms of Mott variable range hopping (equation 2-10):^{267,268}

$$\sigma = \sigma_0 \cdot \exp \left\{ \left(-\frac{T}{T_0} \right)^\gamma \right\} \quad (2-10)$$

In the above equation σ_0 is a pre-exponential parameter, which only depends very weakly on temperature.²⁶⁹ The minimum temperature for hopping is the characteristic hopping temperature T_0 . The exponent γ depends on the dimensionality of the hopping process (1D vs. 2D).²⁶⁹

The electrical properties of CPs, especially the charge carrier mobility, strongly depend on structural features of the polymer such as molecular weight, polydispersity,

crystallinity and regioregularity. Increasing the molecular weight often leads to an enhancement of conductivity.²⁷⁰⁻²⁷² The degree of ordering (state of packing) affects charge carrier transport in CPs.^{273,274} High ordering and packing of the molecular chains directly affects the hopping process by modifying the hopping barrier, hopping activation energy and hopping free path.²⁷⁵ Larger polydispersity of the CPs can hinder efficient packing in CP films.^{276,277} Polythiophenes used in this work enable excellent packing based on their high rigidity and planar structure.⁷⁴ Packing is important, since it also directly correlates with the crystallinity of CPs. Crystalline domains in CP films possess larger charge carrier mobility than amorphous parts.^{71,278} The most important structural factor in charge carrier transport of CPs is the regioregularity, describing the ordering of the monomer units along the polymer chain. Three types of arrangement can be distinguished as depicted in Figure 2-7: head-head, tail-tail and head-tail coupling. The latter is the most prominent conformation in regioregular polythiophenes. High regularity allows dense packing of the polymer chains and enhances charge carrier mobility by several orders of magnitude compared to non-regioregular polythiophenes.⁷⁶

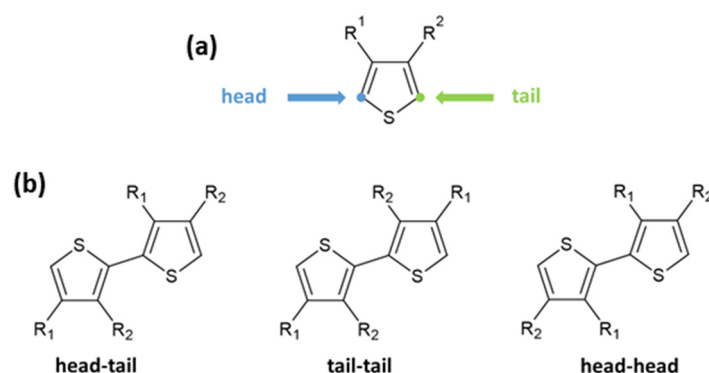


Figure 2-7: (a) Definition of head and tail of one single thiophene monomer. (b) Different types of regioregularity in polythiophenes.

The conductivity of native CPs is low (10^{-10} - 10^{-4} S/cm, semiconductor regime).^{279,280} Doping can enhance this value drastically. Polythiophenes used in this work can reach conductivities in the range of 10 - 10^3 S/cm.^{239,252,253} So far, doped PEDOT:PSS shows the highest reported conductivity values (above 4000 S/cm²⁸¹) of all CPs. Doping is a reversible process and can be performed either by chemical or electrochemical methods.^{253,282} The achieved conductivity of CPs is proportional to the doping level.²⁸³

Similar to inorganic semiconductors, CPs can be p- or n-type doped. The type of doping depends on the HOMO and LUMO levels of the polymer and on the used dopant.^{234,277}

P-doping (oxidation) removes electrons from the HOMO level of the polymer and transfers them to the LUMO of the dopant. This leads to radical cations (positive polarons) along the polymer chain (Figure 2-8a).^{253,284} The positive charges are compensated by the dopant molecules. Chemical p-doping is often performed by exposing the polymers to oxidative vapors such as iodine or to acids (H₂SO₄, HCl, H₃PO₄).²⁸⁵ P-type polymer conductors like the polythiophenes used in this work have a high-lying HOMO: P3HT (HOMO -4.7 eV to -5.2 eV, LUMO -2.6 eV to -3.5),²⁸⁶⁻²⁸⁹ PTEBS (poly[2-(3-thienyl)-ethyloxy-4-butylsulfonate]) (HOMO -5.0 eV to -5.3 eV, LUMO -2.8 to -3.1 eV),²⁹⁰ PEDOT:PSS (HOMO -5.1 eV to -5.3 eV, LUMO -3.3 eV to -3.5 eV).²⁹¹⁻²⁹³ Electron-rich polymers with such high HOMO levels can better stabilize positive charges, which makes them favorable for p-doping.²³⁸ N-doped CPs are usually electron-poor and possess low LUMO levels (below -4 eV),²⁹¹ which stabilizes negative charges.²³⁸ For n-doping (reduction), electrons are added from the HOMO level of the dopant to the LUMO level of the polymers and radical anions (negative polarons) are created (Figure 2-8b).^{253,284} Suitable n-dopants are alkali metals or organic molecules with high lying HOMOs.²⁶⁸

Polarons are formed in low doped CPs, whereas high doping levels lead to bipolaron formation (Figure 2-9).²⁹⁴ Removal of electrons occurs preferentially at the polaron states, since it is energetically more favorable compared with electron removal from the conduction or valence band of the polymer. Hence, bipolarons are thermodynamically more stable and the formation of bipolarons is favored over the development of two polarons.²⁵³ However, bipolarons only form if the complete chain was saturated by polarons beforehand.²⁹⁵ As illustrated in Figure 2-9, polaronic and bipolaronic states can be assigned to intergap electronic levels. While polarons possess a spin, bipolarons are spinless. At very high doping levels, the individual bipolaron states overlap, creating bipolaron bands inside the bandgap region (Figure 2-9), which enhances the conductivity of CPs.²⁹⁵ Polarons and bipolarons are stabilized by delocalization along the polymer chain.^{284,296,297} Upon applying an external electrical field, polarons and bipolarons

become mobile and cause inter-chain charge carrier transport.^{295,298} Hence, polarons and bipolarons are the origin of electrical conduction in CPs.

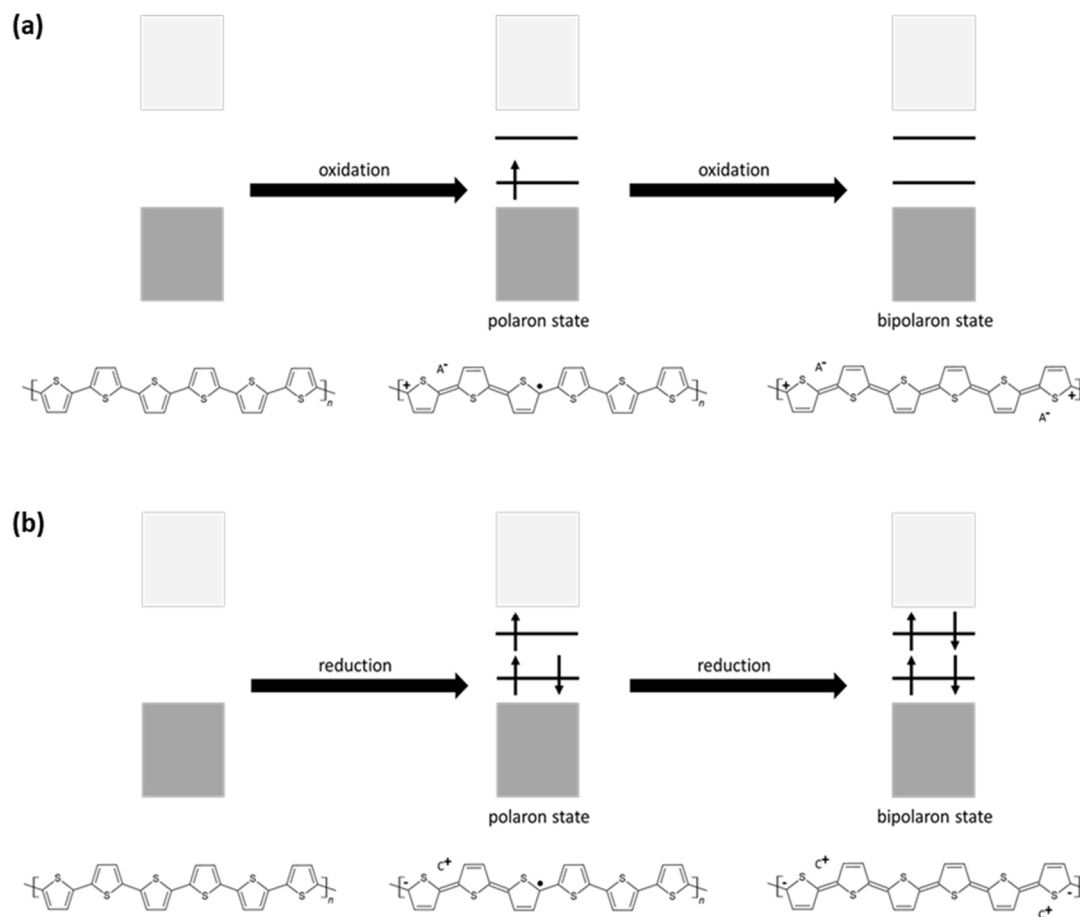


Figure 2-8: (a) Chemical structures and electronic stages upon p-doping (oxidation) of polythiophenes. Oxidation leads to the formation of positive polarons (radical cations). (b) Chemical structures and electronic stages upon n-doping (reduction) of polythiophenes. Reduction leads to the formation of negative polarons (radical anions). Further doping forms bipolarons (positive or negative), regardless of which kind of doping is used. Positive and negative charges of the polarons or bipolarons are compensated by anions (A^-) or cations (C^+) from the dopant. Figure adapted from [238].

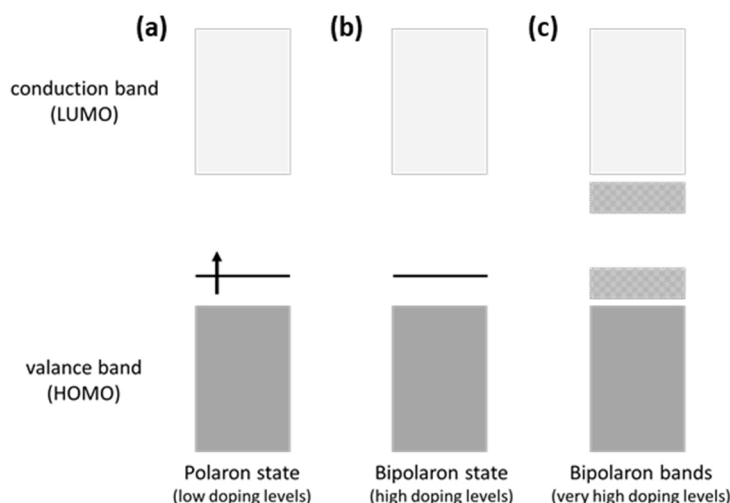


Figure 2-9: Formation of (a) polaron (spin) and (b) bipolaron (spinless) in the bandgap area depending on the doping level. (c) Overlapping of the bipolaron states at very high doping levels creates bipolaron bands.

According to literature, the delocalization of polaron and bipolaron charges is accompanied by a structural deformation from an aromatic structure (random coil conformation) to a quinoid structure (extended chain conformation) as shown in Figure 2-10.^{299,238} Better packing and the lower bandgap in the quinoid structure improves intra- and inter-chain carrier transport.^{300,301}

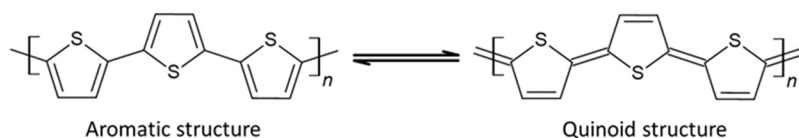


Figure 2-10: Transformation between aromatic and quinoid structure of polythiophenes. The quinoid structure develops upon charge delocalization along the polymer backbone.

It is likely that the electrical properties of the gold-polythiophene hybrid nanoparticles used in this work originate from polaronic and bipolaronic states. The interactions between the gold cores and the polythiophene ligands can lead to efficient electron transfer, generating polarons and bipolarons in the ligand shell. These facilitates charge carrier transport along the polythiophene ligands and likely result in an overall increase of the electrical conductivity of the gold-polythiophene hybrid nanocrystals.

2.2.3 Molecular assembly of polythiophenes on planar inorganic substrates

Polythiophenes deposited from solution on planar inorganic substrates made of silicon or metals, develop two-dimensional lamellar structures, that contain individual layers connected by π - π interactions. Sirringhaus *et al.* first reported that these lamellae can arrange into different textures if physisorbed by spin-coating on silicon substrates.⁷⁶ Most common are edge-on or face-on configurations. Figure 2-11 shows P3HT as a reference system to explain the different molecular configurations of polythiophenes inside layers. In the edge-on configuration, the backbone and the side chains arrange perpendicular to the substrate and the lamellar stacking direction is perpendicular to the substrate, while the π - π stacking direction is along the substrate plane (Figure 2-11a). In the face-on orientation, the lamellar stacking direction is along the substrate plane with the polymer backbone and side chains aligning parallel to the substrate and π - π stacking occurs perpendicular to the substrate (Figure 2-11b). A third vertical configuration (Figure 2-11c), also named flat-on or end-on configuration, in which the polythiophene chains point out vertically from the substrate has occasionally been mentioned in literature.^{74,75,79,302,303} The molecular arrangements in Figure 2-11 describe ideal situations. Domains with different orientations of the polymer chains can occur within one layer of real coatings.

Detailed studies of the molecular arrangement of the polymer chains inside polythiophene films were conducted by X-Ray Diffraction (XRD) methods. Two-dimensional Grazing Incidence X-Ray Diffraction (GIXRD)^{76,247,304–306} and Grazing Incidence Wide-Angle X-Ray Diffraction (GIWAXD) play an important role in the structural analysis of polythiophene layers, since they allow fast detection of diffraction images^{76,247,304–306} Owing to the fact that these methods apply synchrotron radiation, they enable an enhancement in diffraction signal intensity.^{307,308} The detected diffraction patterns allow one to determine if the polymer chains are arranged in an edge-on, face-on or end-on configuration, by analyzing the positions of the (010) and (100) reflections. The (100) reflections represent the lamellar stacking direction, while the (010) reflections correspond to the π - π stacking direction. Each of the three molecular configurations cause a unique pattern of the (010) and (100) reflection.⁷⁵ Hence, XRD allows the qualitatively

(which molecular orientation) and quantitatively (content of different configurations) structural analysis of polythiophene films.

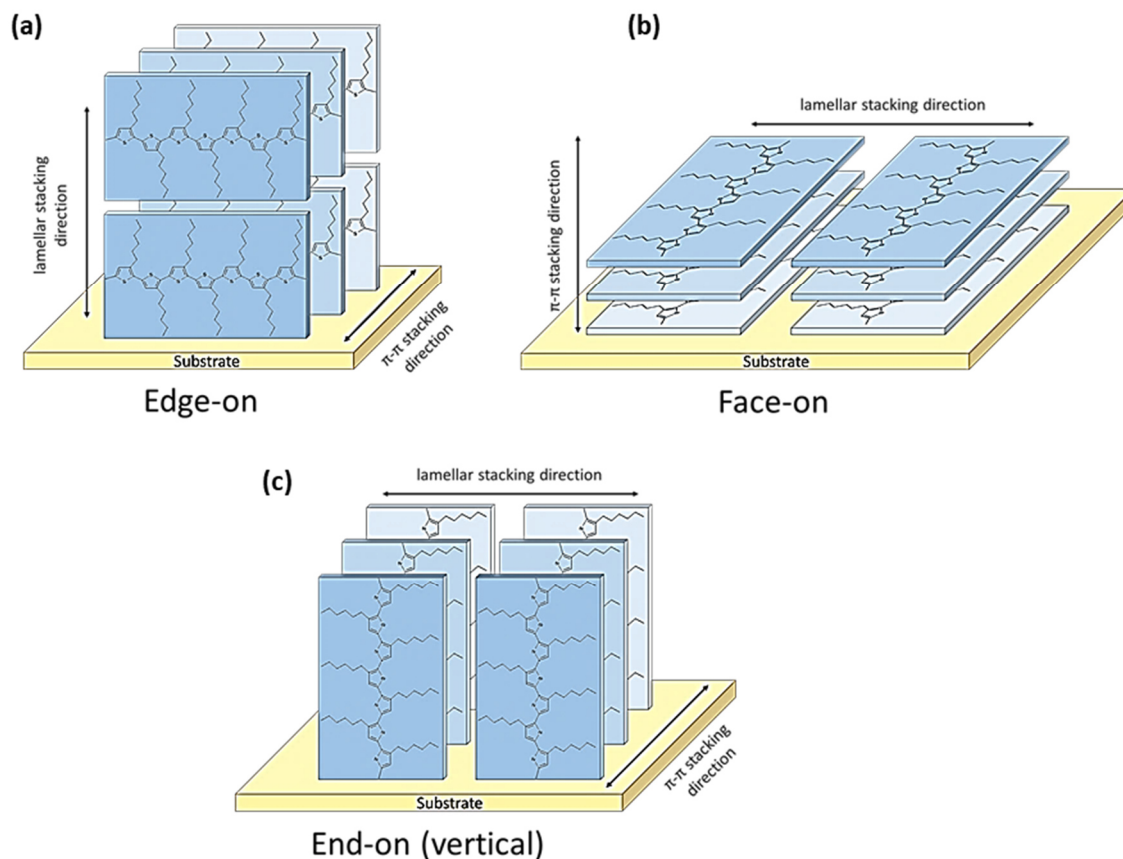


Figure 2-11: Molecular configurations of P3HT on planar inorganic substrates: (a) Edge-on configuration with π - π stacking direction along and lamellar stacking direction perpendicular to the substrate surface. (b) Face-on configuration with π - π stacking direction perpendicular to and lamellar stacking direction along the substrate surface. (c) End-on (vertical) configuration with both, π - π stacking and lamellar stacking directions, along the substrate surface. Charge transfer preferentially occurs along the polythiophene backbones and the π - π stacking directions.

The edge-on configuration is the thermodynamically favored molecular arrangement of polythiophenes on planar silicon or metal substrates.^{309–314} This configuration can be fabricated by slow casting procedures providing conditions close to the equilibrium. Literature reports polythiophene films with molecular edge-on orientation produced by dip-coating, drop-casting^{76,309,315} or spin coating from solvents with high boiling points such as dichlorobenzene.^{306,314} The face-on configuration is kinetically favored^{74,306} for

fast drying during layer formation.^{306,316} Spin-coating with low boiling solvents mostly lead to polythiophene films with molecular face-on configuration.^{76,306} Processing methods introducing shear force, such as mechanical rubbing³¹⁷ or friction transfer,³¹⁸ facilitate the molecular face-on orientation of the polymer chains.^{74,317,318} As-prepared polythiophene films with molecular face-on orientation can also undergo a transition to edge-on arrangement by thermal annealing above the melting point.^{306,319}

Molecular parameters including molecular weight, regioregularity, polydispersity or the length of the polymer side chain, can affect the molecular orientation and crystallinity in polythiophene films.^{74,320,321} For example, P3HT with low regularity tends to arrange in a face-on configuration while highly regioregular P3HT assumes edge-on configuration.⁷⁶ The properties of the substrate can have an additional impact on the molecular structure of polythiophene films. By functionalizing surfaces with silane-based self-assembled monolayers (SAMs) containing different functional groups that interact with the polythiophenes, it is possible to control the molecular orientation of the polymer chains. SAMs containing alkyl end-groups led to a face-on arrangement of P3HT, while on SAMs with amine end-groups P3HT adopted an edge-on configuration.^{312,322}

The highest electrical conductivity in polythiophenes occurs along the conjugated polymer backbone and the π - π stacking direction, while the side chains are insulating, which prevents charge transport along the lamellar stacking direction.⁷⁰⁻⁷⁴ Hence, the molecular orientation has a crucial impact on the electrical properties of polythiophene films. The π - π stacking direction in edge-on configurations increases the in-plane charge-carrier mobility, which makes this orientation beneficial for organic field-effect transistors (OFETs), where large in-plane charge transport is required.^{265,315,323,324} Organic photovoltaics profit from the molecular face-on configuration, in which the π - π stacking direction enhances out-of-plane charge carrier transport.^{71,266,325,326}

Due to the large impact of the molecular arrangement on the electrical properties of polythiophenes, different methods were developed allowing a precise control over the internal order of polythiophene films. One technique to produce highly ordered polythiophene layers from solution with molecular edge-on or face-on configuration is small-molecule epitaxy.^{247,327} For example, Ou *et al.* obtained highly oriented P3HT

using 1,3,5-trichlorobenzene (TCB) as epitaxial template. They achieved that P3HT grew with its backbone parallel to the long axis of the TCB needle-like crystals, resulting in a face-on arrangement of the polymer chains.²⁴⁷ Nano-confinement produced by patterning techniques can also introduce molecular ordering in polythiophene layers.^{78,79} Nanoimprint lithography (NIL) uses a rigid mold with nano-cavities which is pressed into the polymer film with high pressure and at temperatures above the glass transition temperature T_g of the polymer. After cooling to temperatures below T_g the mold is removed, resulting in a patterned polymer layer. NIL can introduce vertical chain arrangement (end-on configuration) in nanogratings and nanopillars, since the polymer chains align along the flow during the imprinting.⁷⁹ A preferential molecular face-on configuration in nanogrooves, with the polymer backbone arranged along the groove axis, was also reported in literature.⁷⁷ The exact molecular arrangement of polythiophenes during NIL depends on many factors such as the geometry of the nanostructures (height and width) inside the mold or the surface properties of the mold.⁷⁴ Molecular order of polymer chains can also be achieved by depositing polythiophenes into the nanopores of anodic aluminum oxide layers (AAO).^{78,80} Ko *et al.* reported mainly face-on configuration of P3HT filled into AAO templates.⁷⁸

2.2.4 Molecular assembly of polythiophenes on nanomaterials

Most research on the molecular assembly of CPs on nanomaterials was focused on graphene and carbon nanotubes (CNTs).^{70,71,278,328,329} Various studies revealed a preferential face-on configuration of polythiophenes on graphene surfaces, which is caused by the strong π - π interactions between the conjugated thiophene backbones and graphene, as well as van der Waals interactions between the polymer alkyl side chains and the graphene surface.^{70,71,278,328,329} Simulations calculated larger binding energies for the face-on arrangement on graphene, resulting in higher stability compared to the edge-on orientation.³²⁹

Similar to graphene, the interactions between polythiophenes and CNTs are determined by non-covalent π - π - and van der Waals interactions.^{330–333} The conjugated π -bonds

present in both, CNTs and polythiophenes, result in strong π - π stacking of polymer chains on the nanotubes' surface. In addition to the π - π interactions of the thiophene rings, the side chains of the polythiophenes interact via van der Waals forces with the nanotubes' surface. Since both, the polymer side chains and the graphitic side walls of the tubes, are hydrophobic, they are attracted to each other in organic solvents.³³³ As for graphene, the π - π - and van der Waals interactions cause a face-on arrangement of polythiophenes on bare CNTs^{302,330,331,334} Simulations based on molecular modeling revealed that the molecular assembly of polythiophenes on CNTs is only marginally affected by the geometry of the CNTs and the molecular mass of the polymer.³³² Thus, the main influencing factors are the interfacial CNTs-polymer interactions.

These interactions can be altered by surface modifications of graphene and CNTs. The sp^2 hybridized carbon surface atoms of both carbon materials are suitable for chemical functionalization.^{302,331} Surface functionalization with thiophenic adducts or surface grafting with thiophenic oligomers on CNTs and graphene modify the interactions between the carbon materials and polythiophenes. This leads to a change in molecular polymer arrangement from face-on on bare surfaces to edge-on on functionalized surfaces and flat-on on grafted surfaces, respectively.^{302,330,331,334} The molecular configuration also affects the electrical properties of the polythiophene-carbon nanostructures. The ordered alignment of polymer chains in polythiophene-carbon nanostructures due to strong interfacial interaction enhances polymer crystallinity.³³⁴ Higher crystallinity leads to increased charger carrier mobility and improves electrical conductivity of the polythiophene-carbon nanostructures.³³⁴ Literature also considers effective electron transfer from the carbon materials to the polythiophenes as further reasons for the excellent electrical properties.³³⁵ The highest conductivities and hole mobilities of polythiophene-carbon nanostructures were achieved for structures with a flat-on polymer configuration.^{302,331,334}

There are only few reports about the molecular structure of conductive polythiophenes on inorganic nanoparticles. Some studies investigated the molecular arrangement of polythiophenes on zinc oxide (ZnO) nanowires.^{81,82} Zhang *et al.* reported an edge-on orientation of PTEBS on ZnO nanowires with the polymer backbones arranging parallel to the long axis of the wires.⁸¹ One goal of this thesis was to detect how polythiophenes

can arrange on gold nanocrystals as well as to identify the main mechanism determining the molecular configuration.

2.3 Hybrid materials

This chapter gives an overview about the characteristics of conductive nanoparticle-polymer hybrid materials. I already discussed the features of gold nanomaterials and conductive polymers, which are the individual components of the gold-polythiophene hybrid nanocrystals introduced in this work. This chapter explains why a combination of gold nanocrystals and conductive polymers can be classified as hybrid materials according to the definitions presented in section 2.3.1

I employed a ligand exchange reaction to produce gold-polythiophene hybrid nanocrystals. Beyond this method, various techniques for the production of conductive nanoparticle-polymer hybrid materials are discussed in literature. The main principles of these techniques, including ligand exchange, are summarized in section 2.3.2. Hybrid materials composed of inorganic materials and biological species (e.g. enzymes, proteins, antibodies and DNA) can be obtained by bioconjugation. I applied this method to covalently link biomolecules to the newly developed biofunctionalizable gold-polythiophene hybrid nanoparticles (chapter 3.4). The principles of bioconjugation are explained in section 2.3.3. Section 2.3.4 summarizes potential application fields of the gold-polythiophene hybrid nanocrystals introduced in this work.

2.3.1 Definition and classification of hybrid materials

Many engineers define that hybrid materials are composed of different types of materials.^{336,337} Chemists assumed a more molecular perspective. The first definition of hybrid materials by Yamada and co-workers from 1989 involves a mixture of at least two materials resulting in new properties based on the formation of electron orbitals between these.³³⁸ Makisima described hybrid materials as sub-micron level mixtures of different

material classes containing newly formed chemical bonds. These classes include metals, organic materials (polymers) and ceramics.^{336,337} Gómez-Romero and Sanchez defined hybrid materials in terms of characteristic scales and material types.³³⁹ They classified hybrid materials as a combination of inorganic and organic or biological materials with characteristic length below 10^3 nm. Ashby described hybrid materials as a combination of two or more materials with defined geometries and scales, having a specific engineering purpose.³⁴⁰ The International Union of Pure and Applied Chemistry (IUPAC) defines a hybrid material as an “intimate mixture of inorganic components, organic components, or both types of components,” where the components mostly interpenetrate on length scales below $1\text{ }\mu\text{m}$.³⁴¹

What these definitions have in common is the fact that they describe hybrid materials as mixtures of different materials. Many hybrids are composed of organic and inorganic species. The gold-polythiophene nanocrystals utilized in this work contain inorganic gold cores and organic polythiophene ligand shells. Literature classified inorganic-organic hybrid materials based on the present interactions (Figure 2-12).^{339,342–345} In class I hybrid materials, only weak van der Waals interactions, hydrogen bonds and weak electrostatic interactions connect the two phases. Class II hybrid materials contain inorganic and organic parts that interact by strong chemical covalent or ionic-covalent bonds. Since there is often a gradual transition between strong and weak interactions,³⁴² it is possible that class I and II interactions can occur within the same hybrid material.³⁴⁵

Blends are typical class I hybrids. They can be made by entrapping inorganic particles inside polymeric matrices via weak physical interactions (Figure 2-12a). Interpenetrating networks (IPNs) of non-interacting inorganic and organic network structures also belong to class I hybrid materials (Figure 2-12c). Class II hybrid materials are created by covalent connection of inorganic particles to organic polymers (Figure 2-12b) or by covalent linkage of inorganic and organic networks (Figure 2-12d). I will show in the upcoming results chapter 3 of this work, that the polythiophene ligands covalently attach to the gold cores due to strong Au-S bonds (Au-S bond dissociation energy is $418\text{ kJ}\cdot\text{mol}^{-1}$),²³⁰ which make them typical class II hybrid materials.

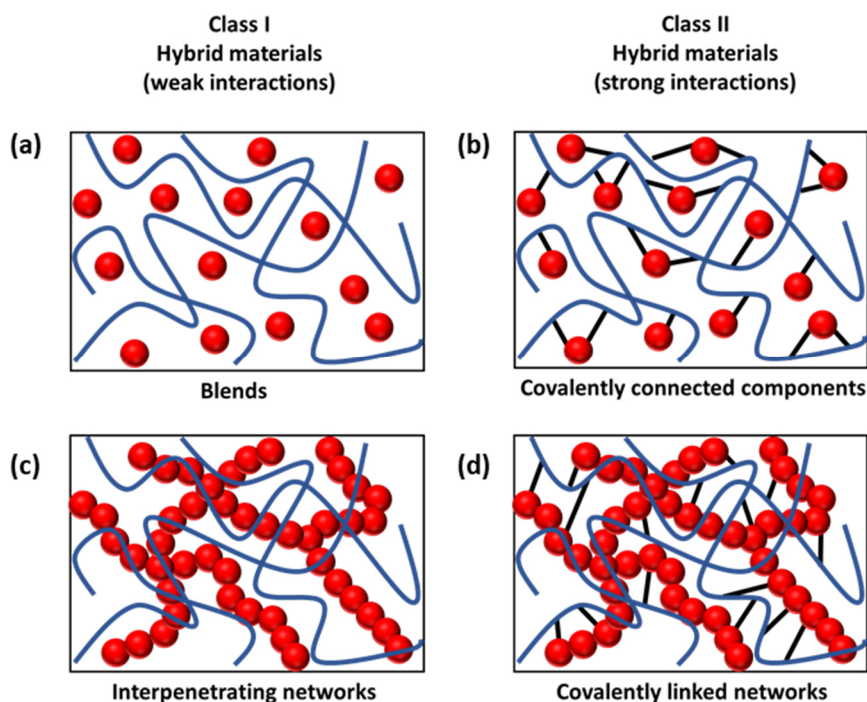


Figure 2-12: Classification of hybrid materials in class I (weak interactions) and class II (strong interactions). Typical class I hybrids include blends (a) and interpenetrating networks (c). Class II hybrids are made of inorganic particles covalently linked to organic polymers (b) or by covalently connected inorganic and organic networks (d).

Inorganic-organic hybrid materials can be additionally divided into organic-in-inorganic and inorganic-in-organic hybrids as illustrated in Figure 2-13. In the first group, inorganic materials are modified by organic moieties, which brings additional functionalities to the inorganic system. This can be realized by incorporating organic species into inorganic structures.³⁴⁶ Examples of this strategy include the incorporation of organic molecules or polymers in inorganic gels or the organic impregnation of porous inorganic matrices.^{343,345,347–350} Organic-in-inorganic hybrid materials can also be obtained by stabilizing inorganic colloidal particles with organic molecules. Surface modification of colloidal inorganic (nano)-particles with organic species can reduce their high surface energy and prevent the formation of larger particle structures due to agglomeration. In addition to colloidal stabilization, surface functionalization of inorganic particles can also change their properties or even add new functionalities.^{351,352} According to the explanation above, the gold-polythiophene hybrid nanocrystals of this work can be

classified as organic-in-inorganic hybrids, since the long and negatively charged polythiophene ligands lend this hybrid nanocrystals sufficient colloidal stability.

Not only can colloidal species be surface-functionalized, they can also be incorporated into organic materials, forming inorganic-in-organic hybrid materials (Figure 2-13). Surface modification of the inorganic particles is important to prevent particle agglomeration and to achieve a homogenous particle distribution inside the organic part. The organic parts of these hybrids are often referred to as matrices. These matrices can have a synthetic or a biological nature. Synthetic matrices include synthetic monomers or polymers, hydrogels, copolymers or polymeric brushes.³⁴⁶ Biological matrices are made from materials occurring in nature, such as proteins, lipids, nucleic acids, microorganisms, bacteria or cells.³⁴⁶

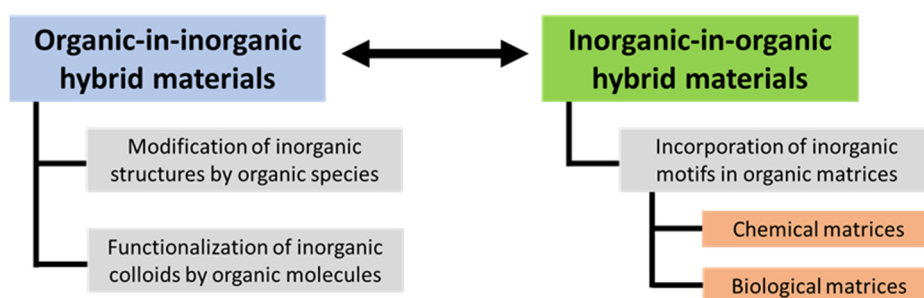


Figure 2-13: Classification of hybrid materials containing inorganic and organic compounds.

The properties of inorganic-organic hybrid materials are not just the sum of the features from the individual compounds. There are strong synergetic effects between the inorganic and organic parts, resulting in new properties which do not exist in the individual components.³⁴⁵ Thus, hybrids include multifunctional materials with improved mechanical strength, enhanced thermal stability and exceptional optical, catalytical, magnetic and electrical properties.³³⁷ Inorganic and organic matter often show complementary properties (‘yin & yang’ properties) as illustrated in Figure 2-14.^{337,346} The formation of inorganic-organic hybrids often has the goal to add missing or complementary functions to organic or inorganic materials. For example, organic matrices which are usually soft and non-conductive, can be transformed to electrically conductive or tough materials due to the incorporation of inorganic particles. Owing to their organic content, hybrid materials can often be processed at lower temperatures with

high shape flexibility (from bulk structures to thin films) compared to inorganic solid-state materials, which require high processing temperatures.³⁴²

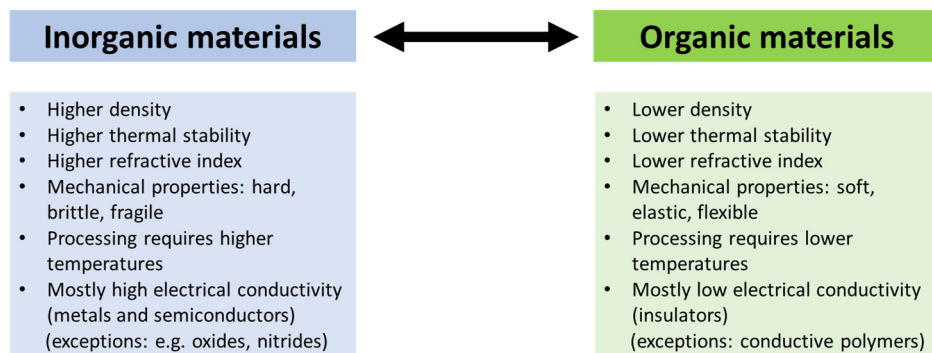


Figure 2-14: Examples of complementary characteristics (‘yin & yang’ properties) of inorganic and organic materials.

The properties of hybrid materials can be tailored for the desired purpose by tuning the physical and chemical properties of the individual components, the structure of the inorganic-organic interfaces and the interactions between the different compounds. Organic species with conjugated π -bonds can interact by electron transfer reactions with inorganic particles affecting optical and electrical properties of the particles themselves and the features of the final hybrid material.³⁴² Similar interactions occur between the polythiophene ligands and the gold nanocrystals in the hybrids developed in this work, resulting in superior electrical properties revealed in the result section (chapter 3).

Hybrid materials are often hard to distinguish from (nano)-composites and there is regularly a gradual transition. In general, composites contain a matrix, in which micron-level structures are incorporated.³³⁶ Nanocomposites contain at least one structural unit (inorganic or organic) with geometrical dimensions of 1-100 nm.^{336,342} Hybrid materials often exhibit superior or new functions, beyond those of the individual components. In contrast, the properties of composites are often the sum of the properties of the individual compounds, which can, for example, be approximated by a mixing rule.^{336,337}

In summary, this section showed that the gold-polythiophene hybrid nanoparticles used in this work can be defined as typical class II and organic-in-inorganic hybrid materials. The surface modification of the gold nanocrystals by polythiophene ligands lends the

particles colloidal stability and also introduces electrical conductivity as well as bio-functionality, which I will demonstrate in the result chapter 3.

2.3.2 Synthesis routes for nanoparticle-polymer hybrid materials

Important routes to nanoparticle-polymer hybrids are summarized in Figure 2-15. One common approach is ligand exchange, where the initial stabilizing ligand of the nanoparticles is substituted after particle synthesis. Possible new ligands are polymers containing anchoring groups that can interact with the nanoparticle's surface. These functional groups can either form covalent chemical bonds with the nanoparticles or interact non-covalently, e.g. by weak electrostatic interactions or hydrogen bonds. Functional anchors can be attached to the polymer chains as terminal or side groups. Since the ratio of end groups to the total amount of polymer units decreases with increasing molecular weight, a side group functionalization is favorable to provide sufficient anchor sites for the nanoparticles.²⁷⁷ Ligand exchange is often performed in a simple one-pot reaction. The as-synthesized nanoparticles are mixed with the polymeric ligands in an appropriate solvent. The exchange reaction is thermodynamically controlled and weakly binding ligands are replaced by ligands possessing stronger interactions with nanoparticles.³⁵³ Weakly binding ligands for aqueous AuNPs are, for example, citrate or alkyl ammonium halides. These ligands can be easily replaced by sulfur-containing polymers to obtain AuNPs-polymer hybrids.³⁵³ Reported examples include the modification of diversely shaped gold nanocrystals with thiolated polyethylene glycol (PEG) or polythiophenes.^{69,354,355} I prepared gold-polythiophene hybrid nanocrystals using a ligand exchange process, whereby the sulfur atoms present in the backbones and side chains of the polythiophenes ensured sufficient driving force for the ligand exchange and the ligands bind covalently to the gold cores by strong Au-S bonds (Au-S bond dissociation energy is $418 \text{ kJ}\cdot\text{mol}^{-1}$).²³⁰

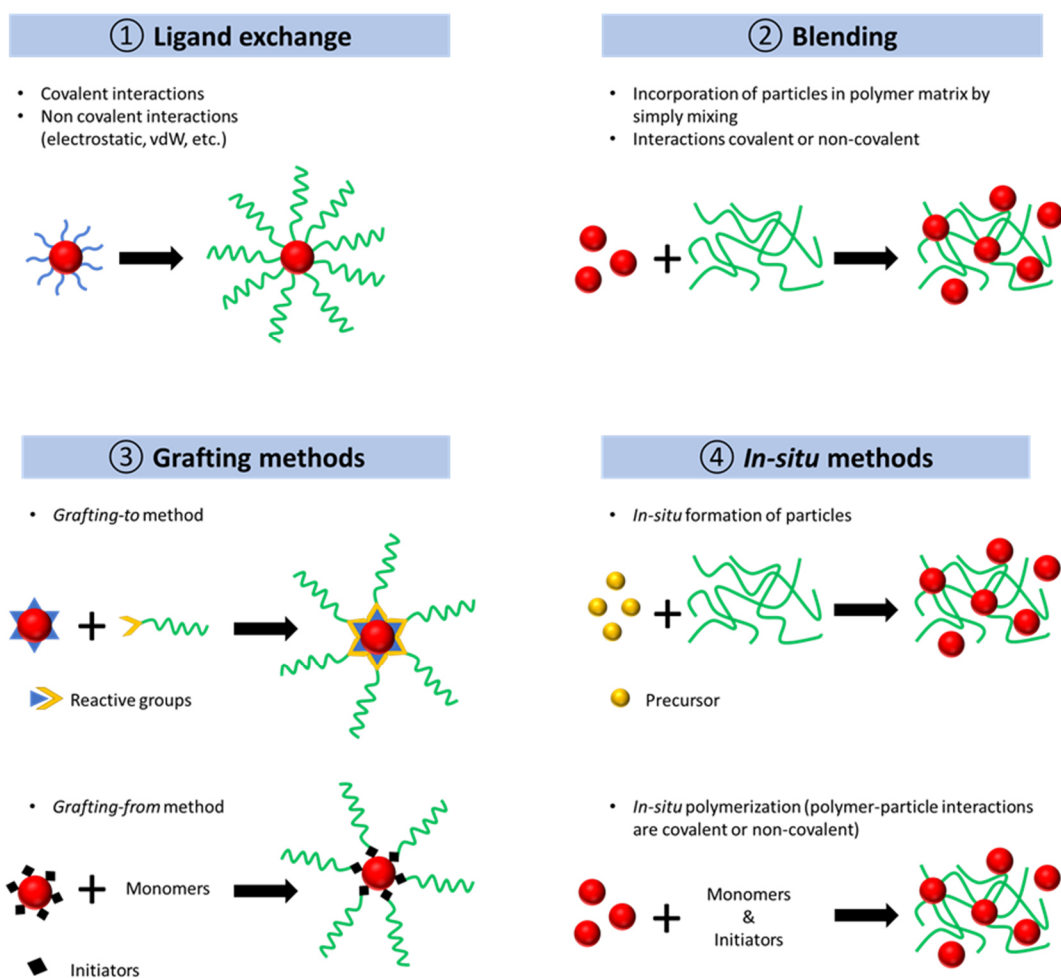


Figure 2-15: Different fabrication methods of inorganic-organic hybrid materials containing inorganic nanoparticles represented as red balls and polymers illustrated as green lines.

Blending of nanoparticles in polymer solutions and melts generates hybrid materials after solvent evaporation and cooling, respectively. Solvent blending is more common, since it can be performed at lower temperatures, allows easier mixing due to lower viscosity of the mixture and enables a better particle distribution inside the polymer.³⁵⁶ Inhomogeneities during blending often complicate the processing and deteriorate the properties of the resulting hybrids. Homogeneous particle distribution in the polymer matrices can be obtained by introducing specific interactions (covalent or non-covalent) between the polymer and the nanoparticles. This can be achieved by targeted surface modification of the nanoparticles or by functionalization of the polymer.³⁵⁶

Surface modification enhances the compatibility between nanoparticles and polymer. Ligand exchange reactions can be used to specifically functionalize the nanoparticles. For example, cadmium selenide (CdSe) nanoparticles with thiolated and thiophene ligands were homogeneously distributed in polythiophene and polyfluorene matrices. The homogeneous distribution was caused by non-covalent electrostatic and non-covalent π - π interactions.^{357–359} Furthermore, introducing hydrophilic parts into co-polymers, can enhance the affinity towards polar nanoparticles.³⁶⁰ Powder blending is suitable for polymers with low solubility in organic solvents or for polymers with high melting points. During the milling process larger agglomerates of inorganic compounds are chopped to smaller particles, which are mixed with the polymer matrix.³⁶⁰

During grafting processes (Figure 2-15), the polymer chains are covalently linked to the nanoparticle. In *grafting-to* methods, nanoparticles and polymers are synthesized separately. Subsequently, the side- or end-functionalized polymer chains react with the linker groups provided by the nanoparticle's ligand.^{361,362} Often the initial ligands of the as-synthesized nanocrystals do not possess appropriate linker functions and a ligand exchange reaction is required to attach the functional ligand to the nanocrystals. The polymers produced by classical polymerization techniques^{361,362} are linked to the nanoparticles by condensation or *click* reactions.^{363,364} Examples of nanoparticle-polymer hybrids obtained by *grafting-to* approaches are CdSe nanoparticles and nanorods grafted with various oligo- and polythiophene derivatives.^{365,366}

The steric hindrance of the linker ligands at the nanoparticle's surface often lead to low grafting densities if *grafting-to* methods are applied.³⁶¹ This problem can be overcome by the implementation of *grafting-from* techniques.³⁶¹ Within this approach, functional initiators are covalently connected to the nanoparticles. These initiators will start the polymerization process via 'surface-initiated polymerization' after the monomers are added to the nanoparticle dispersion.^{361,362,367} These techniques offer mild reaction conditions and good control over the size and architecture of the grafted polymer chains. The obtained polymer grafting densities on nanocrystals for *grafting-from* methods are higher, since the small initiators are sterically less demanding than the more complex linker ligands in the *grafting-to* approach.³⁶¹ Various polymers could be linked to AuNPs

and silica nanoparticles by *grafting-from* methods including poly(methyl methacrylate) (PMMA) and poly(*N*-isopropylacrylamide) (PNIPAM).^{361,367–371}

Nanoparticle-polymer hybrid materials can also be prepared by *in-situ* methods. Nanoparticles can be formed inside a polymer matrix or the polymer network is formed within a nanoparticle dispersion. *In-situ* nanoparticle formation of nanoparticles is beneficial to obtain a homogeneous particle distribution inside the polymer matrix. Additionally, the problem of finding a compatible solvent for the polymer and nanoparticles can be avoided. In this approach, precursor materials for nanoparticle formation and reducing agents are homogeneously mixed into a polymer solution or infiltrated into a polymer template. The nanocrystal growth takes place inside the polymer network. Chemical, thermal or photo-induced (e.g. ultraviolet or infrared light) reduction processes of the precursor materials lead to the formation of nanoparticles.³⁷² The polymer chains can interact with the forming nanocrystals, preventing particle agglomeration. The specific nanoparticle-polymer interactions can further limit nanoparticle growth, leading to nanostructures with well-defined sizes and low polydispersity.^{372–374} *In-situ* nanoparticle-growth often lacks appropriate purification to remove byproducts,³⁷⁵ which could impair the quality of the final hybrids. Examples of the *in-situ* nanoparticle synthesis are the formation of cadmium sulfide CdS nanocrystals inside P3HT networks^{376,377} and the generation of AuNPs in polyaniline.³⁷⁸

Polymer networks can also be formed *in situ* within a nanoparticle dispersion. Monomers, initiators and nanoparticles are thoroughly mixed in an appropriate solvent. Subsequently, polymerization of the monomers is thermally, chemically or light-initiated. The polymerization speed needs to be sufficiently fast to avoid particle agglomeration and to obtain homogeneous particle distribution inside the polymer matrix.^{356,372} Hybrid materials produced by *in-situ* polymerization include various polythiophene derivatives containing CdSe and CdS nanoparticles of different shapes.^{379–381} The simultaneously *in-situ* formation of both, polymers and nanoparticles, is not very common. However, it has been used to produce AuNPs-polyaniline and AuNPs-polypyrrole hybrid materials.^{382,383}

2.3.3 Bioconjugation as a method for hybrid material production

The production of hybrid materials composed of inorganic nanocrystals and organic biological substances (e.g. enzymes, antibodies, DNA, peptides, proteins or cells) is possible via bioconjugation, where the biological species are covalently linked to the inorganics. Often bioconjugation is conducted using EDC/NHS coupling chemistry, since EDC/NHS chemistry is a well-established and one of the most commonly used coupling methods in biology and chemistry.^{384–386} 1-Ethyl-3-(3-dimethylaminopropyl)carbodiimide (EDC) or 1-Ethyl-3-(3-dimethylaminopropyl)carbodiimide hydrochloride (EDAC) are water soluble carbodiimide reagents that can function as crosslinker to couple carboxyl ($-\text{COOH}$) or carboxylate groups ($-\text{COO}^-$) to primary amines ($-\text{NH}_2$), while EDC itself is not incorporated into the final product. Consequently, carboxylated nanoparticles, such as the biofunctionalizable gold-polythiophene hybrid nanocrystals of this work, can be linked to biomolecules containing primary amines. Figure 2-16 illustrates in an exemplary manner the main reactions of such a bioconjugation process based on EDC/NHS coupling.

Upon reaction with carboxyl/carboxylate groups EDC forms an O-acylisourea intermediate, which in a second step reacts with the primary amine upon the formation of a stable amide bond (Figure 2-16a).³⁸⁷ EDC and the O-acylisourea intermediate are not stable in aqueous conditions.^{388,389} Hydrolysis competes with the amide formation and limits the yield of the bioconjugation (Figure 2-16c). Excess of EDC and adjusting the reaction conditions such as pH, temperature or buffer choice, can limit hydrolysis.^{384,390} According to literature the optimal pH for the activation of the carboxyl/carboxylate groups is 3.5 to 4.5, while slightly higher pH values between 4 to 6 lead to the highest yield of the amide formation.^{389,391} However, experimental studies revealed, that the EDC coupling upon amide formation remains feasible with sufficient yield and reaction speed up to pH of 7.5.^{384–386} This neutral pH range is more compatible for most biological species (cells, antibodies, peptides, enzymes, etc.).

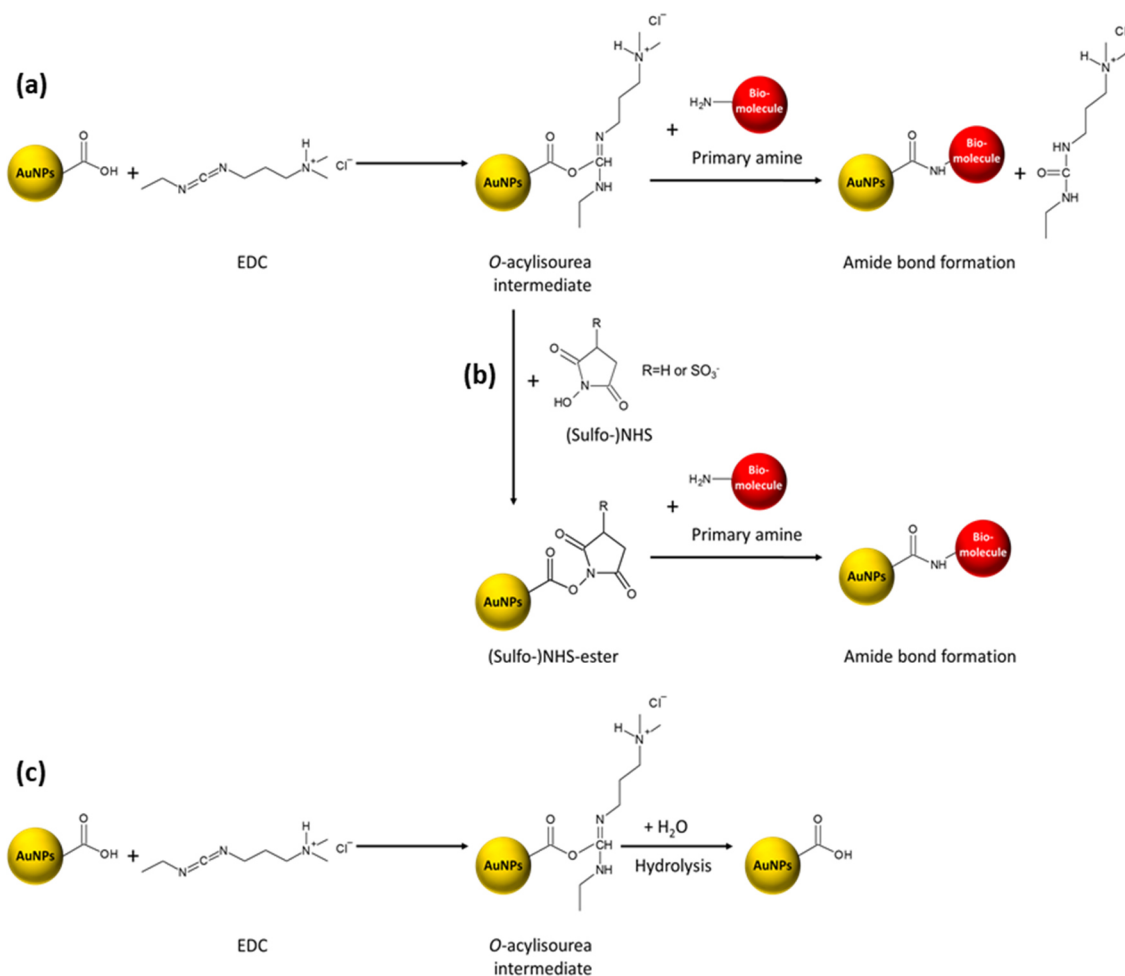


Figure 2-16: Reaction scheme of bioconjugation of carboxyl-functionalized gold nanoparticles with primary amine-containing biomolecules. (a) 1-Ethyl-3-(3-dimethylaminopropyl)carbodiimide (EDC) activates the carboxyl groups by forming an *O*-acylisourea intermediate, which can react with a primary amine by formation of a stable amide bond. (b) The *O*-acylisourea intermediate can also react with *N*-hydroxysuccinimide (NHS) or Sulfo-NHS producing a reactive, but more stable, succinimidyl ester, which can react with a primary amine again upon amide bond formation. (c) A competing side reaction to amide formation is hydrolysis of the *O*-acylisourea intermediate.

Limitations of the EDC bioconjugation process (e.g. instability of *O*-acylisourea intermediate) can be overcome by adding a second coupling agent to the reaction such as *N*-Hydroxysuccinimide (NHS) or its sulfonated analog *N*-Hydroxysulfosuccinimide (Sulfo-NHS), which has a better water solubility. The formed NHS- and Sulfo-NHS esters are highly reactive groups that couple with primary amines via amide formation as illustrated in Figure 2-16b.³⁹² Compared to the *O*-acylisourea intermediate, the succinimidyl ester are more stable and do not hydrolyze as quickly.³⁹³

Two-step protocols are often applied for bioconjugation via EDC/NHS coupling chemistry. In the first step the activation of the carboxyl (-COOH)/carboxylate groups (-COO⁻) and the formation of the succinimidyl ester are conducted at acidic pH between 4.7 to 6.0, e.g. in 2-(N-morpholino)ethanesulfonic acid (MES) buffer with 0.1 M concentration.³⁸⁶ In a second step, the targeted biomolecule (amine reagent) is added to the reaction mixture. Excess reagents can be removed before the amine addition.³⁸⁴ Usually the amide formation in the second step is performed at neutral or slightly basic pH (7 to 8.5). For these conditions, a phosphate buffer such as phosphate-buffered saline (PBS) buffer with a concentration of 0.1 M is a suitable choice.³⁸⁶ It is also possible to conduct the bioconjugation in one step by means of simultaneous addition of EDC, NHS and amine reagents. I applied such a one-step procedure to attach biological species to the biofunctionalizable gold-polythiophene hybrid nanocrystals (chapter 3.4).

Compared to NHS, Sulfo-NHS is more water-soluble and introduces additional charges to the bioconjugation system, since the intermediate Sulfo-NHS esters are negatively charged (Figure 2-16). This can be helpful in the bioconjugation of nanoparticles. The intermediate Sulfo-NHS ester causes negative surface charge of the particles, preventing particle agglomeration by electrostatic repulsion.^{386,394}

2.3.4 Applications of conductive nanoparticle-polymer hybrid materials

Hybrid materials are utilized in many different application areas, such as (micro)-electronics (e.g. printed electronics), soft robotics, optics, functional coatings, mechanics, (photo)-catalysis, energy storage and conversion, photovoltaics, fuel cells, sensors and (bio)-medicine (e.g. drug delivery).^{395–401} Due to their excellent electrical properties and their ability to adopt additional functionalities, gold-polythiophene hybrid nanocrystals could extend the application fields of nanoparticle-polymer hybrids and further improve device performance of electronic devices in which today's state-of-the-art nanoparticle-polymer hybrid materials are utilized.

Conductive nanoparticle-polymer hybrids were successfully used in optoelectronics for light generation (e.g. laser or light-emitting diodes LEDs) or light conversion (e.g. solar cells, phototransistors or photodiodes). Conductive nanoparticle hybrid materials can be employed in different parts of organic light-emitting diodes (OLEDs).³⁹⁸ An OLED contains at least an anode, a cathode, an emissive layer (EML) and a substrate (Figure 2-17a), but can also have a more complex structure (Figure 2-17b). OLEDs with improved device performance were obtained by using flexible hybrid electrodes composed of silver nanowires (AgNWs) embedded into a PEDOT:PSS matrix,⁴⁰² or hole transport layers (HTL) containing hybrids based on silica (SiO₂) nanoparticles integrated to PEDOT:PSS films.⁴⁰³

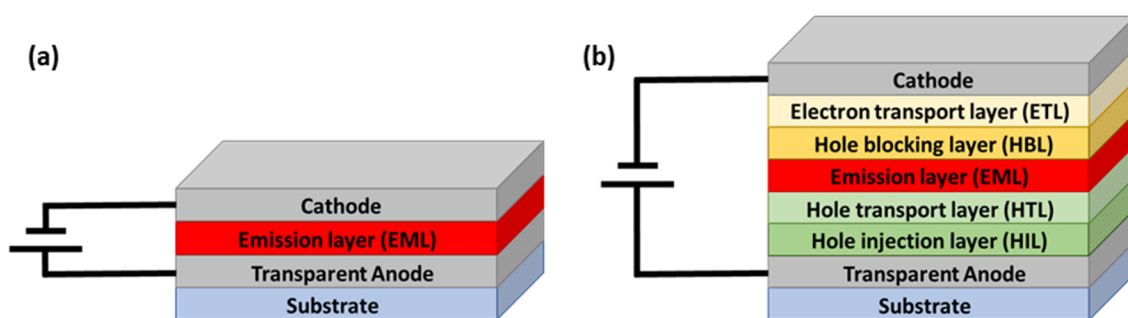


Figure 2-17: Schematic setup of (a) a single-layer OLED and a (b) multilayer OLED.

Additionally, conductive nanoparticle-polymer hybrids materials are often used inside organic photovoltaics (OPVs). Each OPV consists of an active organic layer placed between an anode with a high work function and a cathode possessing a low work function.^{404,405} The active layer contains two different light-absorbing semiconducting materials. One is electron-accepting (acceptor), while the other one is electron-donating (donor). Depending on the arrangement of the donor and acceptor materials, OPVs can be categorized as bilayer and bulk heterojunction cells (Figure 2-18). In the first structure, a planar donor and acceptor layer are in planar contact (Figure 2-18a), while in structures with heterojunctions both materials are blended with each other (Figure 2-18b).^{404,405} Chuang *et al.* incorporated AuNPs immobilized on graphene oxide into PEDOT:PSS or P3HT layers and used these hybrid materials as buffer and photoactive layers in OPVs, which enhanced the photocurrent and improved the overall device efficiency.⁴⁰⁶

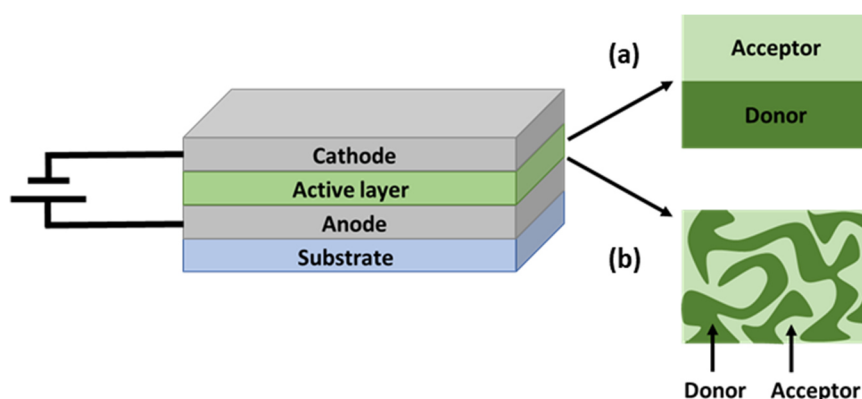


Figure 2-18: Schematic setup of an organic solar cell. The active layer can be a bilayer (a) or a bulk heterojunction (b).

Electrochromism describes the property of a material to change its optical properties upon an applied voltage. Most electrochromic systems switch from a bleached (colorless) to a colored state and vice versa via redox reactions between two redox couples. (Figure 2-19). Electrochromic devices consist of two transparent conductive substrates (e.g. indium tin oxide ITO) and two electroactive materials A and B, which are separated by an electrolyte.³⁹⁸ If a voltage is applied, one of the electroactive materials is oxidized and the other one is reduced, causing a switch in coloration. Literature reports electroactive films made from various conductive polymers, in which AuNPs or AgNPs were incorporated.^{407,408}

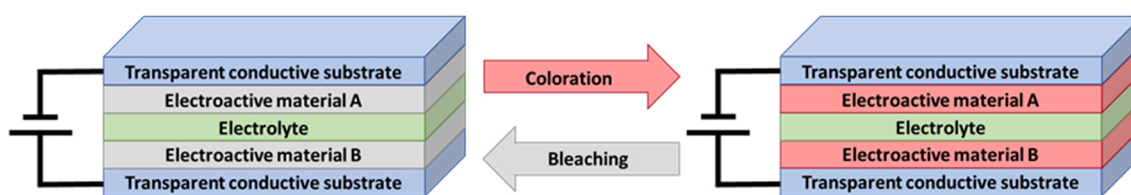


Figure 2-19: Schematic setup of an electrochromic device, that can switch between a colored and a bleached state due to redox reactions.

Conductive nanoparticle-polymer hybrids can also be used as electrode materials in devices for energy storage such as lithium-ion batteries, supercapacitors or fuel cells. Electrodes in batteries or supercapacitors are usually hybrid materials made of active materials and conductive agents/additives imbedded in a polymer matrix (Figure 2-20).⁴⁰⁹ Wu and co-workers used hybrid materials based on PANI hydrogels and SiO₂

nanoparticles as anode material for lithium-ion batteries.⁴¹⁰ Within the hybrid, PANI polymer chains act as ligands stabilizing the SiO₂ nanoparticles and as matrix material forming a 3D network. Lithium-ion batteries with this hybrid material as anode had a prolonged stability. Cho *et al.* fabricated an ink containing PEDOT:PSS, graphene sheets and RuO₂ nanoparticles, which was screen-printed to produce flexible electrodes.⁴¹¹ These electrodes enhanced the specific and cycling performance of supercapacitors, due to the synergetic effects between PEDOT:PSS, RuO₂ nanoparticles and graphene.

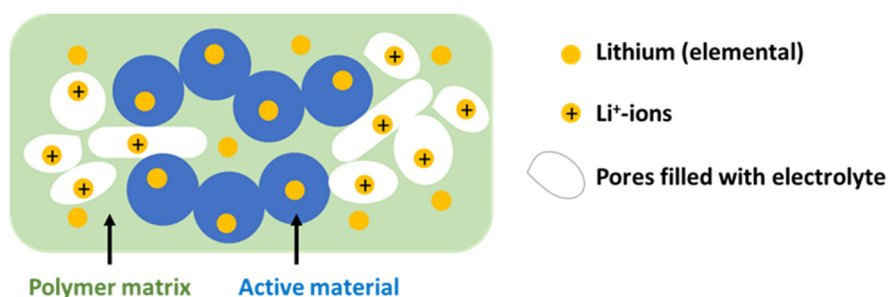


Figure 2-20: Schematic structure of electrodes for energy storage application (e.g. lithium-ion batteries or supercapacitors). The electrodes consist of a conductive polymer matrix with incorporated particles of active material. If the matrix does not consist of conductive polymers, additional conductive agents need to be added to the polymer.

Sensor materials often contain conductive nanoparticle-polymer hybrid materials, too. External stimuli such as mechanical deformation, temperature, contact with chemical (e.g. organic solvent or humidity) or biological target molecules (e.g. carbohydrates or metabolic products), cause an increase or decrease in resistivity of the hybrids, that can be detected. Conductive hybrids made of non-conductive polymer matrices with incorporated conductive filler nanoparticles, can for example be used as temperature- or strain-sensitive materials. Upon external stimuli (heating or deformation), the inter-particle distances between the conductive fillers increase, causing a drop in conductivity. For example, Rybak *et al.* fabricated temperature sensors by embedding AgNPs in a non-conductive copolymer matrix.⁴¹² Depending on the composition and morphology of the hybrid material, they observed the transition from a conductive to an insulating state at a temperature between 45 to 180 °C. Sensitive strain sensors were fabricated by Amjadi and co-workers by embedding silver nanowires (AgNWs) in a polydimethylsiloxane (PDMS) matrix.⁴¹³ The resulting hybrid materials could be stretched up to 70% and

showed good reproducibility in resistance change upon repeating bending and relaxation cycles.

Conductive nanoparticle-polymer hybrids are ideal materials for biosensors. These electrochemical sensors containing a biorecognition compound,⁴¹⁴ which can interact with biological substance, causing a change in electrical signal. This can be used to detect catalytic and redox behavior, adsorption and transport mechanism of biomolecules.^{410,414} As illustrated in Figure 2-21, a typical biosensor consists of several electrodes, including reference (RE), counter (CE) and working electrode (WE). Often insulating layers are deposited on top of the electrodes, preventing shortcuts and defining the reaction area.

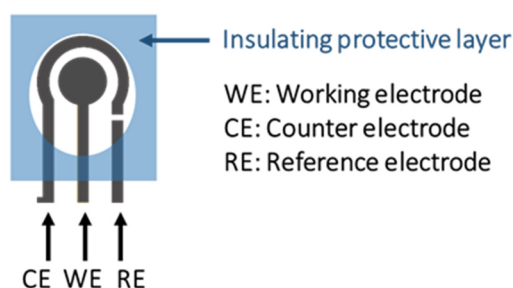


Figure 2-21: Exemplary setup of a biosensor composed of a reference (RE), a counter (CE) and a working (WE) electrode. Often insulating layers are deposited on top to define the reaction area and to prevent shortcuts between the electrodes.

The fabrication of a biosensor often requires the adsorption/attachment of bio-recognizable species such as enzymes, proteins, antibodies or DNA, on at least one of the electrodes. The simplest method to immobilize enzymes on electrodes, is physisorption based on weak interactions such as van der Waals forces or hydrogen bonds.^{415,416} Other methods include covalent bonding (chemisorption), cross-linking or the entrapment of enzymes in films or gels.^{415,416} Conductive polymers offer sufficient electrical conductivity, low ionization potentials and delocalized π -systems that are suitable for enzyme immobilization.^{415,416} Combining conductive inorganic or carbon nanoparticles with conductive polymers enhances the electrical conductivity, the surface area and the number of recognition sites.^{410,414} Miao and co-workers produced hybrid AuNPs stabilized by a polypyrrole shell.⁴¹⁷ The colloidal hybrid particles and the enzyme laccase were immobilized on gold electrodes. These modified electrodes showed enhanced electrocatalytic reduction of oxygen, since the hybrid particles promote direct and fast

electron transfer between the Au electrode and the enzyme. Qui *et al.* fabricated biosensor electrodes made from a PANI film with embedded graphene oxide flakes and platinum (Pt) nanoparticles.⁴¹⁸ The Pt nanocrystals improved the electrocatalytic activity by accelerating the electron transfer. Glucose oxidase (GOx) was immobilized on these hybrid electrodes to fabricate sensors for glucose and hydrogen peroxide (H₂O₂) detection. The sensors had limits of detection (LOD) in the nM and μ M range for H₂O₂ and glucose, respectively.

Another emerging application field for conductive nanoparticle-polymer hybrid materials is printed electronics.² Printing techniques are cost-effective and scalable compared to the traditional microfabrication of electronics, which are often expensive multi-step processes requiring cleanroom conditions. Printing allows high-throughput and rapid processing, even for large-area electronics. While electronics produced by conventional techniques are often rigid, printing on flexible polymer, textile or paper substrates, enables the fabrication of soft, lightweight, flexible, stretchable and wearable electronics. Printable nanomaterial inks are a key factor for the successful production of printed electronics. Several reviews discuss the appropriate formulation of nanomaterial inks and the successful printing of these inks to obtain high-performance printed electronic devices.^{2-4,94,419} The application fields of printed electronics are numerous, including displays, sensors, devices for energy storage and transparent conductors (Figure 2-22).²

Inkjet printing, electrohydrodynamic (EHD) printing, aerosol printing, screen printing, gravure printing, flexographic, roll-to-roll (R2R) printing, slot die coating and spray coating are used for the production of printed electronics. Inkjet printing is a low-cost, fast and accurate method, whereby the ink is deposited through a micrometer-sized printing nozzle. In a drop-on-demand (DOD) inkjet printer, the nozzle only ejects a drop when it receives an electrical signal to do so. Hence, DOD inkjet printing allows the deposition of small ink volumes (picolitre range) and the deposition of various materials on the same substrate.^{3,8} Since inkjet printing is a non-contact method and does not require any masks, the contamination of the substrate is reduced.^{3,7} The printed structures are digitally generated and can easily be changed by the computer, which makes inkjet printing scalable and inexpensive.⁸ Conductive nanoparticle-polymer hybrids have been successfully incorporated in various printed electronics.

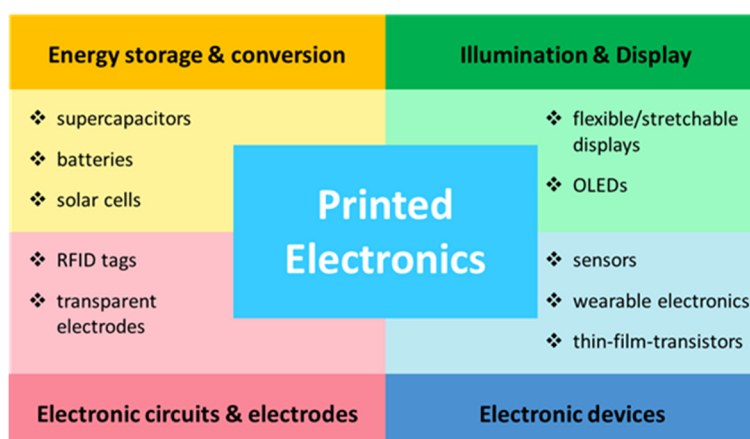


Figure 2-22: Application fields of printed electronics. Figure adapted from [2].

Wu *et al.* fabricated transparent conductors (TCs) by printing hybrid inks with an R2R slot die coating technique.⁴²⁰ The inks contained PEDOT:PSS with mixed AgNWs (Ag content up to 20 wt%). Electro-luminescence lighting devices were fabricated by implementation of the hybrid TCs as electrodes. These devices showed similar performance and durability as the ones containing vacuum-processed ITO electrodes. Highly flexible micro-supercapacitors were produced by a mask-assisted spray coating process of an hybrid ink consisting of PEDOT:PSS and graphene flakes.⁴²¹ The inks were printed on paper and PET foils obtaining flexible supercapacitors. After 100 bending cycles the printed supercapacitors merely lost 1.5% of their capacitance. In addition, the printed devices also withstand random folding and bending without significant loss in the measured capacitance. This makes the printed supercapacitors ideal for implementation in wearable electronics. Min *et al.* created fully printed strain sensors by printing a hybrid ink with an aerosol printing method.⁴²² The hybrid ink was a mixture of AgNPs and multiwalled carbon nanotubes (MWCNTs), which was printed on a PDMS substrate. The fabricated strain sensors had a maximal strain limit of 74% and possessed an excellent durability over 1000 loading-unloading cycles.

The results presented in the upcoming result chapter 3.4 demonstrate, that gold-polythiophene hybrid nanocrystals introduced in this work can be successfully employed for the production of printed electronics. Inks containing gold-polythiophene hybrid nanoparticles were inkjet-printed to produce electrochemical glucose sensors.

3. Results

3.1 Molecular origin of electrical conductivity in gold-polythiophene hybrid nanoparticles*

The molecular arrangement of polythiophene chains at gold-polythiophene interfaces of hybrid nanocrystals affects the electrical properties of the appropriate hybrids. Gold nanocrystals with different shapes (spherical vs. rod-shaped) were functionalized with a commercial polythiophene poly[2-(3-thienyl)-ethyloxy-4-butylsulfonate] (PTEBS, structure shown in Figure 3-1) to investigate if the geometries of the gold cores affect the binding configuration of the polythiophene ligands.

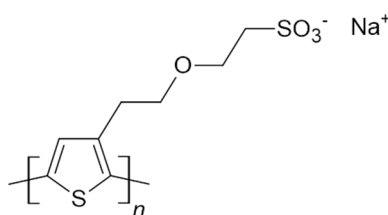


Figure 3-1: Molecular structure of PTEBS.

Films made of the two different types of gold-PTEBS nanocrystals were directly conductive after deposition without sintering. Layers of gold-polythiophene hybrid nanorods were 40% more electrically conductive. Spectroscopic methods (Raman and X-ray photoelectron spectroscopy) were used to identify the binding motifs and the binding configurations. The molecular orientation of polythiophenes (edge-on vs. face-on) affects their charge carrier features as already described in sections 2.2.3 and 2.2.4. The information obtained by spectroscopic methods about the molecular orientation of

* Parts of the presented results in this chapter 3.1 were published and adapted with permission from Backes *et al.* Molecular origin of electrical conductivity in gold-polythiophene hybrid particle films. *J. Phys. Chem. Lett.* **11**, 10538–10547 (2020). Copyright 2020 American Chemical Society.⁴²³ The texts, tables and figures of chapter 3.1 are based on [423].

PTEBS on spherical gold nanoparticles (AuNPs) and gold nanorods (AuNRs) was correlated to the detected electrical properties of the two gold-PTEBS hybrid nanocrystals. The face-on arrangement of PTEBS on AuNRs facilitated charge transport between adjacent AuNRs, resulting in enhanced electrical conductance. The distinct binding configuration of PTEBS on AuNPs and AuNRs can likely be attributed to differences in the gold-PTEBS interactions due to variations in the surface curvature and surface faceting of the two types of nanocrystals.

3.1.1 Structural and colloidal analysis of gold-PTEBS hybrid nanocrystals

I synthesized anisotropic gold nanorods using an established protocol by Ye *et al.*¹⁵⁰ To synthesize quasi-spherical particles with diameters comparable to the long axis of the AuNRs, I slightly modified the AuNRs fabrication protocol. The as-synthesized AuNRs@CTAB and AuNPs@CTAB were stabilized by the cationic surfactant CTAB. These nanocrystals were functionalized with the conductive polymer poly[2-(3-thienyl)-ethyloxy-4-butylsulfonate] (PTEBS) using an existing ligand exchange protocol.⁶⁹ The structures of these hybrid particles, hereinafter referred to as AuNRs@PTEBS and AuNPs@PTEBS, were characterized at a colloidal and molecular level. Details on the nanocrystal synthesis, purification and ligand exchange are provided in sections 6.2.1 and 6.2.2.

As depicted in the transmission electron micrographs (TEMs) of Figure 3-2, the AuNRs@PTEBS possessed uniform cylindrical shape, while the AuNPs@PTEBS were highly faceted and quasi-spherical with various polyhedral shapes. Since the shape of the AuNPs can be approximated by spheres, these nanocrystals are further denoted as nanospheres or spherical nanoparticles. The TEMs clearly show that the ligand exchange had no influence on the morphology of AuNPs and AuNRs. The average length and average diameter of the PTEBS-functionalized gold nanorods obtained by image analysis of 219 AuNRs in TEMs were 93.5 nm and 19.0 nm, respectively (Figure 3-2c). The mean diameter of PTEBS-coated spherical gold nanoparticles was 80.8 nm determined by size analysis with enclosing circles of 264 AuNPs in TEMs (Figure 3-2d).

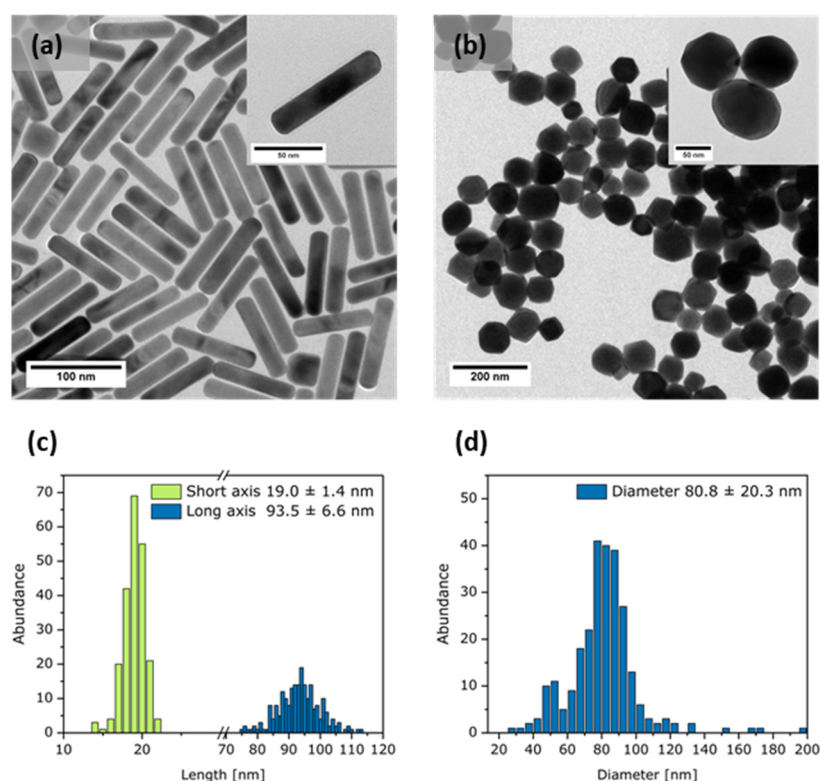


Figure 3-2: Transmission electron micrographs and particle size distribution from TEM analysis of (a, c) gold nanorods AuNRs@PTEBS and (b, d) gold nanospheres AuNPs@PTEBS. TEMs were taken after purification of the nanocrystal dispersions. Reprinted with permission from [423].

The colloidal properties of as-synthesized AuNPs@CTAB and polythiophene-functionalized AuNPs@PTEBS after ligand exchange were analyzed by dynamic light scattering (DLS). Hydrodynamic diameters d_h (Z-average diameters) were obtained from cumulant analysis of DLS data. In addition, the polydispersity index (PDI) was determined to estimate the polydispersity of every sample. The hydrodynamic diameters d_h and polydispersity indices derived from DLS of AuNPs@CTAB and AuNPs@PTEBS are summarized in Table 3-1. The increase in hydrodynamic diameter d_h after ligand exchange is caused by the larger size of the polythiophene PTEBS compared to the single molecule CTAB. The PDI were comparable for AuNPs@PTEBS and AuNPs@CTAB, indicating a homogeneous distribution of the conductive polymer ligand PTEBS and the initial ligand CTAB. After ligand exchange, the PTEBS-stabilized particles were purified by centrifugation, which can lead to loss of smaller particles. This probably explains why the hydrodynamic diameter d_h of AuNPs@PTEBS was slightly smaller than the one of the initial particles AuNPs@CTAB.

Table 3-1: Hydrodynamic diameters d_h and polydispersity indexes (PDI) obtained by DLS for the as-synthesized AuNPs@CTAB and the purified AuNPs@PTEBS after ligand exchange. Reprinted with permission from [423].

	d_h [nm]	PDI
AuNPs@CTAB	90.7	15.70%
AuNPs@PTEBS	85.9	17.50%

Figure 3-3a illustrates the mass loss curves of the as-synthesized AuNRs@CTAB and AuNPs@CTAB obtained by thermogravimetric analysis (TGA). For both nanocrystals most of the CTAB decomposition occurred in the temperature range of 200 °C to 350 °C, corresponding to published literature.^{125,424,425} A small second mass loss step at higher temperatures for AuNRs@CTAB corresponds to the known CTAB bilayer. The outer CTAB layer is first removed, followed by the detachment of the inner CTAB layer, which is covalently bound to the gold surface of AuNRs, at higher temperatures.¹²⁵ The complete removal of the CTAB ligand required lower temperatures for AuNPs@CTAB than AuNRs@CTAB. Literature attributes this to the stronger binding of CTAB to the lateral {110} facets of AuNRs.¹²⁵ The entire weight fraction of CTAB detected by TGA was 4.6 wt% for AuNRs@PTEBS and 1.0 wt% AuNPs@PTEBS, respectively.

TGA results of PTEBS-stabilized AuNRs and AuNPs after ligand exchange are illustrated in Figure 3-3b. The main mass loss step occurred in the range of 200 °C to 600 °C. The slopes of the TGA curves for PTEBS-coated nanocrystals were flatter than the ones of the CTAB-functionalized AuNRs and AuNPs. The mass loss steps of CTAB and PTEBS overlapped and TGA was not a suitable method to detect residual low amounts of CTAB after ligand exchange. Therefore, I employed Raman (section 3.1.3) and X-Ray photoelectron (section 3.1.4) spectroscopy to prove the successful replacement of CTAB by the conductive polymer PTEBS.

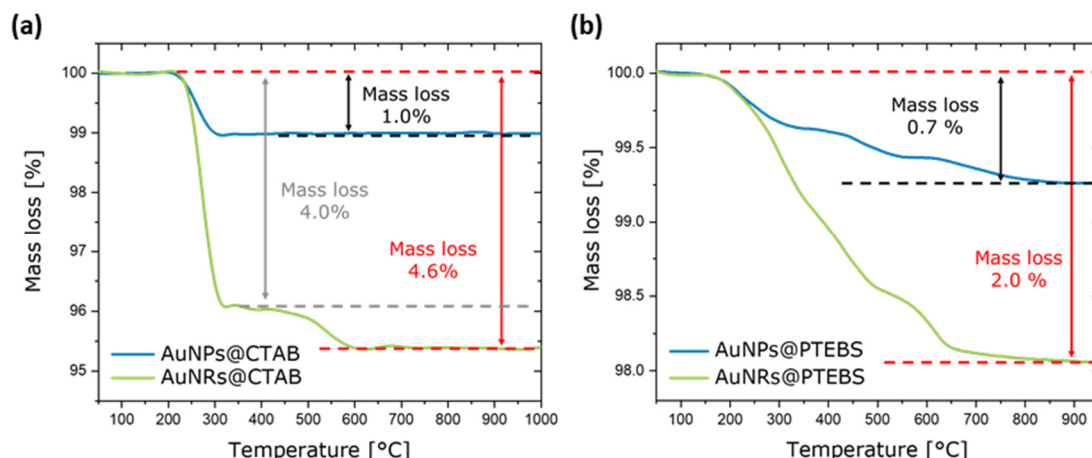


Figure 3-3: TGA curves obtained from dried samples of (a) AuNRs@CTAB and AuNPs@CTAB; (b) AuNRs@PTEBS and AuNPs@PTEBS dispersions. The samples were heated from 50 °C to 1000 °C under nitrogen atmosphere with a heating rate of 10 °C·min⁻¹. Reprinted with permission from [423].

In addition, I used the TGA data to determine the overall quantity of organic components. To calculate the thickness of the PTEBS ligand shell, I applied a geometrical model. The geometrical dimensions (average length and average diameter) of the AuNRs and the AuNPs were determined by image analysis of transmission electron micrographs as explained above. Based on published models,⁶⁹ the surface and volume of gold nanoparticles and gold nanorods were approximated by a perfect sphere and a cylinder having two hemispheres attached at the tips as depicted in Figure 3-4.

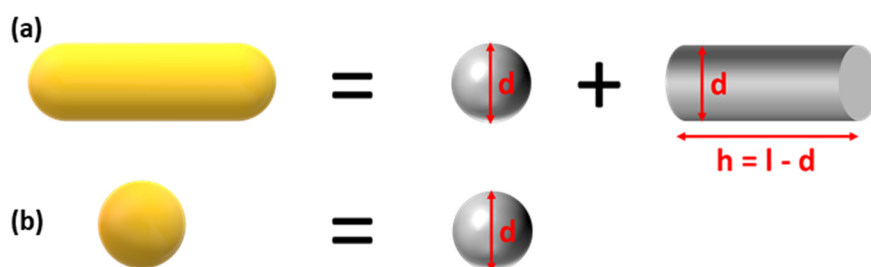


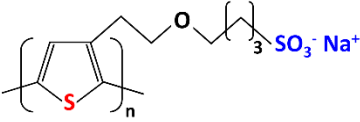


Figure 3-4: Geometrical models for the calculation of surface and volume for (a) AuNRs and (b) AuNPs. The AuNRs are approximated with a cylinder having two hemispheres attached at the tips. The AuNPs are approximated by a sphere. Reprinted with permission from [423].

The detected organic weight fractions obtained by TGA for AuNRs@PTEBS and AuNPs@PTEBS were 2.0 wt% and 0.7 wt%, respectively. Based on the observations made by DLS, I assumed a homogeneous distribution of the conductive polymer around the nanocrystals. This assumption is further supported by the results obtained by XPS, which will be explained in the upcoming section 3.1.4. I presumed that the organic mass fractions derived from TGA originate completely from PTEBS, which homogeneously surrounded the nanocrystals. This implies a successful replacement of CTAB by the conductive polymer PTEBS consistent with Raman spectroscopy and XPS (sections 3.1.3 and 3.1.4).

Table 3-2: Geometrical dimensions of AuNPs and AuNRs obtained from TEM analysis. Calculated surface and volume values of AuNRs and AuNPs. Mass and volume fractions of gold (Au) and PTEBS obtained from TGA. Density value of Au was taken from literature.⁴²⁶ Density value of PTEBS was measured with a gas pycnometer. Reprinted with permission from [423].

	Au core	
		
diameter (TEM)	19.0 nm	80.8 nm
length (TEM)	93.5 nm	/
surface (calculated)	5581 nm ²	20510 nm ²
volume (calculated)	24714 nm ³	276206 nm ³
density (literature) ⁴⁴²	19.30 g·cm ⁻³	19.30 g·cm ⁻³
mass fraction (TGA)	98.0%	99.3%
	Ligand shell	
		
density PTEBS (measured)	2.07 g·cm ⁻³	2.07 g·cm ⁻³
mass fraction (TGA)	2.0%	0.7%
volume (calculated)	4607 nm ³	18948 nm ³
volume fraction (calculated)	18.6%	6.9%
shell thickness	0.9 nm	0.9 nm

The detected mass fractions of AuNRs@PTEBS and AuNPs@PTEBS differed from each other, but they caused identical calculated shell thicknesses of the dried ligand shells being 0.9 nm for both gold-polythiophene nanocrystals (Table 3-2). This calculated shell thickness concurs with previously observed ligand shell thicknesses of AuNRs@PTEBS obtained from TEM and TGA characterization.⁶⁹ The detected ligand shell thicknesses match a configuration with one polymer chain in an upright orientation (edge-on configuration) or two to three polymer chains being stacked parallel to the Au surface (face-on configuration).^{81,248} In the latter configuration, the first polythiophene layer is covalently bound to the gold surface, while the additional layers attach by π - π interactions with a known average polythiophene π - π stacking distance of 0.37-0.39 nm.²⁴⁷⁻²⁴⁹

3.1.2 Electrical conductivity of gold-PTEBS hybrid nanocrystal films

Line patterns were fabricated on glass substrates by drop-casting of dispersions containing AuNRs@PTEBS and AuNPs@PTEBS. Details of the deposition process are listed in section 6.2.4. The patterns were immediately conductive after drying, demonstrating the sinter-free nature of the gold-polythiophene hybrid systems used in this work (Figure 3-5). The precise geometrical dimensions of the lines were determined by confocal microscopy (thickness of each line) and optical transmission microscopy (width and length of each line). The detected thicknesses of the films were between 4 μ m and 10 μ m, with thickness variations within one layer of below 30%. The measured topography data were converted into histograms. By fitting these histograms, the overall film thickness with the corresponding standard deviation was obtained. Details about the thickness calculation and exemplary topography data are given in section 6.3.5. The obtained geometrical dimensions were used to determine the exact cross section of the line patterns and to calculate the material resistivity values ρ .

I contacted the lines by silver paste and detected current-voltage (I - V) curve of six individual samples for each nanocrystal system (AuNRs@PTEBS and AuNPs@PTEBS). The averaged I - V curves for AuNRs@PTEBS and AuNPs@PTEBS are depicted in Figure 3-5a and b. The linear shape of the current-voltage curves, demonstrated the ohmic

behavior (metallic-like electrical conductivities) of films made from hybrid spherical nanoparticles and hybrid nanorods. The material resistivities ρ of AuNRs@PTEBS and AuNPs@PTEBS were calculated according to equation 3-1.

$$\rho = R \cdot t \cdot \frac{w}{l} \quad (3-1)$$

In the equation above R refers to the resistance, t to the thickness, w to the width and l to the length of the hybrid line patterns.

The measured current was normalized to the thickness of each line pattern (Figure 3-5). The material resistivity ρ was calculated by multiplying the ratio of width to length (w/l) by the inverse of the current-voltage curve's slope ($R \cdot t$). The average resistivity values with the corresponding standard deviations were calculated by analyzing six individual samples of each gold-polythiophene hybrid nanocrystal system.

The electrical conductivity of line-shaped films made from AuNPs@PTEBS was 44% below that of AuNRs@PTEBS layers. The average resistivities of the two hybrid materials were $7.10 \cdot 10^{-6} \text{ } \Omega\text{m} \pm 0.15 \cdot 10^{-6} \text{ } \Omega\text{m}$ for AuNPs@PTEBS and $3.96 \cdot 10^{-6} \text{ } \Omega\text{m} \pm 0.28 \cdot 10^{-6} \text{ } \Omega\text{m}$ for AuNRs@PTEBS (\pm one standard deviation, Figure 3-5a), two orders of magnitude above the resistivity of bulk gold ($2.35 \cdot 10^{-8} \text{ } \Omega\text{m}$).¹⁶⁰ The scanning electron micrographs (SEMs) in Figure 3-5c and d show that the conductive lines consisted of individual hybrid nanocrystals without any sign of sintering inside the films.

Films composed of hybrid nanocrystals resemble three-dimensional infinite resistor networks^{196,197} and the contact resistance R_c at the nanoparticle junctions is a key factor influencing the overall conductivity of nanoparticle films (section 2.1.3). This contact resistance is affected by the ligand shells between the metallic cores.²⁰⁶ The PTEBS shell thicknesses were 0.9 nm for both, AuNRs@PTEBS and AuNPs@PTEBS, based on the organic mass fractions obtained from TGA measurements (section 3.1.1). The identical ligand shell thicknesses suggested that the detected conductivity variations between films made of AuNRs@PTEBS and AuNPs@PTEBS did not originate from smaller inter-particle distances between adjacent gold nanocrystals.

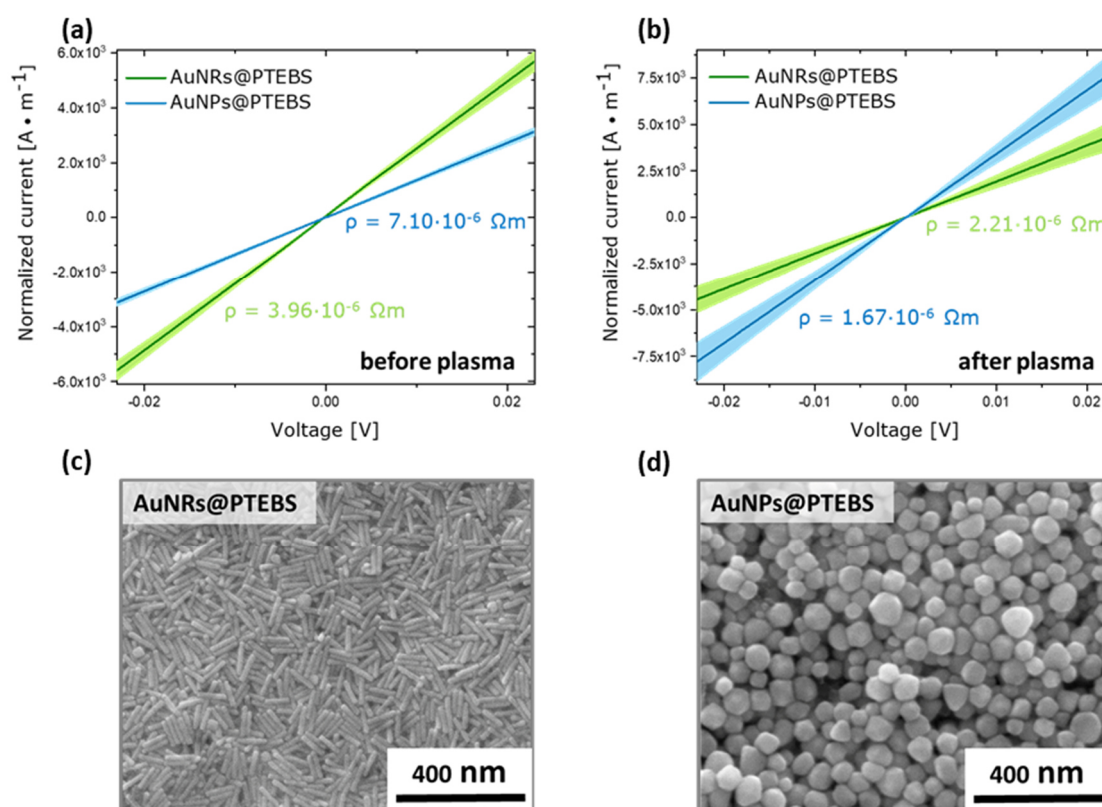


Figure 3-5: (a-b) Average I - V curves with normalized currents to film thicknesses of AuNPs@PTEBS (blue) and AuNRs@PTEBS (green) with the corresponding error ranges (light blue, light green) (a) before and (b) after plasma treatment (Ar/H₂ plasma). Six individual samples were analyzed and two of them were exposed to the plasma. (c, d) Scanning electron micrographs of line patterns on glass substrates deposited from (c) AuNRs@PTEBS dispersions and (d) AuNPs@PTEBS dispersions before plasma treatment. Reprinted with permission from [423].

I analyzed the impact of the PTEBS ligands in layers made from hybrid nanoparticles and hybrid gold nanorods by removing the polymer partially from the inter-particle junctions. Plasma treatment of nanoparticle films removes the polymer ligand, which enhances the overall conductivity (decrease in resistivity) of the hybrid films.⁶⁹ Layers with identical thicknesses ($\approx 5 \mu m$) made from both gold-polythiophene hybrid nanocrystals were exposed to an Ar/H₂ plasma (5% H₂) for 30 minutes and electrically characterized afterwards. As depicted in Figure 3-5b, the plasma treatment caused a decrease in resistivity (increase in conductivity) for AuNPs@PTEBS films by a factor of 4.3 (to $1.67 \cdot 10^{-6} \Omega m \pm 0.03 \cdot 10^{-6} \Omega m$) and for AuNRs@PTEBS layers by a factor of 1.8 (to $2.21 \cdot 10^{-6} \Omega m \pm 0.02 \cdot 10^{-6} \Omega m$). After plasma exposure, films made of AuNPs@PTEBS were 32% more conductive than layers from AuNRs@PTEBS. The SEMs of the hybrid

films before and after plasma exposure in Figure 3-6 show that the plasma treatment had no impact on the film morphology. The AuNPs and AuNRs cores were not affected by the plasma and preserved their shapes and dimensions.

Since the plasma-treated layers had similar thicknesses and packing densities, I assumed comparable plasma penetration depths for layers made from AuNRs@PTEBS and AuNPs@PTEBS and that the conductive polymer PTEBS was removed entirely above the penetration depth, but unchanged below. The plasma-treated volume of the film was transformed into a porous metallic structure, in which the electrical properties of the film are determined by the contact cross-sections (contact areas) and number of contact points between the metallic nanocrystals. Before plasma exposure, layers made from AuNRs@PTEBS were more conductive than those produced by AuNPs@PTEBS. I conclude, that the PTEBS ligand shells lowered the electrical conductivity before plasma treatment and that the effect was different for AuNRs@PTEBS and AuNPs@PTEBS. The removal of less conductive PTEBS should lower the entire resistivity more than the elimination of more conductive PTEBS. I conclude that PTEBS surrounding AuNRs were more conductive than those surrounding AuNPs. Thus, the conductivity of the polymer inside the ligand shell is affected by the nanocrystal geometry. Strong van der Waals interactions between π -conjugated bonds of conductive polymers and carbon nanomaterials caused ordered arrangement of polythiophenes on graphene and carbon nanotubes.^{71,278,331,334} Similar interactions do not exist in our hybrid systems based on the inorganic nature of the metallic nanocrystals. However, literature reports enhanced conductivity due to molecular polymer chain alignment of polythiophenes caused by nano-confinement.^{78,79} It is possible that the gold nanoparticles and gold nanorods used in this work induced similar molecular arrangements of the PTEBS polymer chains depending on the nanocrystals' shape.

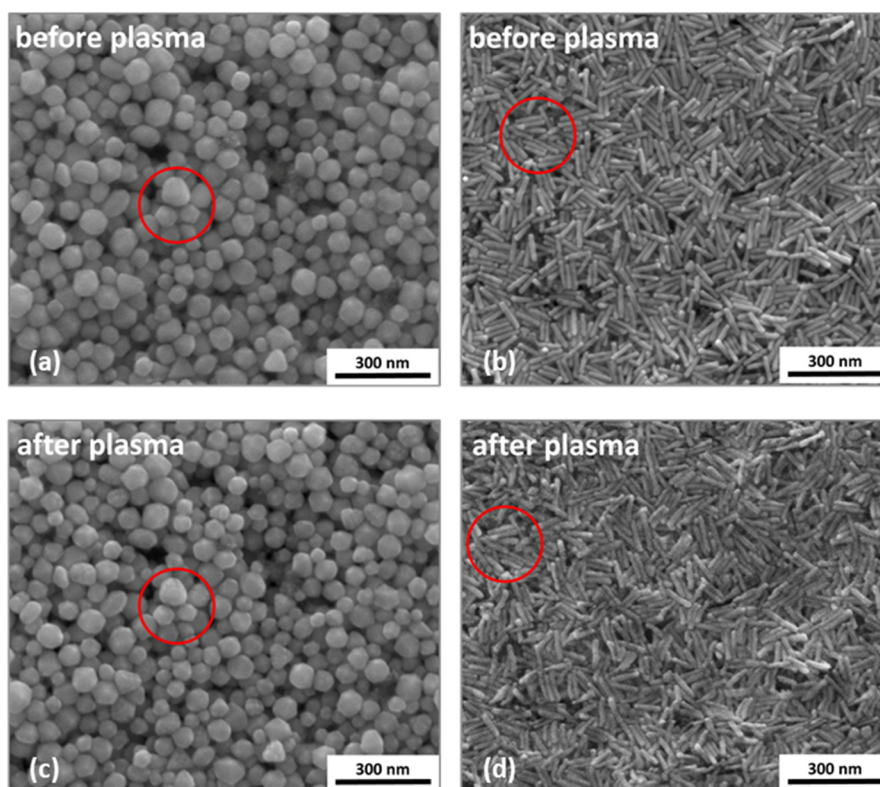


Figure 3-6: Scanning electron micrographs of layers made from AuNPs@PTEBS (a, c) and AuNRs@PTEBS (b, d) before and after plasma exposure with Ar/H₂ plasma for 30 min. The SEMs were recorded at nearly identical positions of the AuNPs@PTEBS and AuNRs@PTEBS films before and after plasma exposure. The red circles mark areas where the plasma treatment caused slight structural changes. Reprinted with permission from [423].

3.1.3 Characterization of ligand binding in gold-PTEBS hybrids by Raman spectroscopy

I used Raman spectroscopy to quantify if the initial ligand CTAB was successfully replaced by PTEBS and to further analyze the molecular arrangement of the conductive polymer chains at gold-polythiophene interfaces. Before ligand exchange, the Raman spectra of AuNRs@CTAB and AuNPs@CTAB exhibited peaks of Au-Br vibrations in the fingerprint region at 177 cm^{-1} (Figure 3-7a), which is characteristic for CTAB-stabilized nanocrystals.⁴²⁷ After ligand exchange, these peaks disappeared, indicating near-complete substitution of CTAB by the conductive polymer PTEBS. In addition, new peaks between 200 cm^{-1} and 300 cm^{-1} occurred (Figure 3-7b), which refer to Au-S

stretching modes, indicating that PTEBS bind to the gold nanocrystals via sulfur atoms.⁴²⁸ All characteristic vibration modes of pure PTEBS were also present in the Raman spectra of AuNRs@PTEBS and AuNPs@PTEBS (Figure 3-7c). The most prominent Raman peaks of polythiophenes are the typical triplet motive between 1300 cm^{-1} and 1550 cm^{-1} , which originate from intra-ring C-C and symmetric and asymmetric C=C stretch modes (Figure 3-7). A detailed peak assignment of the vibrational peaks for pure PTEBS is given in Table 3-3. Since no literature data is available for PTEBS, the peak assignment was based on equivalent polythiophenes (e.g. P3HT) and sulfonate-containing molecules.^{429–}

432

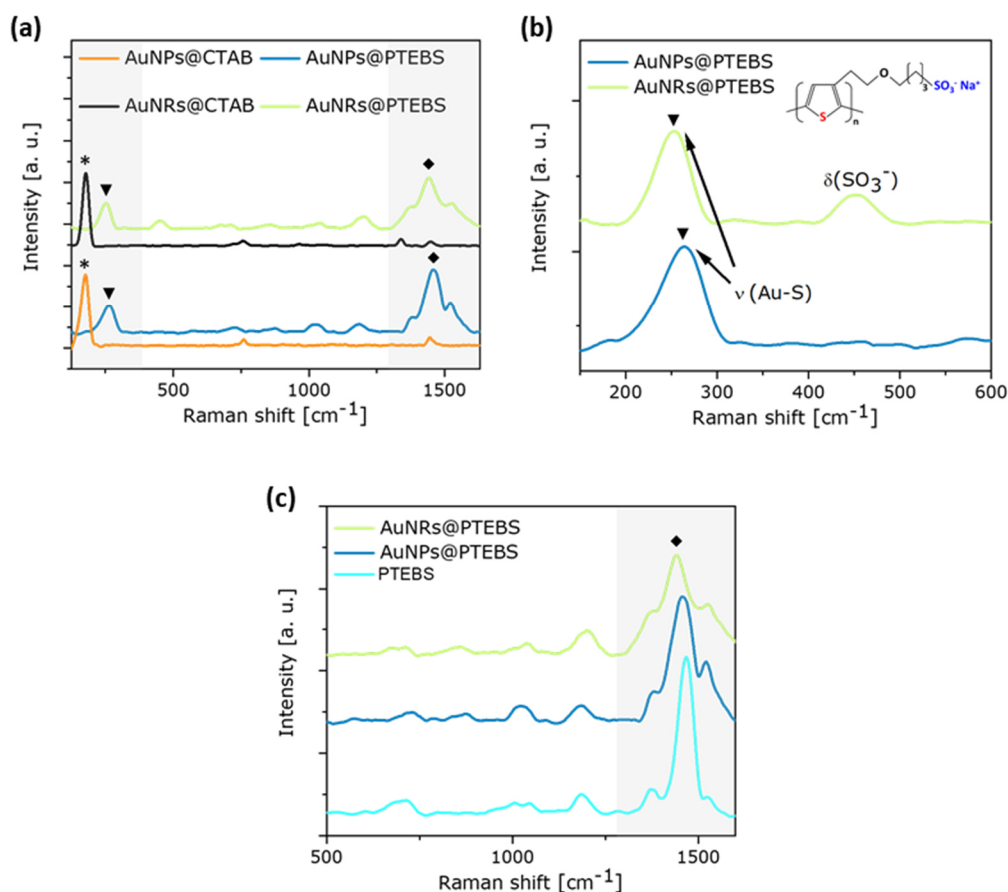


Figure 3-7: (a) Raman spectra of the as-synthesized nanocrystals (AuNRs@CTAB and AuNPs@CTAB) and of the PTEBS-stabilized nanocrystals after ligand exchange (AuNRs@PTEBS and AuNPs@PTEBS). (b) Fingerprint region of the Raman spectra of the PTEBS-stabilized nanocrystals (AuNRs@PTEBS and AuNPs@PTEBS) and structure of PTEBS. (c) Raman spectra of PTEBS-stabilized nanocrystals and of pure PTEBS. Important vibrations modes are marked in the spectrum: $\nu(\text{Au-Br})=*$, $\nu(\text{Au-S})=\blacktriangledown$, $\nu(\text{C-C, C=C})=\blacklozenge$. Reprinted with permission from [423].

Table 3-3: Characteristic vibrational peaks detected in the Raman spectrum of pure PTEBS. The band assignment is based on literature values of equivalent polythiophenes (e.g. P3HT) and sulfonate-containing molecules.^{429–432} Reprinted with permission from [423].

Raman shift [cm^{-1}]	Band assignment
704	$\delta(\text{C-S-C})$ ring deformation mode and $\nu(\text{S=O})$ stretching mode
1000-1070	$\delta(\text{CH}_2)$ bending mode and $\nu(\text{S=O})$ stretching mode
1183	$\delta(\text{C-H})$ bending mode
1374	intra-ring $\nu(\text{C-C})$ stretching mode
1462	symmetric $\nu_s(\text{C=C})$ ring stretching mode
1528	asymmetric $\nu_{as}(\text{C=C})$ ring stretching mode

Compared to the Raman spectrum of pure PTEBS (Figure 3-7c), the triplet peaks in the range of 1300 cm^{-1} to 1550 cm^{-1} were broadened and blue-shifted in the Raman spectra of AuNRs@PTEBS and AuNPs@PTEBS. Similar observations have been reported for doped polythiophenes,^{433,434} whereby doping resulted in the formation of polarons and bipolarons.^{433,434} As described in the theory section 2.2.2, polarons and bipolarons are the origin of electrical conductance in polythiophenes. The Raman results suggest that polarons and bipolarons were also present in the PTEBS ligand shell of the hybrid nanocrystals (AuNRs@PTEBS and AuNPs@PTEBS). It is likely that electron transfer between the gold cores and the PTEBS ligands at the metal-organic interfaces occurred according to the ICT model introduced in section 2.1.4, which result in polaron and bipolaron formation in the polythiophene ligand shell. Since the energetic position of the polaron/bipolaron states in PTEBS, referred to as positive and negative integer charge-transfer states $E_{\text{ICT}+}/E_{\text{ICT-}}$,⁸⁴ likely lies above the Fermi level E_{F} of gold, electrons flow from the PTEBS ligands to the gold cores, resulting in p-doping of the polythiophene ligand shell. The excellent electrical properties of AuNRs@PTEBS and AuNPs@PTEBS presented in section 3.1.2 presumably originated from this p-doping, enhancing inter-particle charge carrier transport between adjacent gold cores. Further details and a comprehensive discussion about the charge transfer at the gold-polythiophene interfaces are given in section 3.2.4. Since the blue-shifting and broadening of the triplet peaks (1300 cm^{-1} to 1550 cm^{-1}) was more pronounced for gold nanorods, I assume that more polarons and bipolarons were present in the case of AuNRs@PTEBS. This concurs with

the detected higher electrical conductivity of films made from gold-polythiophene hybrid nanorods (section 3.1.2).

As already described in section 2.2.3, polythiophenes PTEBS can bind to metal surfaces in two different configurations, denoted as face-on and edge-on configuration (Figure 3-8a-c). The sulfur species of PTEBS bind to the gold cores via physisorption or chemisorption, which are common binding types of sulfur-containing molecules on gold surfaces.^{435–437} In a face-on arrangement both types of sulfur atoms, present in the sulfonate groups and in the thiophene backbone, can bind to gold (Figure 3-8a). By π - π stacking, additional PTEBS chains can organize perpendicularly to the substrate. Due to steric limitations, only one of the sulfur species, the sulfur in the sulfonate groups or the sulfur of the thiophene, can bind to gold if PTEBS attach in an edge-on configuration. For this edge-on arrangement of PTEBS two different binding types can be distinguished. In one, the sulfur atoms of the SO_3^- groups bind to gold (Figure 3-8b), while in the second mode the sulfur atoms of the thiophene backbone bind to gold (Figure 3-8c).

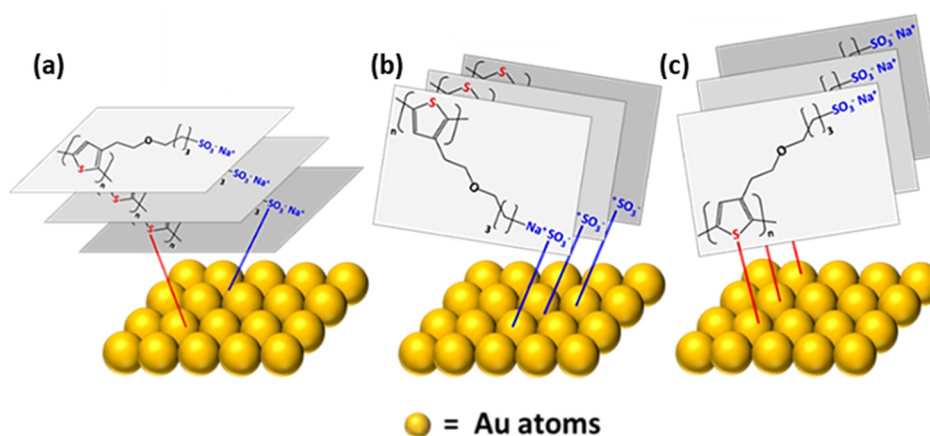


Figure 3-8: (a) Schematic illustrations of sterically possible PTEBS configurations on gold: (a) face-on binding where both sulfur species (thiophene and sulfonate groups) contribute to binding. (b) edge-on binding where only sulfur atoms of the sulfonate groups in the side chain bind to gold. (c) edge-on binding where only the sulfur atoms in the thiophenes of the polymer backbone contribute to the binding. The π - π interactions between the thiophene rings can lead to stacking of additional PTEBS layers in all three configurations. Reprinted with permission from [423].

PTEBS-stabilized spherical gold nanoparticles possessed only one Au-S stretching mode peak at 265 cm^{-1} , while gold nanorods coated with PTEBS had an additional peak at 451 cm^{-1} , which can be related to the deformation vibration of the sulfonate SO_3^- group

according to literature (Figure 3-7a and b).⁴³² Carlini *et al.* characterized gold and silver nanoparticles stabilized with 3-mercaptopropylsulfonate (3-MPS) and detected Au-S stretch mode peaks and deformation vibration peaks that are specific for free SO_3^- groups.⁴²⁹ They concluded that the sulfonate group stayed flexible and did not bind to the gold. The sulfonate groups of PTEBS presumably behaved equally and did not bind entirely to AuNRs and AuNPs. These mobile SO_3^- groups resulted in the observed deformation vibration peak for AuNRs@PTEBS (Figure 3-7b). Since this peak disappears upon binding of the sulfonate groups to the gold cores, Raman data imply lower fractions of bound sulfonate groups for gold nanorods compared to spherical gold nanoparticles (Figure 3-7). Unbound sulfonate groups can be induced by PTEBS binding in edge-on configuration with thiophene binding mode (Figure 3-8c) or by additional π -stacked PTEBS layers with face-on configuration above the covalently bound first polymer layer (Figure 3-8a). Based on the Raman results, I presumed that one of these configurations is more frequent for nanorods than for spherical nanoparticles. To determine the fractions of the different PTEBS binding configurations surrounding AuNRs and AuNPs, X-ray photoelectron spectroscopy (XPS) was applied (section 3.1.4).

3.1.4 Spectroscopic characterization of the molecular polymer orientation in gold-PTEBS hybrid nanocrystals[†]

X-ray photoelectron spectroscopy (XPS) was used to quantitatively detect the polymer binding configuration depending on the shape of the gold nanocrystals. Different binding states of the two sulfur species, thiophene and sulfonate group, were identified by detailed analysis of the S 2p region in the XPS spectra. XPS survey spectra of AuNRs@PTEBS and AuNPs@PTEBS are depicted in Figure 3-9b and d. Both XPS spectra exhibited peaks from Au, Ag, C, O, S and Na. Detailed element distribution obtained by XPS analysis is listed in Table 3-4.

[†] All XPS, STM and STS measurements and the corresponding data analyses presented in this section were performed by Dr. Frank Müller and Dr. Anne Holtsch (group of Prof. Jacobs, Experimental Physics and Center for Biophysics, Saarland University, Saarbrücken, Germany).

Table 3-4: Detected element distribution by XPS and recalculated element distribution related to the stoichiometric composition of PTEBS-stabilized gold nanorods and spherical gold nanoparticles. Reprinted with permission from [423].

AuNRs@PTEBS (detected)					
Au (at-%)	Ag (at-%)	C (at-%)	O (at-%)	S (at-%)	Na (at-%)
41.6	11.4	28	11.1	6	1.9
AuNPs@PTEBS (detected)					
Au (at-%)	Ag (at-%)	C (at-%)	O (at-%)	S (at-%)	Na (at-%)
40	11.2	30.3	11.5	5.8	1.2
AuNRs@PTEBS (normalized)					
		C	O	S	Na
		10.13	4.01	2.17	0.69
AuNPs@PTEBS (normalized)					
		C	O	S	Na
		10.57	4	2.02	0.43

The detected silver impurities originate from the silver nitrate (AgNO_3) used during the synthesis of gold nanorods and spherical gold nanoparticles. The XPS data clearly show that silver ions were incorporated inside the gold nanocrystals. Normalizing the element distribution of the polymer ligand (C, O, S and Na fractions) to the number of atoms in a PTEBS monomer unit (excluding hydrogen atoms, which are not detectable by XPS) results in the expected stoichiometric composition of pristine PTEBS (Table 3-4). The data prove that no decomposition of the conductive polymer occurred upon binding to spherical or rod-shaped gold nanocrystals and during XPS measurements. Scanning tunneling microscopy (STM) images detected in ultra-high vacuum (UHV) (Figure 3-9a and c) show the gold nanorods and the polyhedral shape of AuNPs on the surface of the probed films made from AuNRs@PTEBS and AuNPs@PTEBS, respectively. The dimensions of AuNRs and AuNPs detected by STM corresponded to the values obtained by TEM analysis (section 3.1.1).

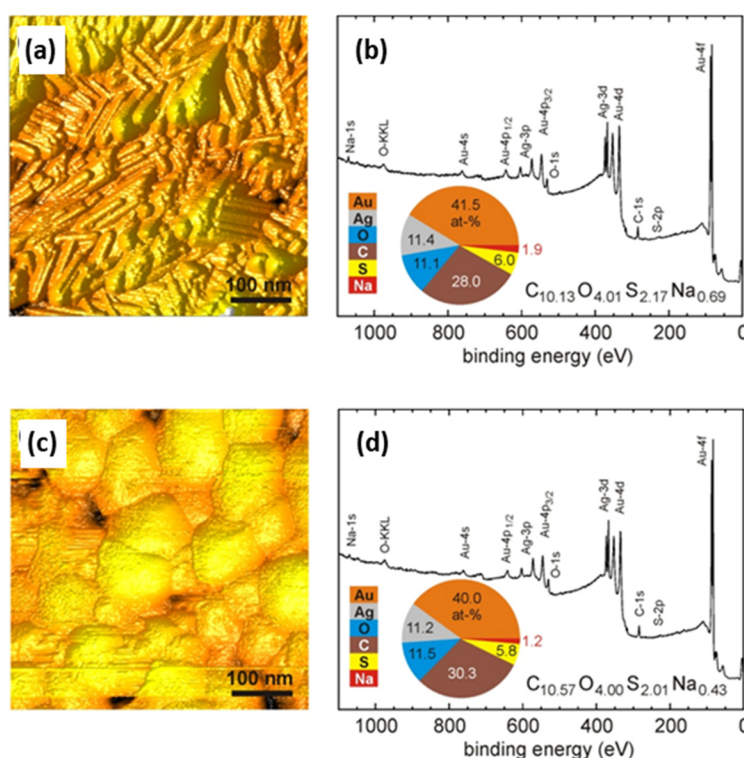


Figure 3-9: (a) Scanning tunneling micrograph of AuNRs@PTEBS deposited on Si substrate (500 x 500 nm² area, tunneling current 0.1 nA, bias voltage -100 mV). (b) XPS survey spectrum of AuNRs@PTEBS. (c) Scanning tunneling micrograph of AuNPs@PTEBS (500 x 500 nm² area, tunneling current 20 pA, bias voltage 50 mV). (d) XPS survey spectrum of AuNPs@PTEBS. Reprinted with permission from [423].

Figure 3-10a illustrates a reference S 2p XPS spectrum of a pristine PTEBS layer on a silicon (Si) substrate. Silicon was chosen as substrate for all XPS samples, since it does not interact with PTEBS and the polythiophene-stabilized nanocrystals. The spectra of pure PTEBS show two distinct peaks at binding energies of about 168 eV (S1, blue) and 164 eV (S2, red). These peaks originate from the sulfur species of the sulfonate groups in the polymer side chain (S1, blue)^{438,439} and of the thiophene in the conjugated backbone of the polymer (S2, red),^{440,441} respectively. Each peak was fitted to the sum of two Gaussian functions with identical widths (FWHM=1.62 eV) separated by a spin orbit splitting of 1.31 eV (Figure 3-10a). Related to the multiplicities of the 2p_{3/2} and 2p_{1/2} states, the fitting intensity ratios were 1:2. The overall areal ratio of the S1 and S2 peaks was 50.9 at% to 49.1 at%. This result corresponds to the stoichiometric 1:1 ratio of sulfonate and thiophene sulfur atoms in the PTEBS polymer.

Both sulfur species (thiophene and sulfonate) in the PTEBS polymer chain can bind to the gold nanocrystals' surface. These additional bonds result in a shift of some spectral weight from the two S 2p peaks (S1 and S2) to lower binding energies in the range of about 161-162 eV, creating a new peak S3 of Au-bound sulfur species (Figure 3-10b-d).^{442,443} Published XPS data of various chemisorbed sulfur-containing molecules on planar Au surfaces indicated no relevant impact of the precise crystallographic structure of the Au surface on the detected binding energies.⁴⁴²⁻⁴⁴⁴ In a face-on binding configuration of PTEBS on a gold surface, both sulfur species bind to gold and contribute equally to S3 with a spectral weight fraction α (Figure 3-10b, e). This leads to an identical decrease in the original S1 and S2 intensities by α . Based on steric limitations, only one sulfur species (sulfonate or thiophene) can bind to the metal, if PTEBS adopts an edge-on binding configuration on gold surfaces. If the sulfur atom of the sulfonate group binds to gold (Figure 3-10f), only the S1 peak shifts a spectral weight fraction β to the binding peak S3 (Figure 3-10c). If the sulfur atoms of the thiophene binds to gold (Figure 3-10g), only the S2 peak shifts a weight fraction γ to the new binding peak S3 (Figure 3-10d).

The schematic binding modes depicted in Figure 3-10 represent ideal conditions in which all monomer units of the PTEBS chains bind to the gold surface in identical configurations, creating a molecular monolayer. Combinations of face-on and edge-on binding on the same gold nanorod or nanosphere would influence the contributions of the Au-unbound S1 and S2 peaks to the low-energy binding peak S3 and lead to the formation of intermediate binding states. The ratio of monomer units in different binding configuration correlates with the spectral weight fractions of the detected peaks. Face-on bound PTEBS can form π - π stacks which lead to the creation of multilayers on the gold surface (Figure 3-10e) and affect the spectral weight fractions. A uniform face-on binding of n PTEBS layers would create a spectral shift of $\alpha=1/n$.

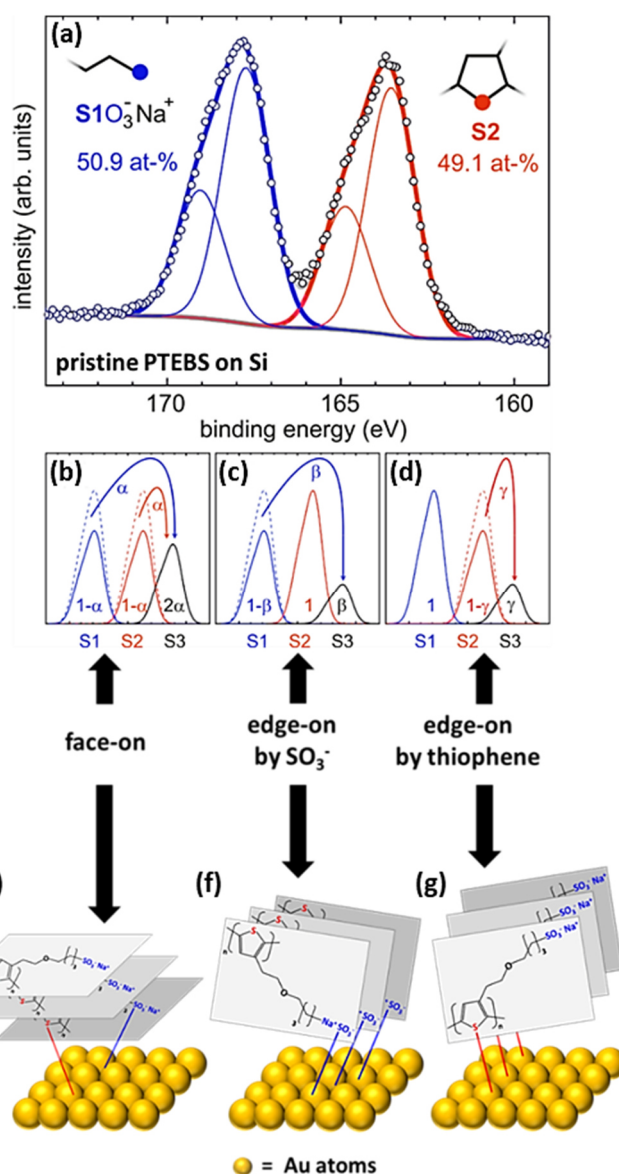


Figure 3-10:(a) X-ray Photoelectron Spectroscopy (XPS) S 2p spectrum of pure PTEBS on a silicon substrate with two S 2p doublets of the S1 sulfur in the sulfonate side chain (blue) and the S2 sulfur in the aromatic backbone (red) of the PTEBS polymer. (b) Transfer of spectral weight from S1 and S2 upon Au-S bonding for a face-on configuration with S1 and S2 contributing equally to S3. (c) Transfer of spectral weight upon Au-S bonding for an edge-on configuration with only S1 contributing to S3. (d) Transfer of spectral weight upon Au-S bonding for an edge-on configuration with only S2 contributing to S3. Illustrations of sterically possible PTEBS configurations on gold: (e) face-on binding where both sulfur species (thiophene and sulfonate groups) contribute to binding. (f) edge-on binding where only sulfur atoms of the sulfonate groups in the side chain bind to gold. (g) edge-on binding where only the sulfur atoms in the thiophenes of the polymer backbone contribute to the binding. The π - π interactions between the thiophene rings can lead to stacking of additional PTEBS layers in all three configurations. Reprinted with permission from [423].

The high-resolution S 2p spectrum of gold nanorods (AuNRs@PTEBS) in Figure 3-11 possesses an additional binding peak S3 at about 161.5 eV. Fitting the peaks using the parameters obtained for pristine PTEBS@Si (Figure 3-10a) revealed almost equal contributions of S1 and S2 (in the range of experimental error) to S3 with $\alpha(\text{S1})=0.377$ and $\alpha(\text{S2})=0.372$, respectively. This result corresponds to pure face-on binding of the PTEBS monomer units as illustrated in Figure 3-10b. The number of stacked polymer layers is given by $n=1/\alpha=2.7$.

Based on published data, the π - π stacking distance of polythiophenes is estimated to be in the range of 0.3 nm to 0.4 nm.^{247–249} Therefore, the 2-3 stacked PTEBS layers detected by XPS measurements comply with the ligand shell thickness of 0.9 nm obtained from TGA data (Table 3-2 in section 3.1.1). The monomer units in the lower first polymer layer were covalently bound to the gold surface, whereas the upper two layers were attached by π - π stacking (Figure 3-11b). The determined ligand shell thickness of AuNRs@PTEBS in this work is consistent with previously reported TEM analysis, indicating PTEBS shell thickness on gold nanorods being below 3 nm.⁶⁹

The uniform coating of PTEBS around AuNRs is supported by scanning tunneling spectroscopy (STS). Figure 3-12a depicts an STM scan of one single PTEBS coated gold nanorod. The detected length of 126.4 nm and diameter of 32.1 nm obtained by STM evaluation correspond well (in the range of experimental error) to the AuNRs dimensions determined by TEM analysis (Figure 3-2c in section 3.1.1). In Figure 3-12a, points along the long and short axes of the gold nanorod are marked where STS measurements were conducted. Representative I - V curves obtained by STS are illustrated in Figure 3-12b and d.

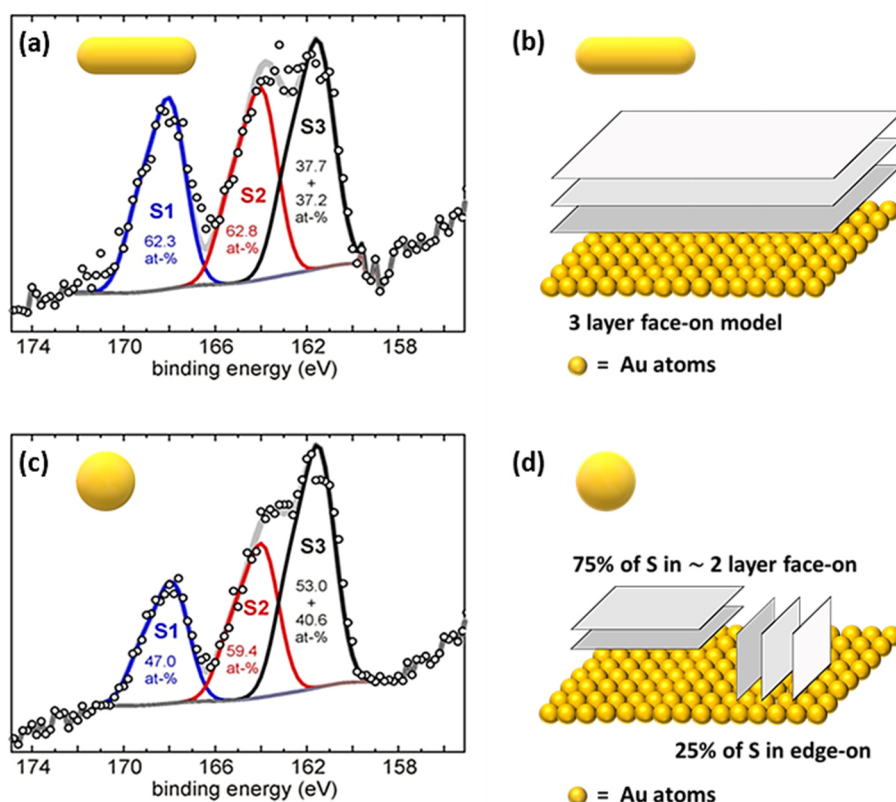


Figure 3-11: (a) High-resolution XPS S 2p spectrum of AuNRs@PTEBS. The detected peaks correspond to the sulfur species of the sulfonate group (S1, blue) and of the thiophene (S2, red). The S3 peak (black) indicates that the sulfur from both species additionally form Au-S bonds to AuNRs. (b) Fitting the peaks in the spectra (a) with the face-on binding model illustrated here, suggests approximately 3 layers of PTEBS surrounding each gold nanorod. (c) High-resolution XPS S 2p spectrum of AuNPs@PTEBS with detected peaks of sulfur in sulfonate (S1, blue), thiophene (S2, red) and sulfur from both groups that forms additional bonds to Au (S3, black). (d) Combined face-on and edge-on model on AuNPs. Approximately 75% of the PTEBS chains bind in face-on configuration with an average thickness of 2 layers, whereas the residual 25% of the PTEBS chains bind in edge-on configuration on spherical gold nanoparticles. Reprinted with permission from [423].

The I - V curves of the rod's central regions are equivalent to the I - V curves at the edges of the AuNR within the range of experimental error. These results suggest no variation in the distribution and binding configuration of PTEBS on gold nanorods, since edge-on and face-on binding of the polymer should cause differences in the local electrical properties. The resistance values were calculated using the inverse slope of the I - V curves. For AuNRs@PTEBS aligned parallel to the surface, the resistance at the rods' long axis was $R=648.0 \text{ M}\Omega$ and at the rods' short axis $R=681.3 \text{ M}\Omega$. Hence, the detected STS data

revealed uniform conductivity over all regions of one AuNR, which supports the picture of a uniform PTEBS ligand shell around the gold nanorods obtained by XPS results.

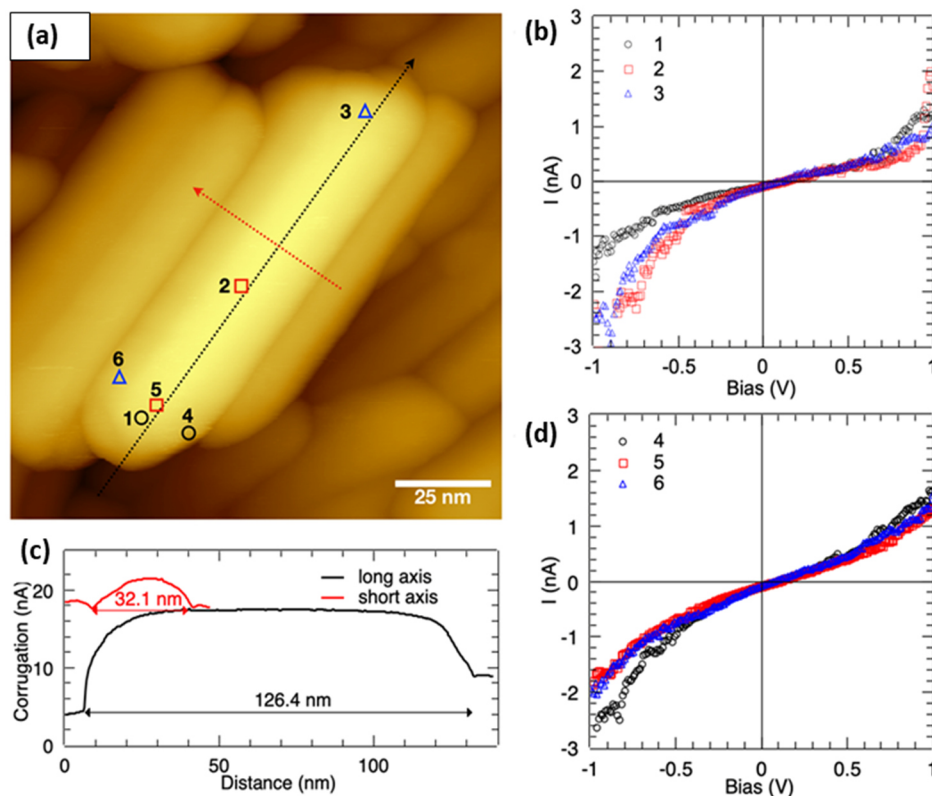


Figure 3-12: Scanning tunneling micrograph of one AuNR@PTEBS. Tunneling current 100 pA, sample bias 100 mV. (b) STS measurements along the long axis. (c) Profile of the AuNR@PTEBS along the long (black) and short (red) axis in (a). (d) STS measurements along the short axis. Reprinted with permission from [423].

The high-resolution S 2p spectrum of gold spheres (AuNPs@PTEBS) is shown in Figure 3-11c. Despite their crystallographic facets at their surfaces, both AuNRs@PTEBS and AuNPs@PTEBS possessed a binding peak S3 at about 161.5 eV in their XPS spectra. This is consistent with results for planar Au surfaces, where the exact crystallographic structure of the Au plane had no impact on the detected binding energies of chemisorbed sulfur-containing organic molecules on gold.^{442–444} The S1 and S2 peak in the spectra of spherical gold nanoparticles did not contribute equally to S3 as in spectra of gold nanorods. S1 contributed more strongly, indicating increased Au-binding of the sulfonate group, which most likely originated from a partial edge-on configuration of the PTEBS chains (Figure 3-10f). Fitting the data of AuNPs@PTEBS with the parameters obtained

for pristine PTEBS, indicated that 75% of the sulfur atoms were bound in face-on configuration with a mean thickness of about 1.85 layers. The remaining 25% of the sulfur species were bound in an edge-on configuration via sulfonate binding mode (Figure 3-11d). The packing density of edge-on bound PTEBS on gold is difficult to determine from XPS data. It is likely that π - π -stacking occurred in edge-on configuration, too.²⁴⁶

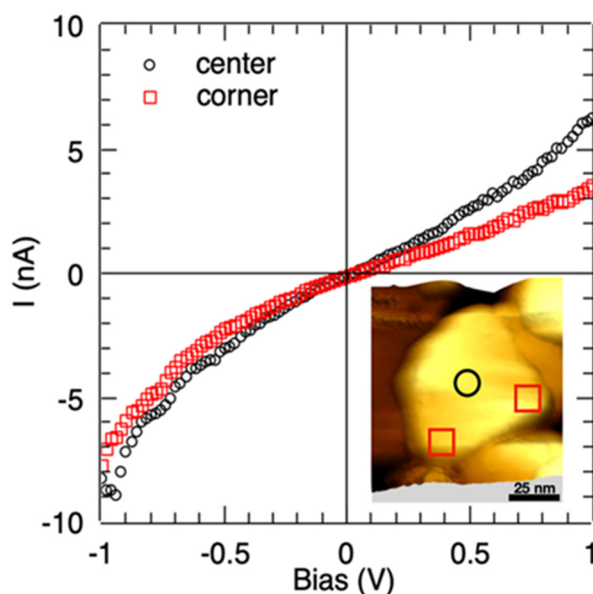


Figure 3-13: STS measurements of one AuNP@PTEBS at the center and at the corners. Inset: Scanning tunneling micrograph of the AuNP@PTEBS. Tunneling current 500 pA, sample bias 100 mV. Reprinted with permission from [423].

A mixed face-on and edge-on binding of PTEBS on gold nanospheres is supported by STS measurements. Despite AuNRs@PTEBS, the STS results of AuNPs@PTEBS strongly depended on the exact position where the STS measurements were conducted. Different I - V curves measured at various positions of one special gold nanoparticle are illustrated in Figure 3-13. The detected I - V curves in the central region of the sphere (black circle in Figure 3-13) possessed a steeper slope than the ones at the corner regions (red rectangles in Figure 3-13). This corresponds to a higher conductivity (lower resistance) in the center. The resistances calculated from the I - V curves of Figure 3-13 are $R=163.9\text{ M}\Omega$ for the central region and $R=266.3\text{ M}\Omega$ at the corners. The observed differences obtained by STS in the local conductivity at the center and edges of one gold

nanosphere indicate a non-uniform PTEBS binding configuration on AuNPs@PTEBS. This matches the mixed face-on and edge-on binding model derived from XPS analysis.

3.1.5 Origin of molecular PTEBS configurations on different gold nanocrystals

Differences in the exposed crystallographic surface facets and the overall surface curvatures of the nanocrystals affect the binding configuration of the polymer ligand. Various polyhedral, quasi-spherical geometries for CTAB-functionalized AuNPs are reported in literature,⁴⁴⁵ a common one is the cuboctahedron schematically depicted in Figure 3-14a. Other possible particle morphologies for AuNPs@CTAB are identifiable in the TEM image in Figure 3-2b presented in section 3.1.1. According to published literature, the two low-energy facets $\{111\}$ and $\{100\}$ occur frequently on polyhedral gold nanoparticles with face-centered cubic (fcc) structure as shown in Figure 3-14b.^{143,445} The tips of gold nanorods are enclosed by $\{111\}$ and $\{100\}$ facets. Their sides, that constitute 84% of their overall surface area, are terminated by higher-energy $\{110\}$ planes, as well (Figure 3-14a). These facets possess larger inter-atomic distances and weaker bonds to the surface atoms;^{142,143} they are stabilized by adsorbed CTAB molecules during synthesis.^{142,446} Experimental studies and simulations based on density functional theory (DFT) revealed a stronger absorbance and higher grafting density of CTAB molecules on $\{110\}$ compared to other facets.⁴⁴⁷ Since PTEBS can form more bonds per monomer unit when binding in face-on than edge-on configuration (Figure 3-10e-g), comparable mechanisms could stabilize the otherwise thermodynamically less favorable face-on configuration³¹³ on $\{110\}$ planes.

The average surface curvature of the crystals can influence the binding configuration and density of the attached polythiophene ligands.^{448,449} Consider the curvatures of a sphere and a regular cylinder, which approximate the shape of the AuNPs and AuNRs, respectively. Molecules can arrange on the sidewalls of a cylinder and align along its long axis without curvature. In contrast, an alignment at the cylindrical tips requires a considerable deformation of the arranged molecules. The local curvature at the cylindrical tips is greater than that of the spherical particle. Polythiophenes as PTEBS are relatively

stiff and the motion in their aromatic backbone is sterically aggravated. The persistence length l_p describes the stiffness of the polymer backbone; it is about 3 nm (5-12 monomer units) for polythiophenes.^{243–245} This is far above persistence lengths of flexible polymers e.g. polyethylene ($l_p=0.7$ nm)²⁴³ and polyisoprene ($l_p=0.43$ nm)²⁴⁵. The stiffness of polythiophenes enables dense packing of the polymer chains and enhances the electrical conductivity.⁷⁴

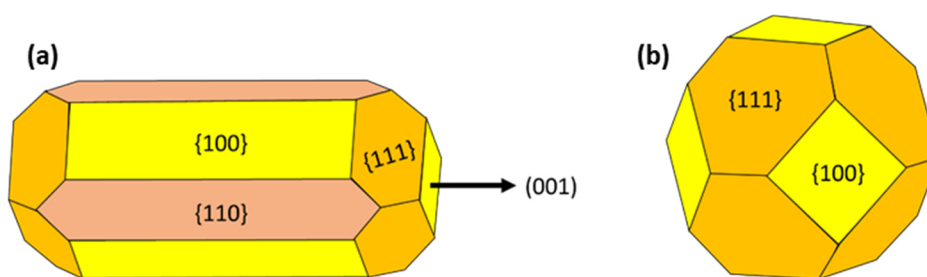


Figure 3-14: (a) Scheme of one AuNR with the main facets $\{100\}$, $\{110\}$ and $\{111\}$. The long axis of the AuNR is oriented along the (001) crystallographic direction. (b) Schematic illustration of one polyhedral AuNP with cuboctahedron shape terminated by the two main $\{110\}$ and $\{111\}$ facets. Reprinted with permission from [423].

The rigid PTEBS aligns along the long axis of the AuNRs and attaches via face-on binding to the side facets more easily than to the curved surfaces of the gold nanorod tips and gold nanospheres. This is likely the reason for the detected edge-on configuration of PTEBS on AuNPs. An edge-on configuration in AuNPs@PTEBS is favorable, since it reduces the required bending of the polymer chains upon binding to the gold nanospheres. It is likely that PTEBS adopts edge-on configuration, at least partially, on the tips of gold nanorods, too. However, since the tip regions only contribute by 16% to the complete surface of the gold nanorod, edge-on configurations could not be detected by XPS or Raman spectroscopy for AuNRs@PTEBS. The same amount of PTEBS chains attached in an edge-on configuration require more volume than face-on bound polymer chains. Since a curved surface possesses more free volume above it than a plane surface, this also facilitates edge-on binding on highly curved surfaces or facets.⁴⁵⁰ In addition, sulfonate groups in the polymer side chain have more conformational freedom than the sulfur species in the polymer backbone. This explains why edge-on binding to the gold nanocrystals preferentially occurred via the sulfonate sulfur atoms.

It is now possible to explain the effect of PTEBS at the interfaces on the electrical properties. Inter-chain and intra-chain hopping processes dominate electron transport in polythiophenes such as PTEBS.²⁴⁷ These processes are strongly influenced by the configuration of the polymer chains.²⁴⁷ Face-on binding increases out-of-plane electron transport along the π - π stack direction,^{79,325} which is perpendicular to the Au surface, while edge-on binding improves in-plane charge carrier transport.²⁶⁵ The experimental STS data of this work supports this behavior, since the detected current on the surface of AuNPs@PTEBS depended on the measurement position of the tip, indicating different configurations of PTEBS under the tip. No current variations were detected for AuNRs@PTEBS, suggesting a homogeneous PTEBS configuration along the nanorods' surface. Face-on binding of polythiophenes can enhance inter-particle charge carrier transport if π - π stacks electrically connect adjacent nanocrystals. This causes a drop in contact resistance between individual AuNRs with face-on bound PTEBS ligands and explains why polymer removal with a plasma increased the conductivity of AuNPs@PTEBS more than that of AuNRs@PTEBS. Kanehara *et al.* observed similar effects in gold particle films, where face-on attachment of phthalocyanine derivatives on gold nanoparticles led to high electrical conductivity, although these small molecules are not exactly comparable to the large polythiophene ligands used in this study.^{451–453}

3.1.6 Summary

This chapter describes how the molecular orientation of conductive polymer PTEBS sets the electrical properties of gold-polythiophene hybrid nanocrystals. The measured bulk conductivity of AuNRs@PTEBS was more than 40% greater than that of AuNPs@PTEBS. Raman spectroscopy and XPS measurements clearly identified that the sulfur atoms inside PTEBS bind to the gold surface of both nanocrystals (AuNRs and AuNPs). High resolution S 2p sulfur spectra showed that each gold nanorod was, on average, surrounded by 2-3 layers of PTEBS attached in a face-on configuration in which the sulfur species of the sulfonate groups and the thiophene backbone bind to gold. In contrast, only 75% of the PTEBS chains were in a face-on configuration for gold nanospheres and the remaining 25% arranged in an edge-on configuration with sulfonate

binding mode. This edge-on arrangement of the polymer ligand lowered the electron mobility perpendicular to the Au surface and reduces the overall conductivity. Surface curvature effects and strong interactions between the high-energy {110} facets of AuNRs and adsorbed molecules lead to preferential formation of the energetically less favorable face-on configuration on AuNRs@PTEBS.

Further studies should explore the impact of faceting and surface curvature on the molecular arrangements of polymer ligands by functionalizing nanowires, nanoplates, nanostars, nanoprisms, or nanopyramids with various conductive polymers.^{454–458} For example, nanowires could increase the number of contact points inside films, while the low surface curvature of nanoflakes could facilitate face-on binding of the polymer ligands. Both effects should influence the electrical properties of the hybrid particle films. Variations in the diameter of nanocrystals will likely also modify the surface curvature and the related binding configuration of the ligand. Hence, it would be interesting to systematically analyze the influence of the core sizes of various particle shapes on the electrical properties in upcoming studies. These investigations could create new possibilities to tailor the molecular packing and arrangement in (semi)-conductor polymer hybrids beyond process control or chemical modification, which are commonly used today to enhance electrical conductivity.

3.2 Tailored ligands for improved electrical conductivity in gold-polythiophene hybrid nanoparticles[‡]

This chapter deals with a new class of hybrid gold nanoparticles carrying π -conjugated conductive polythiophene ligands referred to as PFS-Na, which differ from commercial polythiophenes in terms of their molecular and electronic structure. PFS-Na was first synthesized by Cui and co-workers. Compared to classical polythiophenes, PFS-Na also possesses fused aromatic motifs (fluorene units) besides the thiophene units in its polymer backbone (Figure 3-15). The sulfonate groups (SO_3^-) in the side chains of PFS-Na, make the conductive polymer water-soluble.

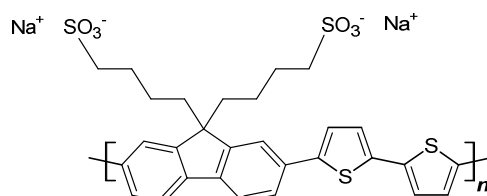


Figure 3-15: Molecular structure of the π -conjugated polymer PFS-Na.

Figure 3-16 summarizes the reported HOMO (highest occupied molecular orbital) levels of several commercially available conductive polythiophenes and PFS-Na. The HOMO of PFS-Na is located at -5.4 eV, slightly below the HOMO positions of the other commercial polythiophenes. Reported work functions Φ_m of clean gold surfaces vary between 5.1 eV and 5.47 eV.^{226–228} Assuming a work function of 5.1 eV, the Fermi level of gold is located between the HOMO and LUMO of many polythiophenes as illustrated in Figure 3-16. According to the ICT model introduced in section 2.1.4, in this energetic situation no charge carriers are transferred between the polythiophenes and gold across the interface. However, there are several reports about charge transfer between metallic nanoparticles and polythiophene ligands.^{459,460} The detected high electrical conductivity of gold-polythiophene hybrid nanocrystals introduced in this work, indicate interactions between the gold cores and the polythiophene ligands that enhance charge transport.

[‡] The synthesis and purification of the conductive and water-soluble polymer PFS-Na was conducted by collaborators from the group of Associate Prof. Dr. Bob Schroeder (University College London, UK).

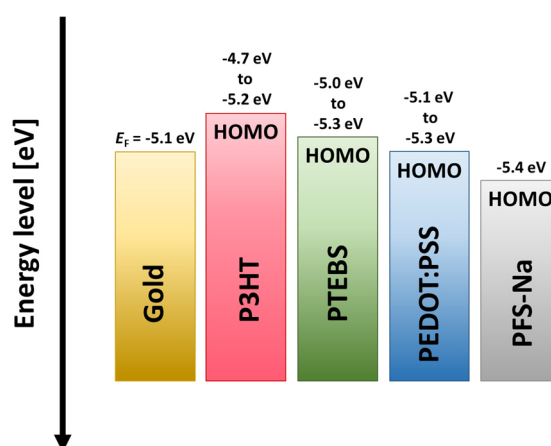


Figure 3-16: Reported HOMO levels of classical polythiophenes (P3HT,^{286–289} PTEBS²⁹⁰ and PEDOT:PSS^{291–293}) and of PFS-Na.⁴⁶¹ The Fermi level of gold is derived from reported work functions Φ_m of gold, which vary between 5.1 eV to 5.47 eV.^{226–228}

The main reason for charge carrier transfer between gold nanoparticles and polythiophenes is the existence of polaron and bipolarons in conductive polymers, which creates energetic states (E_{ICT+} and E_{ICT-}) in the HOMO-LUMO gap (section 2.2.2).⁸⁴ The state of positive integer charge-transfer E_{ICT+} lies above the HOMO of the conductive polymer and describes the energy needed to remove an electron from the polymer, resulting in a fully electronical and geometrical relaxed state (Figure 3-17).⁸⁴ The negative integer charge-transfer state E_{ICT-} defines the energy gained when an electron is added to the polymer, yielding a fully electronical and geometrical relaxed state.⁸⁴ The E_{ICT-} is located below the LUMO of the polymer (Figure 3-17). The energy difference between the HOMO/LUMO and the E_{ICT+}/E_{ICT-} can be significantly large. For example, the E_{ICT+} of the conductive polythiophene P3HT lies 0.5 eV above the HOMO level of the polymer.^{84,462} If the E_{ICT+}/E_{ICT-} positions match the metals' Fermi level E_F , charges can flow across the metal-organic surface. In this case, according to the ICT model, the electrons will flow from the polythiophene ligands to the gold nanocrystals or vice versa until the integer charge-transfer states (E_{ICT+} and E_{ICT-}) align with the Fermi level E_F of gold (Figure 3-17). Hence, the existence of E_{ICT+}/E_{ICT-} states in polythiophenes enable charge transfer between the polythiophene ligands and the gold nanoparticles, although the HOMO/LUMO levels of the polythiophenes do not match the Fermi level E_F of gold.

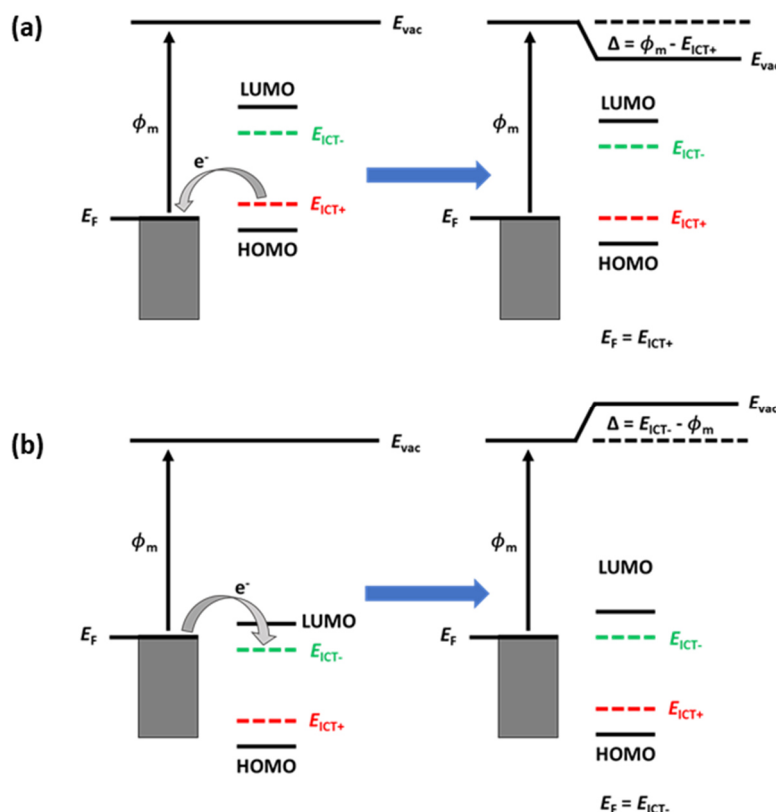


Figure 3-17: Schematic illustration of energy level alignment at the metal-organic interface when (a) $\Phi_m > E_{ICT+}$ (Fermi level pinning to positive integer charge-transfer state E_{ICT+}) and (b) $\Phi_m < E_{ICT-}$ (Fermi level pinning to negative integer charge-transfer state E_{ICT-}). Electron flow between metal and organic compound creates a dipole, which causes a shift Δ of the vacuum level E_{vac} . Figure adapted from [84,86].

PFS-Na is an interesting alternative to commercially available conductive polythiophenes that has energetically lower located HOMO (Figure 3-16) and fluorene motifs in the polymer backbone (Figure 3-15), which makes this polymer less flexible and sterically more hindered. I functionalized quasi-spherical AuNPs@CTAB by PFS-Na using a ligand exchange procedure. PFS-Na polymer was synthesized and provided by Associate Prof. Dr. Bob Schroeder and co-workers (University College London, UK). The new hybrid nanoparticles AuNPs@PFS-Na, were characterized regarding their structural and colloidal properties. While the morphology of the AuNPs was not affected by the surface functionalization, the colloidal stability of AuNPs@PFS-Na in various water-organic solvent mixtures was enhanced compared to as-synthesized AuNPs@CTAB. Raman spectroscopy showed that PFS-Na binds to gold by sulfur motifs. The binding signal in the Raman spectra of AuNPs@PFS-Na indicated strong interactions between the

thiophene rings of PFS-Na with the gold nanoparticles. They likely enabled a face-on arrangement of the thiophene units in the PFS-Na polymer backbone.

In order to analyze the impact of PFS-Na on the electrical conductivity of gold-polythiophene hybrid nanocrystals, I formulated aqueous dispersions of AuNPs@PFS-Na and deposited films on glass substrates. I compared the electrical properties of these films with the hybrids presented in chapter 3.1. Films made of AuNPs@PFS-Na were over 40% more conductive than layers consisting of AuNPs@PTEBS. The higher conductivity of AuNPs@PFS-Na is likely based on a better energy level alignment of gold's Fermi level with the HOMO of the polythiophene ligand PFS-Na (Figure 3-16). This caused smaller injection barriers for charge carriers and facilitated the electron flow from the polythiophene ligand shell to the gold nanoparticles (Figure 3-17). Thus, the polymer ligands at the gold-polythiophene interface became p-doped, improving the inter-particle charge transport.

3.2.1 Structural and UV-vis spectroscopic analysis of gold-PFS-Na hybrid nanoparticles

The as-synthesized AuNPs@CTAB were functionalized with the polythiophene PFS-Na applying a modified ligand exchange protocol established by Reiser *et al.*⁶⁹ Transmission electron micrographs (TEMs) of as-synthesized AuNPs@CTAB and AuNPs@PFS-Na after ligand exchange reaction are presented in Figure 3-18a and b. In both cases the quasi-spherical AuNPs were highly faceted and had different polyhedral shapes, which is typical for CTAB-functionalized AuNPs.⁴⁴⁵ Hence, TEM analysis revealed that the replacement of CTAB by PFS-Na via ligand exchange had no significant effect on the morphology of the gold nanoparticles. Size analysis with enclosing circles in TEMs of 274 AuNPs@CTAB and 243 AuNPs@PFS-Na provided histograms, which are depicted in Figure 3-18c and d. The as-synthesized AuNPs@CTAB had a mean diameter of $82.5 \text{ nm} \pm 18.2 \text{ nm}$ (mean \pm standard deviation), while the polythiophene-functionalized AuNPs@PFS-Na possessed a slightly smaller average diameter of $71.0 \text{ nm} \pm 16.2 \text{ nm}$ (Figure 3-18d). In order to remove excess polythiophene PFS-Na, the particle dispersions needed to be centrifugated and filtered several times, which probably caused loss of larger

gold nanoparticles (Figure 3-18d). Experimental details about the purification method are given in section 6.2.2

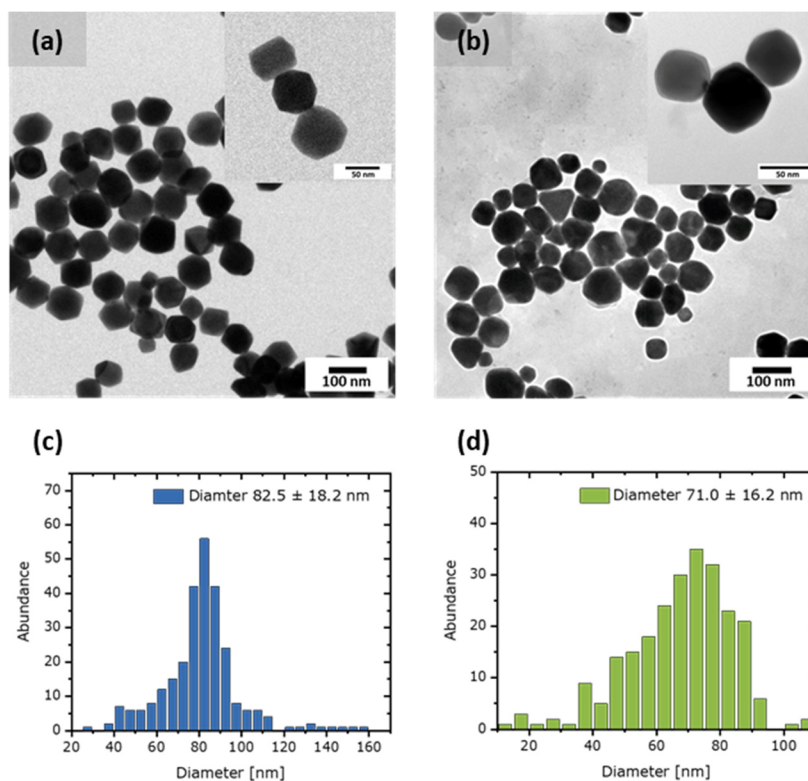


Figure 3-18: Transmission electron micrographs and particle size distribution from TEM analysis of (a, c) as-synthesized gold nanoparticles AuNPs@CTAB and (b, d) gold nanoparticles stabilized by polythiophene ligands AuNPs@PFS-Na. TEMs were taken after purification of the nanoparticle dispersions.

Figure 3-19a depicts the UV-vis absorption spectra of as-synthesized AuNPs@CTAB and of the polythiophene-stabilized AuNPs@PFS-Na after ligand exchange. The intensity and resonant wavelength of the SPR depend on electron charge density, which is affected by the type of metal, size, shape and composition of the nanocrystal and the relative permittivity of the environment close to the nanocrystal's surface.⁴⁶³ Upon absorbing of new ligands on the AuNPs surface during ligand exchange, the refractive index of the surrounding medium changes, which results in a detectable shift of the SPR band.^{464–466}

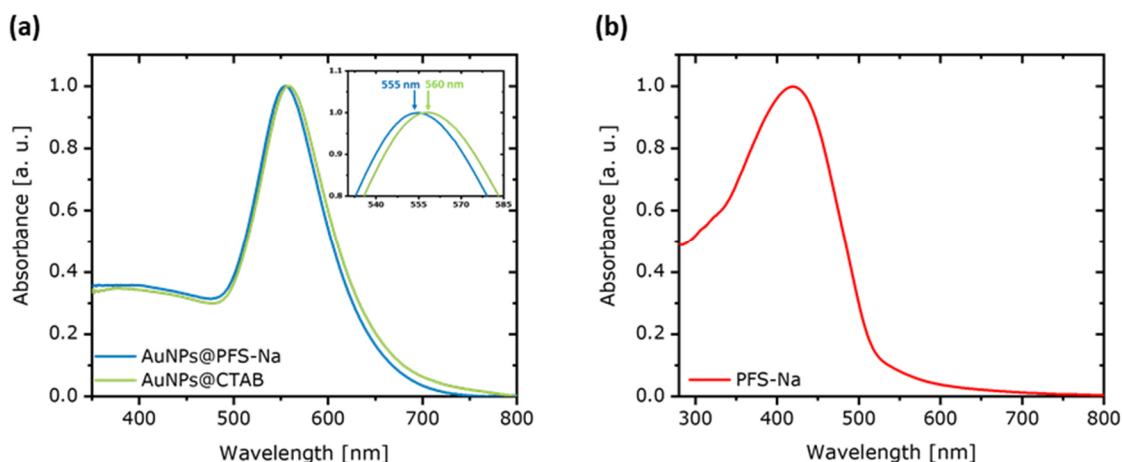


Figure 3-19: (a) UV-vis absorption spectra of as-synthesized AuNPs@CTAB and of gold nanoparticles modified by the polythiophene PFS-Na. The inset illustrates the blue-shift of the absorption maximum upon ligand exchange. (b) UV-vis absorption spectrum of an aqueous solution containing the pure polymer PFS-Na.

The absorption spectra of AuNPs@CTAB and AuNPs@PFS-Na possess similar shapes with absorption maxima of about 550-560 nm, which is characteristic for colloidal gold nanoparticles in the size range of 70 nm to 80 nm (Figure 3-19a). This size range corresponds to the dimensions of AuNPs@CTAB and AuNPs@PFS-Na determined by TEM analysis (section 3.2.1). The exact position of the absorption maximum was blue-shifted by 5 nm in the case of AuNPs@PFS-Na (inset of Figure 3-19a), indicating changes in the surrounding environment of the gold nanoparticle cores. Removal or addition of charges to a plasmonic nanoparticle alters its electron density at the surface and causes shift in the SPR band.⁴⁶⁷ Mulvaney and co-workers introduced charge to a single AuNR and observed a shift of the longitudinal surface plasmon resonance (LSPR) band to lower wavelength, since the electron density of the nanorod was increased by the external charge.⁴⁶⁸ The blue-shift of the SPR for AuNPs@PFS-Na here can be attributed to the delocalized π -electrons of the polythiophene ligand, which can interact with the AuNPs, enhancing their electron density.

Comparison of the UV-vis absorption spectra of AuNPs@CTAB, AuNPs@PFS-Na and PFS-Na (Figure 3-19a and b), reveals that the absorption behavior of the polythiophene-stabilized nanoparticles is dominated by the SPR band of the metal core, resulting in an absorption maximum at about 550-560 nm. In contrast, the UV-vis spectrum of aqueous

PFS-Na solution (Figure 3-19b) is dominated by a broad absorption peak at about 420 nm, which is characteristic for polythiophenes and originates from π - π^* intraband transitions.^{469,470} In classical thiophenes the absorption peak due to these π - π^* intraband transitions occurs at higher wavelength than in the case of PFS-Na. The shift is likely caused by the structural fluorene motifs in the backbone and sulfonate (SO_3^-) groups in the side chains of PFS-Na. This hypothesis is supported by the UV-vis absorption spectra of PFS-Na that resembles the absorption spectrum of the polythiophene PTEBS (λ_{max} 415-435 nm), which also contains sulfonate groups in the polymer side chains.^{69,290,471}

The absence of any absorption features of PFS-Na in the UV-vis spectrum of AuNPs@PFS-Na indicates that no excess polymer was present, illustrating successful purification by the developed cleaning procedure based on centrifugation and filtration.

3.2.2 Colloidal analysis of gold-PFS-Na hybrid nanoparticles

Dynamic light scattering (DLS) and zeta measurements illuminated the colloidal properties of the as-synthesized AuNPs@CTAB and the purified polythiophene-stabilized AuNPs@PFS-Na after ligand exchange (Table 3-5). AuNPs@CTAB possessed a highly positive effective surface charge (ζ potential) of +29.4 mV, consistent with published values from +25 mV to 40 mV.^{69,354,472} The positive ζ potentials of CTAB-functionalized nanocrystals results from the CTAB bilayers with charged headgroups of the outer layer aligned towards the surrounding aqueous medium.^{125,473}

After ligand exchange the ζ potential of AuNPs@PFS-Na was highly negative (-35.1 mV), indicating successful replacement of CTAB by the polythiophenes with negatively charged sulfonate (SO_3^-) groups in their side chains. Colloidal nanoparticles require zeta potentials ζ larger than -30 mV to have sufficient colloidal stability,⁴⁷⁴⁻⁴⁷⁶ suggesting stable AuNPs@PFS-Na dispersions. Ligand exchange with PFS-Na caused an increase in hydrodynamic diameters d_h as shown in Table 3-5. The as-synthesized AuNPs@CTAB had a hydrodynamic diameter d_h of 86.0 nm, which is consistent with dimensions obtained by TEM image analysis ($d_o=82.5$ nm) and a CTAB bilayer

surrounding the AuNPs of 3.2 nm to 3.9 nm.^{477–479} The increase in hydrodynamic diameter d_h further suggests a replacement of the small CTAB molecules by the larger polythiophene ligands. The slight increase in the PDI after ligand exchange of AuNPs@PFS-Na compared to as-synthesized AuNPs@CTAB likely originated from the molecular mass distribution (variation of polymer chain length) of the polythiophene.

Table 3-5: Zeta potentials ζ (mean \pm standard deviation) and hydrodynamic diameters d_h with corresponding polydispersity indexes (PDI) of as-synthesized AuNPs@CTAB and purified AuNPs@PFS-Na after ligand exchange. The hydrodynamic diameters d_h and PDI were obtained by DLS.

	d_h [nm]	PDI [%]	ζ [mV]
AuNPs@CTAB	86.0	17.5	$+29.4 \pm 1.4$
AuNPs@PFS-Na	100.8	20.8	-35.1 ± 1.3

I tested the colloidal stability of AuNPs@PFS-Na in different water-organic solvent mixtures by UV-vis spectroscopy (Figure 3-20a). Considering the different refractive indices and viscosities of the various mixtures, all spectra were dominated by SPR peaks at about 550 nm, which is characteristic for gold nanoparticles with diameters of 70 nm to 80 nm.^{463,480} Additionally, all dispersion had the characteristic red color of colloidal stable gold nanoparticles (Figure 3-20b). In contrast, UV-vis absorption spectra of AuNPs@CTAB in different water-organic solvent mixtures indicated nanoparticle agglomeration (Figure 3-20c) by red-shift of the SPR absorption peak, decrease in SPR band absorption intensity and increase of absorption signals at higher wavelengths (> 600 nm).^{369–373} The nanoparticle agglomeration of AuNPs@CTAB in different water-organic solvent mixtures also caused a characteristic color change from red to purple/blue^{481–484} as illustrated in the photographs in Figure 3-20d.

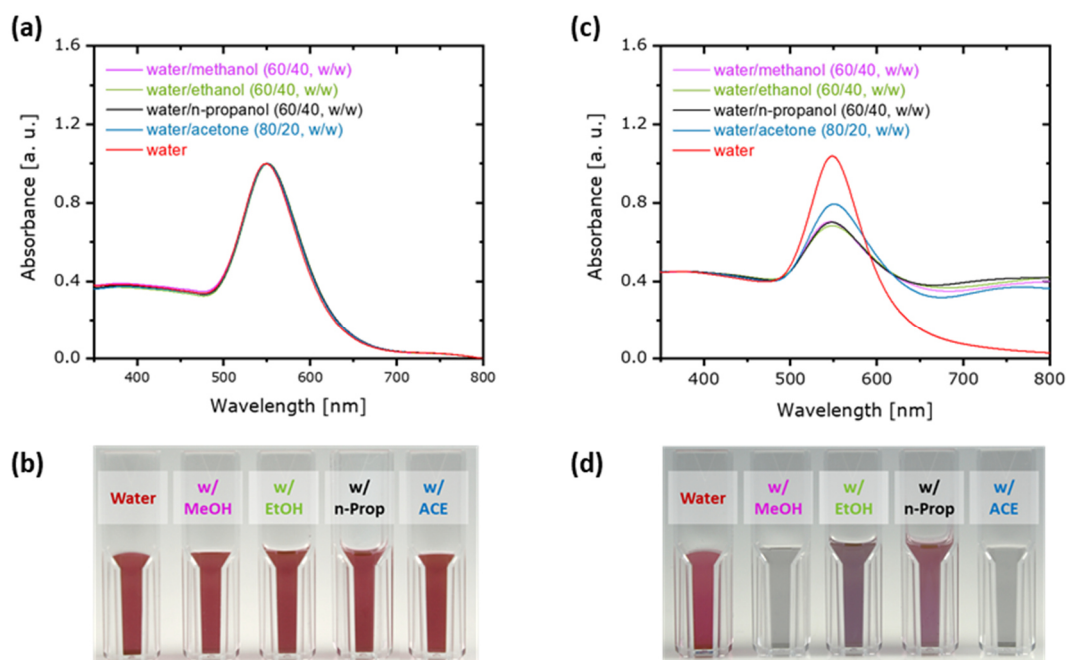


Figure 3-20: UV-vis absorption spectra of (a) AuNPs@PFS-Na and (b) AuNPs@CTAB in pure water and different water-organic solvent mixtures. Photographs of the colloidal dispersions in water and various water-organic solvent mixtures containing (c) AuNPs@PFS-Na and (d) AuNPs@CTAB.

AuNPs@PFS-Na in water and different aqueous organic solvent mixtures were further analyzed by DLS and zeta measurement (Table 3-6). AuNPs@PFS-Na possessed comparable ζ potentials of about -35 mV in water and in different water-organic solvent mixtures, indicating sufficient colloidal stability.^{474–476} AuNPs@PFS-Na had smaller hydrodynamic diameters d_h in water-organic solvent mixtures than in pure water (Table 3-6), which is likely caused by the different polarities of the used solvents (Table 3-7). PFS-Na as a polyelectrolyte undergoes a transition from an extended random coil configuration in a good solvent to a collapsed globule state with smaller dimensions in a bad solvent.^{485–487} The solvent quality for PFS-Na decreased with decreasing solvent polarity. According thereto, AuNPs@PFS-Na should have the smallest hydrodynamic diameter d_h in water-acetone mixtures. However, the higher amounts of alcohols (40 vol%) compared to acetone (20 vol%) led to smaller hydrodynamic dimensions of AuNPs@PFS-Na in water-n-propanol mixtures.

Table 3-6: Hydrodynamic diameters d_h with corresponding polydispersity indexes (PDI) obtained by DLS and zeta potentials ζ (mean \pm standard deviation) for AuNPs@PFS-Na and AuNPs@CTAB in water and various water-organic solvent mixtures. Since zeta measurements are limited to colloiddally stable nanoparticles, no zeta analysis was performed for the agglomerated AuNPs@CTAB in the different water-organic solvent mixtures.

AuNPs@PFS-Na	d_h [nm]	PDI [%]	ζ [mV]
water	100.8	20.8	-35.1 ± 1.3
water/methanol (60/40, w/w)	94.9	20.9	-36.1 ± 1.7
water/ethanol (60/40, w/w)	92.9	20.0	-36.8 ± 1.6
water/n-propanol (60/40, w/w)	91.8	17.6	-35.6 ± 1.6
water/acetone (80/20, w/w)	97.9	19.1	-34.2 ± 1.2
AuNPs@CTAB	d_h [nm]	PDI [%]	ζ [mV]
water	78.1	12.5	$+31.6 \pm 1.0$
water/methanol (60/40, w/w)	167.9	23.9	n/a
water/ethanol (60/40, w/w)	132.4	23.9	n/a
water/n-propanol (60/40, w/w)	132.6	23.5	n/a
water/acetone (80/20, w/w)	131.1	22.7	n/a

Corresponding to results obtained by UV-vis spectroscopy, DLS characterization further indicated nanoparticle agglomeration of AuNPs@CTAB in water-organic solvent mixtures (Table 3-6). The replacement of CTAB by the polythiophene PFS-Na enhanced the colloidal stability of AuNPs due to electro-steric stabilization caused by long and negatively charged polythiophene chains.

Table 3-7: Empirical parameters of solvent polarity taken from [488].

	$E_T(30)$ [kJ·mol ⁻¹]
water	63.1
methanol	55.4
ethanol	51.9
n-propanol	50.7
acetone	42.2

3.2.3 Characterization of ligand binding in gold-PFS-Na hybrids by Raman spectroscopy

Features in the Raman spectrum of pure PFS-Na (Figure 3-21d) can be clearly attributed to the polythiophene units or to the aromatic motifs (fluorene units) of the polymer backbone. Similar to the Raman spectra of other polythiophenes (PTEBS, P3KBT, P3KPT, P3KHT and P3KHepT), the spectrum of PFS-Na possessed peaks in the region between 1300 cm^{-1} and 1550 cm^{-1} , which refer to the characteristic thiophene ring vibrations (intra C-C and symmetric and asymmetric C=C stretch modes). Normally, these ring vibrations result in a specific triplet peak motif in Raman spectra as shown by way of example in the Raman spectra of PTEBS (Figure 3-21d). In the case of PFS-Na, the Raman spectrum exhibited only a doublet motif in the range between 1300 cm^{-1} and 1550 cm^{-1} (red area in Figure 3-21d).

The lower triplet peak, belonging to the intra-ring $\nu(\text{C}-\text{C})$ stretching modes, was not pronounced in the Raman spectra of PFS-Na. In contrast to classical polythiophenes such as PTEBS, the thiophene backbone of PFS-Na is interrupted by aromatic motifs (fluorene units). Only two thiophene units are adjacent to each other in the case of PFS-Na (Figure 3-15). It is likely that this molecular differences in the structure of PFS-Na affect the intra-ring $\nu(\text{C}-\text{C})$ stretching modes, which makes them not visible in the Raman spectrum of PFS-Na.

Pronounced peaks in the PFS-Na Raman spectrum at higher wavenumbers ($> 1600\text{ cm}^{-1}$) can be attributed to the fluorene units of PFS-Na, which match reported Raman data of pure fluorene. Additional peaks in the range of 1000 cm^{-1} to 1300 cm^{-1} likely arose from both thiophene and fluorene motifs. A detailed peak assignment of the vibrational peaks for pure PFS-Na is given in Table 3-8. Since no literature data is available for PFS-Na, I used published Raman data of equivalent polythiophenes (e.g. P3HT)^{430,431} and of pure fluorene⁴⁸⁹⁻⁴⁹² to assign the most prominent peaks in the Raman spectrum of PFS-Na.

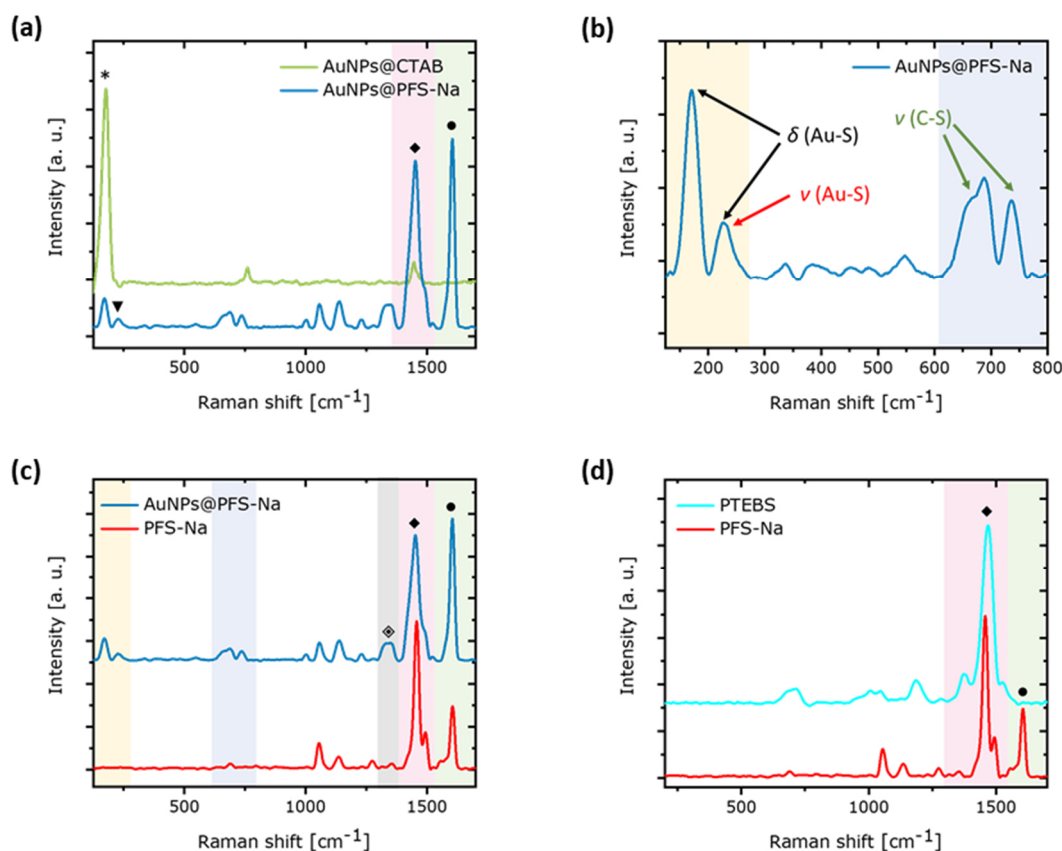


Figure 3-21: (a) Raman spectra of the as-synthesized AuNPs@CTAB and AuNPs@PFS-Na after ligand exchange. (b) Fingerprint region of the Raman spectrum of AuNPs@PFS-Na. (c) Raman spectra of PFS-Na-stabilized nanoparticles and of pure PFS-Na. (d) Raman spectra of bulk polymer films of PFS-Na and PTEBS. Important areas of the Raman spectra are highlighted with different colors: (red) thiophene ring vibrations based intra-ring $\nu(\text{C}-\text{C})$ and $\nu_{\text{s}}(\text{C}=\text{C})/\nu_{\text{as}}(\text{C}=\text{C})$, (green) vibrations of the fluorene rings, (yellow) stretching and bending modes of Au-S bonds, (blue) C-S stretching modes and (grey) intra-ring $\nu(\text{C}-\text{C})$ stretching modes. Important vibrations modes are additionally marked in the spectra: $\nu(\text{Au}-\text{Br})=*$, $\delta(\text{Au}-\text{S})$, $\nu(\text{Au}-\text{S})$, $\nu/\delta(\text{fluorene})=\bullet$, thiophene $\nu(\text{C}=\text{C})=\blacklozenge$, thiophene $\nu(\text{C}-\text{C}, \text{intra})=\blacklozenge$.

Raman spectroscopy can reveal bonds between the metallic nanoparticles and the polymer ligands. The Raman spectra of as-synthesized AuNPs@CTAB exhibited a peak at about 177 cm^{-1} (Figure 3-21a), which can be attributed to Au-Br vibrations.⁴²⁷ These Raman signals are typical for CTAB-stabilized nanocrystals. After ligand exchange the Au-Br peak vanished in the Raman spectrum of AuNPs@PFS-Na (Figure 3-21a), suggesting near-complete replacement of the initial ligand CTAB by the polymer PFS-Na. A new peak evolved in the region of 200 cm^{-1} and 300 cm^{-1} (Figure 3-21b), which can be assigned to Au-S stretching modes.⁴²⁸ Similar Au-S peaks were also present

in the Raman spectra of other gold-polythiophene hybrid nanoparticles (e.g. AuNPs@PTEBS and AuNRs@PTEBS). The Au-S stretching peak of AuNPs@PFS-Na was located at lower (227 cm^{-1}) wavenumbers in the Raman spectrum compared to the peak position of the other gold-polythiophene hybrid nanocrystals studied here. However, the Au-S peak position of AuNPs@PFS-Na is still consistent with literature, since simulations yielded Au-S stretching modes in the range of 220 cm^{-1} to 280 cm^{-1} .⁴⁹³

Table 3-8: Characteristic vibrational peaks detected in the Raman spectra of pure PFS-Na. The band assignment is based on literature values of equivalent polythiophenes (e.g. P3HT)^{430,431} and of pure fluorene.^{489–492}

Raman shift [cm^{-1}]	Band assignment
690	Thiophene $\delta(\text{C-S-C})$ ring deformation mode
1000-1070	Thiophene $\delta(\text{CH}_2)$ bending mode
1020-1050	Fluorene $\delta(\text{C-C-C})$ and $\delta(\text{C-H})$ in-plane bending modes
1130	Thiophene $\delta(\text{C-H})$ bending mode
1230-1275	Fluorene $\delta(\text{C-C-C})$ and $\delta(\text{C-H})$ in-plane bending modes
	Fluorene scissoring (CH_2)
1374	Thiophene intra-ring $\nu(\text{C-C})$ stretching mode
1450	Thiophene symmetric $\nu_s(\text{C=C})$ ring stretching mode
14980-1490	Thiophene asymmetric $\nu_{as}(\text{C=C})$ ring stretching mode
	Fluorene $\delta(\text{C-C-C})$ and $\delta(\text{C-H})$ in-plane bending modes
	Fluorene scissoring (CH_2)

An additional peak in the low wavenumber region (yellow area in Figure 3-21b) cannot be assigned to Au-Br vibration due to remaining CTAB molecules, since the exact peak (170 cm^{-1}) position and peak intensity (Au-Br vibrations yield strong Raman signals) do not match reported literature data.⁴²⁷ Simulations predicted Au-S bending modes in Raman spectra being in the range of 150 cm^{-1} to 215 cm^{-1} ,^{493–495} I attributed the detected peak at 170 cm^{-1} to Au-S bending. Peaks in the region of 600 cm^{-1} to 760 cm^{-1} (blue area in Figure 3-21b) can be attributed to C-S stretching vibrations.^{496–499} The broad peak in the range between 1280 cm^{-1} and 1380 cm^{-1} (grey area in Figure 3-21c), belongs to intra-ring C-C stretching vibrations of the thiophene units in the backbone of PFS-Na.^{430,431} Both, C-S stretching and intra-ring C-C stretching modes, were not present in the Raman spectrum of pure PFS-Na (Figure 3-21c), indicating interactions of the thiophene rings with the gold surface, which enhanced the appropriate Raman signals. These observations

correspond to interactions of aromatic thiols with gold and silver nanoparticles, where the C-S stretching modes were enhanced due to the SERS (surface-enhanced Raman scattering) of the metallic nanoparticles.^{500,501}

Although PTEBS possesses similar sulfonate-containing side chains as PFS-Na (Figure 3-1 and Figure 3-15), I did not observe Au-S bending and C-S stretching vibrations in the Raman spectrum of AuNPs@PTEBS (section 3.1.3). I concluded that Au-S bending signals originated from the interactions between the thiophene units in the PFS-Na backbone with AuNPs. The appearance of intra-ring C-C and C-S stretching in the Raman spectrum of AuNPs@PFS-Na further supported these interactions between the thiophene rings of PFS-Na with AuNPs and suggested a different configuration of the PFS-Na polymers in AuNPs@PFS-Na than in bulk polymer film. The gold-thiophene-ring interactions were likely caused by the conjugated π -electrons of PFS-Na and probably required a face-on binding configuration of the thiophene units in the PFS-backbone. I did not observe similar interactions between the AuNPs and the π -system of PTEBS, although I revealed that the sulfur atoms of the thiophene unit in the PTEBS backbone can interact with gold nanocrystals. Hence, it is likely that the unique structure of PFS-Na, which differs from classical polythiophenes, facilitates the interactions between the thiophene π -electrons and the AuNPs. The fluorene units in the PFS-Na backbone reduce the flexibility of the polymer chains and may also influence the arrangement of PFS-Na ligands on spherical AuNPs. In sections 3.1.3 and 3.1.4, I showed that face-on binding of PTEBS on gold nanorods was realized by Au-S bonds of both sulfur motifs, the sulfur species in the sulfonate (SO_3^-) groups of the polymer side chains and the sulfur species of the thiophene in the polymer backbone. In the case of PFS-Na, the sulfonate-containing side chains are not directly attached to the thiophene units of the polymer backbone (Figure 3-15). Hence, a face-on arrangement of the thiophene units in PFS-Na does not necessarily imply a face-on (flat-lying) arrangement of the polymer side chains. It is possible that thiophene units bind in a face-on configuration to the AuNPs, while the polymer side chains adapt a different orientation, e.g. perpendicular (edge-on configuration) to the gold surface. Raman data cannot fully reveal the arrangement of the fluorene units in the PFS-Na backbones attached to AuNPs. Detailed analysis of the exact binding configuration (arrangement of polymer side chains, thiophene and fluorene units

in the polymer backbone) will require further characterization of AuNPs@PFS-Na by X-ray photoelectron spectroscopy (XPS).

The symmetric and asymmetric C=C stretching modes of the thiophene rings were slightly blue-shifted and broadened in the case of AuNPs@PFS-Na. Similar effects were also observed in the Raman spectra of doped polythiophenes due to the formation of polarons and bipolarons.^{433,434} These quasi-particles are the main charge carrier species in conductive π -conjugated polymers, enhancing the overall electrical conductivity of those polymers (section 2.2.2). The measured Raman signals of AuNPs@PFS-Na indicated polaron and bipolaron formation in the PFS-Na ligand shell, which further supported the presence of interactions between the gold nanoparticles and the PFS-Na polymer chains.

In summary, Raman spectroscopy revealed that ligand exchange was successful and the initial ligand CTAB was replaced by the PFS-Na polymer, consistent with zeta and DLS characterization (section 3.2.2). Raman data also indicated that the PFS-Na polymer bind to AuNPs by sulfur species. Pronounced Au-S bending modes in the spectra of AuNPs@PFS-Na suggested specific interactions between PFS-Na and AuNPs that distinctly differ from interactions between AuNPs and classical polythiophenes such as PTEBS or P3KHT. These correlations may be caused by the more planar structure of PFS-Na due to its fluorene motifs, which enable interactions with both sulfur species (sulfonate groups and thiophenes) and the π -electrons of the thiophene rings.

3.2.4 Electrical conductivity of gold-PFS-Na hybrid nanoparticle films

The electronic structure of PFS-Na differs from classical polythiophene ligands, which should influence the energy level alignment at the gold-polythiophene interfaces and alter the electronic properties of the gold-polythiophene hybrid nanoparticles. To verify this hypothesis, I fabricated line patterns on glass substrates by drop-casting of dispersions containing AuNPs@PFS-Na and electrically characterized them. The hybrid gold films were conductive after complete drying. I determined the precise length and width of each

line pattern by optical transmission microscopy. Topography histograms obtained by confocal microscopy were fitted by Gaussian functions to determine the average film thickness with the corresponding standard deviations. Thicknesses of the layers ranged between 0.9 μm to 3.9 μm . The thickness variation within one layer was below 30%.

The produced line patterns were contacted with silver paste and were electrically characterized to provide current-voltage (I - V) curves of six individual samples made of AuNPs@PFS-Na. I calculated the mean I - V curve, which is shown in Figure 3-22a. For comparison, the mean I - V curve obtained for films made of AuNPs@PTEBS (section 3.1.2) is also shown in Figure 3-22a. All hybrid films had metal-like linear ohmic behavior. I used the determined geometrical dimensions (width, length and thickness) to calculate the material resistivity ρ according to equation 3-1 introduced in section 3.1.2. The detected current was normalized to the thickness of each gold-polythiophene hybrid nanoparticle film as depicted in Figure 3-22a. The resistivity ρ for AuNPs@PFS-Na was $3.97 \cdot 10^{-6} \Omega\text{m} \pm 0.37 \cdot 10^{-6} \Omega\text{m}$ (mean value \pm one standard deviation), two orders of magnitude above the resistivity of bulk gold ($2.35 \cdot 10^{-8} \Omega\text{m}$).¹⁶⁰

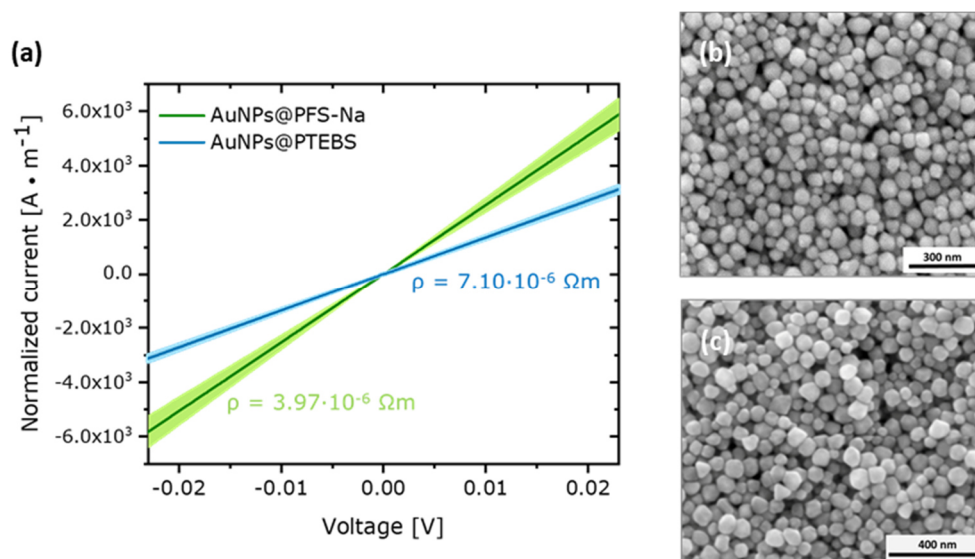


Figure 3-22: (a) Average I - V curves with normalized currents to film thicknesses of AuNPs@PTEBS (blue) and AuNPs@PFS-Na (green) with the corresponding error ranges (light blue and light green areas). Scanning electron micrographs of deposited films on glass substrates consisting of (b) AuNPs@PFS-Na and (c) AuNPs@PTEBS.

Compared to layers composed of AuNPs@PTEBS ($\rho=7.10\cdot10^{-6} \text{ } \Omega\text{m} \pm 0.15\cdot10^{-6} \text{ } \Omega\text{m}$, section 3.1.2), AuNPs@PFS-Na films possessed an over 44% lower material resistivity (Figure 3-22a.) Scanning electron micrographs (SEMs) illustrated in Figure 3-22b and c, show gold nanoparticles without sintering inside the hybrid nanoparticle layers. The reduced resistivity ρ of AuNPs@PFS-Na likely did not originate from shorter inter-particle distances due to thinner ligand shells. Thermogravimetric analysis determined an organic weight fraction of 1.6 wt% for AuNPs@PFS-Na (Appendix A, Figure A-1a), which was above that of AuNPs@PTEBS (0.7 wt%). Assuming similar densities of PFS-Na and PTEBS, TGA implied shorter inter-particle distances in films made of AuNPs@PTEBS, since the dimensions of the gold cores were similar for both types of gold-polythiophene nanocrystals (sections 3.1.1 and 3.2.1).

The improved electrical properties of AuNPs@PFS-Na must arise from the unique molecular and electronic structure of the PFS-Na polymer. Raman spectroscopy revealed that the PFS-Na polymer binds to gold nanoparticles via sulfur species and indicated a strong interaction of the thiophene rings in the polymer backbone of PFS-Na with the gold nanoparticles, which were not observed for the other gold-polythiophene hybrid nanocrystals introduced in this work. These interactions suggested a face-on arrangement of the thiophene units in the PFS-Na backbones. Face-on binding of PTEBES on AuNRs also increased the electrical conductivity (sections 3.1.2 and 3.1.4), since face-on binding enhances the out-of-plane electron transport along the π - π stack direction^{325,79} perpendicular to the Au surface. Thus, the probable face-on arrangement of PFS-Na chains on AuNPs raised the overall electrical conductivity of AuNPs@PFS-Na.

Further XPS studies are needed to support this hypothesis and identify the exact binding configuration of PFS-Na polymer chains on spherical AuNPs. Raman data of AuNPs@PTEBS (section 3.1.3) and AuNPs@PFS-Na (section 3.2.3) indicated the formation of polarons and bipolarons in the polymer ligands, which resulted in the superior electrical conductivity of the gold-polythiophene hybrid nanocrystals. This formation of polarons/bipolarons requires electron transfer between the gold nanoparticles and the surrounding ligand. The injection barriers for electrons Φ_B^e and holes Φ_B^h at the gold-polythiophene interfaces are determined by the match between the HOMO or LUMO of the polythiophene and the Fermi level E_F of gold (section 2.1.4).

Since the HOMO of PFS-Na (-5.4 eV)⁴⁶¹ lies slightly lower than the HOMO of PTEBS (-5.0 eV to -5.3 eV),⁴⁶¹ the injection barriers for charge carriers are different for AuNPs@PFS-Na and AuNPs@PTEBS according to equations 2-8 and 2-9 (section 2.1.4).

Polarons and bipolarons form new electronic states in the HOMO-LUMO bandgap.^{84,502} These states refer to positive integer charge-transfer state E_{ICT+} and negative integer charge-transfer state E_{ICT-} (section 2.1.4).⁸⁴ The EA of π -conjugated polymers is determined by the energy difference between the E_{ICT-} and the vacuum level E_{vac} . The IE of π -conjugated polymers is calculated as the energy difference of E_{ICT+} and the vacuum level E_{vac} .⁸⁴ Figure 3-23 illustrates the pronounced electronic situation at the gold-PFS-Na and gold-PTEBS interfaces in gold-polythiophene hybrid nanoparticles presuming a gold work function of 5.1 eV (reported values range from 5.1 eV to 5.47 eV).^{226–228} The reported HOMO level of PFS-Na is located at -5.4 eV⁵⁰² and the HOMO of PTEBS lies between -5.0 eV to -5.3 eV.²⁹⁰ A HOMO level of -5.2 eV for PTEBS was assumed for calculating the hole injection barriers using equations 2-8 and 2-9 (section 2.1.4). The E_{ICT+} lies above the actual HOMO of the polythiophenes. For P3HT, a comparable polythiophene, an E_{ICT+} level was reported 0.5 eV above the HOMO level.^{84,462} Assuming the same situation for PFS-Na and PTEBS, lead to E_{ICT+} positions of -4.9 eV and -4.7 eV, respectively.

The calculated hole injection barriers Φ_B^h at the gold-PFS-Na interface are 0.2 eV and 0.4 eV at the gold-PTEBS interface (Figure 3-23). For both systems, AuNPs@PFS-Na and AuNPs@PTEBS, electrons will flow from the polythiophene shell to the gold cores until the metal's Fermi level aligns with the E_{ICT+} of the polymer ligands. The lower injection barrier of AuNPs@PFS-Na likely facilitates the electron flow from the surrounding polythiophene ligand to the gold nanoparticle. This may explain the higher electrical conductivity of AuNPs@PFS-Na compared to AuNPs@PTEBS. It is likely that more electrons were transferred to the gold nanoparticles in the case of AuNPs@PFS-Na due to the smaller injection barrier Φ_B^h . If more electrons flow to the metallic core, more holes are created inside the polythiophene shell, resulting in enhanced p-doping of the polythiophene ligands. It is likely that the PFS-Na ligand shell was more doped due to the gold-ligand charge carrier transfer than the PTEBS ligand shell. The higher doping

probably increased the intrinsic conductivity of the polythiophene ligand, yielding to enhanced inter-particle charge carrier transport, explaining the higher overall electrical conductivity of AuNPs@PFS-Na.

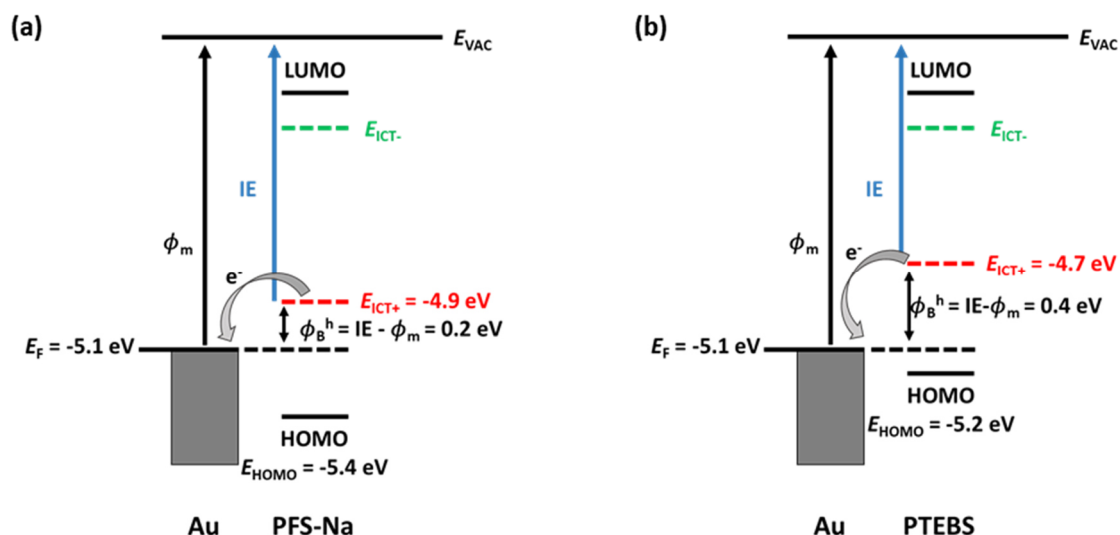


Figure 3-23: Schematic energy level alignment at the (a) gold-PFS-Na and (b) gold-PTEBS interface. Work function of gold was assumed to be 5.1 eV. Reported values of gold work function vary between 5.1 eV and 5.47 eV.^{226–228} HOMO level of PFS-Na was assumed at -5.4 eV based on literature.⁴⁶¹ HOMO of PTEBS was assumed to be -5.2 eV. Reported HOMO position of PTEBS lies between -5.0 eV to -5.3 eV.²⁹⁰ Positive E_{ICT+} and negative E_{ICT-} integer charge-transfer states are formed in the HOMO-LUMO gap due to polaronic and bipolaronic states. The position of E_{ICT+} was assumed to be 0.5 eV above the HOMO levels of PFS-Na and PTEBS. Literature reports that E_{ICT+} of π -conjugated polymers is located 0.4 eV to 0.7 eV above the HOMO of the corresponding polymers.⁴⁶² IE defines the ionization energy of PFS-Na and PTEBS, respectively.

This reasoning assumes identical energy differences of 0.5 eV between the HOMO level and the E_{ICT+} for PFS-Na and PTEBS. Since the reported energy difference between HOMO and E_{ICT+} for π -conjugated polymers varies from 0.4 eV to 0.7 eV,⁴⁶² it is possible that the E_{ICT+} of PFS-Na lies even lower and the one of PTEBS even higher. This would cause an even larger difference in the injection barrier Φ_B^h , contributing to the electrical conductivity of AuNPs@PFS-Na. Hence, future studies should include ultraviolet photoelectron spectroscopy (UPS), that can identify the precise HOMO levels and polaronic energies (positions of E_{ICT+}) of polythiophenes, providing detailed information about the electronic structure of gold-polythiophene hybrid nanocrystals. In addition,

UPS could reveal how the work function of the gold nanoparticles is affected by the different polythiophene ligands, providing information about injection barriers and gold-ligand charge carrier transfer. To gain a complete picture of the electronic structure in gold-polythiophene hybrid nanocrystals, future experiments should also include inverse photoemission spectroscopy (IPES), which provides additional information about the LUMO and E_{ICT} of the polythiophenes. UPS and IPES are adequate methods to experimentally support the theoretical hypothesis of different charge carrier injections barriers in AuNPs@PFS-Na and AuNPs@PTEBS.

3.2.5 Summary

In contrast to classical polythiophenes, PFS-Na possesses thiophene and fluorene units in the polymer backbone, which makes the polymer sterically more hindered and less flexible. Gold-polythiophene hybrid nanoparticles AuNPs@PFS-Na were colloidally stable in aqueous solution and different water-alcohol mixtures. Raman spectroscopy revealed that PFS-Na binds to gold nanoparticles by Au-S bonds. Au-S bending, which did not occur in the Raman spectra of other gold-polythiophene hybrid nanoparticles (e.g. AuNPs@PTEBS, AuNPs@P3KHT), suggested different binding of PFS-Na to AuNPs than classical polythiophene ligands. Strong C-S stretching and intra-ring C-C stretching in the Raman spectra of AuNPs@PFS-Na indicated strong interaction between the gold nanoparticle cores and the π -electrons of the thiophene rings. The interactions between AuNPs and PFS-Na are not only limited to Au-S bonds as in the case of gold-PTEBS hybrid nanoparticles. The thiophene ring system of the PFS-Na ligands also contributes to the ligand-nanoparticle interactions, suggesting a face-on attachment of the thiophene units in PFS-Na. It is likely that the binding configuration of PFS-Na and the unique ligand-gold interactions are driven by the limited flexibility of PFS-Na polymer chains due to fluorene units (fused aromatic rings) in the polymer backbone.

Dried films made of AuNPs@PFS-Na were immediately conductive and had conductivities 40% above that of layers composed of AuNPs@PTEBS. Better energy level alignment between the molecular orbitals of PFS-Na to the Fermi level of the gold

nanoparticles probably reduced charge carrier injection barriers between the nanoparticles and the surrounding ligands. The PFS-Na ligands were p-doped by electron transfer from the gold cores, which likely caused an increase in the overall electrical conductivity of AuNPs@PFS-Na. Further understanding about the energy level alignment at the gold-ligand interface in gold-polythiophene hybrid nanoparticles is essential to understand why AuNPs@PFS-Na were more conductive than other gold-polythiophene hybrid nanoparticles in this work. In order to obtain comprehensive knowledge about the electronic structure of conductive polythiophene ligands, further studies should also include ultraviolet photoelectron spectroscopy and photoemission spectroscopy. These techniques will deliver information about the molecular orbitals and polaronic energies ($E_{\text{ICT-}}$ and $E_{\text{ICT+}}$) of the different polythiophenes.

Since PFS-Na is less flexible and more sterically hindered than classical polythiophenes due to the fluorene units in the polymer backbone, further studies should examine if the molecular orientation of PFS-Na is also affected by faceting and surface curvature of nanocrystals. PFS-Na could be used to modify nanocrystals with different shapes including nanowires, nanoplates, nanostars, nanoprisms, or nanopyramids.^{454–458} Nanocrystals with low surface curvature require less deformation of the polymer ligands upon binding, which could facilitate the binding of the stiff PFS-Na. Additionally, further studies could focus on functionalizing gold nanocrystals with various polymers ligands with different electronic structures to gain detailed information about the energy level alignment at the gold-polymer interfaces. Not only polythiophenes but also other conductive polymers, such as polyaniline or polypyrrole, could be used as conductive ligands.^{503–506} Detailed knowledge about the correlation of energy level alignment and electrical conductivity of hybrid nanoparticles would introduce new possibilities in the design of modern (opto)electronics with improved performance.

3.3 Analysis of biofunctionalizable gold-polythiophene hybrid nanoparticles

A considerable advantage of gold-polythiophene hybrid nanoparticles compared to classical conductive nanoparticles is the ability to introduce additional functionality beyond electrical conductivity. This chapter discusses the addition of bio-functionality. Biofunctionalizable gold-polythiophene hybrid nanoparticles were obtained with polythiophene ligands carrying carboxyl/carboxylate groups that can react with primary amines of biological substances such as enzymes, proteins, antibodies or DNA (Figure 3-24). Bioconjugation using EDC/NHS coupling chemistry yields covalent amide bonds between carboxylated polythiophene ligands and biological species containing primary amines (section 2.3.3). Since biofunctionalizable gold-polythiophene hybrid nanoparticles combine high electrical conductivity with bio-functionality, they are interesting materials for the production of biomedical electronics.

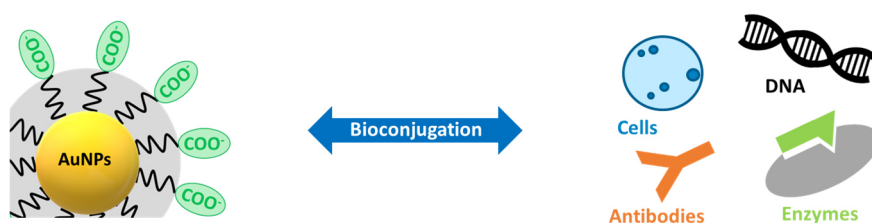


Figure 3-24: Schematic illustration of interactions between the biofunctionalizable gold-polythiophene hybrid nanoparticles and various biological species. The carboxylate groups (COO^-) in the polymer ligand shell of the hybrid particles enable EDC/NHS bioconjugation.

I tested four different commercially available carboxylated polythiophenes for the production of colloidally stable, electrically conductive and biofunctionalizable gold-polythiophene hybrid nanocrystals (Figure 3-25). Biofunctionalizable hybrid nanoparticles were obtained by modification of quasi-spherical AuNPs using ligand exchange reactions according to an established protocol.⁶⁹ Depending on the used polymer, these newly formed hybrid materials are further denoted as AuNPs@P3KBT, AuNPs@P3KPT, AuNPs@P3KHT or AuNPs@P3KHpT, respectively. Functionalization of the quasi-spherical AuNPs with the different polymers had no impact

on their morphology (section 3.3.1). After ligand exchange, a purification process based on centrifugation and filtration was needed to remove excess polythiophenes. Monitoring this purification process by UV-vis spectroscopy, DLS and zeta potential measurements revealed that AuNPs stabilized by the polythiophene P3KHT yielded the most colloiddally stable biofunctionalizable hybrid nanoparticles (section 3.3.2)

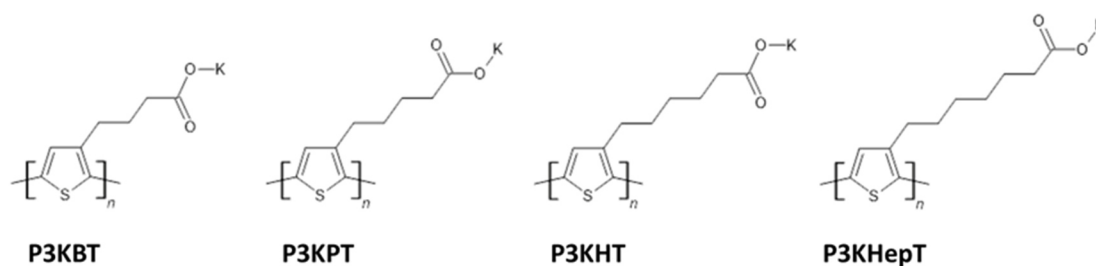


Figure 3-25: Chemical structures of the repeating unit of poly[3-(potassium-4-butanoate)thiophene-2,5-diyl] (P3KBT), poly[3-(potassium-5-pentanoate)thiophene-2,5-diyl] (P3KPT), poly[3-(potassium-6-hexanoate)thiophene-2,5-diyl] (P3KHT) and poly[3-(potassium-7-heptanoate)thiophene-2,5-diyl] (P3KHepT).

Raman data presented in section 3.3.3 demonstrated that all of the tested carboxylated polythiophenes bound by sulfur-species to the AuNPs. Electrical characterization of hybrid films made of AuNPs@P3KHT (section 3.3.4) showed that biofunctionalizable gold-polythiophene hybrid nanoparticles films had a resistivity ρ of $8.67 \cdot 10^6 \Omega\text{m} \pm 0.51 \cdot 10^6 \Omega\text{m}$, which is comparable to non-biofunctionalizable gold-polythiophene hybrids in this work. These results clearly show that electrical conductivity and biofunctionality of hybrid materials are not mutually exclusive. Hybrid films containing AuNPs@P3KHT maintained their electrical properties under wet conditions, revealing their suitability for biological or biomedical applications in liquid media. The results of this chapter illustrate the potential of biofunctionalizable gold-polythiophene hybrids that enable the efficient combination of conductive inorganic matter with biological species.

Parts of the presented results in chapter 3.3 led to the patent application *Conductive functionalizable nanocomposites* (DE102019135645A1).

3.3.1 Structural analysis of biofunctionalizable gold-polythiophene hybrid nanoparticles

AuNPs@CTAB were obtained by a modified procedure established by Ye *et al.*¹⁵⁰ and functionalized with the four different carboxylated polythiophenes according to an existing ligand exchange protocol⁶⁹ (sections 6.2.1 and 6.2.2). Transmission electron micrographs (TEMs) of as-synthesized AuNPs@CTAB and one gold-polythiophene hybrid nanoparticle system (AuNPs@P3KHT) are shown in Figure 3-26a and b. Both nanoparticle types were highly faceted and possessed numerous polyhedral shapes, indicating that the ligand exchange had no impact on the nanoparticles' morphology.

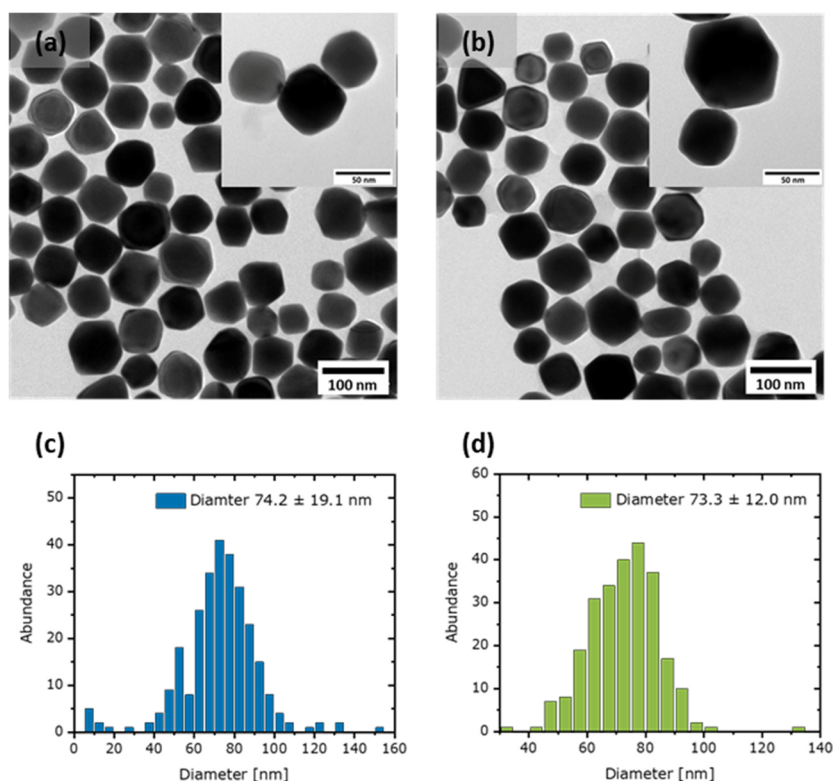


Figure 3-26: Transmission electron micrographs and particle size distribution from TEM analysis of (a, c) as-synthesized gold nanoparticles AuNPs@CTAB and (b, d) gold nanoparticles stabilized by carboxylated polythiophene AuNPs@P3KHT. TEMs were taken after purification of the nanoparticle dispersions.

The mean diameters of the nanoparticles were determined by size analysis with enclosing circles of 278 AuNPs@CTAB and 253 AuNPs@P3KHT in TEMs. As depicted in the histogram of Figure 3-26c, the as-synthesized AuNPs@CTAB possessed an average diameter of 74.2 ± 19.1 nm (mean \pm standard deviation). The polythiophene-stabilized

AuNPs@P3KHT had a mean diameter of 73.3 ± 12.0 nm (Figure 3-26d). The smaller dimensions of AuNPs@P3KHT can be attributed to the purification process after ligand exchange. Excess polymer was eliminated by centrifugation and filtration, whereby larger AuNPs were probably removed, too. The histogram in Figure 3-26d supports this hypothesis and illustrates that the abundance of nanoparticles with diameters above 100 nm were reduced after ligand exchange.

3.3.2 Colloidal analysis of biofunctionalizable gold-polythiophene hybrid nanoparticles

The biofunctionalizable hybrid nanoparticle dispersions contained free, unbound polymers after ligand exchange. I developed a purification procedure to remove these excessive polymers based on various centrifugation and filtration steps. Pure Milli-Q water ($18.2 \text{ M}\Omega\cdot\text{cm}^{-1}$) and an aqueous solution containing the nonionic surfactant Tween 20 (Figure 3-27) were compared regarding their suitability as a washing medium using UV-vis spectroscopy (Figure 3-28). Experimental details are described in

s 6.2.2 and 6.3.11.

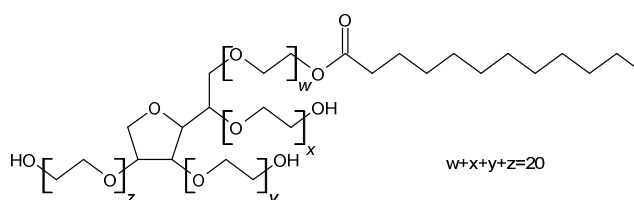


Figure 3-27: Molecular structure of the surfactant Tween 20.

All UV-vis absorption spectra were dominated by the SPR peak at about 550 nm, which is characteristic for AuNPs with a size of 70 nm to 80 nm (Figure 3-28).^{463,480} This size range corresponds to the dimensions of the biofunctionalizable gold-polythiophene hybrid nanoparticles obtained by image analysis of TEMs (Figure 3-26 in section 3.3.1). The order of the absorption intensities remained unchanged during purification in both media (Milli-Q water and aqueous Tween 20 solution) and was AuNPs@P3KHT > AuNPs@P3KBT > AuNPs@P3KPT > AuNPs@P3KHep. In addition, the overall absorption intensities of all biofunctionalizable gold-polythiophene

hybrid nanoparticles decreased with proceeding washing steps. Since the absorption intensities directly correlate with the gold concentration in the dispersions,⁵⁰⁷ the UV-vis data indicate a loss of AuNPs upon purification. The drop in absorption intensities was much more pronounced (Figure 3-28a-d) in Milli-Q water than for samples purified with aqueous Tween 20 solution (Figure 3-28e-h). The larger decrease in AuNPs concentration was likely caused by irreversible nanoparticle agglomeration. Samples of all biofunctionalizable gold-polythiophene hybrid nanoparticles washed in Milli-Q water remained partly agglomerated after the second centrifugation cycle and the centrifugation sediments could not be redispersed completely.

The increased colloidal stability of the biofunctionalizable gold-polythiophene hybrid nanoparticles in aqueous Tween 20 solution is likely based on synergetic stabilizing effects between the polythiophene ligands and the nonionic surfactant. Similar phenomena were observed for AuNPs and AuNRs stabilized by polyethylene glycol (PEG), where the addition of nonionic surfactants from the Tween series (Tween 20, Tween 40, Tween 60 and Tween 80) reduced the agglomeration of the nanocrystals.^{508–510} These reports claim that the surfactant molecules can adsorb on the surface of the gold nanocrystals, using the residual space between the attached PEG chains, which enhances the colloidal stability of the nanocrystals.

Nonionic surfactants can even improve the electrical conductivity of polythiophene films,^{511,512} enhancing the inter-chain π - π stacking between polythiophenes, which is beneficial for effective charge carrier transport.⁵¹² However, in the case of the biofunctionalizable gold-polythiophene hybrid nanoparticle the implementation of the nonionic Tween 20 surfactant during purification did not improve the electrical properties of the hybrids. The amount of Tween 20 (0.05 vol%) was probably too low to cause a significant effect. It is unknown whether surfactant molecules can affect the bioconjugation ability of the carboxylate groups presented in the side chains of the polymers. Hence, I reduced the amount of adsorbed Tween 20 molecules by performing the last centrifugation step in pure Milli-Q water, employing mild centrifugation conditions (section 6.2.2). It should be noted that even the implementation of Tween 20 could not prevent nanoparticle loss entirely, illustrated by the decreasing absorption intensities in the detected UV-vis spectra in Figure 3-28e-h.

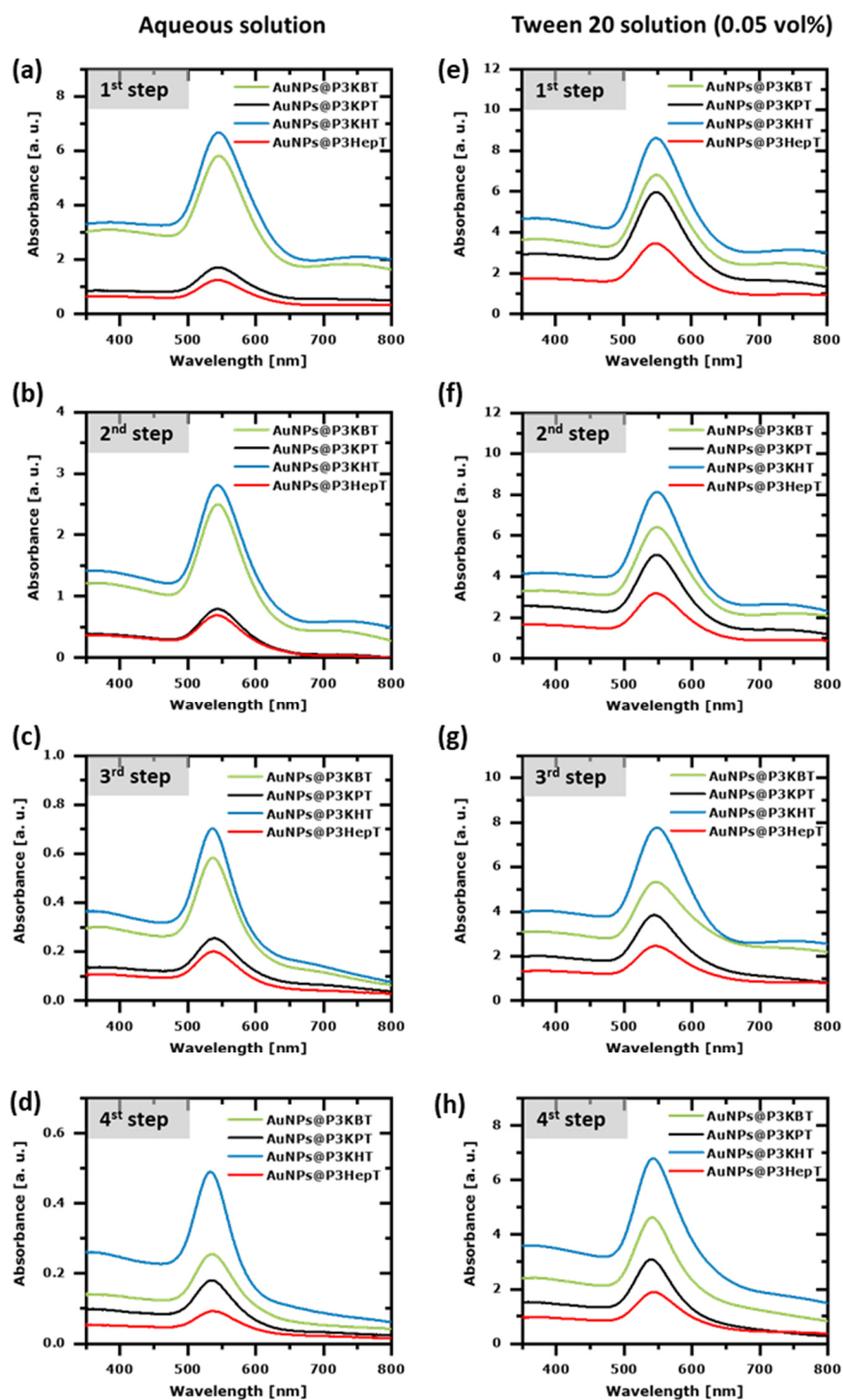


Figure 3-28: UV-vis absorption spectra of biofunctionalizable gold-polythiophene hybrid nanoparticles AuNPs@P3KBT, AuNPs@P3KPT, AuNPs@P3KHT and AuNPs@P3KHepT obtained after different centrifugation steps in (a-d) pure Milli-Q water ($18.2 \text{ M}\Omega\cdot\text{cm}^{-1}$) or in (e-h) an aqueous Tween 20 solution (0.05 vol%). All samples were diluted in the same ratio to ensure comparable conditions.

In summary, UV-vis characterization during the purification process revealed that Tween 20 is needed to increase colloidal stability of the gold-polythiophene hybrid nanoparticles and to suppress nanoparticle agglomeration. Functionalization with the polymer P3KHT yielded the most colloidally stable hybrid nanoparticle dispersion. UV-vis absorption spectra of the biofunctionalizable gold-polythiophene hybrid nanoparticles did not show any absorption features of the pure carboxylated polythiophenes (Figure 3-29a), indicating successful removal of excessive polymers by the newly developed purification procedure.

The UV-vis absorption spectra of the four carboxylated polythiophenes in Figure 3-29a illustrate broad absorption peaks in the region of 480 nm to 620 nm caused by to π - π^* intraband transitions.^{469,470} The red-shift of the absorption maxima and the appearance of a shoulder peak in the case of P3KHT and P3KHepT indicated enhanced inter-chain interactions.^{469,470,513} Since such interactions are more pronounced for polythiophenes with high molecular weights ($M_w > 30$ kDa),⁵¹⁴ the detected UV-vis data suggested longer polymer chains for P3KHT and P3KHepT. This corresponds to the information provided by the supplier, which states molecular weight distributions M_w of 12-16 kDa for P3KBT, of 20-30 kDa for P3KPT and of 55-65 kDa for P3KHT and P3KHepT. The longer polymer chains of P3KHT likely lend the AuNPs enhanced steric stabilization, explaining why AuNPs@P3KHT possessed the best colloidal stability. Surprisingly P3KHepT, which should possess similar molecular weights as P3KHT, did not yield colloidally stable hybrid nanoparticles. It is likely that the longer polymer side chains of P3KHepT limited its water-solubility, which reduced the stability of AuNPs@P3KHepT during purification (Figure 3-28).

The SPR depends on the electron charge density, which can be altered by the size, shape and composition of the nanocrystal, as well as by the permittivity of the environment close to the nanocrystal's surface, which depends on the absorbed ligands.⁴⁶³ The replacing of ligands during ligand exchange causes a change in the refractive index of the surrounding medium, yielding a detectable shift of the SPR band.⁴⁶⁴⁻⁴⁶⁶ The UV-vis absorption spectra of as-synthesized AuNPs@CTAB and the most colloidally stable AuNPs@P3KHT are depicted in Figure 3-29b. While the shape of the peak was not changed upon ligand exchange (no peak broadening), the maximum of the absorption

peak was blue-shifted by 5 nm (inset of Figure 3-29b). The addition and removal of charges to plasmonic nanocrystals modifies their electron density at the surface, resulting in a shift of the SPR band.⁴⁶⁷ This was illustrated by Mulvaney and co-workers, who added external charge to a single AuNR, causing a blue-shift of the longitudinal surface plasmon resonance (LSPR) due to the increased electron density of the nanorod by the external charge.⁴⁶⁸ The blue-shift in the case of AuNPs@P3KHT can be assigned to interactions between the delocalized π -electrons of the P3KHT polymer and the AuNPs, increasing the electron density of the metal cores. Thus, UV-vis spectroscopy indicated replacement of CTAB molecules by P3KHT chains.

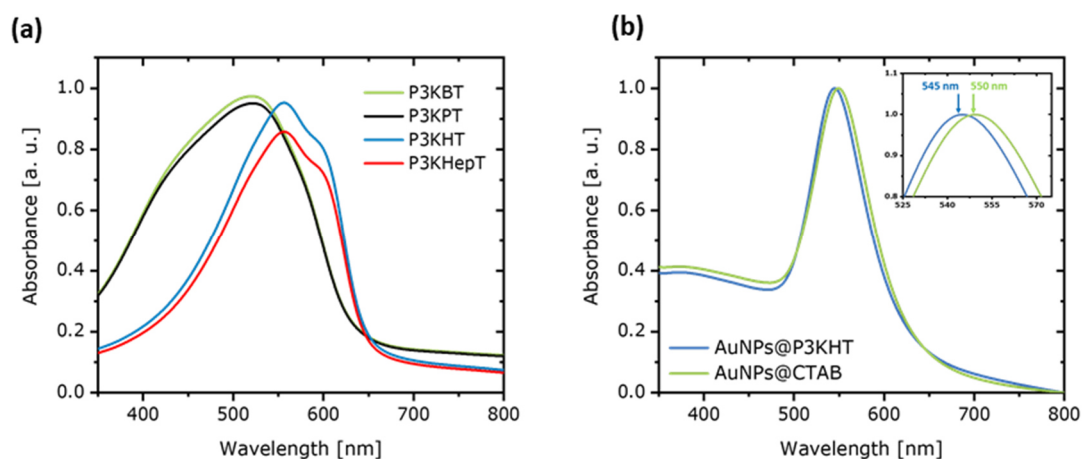


Figure 3-29: (a) UV-vis absorption spectra of aqueous solutions of the four different carboxylated polythiophenes P3KBT, P3KPT, P3KHT and P3KHepT. (b) UV-vis absorption spectra of as-synthesized AuNPs@CTAB and of gold nanoparticles functionalized with the carboxylated polythiophene P3KHT (AuNPs@P3KHT) after ligand exchange. The inset illustrates the blue-shift of the absorption maximum upon ligand exchange.

The detected zeta potentials ζ (Table 3-9 and Table 3-10) and hydrodynamic diameters d_h (Table 3-11 and Table 3-12) of the various biofunctionalizable gold-polythiophene hybrid nanoparticles during the purification process (Milli-Q water vs. Tween 20 solution), further supported that AuNPs@P3KHT possessed the best colloidal stability. As explained above, not all the precipitate of the samples centrifuged in Milli-Q water could be redispersed after the second centrifugation step due to irreversible particle agglomeration. Zeta and DLS data presented in the tables below were limited to the redispersible parts of the residues. I tried to gain more information on nanoparticle

agglomeration by partially breaking the non-dispersible sediments using ultrasonication (30 min). DLS data (Appendix C) of the ultrasonicated samples revealed that the non-dispersible residues were composed of nanoparticle agglomerates with dimensions of several hundreds of nanometers.

Before ligand exchange, the effective surface charge (ζ potential) of AuNPs@CTAB was highly positive (+31.6 mV), consistent with published zeta values (+25 mV to +40 mV) of CTAB-stabilized nanocrystals.^{69,354,472} The positive surface charge originates from the CTAB bilayer surrounding the nanocrystals, in which the charged headgroups of the outer layer face the aqueous medium.^{125,473} Ligand exchange with all carboxylated polythiophenes caused negative zeta potentials ζ . Since the carboxylated polythiophenes are negatively charged due to the carboxylate groups in their polymer side chains, the change in zeta potential ζ indicated successful replacement of the initial CTAB ligands by the appropriate carboxylated polythiophenes. With proceeding centrifugation in the Milli-Q water, the measured zeta potential ζ values of all biofunctionalizable gold-polythiophene hybrid nanoparticles increased (became more positive) continuously (Table 3-9), that can be attributed to detachment of excessive polythiophene chains, which were only loosely adsorbed and not covalently bound to the nanoparticles' surface. The reduction in negatively charged polythiophene chains surrounding the nanoparticles likely induced the observed increase in the effective surface charges of the hybrid AuNPs.

Table 3-9: Zeta potentials ζ (mean \pm standard deviation) of the biofunctionalizable gold-polythiophene hybrid nanoparticles AuNPs@P3KBT, AuNPs@P3KPT, AuNPs@P3KHT and AuNPs@P3KHepT after different centrifugation steps in pure Milli-Q water (18.2 M Ω ·cm⁻¹). The measured zeta potential ζ of AuNPs@CTAB before ligand exchange is also given. All measurements refer to the redispersible parts of the samples.

	ζ [mV]			
AuNPs@CTAB	+31.6 \pm 1.0			
	1 st step	2 nd step	3 rd step	4 th step
	ζ [mV]	ζ [mV]	ζ [mV]	ζ [mV]
AuNPs@P3KBT	-52.9 \pm 1.3	-46.8 \pm 1.5	-38.5 \pm 1.9	-37.8 \pm 1.5
AuNPs@P3KPT	-50.3 \pm 1.7	-48.1 \pm 1.4	-37.6 \pm 1.7	-34.2 \pm 1.7
AuNPs@P3KHT	-54.3 \pm 2.0	-45.4 \pm 1.0	-41.2 \pm 1.2	-39.3 \pm 0.8
AuNPs@P3KHepT	-49.8 \pm 1.5	-49.1 \pm 2.4	-37.3 \pm 1.3	-33.2 \pm 1.5

Table 3-10: Zeta potentials ζ (mean \pm standard deviation) of the biofunctionalizable gold-polythiophene hybrid nanoparticles AuNPs@P3KBT, AuNPs@P3KPT, AuNPs@P3KHT and AuNPs@P3KHepT after different centrifugation steps in aqueous Tween 20 solution (0.05 vol%). The measured zeta potential ζ of AuNPs@CTAB before ligand exchange is also given. All measurements refer to the redispersible parts of the samples.

	ζ [mV]			
AuNPs@CTAB	$+31.6 \pm 1.0$			
	1 st step	2 nd step	3 rd step	4 th step
	ζ [mV]	ζ [mV]	ζ [mV]	ζ [mV]
AuNPs@P3KBT	-36.4 ± 1.6	-30.4 ± 1.0	-39.2 ± 0.8	-37.8 ± 1.5
AuNPs@P3KPT	-43.9 ± 1.2	-28.2 ± 1.3	-37.2 ± 1.3	-35.3 ± 0.8
AuNPs@P3KHT	-35.9 ± 0.9	-28.3 ± 1.0	-40.1 ± 0.5	-38.3 ± 0.6
AuNPs@P3KHepT	-41.7 ± 0.7	-33.2 ± 1.1	-34.6 ± 1.0	-34.8 ± 1.0

In contrast, there was no clear trend in the zeta potentials ζ of biofunctionalizable gold-polythiophene hybrid nanoparticles washed in aqueous Tween solution. Until the second centrifugation step in Tween 20 solution, the zeta potentials ζ of the hybrid nanoparticles increased due to the removal of excessive polymer ligands (Table 3-10). However, after the third washing step the zeta potentials ζ of all biofunctionalizable hybrid nanoparticles decreased (became more negative) distinctly (Table 3-10). This phenomenon can be attributed to a coil-to-rod transition of the carboxylated polythiophene ligands surrounding the AuNPs, which was likely introduced by Tween 20 surfactant molecules. With proceeding washing more and more Tween 20 molecules could adsorb on the residual space between the polythiophene ligands.^{508–510} This reduced the accessible volume and the conformational freedom of the polythiophene chains, yielding a drop in polymer entropy. The infiltrating Tween 20 molecules likely caused an unfolding of the polythiophene ligands, resulting in a disorder-order transition. The polymer chains altered their structure from a disordered random coil arrangement with high entropy to a more ordered rod conformation with lower entropy and larger dimensions.^{515,516} In this rod conformation the charges of the polythiophene chains are more exposed to the surrounding media. It is likely that such a coil-to-rod transition occurred during the third centrifugation step in Tween 20 solution, yielding the observed decrease in zeta potentials ζ .

After complete purification in pure Milli-Q water or aqueous Tween 20 solution all biofunctionalizable hybrid nanoparticles possessed zeta potentials ζ below -30 mV, indicating sufficient colloidal stability.^{474–476} Regardless of which purification medium was used, AuNPs@P3KHT possessed the lowest zeta potentials ζ , suggesting the best colloidal stability, consistent with results from UV-vis spectroscopy (Figure 3-28).

Before ligand exchange the as-synthesized AuNPs@CTAB had a hydrodynamic diameter d_h of 78.1 nm. This is in conformity with TEM analysis (74.2 nm), since the dimensions of a CTAB bilayer surrounding the AuNPs is about 3.2 nm to 3.9 nm based on published literature.^{477–479} Ligand exchange with the four different carboxylated polythiophenes yielded hybrid nanoparticles with larger dimensions and higher polydispersity indexes (PDI), indicating the successful replacement of CTAB molecules. The increase in PDI likely originated from the molecular mass distribution of the carboxylated polythiophenes.

Washing in Milli-Q water resulted in a proceeding decrease in the detected hydrodynamic diameters d_h of all biofunctionalizable hybrid nanoparticles during the first three centrifugation steps (Table 3-11), which can be related to the removal of loosely bound excessive polythiophene ligands, consistent with the zeta potentials ζ discussed above. Since larger AuNPs are more prone to agglomeration, it is also possible that the observed nanoparticle agglomeration in Milli-Q water further promoted the decrease in hydrodynamic diameters d_h . After the last centrifugation steps the hydrodynamic diameters d_h of all biofunctionalizable gold-polythiophene hybrid nanoparticles increased again (Table 3-11), indicating further agglomeration of even smaller AuNPs.

Purification in aqueous Tween 20 solution (0.05 vol%) led to larger hydrodynamic diameters d_h , which probably originated from the adsorbed bulky surfactant molecules (Table 3-12). Similar to the washing in Milli-Q water, the hydrodynamic diameters d_h of biofunctionalizable gold-polythiophene hybrid nanoparticles also decreased during the first two centrifugation steps in aqueous Tween 20 solution due to the removal of excessive polythiophene ligands. After the third centrifugation step, the hydrodynamic diameters d_h increased again (Table 3-12), which further supported the hypothesis that surfactant molecules introduced a coil-to-rod transition of the polythiophene ligands, as

explained above.^{515,516} The infiltrating Tween 20 molecules likely caused an unfolding of the polythiophene chains, resulting in increased hydrodynamic dimensions of the hybrid nanoparticles. Since the final washing step was performed in pure Milli-Q water again to remove the Tween 20 molecules, I expected a decrease in hydrodynamic diameters d_h . However, except for AuNPs@P3KHT, the hydrodynamic dimensions of the biofunctionalizable hybrid nanoparticles increased (Table 3-12) indicating particle agglomeration. Consistent with zeta and UV-vis characterization (Figure 3-28), DLS also revealed that AuNPs@P3KHT possessed the best colloidal stability, which can be further enhanced by the implementation of the surfactant Tween 20 during purification.

Table 3-11: Hydrodynamic diameters d_h and polydispersity indexes (PDI) obtained by DLS of the biofunctionalizable gold-polythiophene hybrid nanoparticles AuNPs@P3KBT, AuNPs@P3KPT, AuNPs@P3KHT and AuNPs@P3KHepT after different centrifugation steps in pure Milli-Q water ($18.2 \text{ M}\Omega\cdot\text{cm}^{-1}$). The detected hydrodynamic diameter d_h and PDI of AuNPs@CTAB before ligand exchange are also given. All measurements refer to the redispersible parts of the samples.

	d_h [nm]	PDI [%]		
AuNPs@CTAB	78.1	12.5		
	1 st step		2 nd step	
	d_h [nm]	PDI [%]	d_h [nm]	PDI [%]
AuNPs@P3KBT	84.4	16.4	77.5	18.2
AuNPs@P3KPT	82.3	17.7	77.4	17.8
AuNPs@P3KHT	87.8	17.8	79.6	18.0
AuNPs@P3KHepT	87.2	17.2	79.0	18.5
	3 rd step		4 th step	
	d_h [nm]	PDI [%]	d_h [nm]	PDI [%]
AuNPs@P3KBT	74.9	24.3	80.9	24.7
AuNPs@P3KPT	73.9	24.8	74.9	23.9
AuNPs@P3KHT	85.8	23.4	88.6	23.2
AuNPs@P3KHepT	77.0	24.9	84.9	26.2

Table 3-12: Hydrodynamic diameters d_h and polydispersity indexes (PDI) obtained by DLS of the biofunctionalizable gold-polythiophene hybrid nanoparticles AuNPs@P3KBT, AuNPs@P3KPT, AuNPs@P3KHT and AuNPs@P3KHepT after different centrifugation steps in aqueous Tween 20 solution (0.05 vol%). The detected hydrodynamic diameter d_h and PDI of AuNPs@CTAB before ligand exchange are also given. All measurements refer to the redispersible parts of the samples.

	d_h [nm]	PDI [%]		
AuNPs@CTAB	78.1	12.5		
	1 st step		2 nd step	
	d_h [nm]	PDI [%]	d_h [nm]	PDI [%]
AuNPs@P3KBT	94.4	17.6	93.6	18.6
AuNPs@P3KPT	94.7	18.1	93.1	17.8
AuNPs@P3KHT	102.3	17.8	99.4	17.2
AuNPs@P3KHepT	97.1	17.5	96.3	19.0
	3 rd step		4 th step	
	d_h [nm]	PDI [%]	d_h [nm]	PDI [%]
AuNPs@P3KBT	98.7	22.8	146.9	24.5
AuNPs@P3KPT	106.2	22.5	151.4	25.3
AuNPs@P3KHT	103.7	19.1	88.5	19.0
AuNPs@P3KHepT	115.2	24.3	180.9	28.4

I analyzed the colloidal properties of AuNPs@P3KHT in different water-organic solvent mixtures. UV-vis absorption spectra revealed no pronounced differences in water and in the different water-organic solvent mixtures, indicating colloidal stability of the AuNPs@P3KHT (Figure 3-30a). This was further supported by the red color of all AuNPs@P3KHT dispersions (Figure 3-30b).^{481–484} In contrast, the UV-vis absorption spectra of as-synthesized AuNPs@CTAB in different water-organic solvent mixtures exhibited features of nanoparticle agglomeration, such as peak broadening, red-shifting and intensity decrease of the SPR peak (Figure 3-30c).^{481–484,517} The irreversible agglomeration of AuNPs@CTAB caused a color change from red to purple/blue (Figure 3-30d).^{481–484}

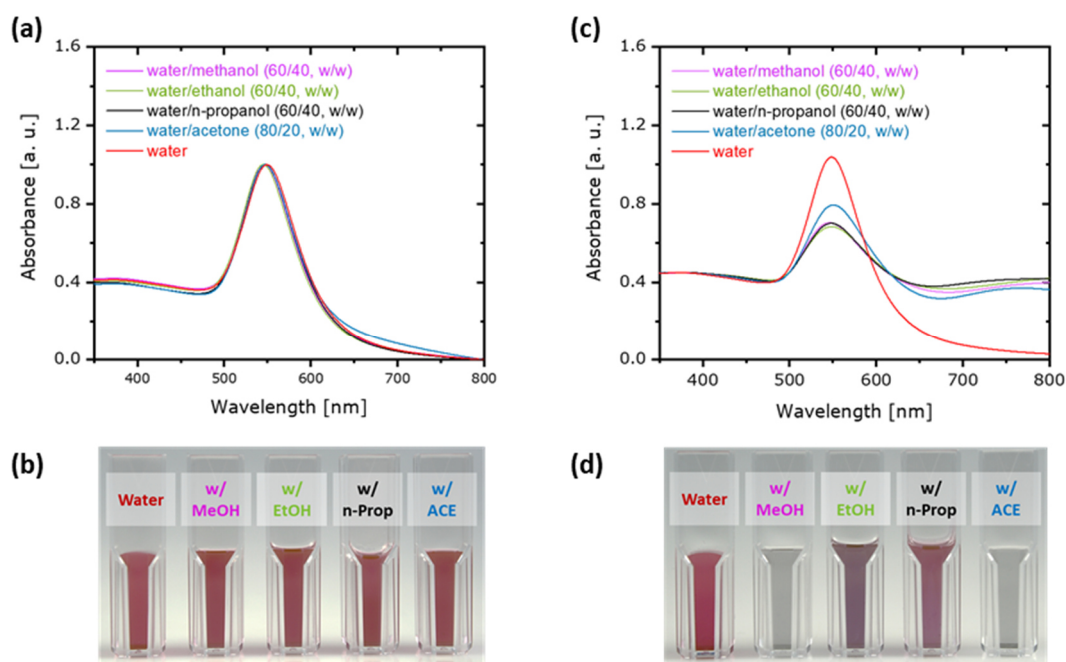


Figure 3-30: UV-vis absorption spectra of (a) AuNPs@P3KHT and (b) AuNPs@CTAB in pure water and different water-organic solvent mixtures. Photographs of the colloidal dispersions in water and various water-organic solvent mixtures containing (c) AuNPs@P3KHT and (d) AuNPs@CTAB.

The detected zeta potentials ζ of AuNPs@P3KHT in pure water and in the various water-organic solvent mixtures were all about -40 mV (Table 3-13), indicating sufficient colloidal stability of AuNPs@P3KHT in all tested dispersants.^{474–476} The hydrodynamic diameter d_h of AuNPs@P3KHT obtained from DLS was largest in pure aqueous solution and decreased in the different alcoholic mixtures with increasing polarity of the used alcohol (Table 3-13). Similar observations were also found for AuNPs@PFS-Na (section 3.2.2), indicating a transition of the polythiophene ligands from an extended random coil configuration in a good solvent to a collapsed globule state with smaller dimensions in a bad solvent.^{485–487} This is a typical phenomenon of polyelectrolytes and likely explains the observed trend in hydrodynamic diameter d_h of AuNPs@P3KHT, as well. Thus, increasing polarity of the used organic solvent decreased the solvent quality of the charged polythiophene ligand P3KHT. This caused a shrinkage of the ligand shell dimensions and led to a reduced hydrodynamic diameter d_h . Although acetone has the highest polarity of the tested solvents, AuNPs@P3KHT possessed the lowest hydrodynamic diameter d_h in mixtures containing n-propanol, which can be attributed to

the lower amount of acetone (20 wt%) in the mixture compared to the quantity of alcohols (40 wt%).

Table 3-13: Hydrodynamic diameters d_h and polydispersity indexes (PDI) obtained by DLS and zeta potential ζ values (mean \pm standard deviation) for AuNPs@P3KHT in water and various water-organic solvent mixtures.

	d_h [nm]	PDI [%]	ζ [mV]
water	86.0	14.8	-39.8 ± 1.2
water/methanol (60/40, w/w)	79.2	12.9	-40.1 ± 1.9
water/ethanol (60/40, w/w)	75.3	11.0	-37.1 ± 1.8
water/n-propanol (60/40, w/w)	74.1	13.2	-41.8 ± 1.7
water/acetone (80/20, w/w)	83.2	12.2	-39.4 ± 1.9

In summary, replacement of CTAB molecules by the carboxylated polythiophene ligand P3KHT increased the colloidal stability of gold nanoparticles. The stabilization is likely caused by an electro-steric stabilization effect of the long and negatively charged polythiophene ligands. Increased stability is beneficial, since many applications, e.g. the formulation of printable nanoparticle inks suitable for the production of printed electronics, often require additives or solvents beyond aqueous media. Since the results presented in this section clearly show that AuNPs@P3KHT were the most colloiddally stable biofunctionalizable gold-polythiophene hybrid nanoparticles, I chose this system for all further studies presented in this work (except Raman characterization presented in section 3.3.3).

3.3.3 Characterization of ligand binding in gold-P3KHT hybrids by Raman spectroscopy

Raman spectroscopy of the biofunctionalizable gold-polythiophene hybrid nanoparticles indicated a successful ligand exchange between CTAB and the carboxylated polythiophenes consistent with the results obtained by UV-vis spectroscopy and DLS (section 3.3.2). As illustrated in Figure 3-31a and b, the as-synthesized AuNPs@CTAB had an Au-Br vibration peak at about 177 cm^{-1} , which is characteristic for nanoparticles functionalized by CTAB.⁴²⁷ After ligand exchange with all four carboxylated

polythiophenes, this peak vanished from the Raman spectra of biofunctionalizable gold-polythiophene nanoparticles (Figure 3-31a and b), indicating near complete replacement of CTAB. New peaks between 200 cm^{-1} and 300 cm^{-1} refer to Au-S stretching modes,⁴²⁸ suggesting that the four polymers bound to gold nanocrystals via sulfur species, similar to the other non-biofunctionalizable gold-polythiophene hybrid nanoparticles introduced in this work (sections 3.1.3 and 3.2.3). In contrast to PTEBS and PFS-Na, the carboxylated polythiophenes only possess sulfur species in their thiophene backbones and not in their side chains. Hence, they can only bind to the AuNPs via the thiophene rings present in the polymer backbones.

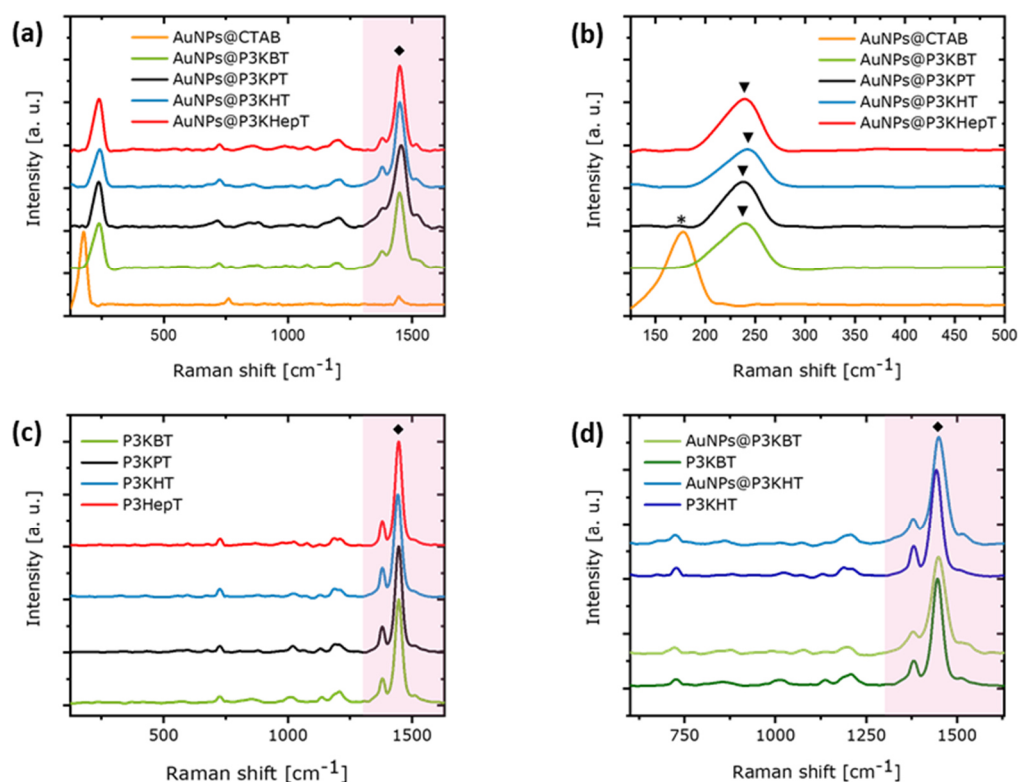


Figure 3-31: (a) Raman spectra of as-synthesized AuNPs@CTAB and biofunctionalizable gold-polythiophene hybrid nanoparticles after ligand exchange (AuNPs@P3KBT, AuNPs@P3KPT, AuNPs@P3KHT and AuNPs@P3KHepT). (b) Fingerprint region of the Raman spectra of the biofunctionalizable gold-polythiophene hybrid nanoparticles and AuNPs@CTAB. (c) Raman spectra of the pure carboxylated polythiophenes P3KBT, P3KPT, P3KHT and P3KHepT. (d) Comparison between the Raman spectra of AuNPs@P3KBT and AuNPs@P3KHT with the spectra of the corresponding carboxylated polythiophenes. The ranges of the characteristic thiophene ring vibrations are highlighted in light red. Important vibrations modes are additionally marked in the spectra: $\nu(\text{Au-Br})=*$, $\nu(\text{Au-S})=\blacktriangledown$, $\nu(\text{C-C, C=C})=\blacklozenge$.

The Raman spectra of the pure polymers possessed characteristic polythiophene vibrations in the range of 1300 cm^{-1} to 1550 cm^{-1} (light red area in Figure 3-31c), which originate from intra-ring C-C as well as from symmetric and asymmetric C=C stretch modes. These vibrations were also present in the Raman spectra of the four gold-polythiophene hybrid nanocrystals (light red area in Figure 3-31a). Since no Raman data of the four different carboxylated polythiophenes are available in literature, I used equivalent polythiophenes (e.g. P3HT) for a detailed peak assignment.^{430,431} The peak assignment shown in Table 3-14 applies to all four used carboxylated polythiophenes.

Table 3-14: Characteristic vibrational peaks detected in the Raman spectra of the pure carboxylated polythiophenes P3KBT, P3KPT, P3KHT and P3KHepT. The band assignment is based on literature values of equivalent polythiophenes (e.g. P3HT).^{430,431}

Raman shift [cm^{-1}]	Band assignment
723	$\delta(\text{C-S-C})$ ring deformation mode
1000-1070	$\delta(\text{CH}_2)$ bending mode
1200	$\delta(\text{C-H})$ bending mode
1380	intra-ring $\nu(\text{C-C})$ stretching mode
1449	symmetric $\nu_s(\text{C=C})$ ring stretching mode
1520	asymmetric $\nu_{as}(\text{C=C})$ ring stretching mode

For better comparison, the Raman spectra of two biofunctionalizable hybrid particles (AuNPs@P3KBT and AuNPs@P3KHT) and the spectra of the two corresponding carboxylated polythiophenes are illustrated by way of example in Figure 3-31d. Compared to the Raman data of the pure polythiophenes, the characteristic thiophene ring peaks in the range of 1300 cm^{-1} to 1550 cm^{-1} were broadened and intensified. Especially the peaks at about 1550 cm^{-1} , corresponding to the asymmetric $\nu_{as}(\text{C=C})$ ring stretching mode, were more pronounced in the spectra of the biofunctionalizable gold-polythiophene hybrid nanocrystals. According to literature, doping of polythiophenes broadens and enhances thiophene ring vibrations.⁴³⁴ Upon doping, polaron and bipolaron states are created inside the polythiophene chains, increasing the overall electrical conductivity of the polymers. The detected Raman data of all tested biofunctionalizable gold-polythiophene hybrid nanoparticles, indicated that due to charge transfer processes between the carboxylated polythiophenes and the gold cores, polarons and bipolarons were formed inside the polythiophene ligand shells.

3.3.4 Electrical conductivity of gold-P3KHT hybrid nanoparticle films

I produced line patterns on glass substrates by drop-casting of dispersions containing AuNPs@P3KHT. The dried lines were conductive without any post-deposition treatments, indicating the sinter-free nature of biofunctionalizable gold-polythiophene hybrid nanoparticles. The exact width and length of each line was detected by optical transmission microscopy and confocal microscopy was employed to obtain the thicknesses of the lines. The lines were between 1 μm and 3 μm thick, with thickness variations within one layer of below 30%. Further experimental details about the characterization are given in sections 6.3.3 and 6.3.5.

I electrically characterized six individual line patterns composed of AuNPs@P3KHT. Averaged I - V curves of layers made from biofunctionalizable AuNPs@P3KHT and of films made from non-biofunctionalizable AuNPs@PTEBS are depicted in Figure 3-32a. Their linear shape indicated ohmic metal-like electrical conductivities. The determined material resistivity ρ of AuNPs@P3KHT (equation 3-1 in section 3.1.2) was $8.84 \cdot 10^{-6} \Omega\text{m} \pm 0.11 \cdot 10^{-6} \Omega\text{m}$ (mean \pm one standard deviation), almost 25% above the material resistivity ρ of AuNPs@PTEBS ($7.10 \cdot 10^{-6} \Omega\text{m} \pm 0.15 \cdot 10^{-6} \Omega\text{m}$). The higher material resistivity is likely caused by larger inter-particle distances in the hybrid AuNPs@P3KHT layers. TGA data presented in Appendix A (Figure A-1b) revealed an organic content of 1.5 wt% for AuNPs@P3KHT, more than twice the organic weight fraction (0.7 wt%) of AuNPs@PTEBS (section 3.1.1). Assuming similar densities of the two polythiophenes, the ligand shell must be thicker in the case of AuNPs@P3KHT. Thicker shells likely limited charge carrier transport within the AuNPs@P3KHT films, increasing the material resistivity. However, the determined material resistivities of both AuNPs@P3KHT and AuNPs@PTEBS were in the same range ($10^{-6} \Omega\text{m}$), two orders of magnitude above bulk gold ($2.35 \cdot 10^{-8} \Omega\text{m}$).¹⁶⁰

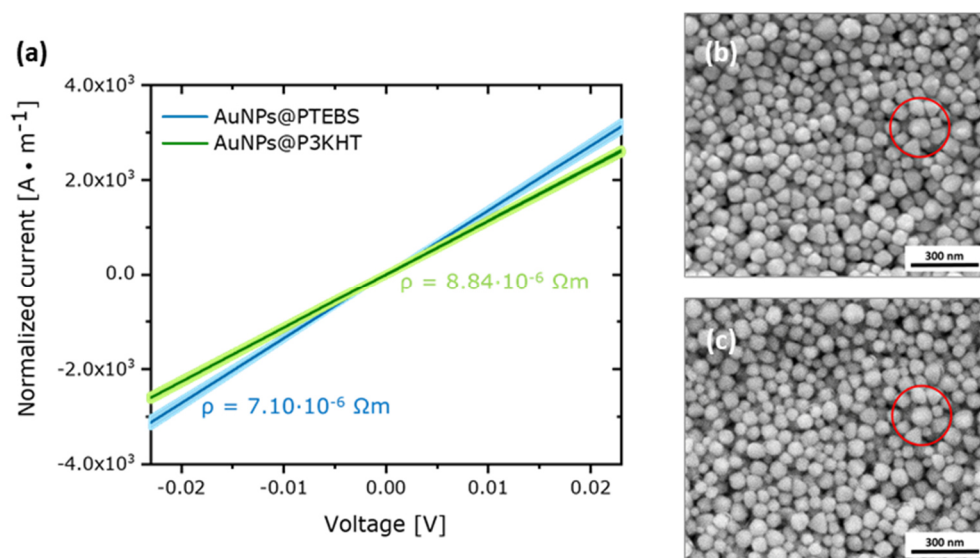


Figure 3-32: (a) Average I - V curves with normalized currents to film thicknesses of AuNPs@PTEBS (blue) and AuNPs@P3KHT (green) with the corresponding error ranges (light blue and light green areas). Scanning electron micrographs of layers made from AuNPs@P3KHT on glass substrates (b) before and (c) after exposure to water. The SEMs were recorded at nearly identical positions of the AuNPs@P3KHT films before and after water exposure. The red circles mark areas to illustrate that water exposure caused no significant structural changes in the layer morphology.

Scanning electron micrographs (SEMs) of dry films made from AuNPs@P3KHT in Figure 3-32b revealed that they consisted of individual hybrid nanoparticles and the detected electrical conductivity of the line patterns was not caused by sintering. Since many biological applications require a liquid medium, I investigated how the layers made of biofunctionalizable gold-polythiophene nanoparticles behave under wet conditions. The AuNPs@P3KHT films on glass were submerged in Milli-Q water at room temperature for 10 min, dried under ambient conditions and the resistivity ρ of the samples was measured. SEMs of the AuNPs@P3KHT layers before and after water exposure in Figure 3-32b and c indicated no obvious rearrangements and changes in morphology of the AuNPs at the surface of the films. Average I - V curves of six individual line patterns made from AuNPs@P3KHT in the dried, wet and re-dried state are shown in Figure 3-33a, b and c. All three I - V curves were similar without pronounced differences in the progressions or slopes of the curves. The calculated average resistivity ρ in the dried ($8.84 \cdot 10^{-6} \Omega m$), wet ($8.85 \cdot 10^{-6} \Omega m$) and re-dried ($8.84 \cdot 10^{-6} \Omega m$) state were identical

in the range of experimental error. Hence, the biofunctionalizable hybrid films retained their electrical properties during wetting and drying.

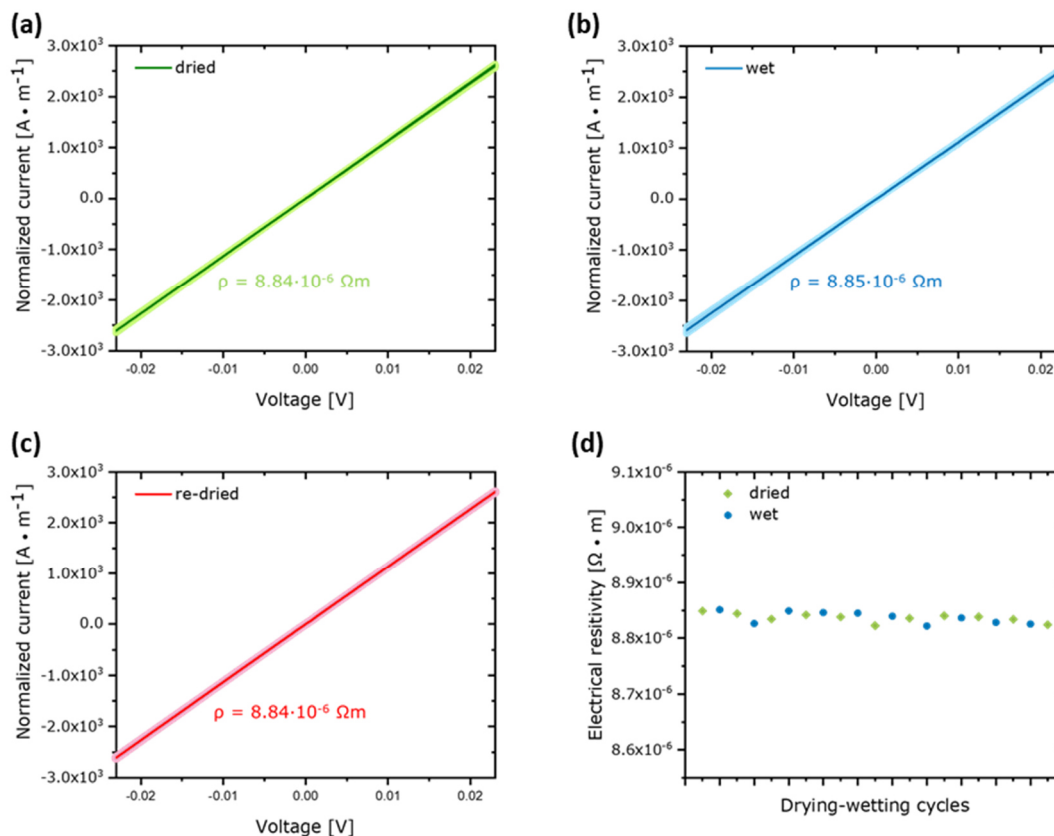


Figure 3-33: Average I - V curves with normalized currents to film thicknesses of AuNPs@P3KHT (a) before, (b) during and (c) after water exposure. The corresponding error ranges are marked in (a) light blue, (b) light green and (c) light red. (d) Detected material resistivity ρ upon ten wetting-drying cycles of AuNPs@P3KHT. All experiments were conducted under ambient conditions.

To test the durability of the layers made from AuNPs@P3KHT, I exposed four individual samples to ten wetting-drying cycles and tracked the resistivity ρ (Figure 3-33d). There were no significant differences in the resistivity ρ and I did not observe any delamination of the layers from the underlying glass substrates. The high electrical conductivity and stability of films composed of AuNPs@P3KHT make the biofunctionalizable gold-polythiophene hybrid nanoparticles developed in this work promising materials for different biological applications, including platforms for cell growth or electrodes for biosensors.

3.3.5 Summary

This chapter describes colloiddally stable and electrically conductive biofunctionalizable hybrid nanoparticles obtained by modification of gold nanocrystals with carboxylated polythiophene ligands. The COO^- groups present in the side chains of the polythiophenes enable specific interactions with biological species containing primary amines such as enzymes, proteins, antibodies or DNA. Among the four tested carboxylated polythiophenes (P3KBT, P3KPT, P3KHT and P3KHepT), the ligand P3KHT yielded the most colloiddally stable biofunctionalizable gold-polythiophene hybrid nanoparticles (AuNPs@P3KHT). Raman spectroscopy revealed that all examined carboxylated polythiophenes were able to replace the initial ligand CTAB and bind via sulfur motif to the gold cores resulting in stable Au-S bonds. Modification of the AuNPs by P3KHT increased their colloidal stability not only in aqueous solution, but also in different water-organic solvent mixtures. Additionally, the results in this chapter clearly demonstrated that the biofunctionality of the polythiophene ligand did not affect the electrical properties of the biofunctionalizable hybrid nanocrystals. Films composed of AuNPs@P3KHT were directly conductive after solvent evaporation, demonstrating the sinter-free nature of the gold-polythiophene hybrid nanoparticles. The determined material resistivity ρ of AuNPs@P3KHT ($8.84 \cdot 10^{-6} \Omega\text{m} \pm 0.11 \cdot 10^{-6} \Omega\text{m}$) was in the same range as that of non-biofunctionalizable gold-polythiophene hybrid nanoparticles developed in this work. Layers made of AuNPs@P3KHT retained their electrical properties under water, which makes them suitable for biomedical applications.

Since carboxyl groups are not the only functional groups which facilitate interactions with biological species, upcoming studies could investigate if polythiophene ligands with different functional groups would also yield biofunctionalizable hybrid nanocrystals. Possible functional groups which should be analyzed regarding their biofunctionality are amine ($-\text{NH}_2$) or thiol ($-\text{SH}$) groups, since those groups have already been successfully introduced in the polymer side chains of various polythiophenes.^{518–521} Furthermore, cationic polythiophenes could be interesting for the production of new biofunctionalizable hybrids, since these polymers are distinctly responsive towards DNA.^{522,523}

3.4 Bioconjugation of gold-polythiophene hybrid nanoparticles

This chapter deals with the bioconjugation AuNPs@P3KHT, using EDC/NHS chemistry, an established bioconjugation method.^{394,524–528} I employed this technique to covalently attach biomolecules to AuNPs@P3KHT before or after film deposition (Figure 3-34). In surface bioconjugation, films are fabricated by different deposition techniques (drop-casting, inkjet printing, spin coating, etc.) and the biomolecules are bioconjugated to dry layers (Figure 3-34a). Only the nanoparticles at the surface and closely below are functionalized with biomolecules. This limits the number of biomolecules coupled to the gold-polythiophene hybrid nanoparticles.

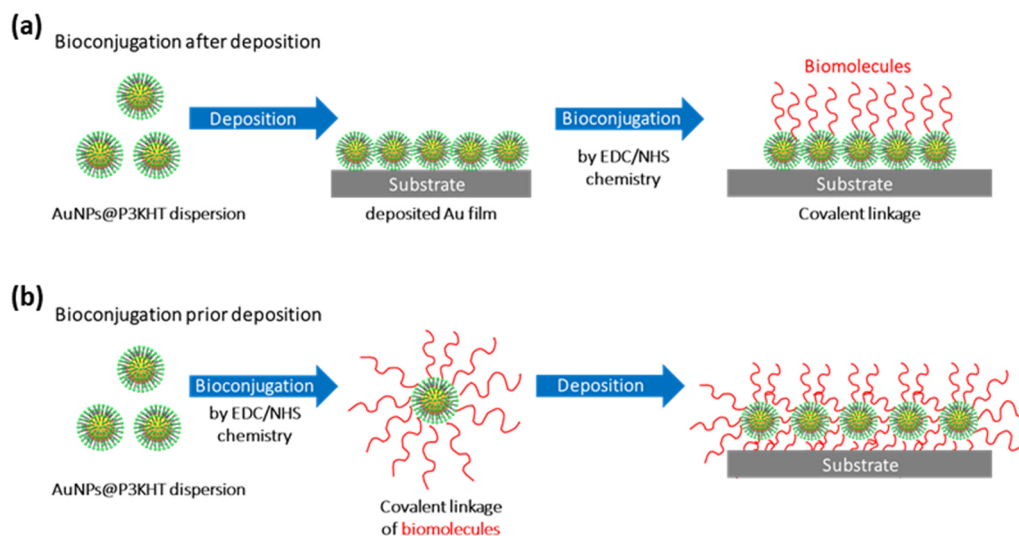


Figure 3-34: Schematic bioconjugation procedure of the biofunctionalizable gold-polythiophene hybrid nanoparticles AuNPs@P3KHT, which can be performed (a) after film formation by deposition (surface bioconjugation) or before deposition in the particle dispersion (solution bioconjugation).

Alternatively, AuNPs@P3KHT can be bioconjugated in solution prior to the layer deposition (solution bioconjugation). In this case, biomolecules can be covalently linked to all gold-polythiophene hybrid nanoparticles in the entire film as depicted in Figure 3-34b. The number of linked biomolecules is limited by the available space around the AuNPs@P3KHT and the number of activated carboxylate groups. Since solution

bioconjugation alters the properties of the particle dispersion, it can influence the deposition process negatively and cause particle agglomeration, leading to inhomogeneous film formation. Surface bioconjugation of AuNPs@P3KHT films was performed by adapting a protocol for bioconjugation of hydrogels,^{529,530} while for solution bioconjugation a new one-step procedure was introduced.

I chose glucose oxidase (GOx) as a model system. This enzyme is commercially available, stable, relatively inexpensive^{531–533} and well-studied in glucose biosensing.^{534–539} Sections 3.4.1 and 3.4.2 reveal how the linkage of GOx to AuNPs@P3KHT affected the colloidal and structural properties of the gold-polythiophene hybrid nanoparticles. I used Raman spectroscopy to characterize the attachment of GOx to AuNPs@P3KHT (section 3.4.3). Section 3.4.4 deals with the effect of bioconjugation on the electrical properties of the gold-polythiophene hybrid nanoparticle films.

Bioconjugation influences the properties of the coupled biomolecules. Thus, I analyzed the enzymatic activity of GOx molecules attached to AuNPs@P3KHT using colorimetric bioassays for glucose detection (section 3.4.5). In a further step, I tested AuNPs@P3KHT-GOx for electrochemical glucose sensing by inkjet printing biosensors. The printed biosensors were flexible and possessed sufficient sensitivity for electrochemical glucose detection. They combined the excellent electrical conductivity of the gold nanoparticles with the high enzymatic activity of GOx (section 3.4.6). Finally, section 3.4.7 introduces biofunctionalizable gold-polythiophene hybrid nanoparticles that were bioconjugated with cell growth supporting peptides. Films composed of these hybrids distinctly enhanced cell growth of fibroblast and neural cells compared to unmodified substrates.

Parts of the results incorporated in chapter 3.4 led to the patent application *Conductive functionalizable nanocomposites* (DE102019135645A1).

3.4.1 Colloidal analysis of bioconjugated gold-P3KHT hybrid nanoparticles

I chose the enzyme glucose oxidase (GOx) as a model system for bioconjugation to AuNPs@P3KHT, since this enzyme is commercially available, stable and relatively inexpensive.^{531–533} Furthermore, GOx has been well studied regarding its applicability in glucose biosensors.^{534–539} Bioconjugation is often conducted in a two-step protocol, where the first step is performed under acidic conditions in a MES buffer (0.1 M, pH=4.7) and the second step (amide bond formation) is conducted at higher pH up to 6–7.5 in a PBS buffer (section 2.3.3).^{396,397,398,401,402,403} Such a procedure did not work for the bioconjugation of AuNPs@P3KHT, since the gold-polythiophene hybrid nanoparticles were not stable in different MES and PBS buffers. The UV-vis absorption spectra in Figure 3-35a show distinct features of particle agglomeration, such as the decrease in SPR band intensity and the increase of absorption intensity at higher wavelength (> 600 nm).^{481–484,517} Nanoparticle agglomeration caused a color change of the nanoparticle dispersion from pinkish-red to purple-blue,^{540–544} which was visible to the naked eye (Figure 3-35b). It is not clear if the pH itself or the high ionic strength present in the buffers caused the irreversible agglomeration of AuNPs@P3KHT, since both effects are known to destabilize colloidal gold nanoparticles.^{540–544}

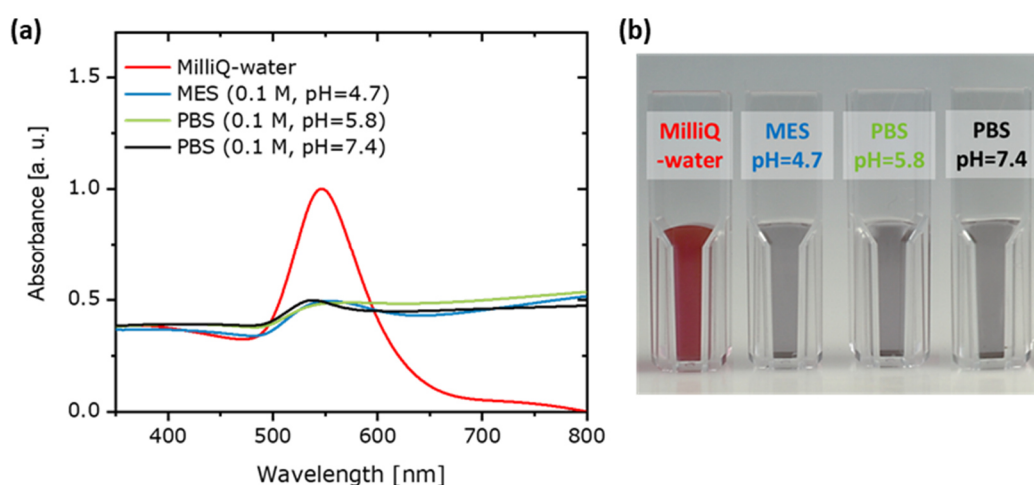


Figure 3-35: (a) UV-vis absorption spectra of AuNPs@P3KHT in Milli-Q water, MES buffer (0.1 M, pH=4.7), PBS buffer (0.1 M, pH=5.8) and PBS buffer (0.1 M, pH=7.4). (b) Photographs of AuNPs@P3KHT dispersions in Milli-Q water, MES buffer (0.1 M, pH=4.7), PBS buffer (0.1 M, pH=5.8) and PBS buffer (0.1 M, pH=7.4). The color change from red to purple-blue reveals particle agglomeration.

I developed a one-step procedure for the bioconjugation of GOx to AuNPs@P3KHT. Simultaneous addition of the EDC/NHS reagent and the amine compound can reduce the risk of hydrolyzing the active NHS-ester immediately and it is often performed at physiological conditions (pH in neutral range, close to the isoelectric point of the biomolecules), which limits the activity loss of biomolecules such as enzymes.⁵⁴⁵ These conditions do not inhibit the bioconjugation process, since the EDC/NHS coupling upon amide formation proceeds successfully up to pH of 7.5.^{384–386} According to this and to avoid buffer solutions, I performed the bioconjugation in Milli Q water. I detected an almost neutral pH of 6.8 for the Milli-Q water produced in our laboratory. Additionally, I employed Sulfo-NHS instead of NHS, which introduces additional negative surface charges to the nanoparticles, creating electrostatic repulsion which can prevent particle agglomeration during bioconjugation.³⁸⁶ In order to find the optimal conditions for bioconjugation in solution, I tested several concentrations of EDC/Sulfo-NHS reagent, ranging from 0.5 vol% to 3 vol% of the total reaction volume. I performed centrifugation after bioconjugation to remove excess of free enzyme, non-reacted EDC/Sulfo-NHS reagent and other byproducts. Experimental details of the bioconjugation and purification process are given in section 6.2.3. After each centrifugation step, I took samples and characterized them by DLS and zeta potential measurements. The results are summarized in Table 3-15 and Table 3-16.

The diameter of the enzyme-functionalized AuNPs@P3KHT-GOx increased with increasing concentration of EDC/Sulfo-NHS reagent (Table 3-15), since higher concentrations of EDC/Sulfo-NHS reagent led to more activated carboxylate groups in the polythiophene ligand shell, resulting in more bioconjugated GOx molecules. In addition, the hydrodynamic diameters d_h decreased during purification (Table 3-15), since GOx molecules which were loosely bound by physisorption to the AuNPs were removed during the centrifugation steps. It should be noted that bioconjugation with 3.00 vol% of EDC/Sulfo-NHS reagent yielded to nanoparticle agglomeration after the third centrifugation step of the purification procedure.

Table 3-15: Hydrodynamic diameters d_h and polydispersity indexes (PDI) obtained by DLS for enzyme-functionalized AuNPs@P3KHT-GOx after different centrifugation steps. The bioconjugation with glucose oxidase GOx was performed in solution using varying concentrations of EDC/Sulfo-NHS reagent. Purification was done by centrifugation in Milli-Q water. The measured hydrodynamic diameter d_h and PDI of AuNPs@P3KHT before bioconjugation are also given.

	d_h [nm]	PDI [%]		
AuNPs@P3KHT	86.0	14.8		
	1 st step		2 nd step	
AuNPs@P3KHT-GOx	d_h [nm]	PDI [%]	d_h [nm]	PDI [%]
EDC/Sulfo-NHS reagent (0.50 vol%)	91.4	17.3	90.3	16.5
EDC/Sulfo-NHS reagent (0.75 vol%)	93.2	17.9	91.1	16.5
EDC/Sulfo-NHS reagent (1.00 vol%)	96.3	17.4	92.2	16.3
EDC/Sulfo-NHS reagent (1.50 vol%)	98.2	20.0	96.4	15.8
EDC/Sulfo-NHS reagent (2.00 vol%)	100.3	17.5	97.7	16.5
EDC/Sulfo-NHS reagent (3.00 vol%)	102.1	17.3	218.5	26.2
	3 rd step		4 th step	
AuNPs@P3KHT-GOx	d_h [nm]	PDI [%]	d_h [nm]	PDI [%]
EDC/Sulfo-NHS reagent (0.50 vol%)	87.9	16.3	87.7	17.2
EDC/Sulfo-NHS reagent (0.75 vol%)	89.9	16.6	89.7	16.9
EDC/Sulfo-NHS reagent (1.00 vol%)	90.5	16.8	90.3	16.6
EDC/Sulfo-NHS reagent (1.50 vol%)	95.1	16.0	94.9	16.0
EDC/Sulfo-NHS reagent (2.00 vol%)	96.9	16.4	96.5	16.6
EDC/Sulfo-NHS reagent (3.00 vol%)	n/a	n/a	n/a	n/a

The maximal increase of hydrodynamic diameter d_h for stable AuNPs@P3KHT-GOx was about 10 nm using 2.00 vol% EDC/Sulfo-NHS reagent. Glucose oxidase is a bulky molecule with dimensions of 60 x 52 x 77 Å³ and a hydrodynamic diameter of 8.9 nm.^{546,547} A complete GOx corona around the AuNPs@P3KHT should cause an increase in diameter of about 18 nm. Thus, DLS suggested that either not all carboxylate groups in the polythiophene ligand shell were transferred to amide bonds, or that GOx molecules change their conformation upon bioconjugation, resulting in reduced enzyme dimensions. Such conformational changes of GOx upon immobilization on nanomaterials are reported in literature.^{548,549} Since surface charges due to unreacted carboxylate groups are crucial for the colloidal stability of the enzyme-functionalized AuNPs@P3KHT-GOx,

I assumed that a certain amount of carboxylate groups remained after bioconjugation. This hypothesis is further supported by the zeta measurements summarized in Table 3-16.

The detected zeta potentials ζ revealed two trends. Firstly, the zeta potentials ζ increased (became less negative) with increasing amount of activated carboxylate groups (higher concentrations of EDC/Sulfo-NHS reagent), since the bioconjugation transferred the negatively charged carboxylate groups to neutral amide bonds. Secondly, the zeta potentials ζ decreased (became more negative) with proceeding purification steps, regardless of which concentration of EDC/Sulfo-NHS reagent was used. This decrease indicated the removal of physisorbed and excessive GOx enzymes, since these molecules can shield the surface charge of the AuNPs@P3KHT hybrid nanoparticles. After the fourth purification step, the zeta potential ζ values were above -30 mV, which is usually the limit for colloidal stability based on electrostatic stabilization.^{474–476} The negative surface charges suggested electrosteric stabilization, whereby the remaining COO⁻ groups caused electrostatic repulsion and the bulky structure of the bioconjugated GOx molecules further introduced improved steric stabilization.

Table 3-16: Detected zeta potentials ζ (mean \pm standard deviation) of enzyme-functionalized AuNPs@P3KHT-GOx after different centrifugation steps. The bioconjugation with glucose oxidase was performed in solution using varying concentrations of EDC/Sulfo-NHS reagent. Purification was done by centrifugation in Milli-Q water. The measured zeta potential ζ of AuNPs@P3KHT before bioconjugation is also listed.

	ζ [mV]			
AuNPs@P3KHT	-39.8 ± 1.2			
	1 st step	2 nd step	3 rd step	4 th step
AuNPs@P3KHT-GOx	ζ [mV]	ζ [mV]	ζ [mV]	ζ [mV]
EDC/Sulfo-NHS reagent (0.50 vol%)	-20.5 ± 0.7	-22.2 ± 1.0	-30.0 ± 0.7	-30.4 ± 0.7
EDC/Sulfo-NHS reagent (0.75 vol%)	-17.4 ± 0.8	-20.6 ± 1.0	-27.4 ± 0.6	-27.8 ± 0.7
EDC/Sulfo-NHS reagent (1.00 vol%)	-16.5 ± 0.8	-19.7 ± 0.8	-26.6 ± 0.4	-26.9 ± 0.6
EDC/Sulfo-NHS reagent (1.50 vol%)	-15.7 ± 0.7	-18.7 ± 0.7	-25.4 ± 0.7	-25.8 ± 0.5
EDC/Sulfo-NHS reagent (2.00 vol%)	-14.4 ± 0.7	-17.3 ± 0.8	-23.1 ± 0.6	-23.3 ± 1.1
EDC/Sulfo-NHS reagent (3.00 vol%)	-10.0 ± 0.5	-16.0 ± 0.7	n/a	n/a

The increase in hydrodynamic diameters d_h and zeta potential ζ upon bioconjugation of GOx to AuNPs@P3KHT is consistent with published results about the bioconjugation of antibodies, peptides by EDC/NHS coupling.^{550,551} None of the hydrodynamic diameters d_h and none of the zeta potentials ζ decreased significantly in the fourth centrifugation step (Table 3-15 and Table 3-16), suggesting that most of the excessive GOx molecules were removed beforehand. In all subsequent bioconjugation experiments, one low (0.75 vol%) and one high (2.00 vol%) concentration of EDC/Sulfo-NHS reagent, further denoted as EDC/S-NHS_{low} (0.75 vol%) and EDC/S-NHS_{high} (2.00 vol%), and four centrifugation steps were applied.

I analyzed whether the bioconjugation with glucose oxidase had an impact on the colloidal properties of gold-polythiophene hybrid nanoparticles. The UV-vis absorption spectra and photographs of non-functionalized AuNPs@P3KHT and enzyme-functionalized AuNPs@P3KHT-GOx in Milli-Q water and different buffer solutions are depicted in Figure 3-36. The non-functionalized AuNPs@P3KHT were only stable in Milli-Q water (Figure 3-36a), while in all tested buffer solutions nanoparticle agglomeration occurred. This agglomeration was accompanied by a color change from red to purple-blue with decreasing color intensity⁴⁸¹⁻⁴⁸⁴ and a decrease of the SPR peak in the corresponding UV-vis absorption spectra (Figure 3-36b-d).^{499-502,53}

All enzyme-functionalized AuNPs@P3KHT-GOx were stable in water and every tested buffer. The dispersions retained their red color and their characteristic absorption properties dominated by the SPR band at about 550 nm, which is characteristic for colloidally stable gold nanoparticles with a size range of 70 nm to 80 nm.^{463,480} The increased colloidal stability of AuNPs@P3KHT by bioconjugation is consistent with results obtained for protein-functionalized gold nanoparticles.⁵⁵²⁻⁵⁵⁴ Studies showed that adsorption of proteins on AuNPs led to (electro)-steric stabilization due to the resulting protein corona, which lent the AuNPs enhanced colloidal stability even at high ionic strengths.⁵⁵³ According to this, the improved colloidal stability of AuNPs@P3KHT was probably caused by steric stabilization due to the covalently linked GOx molecules.

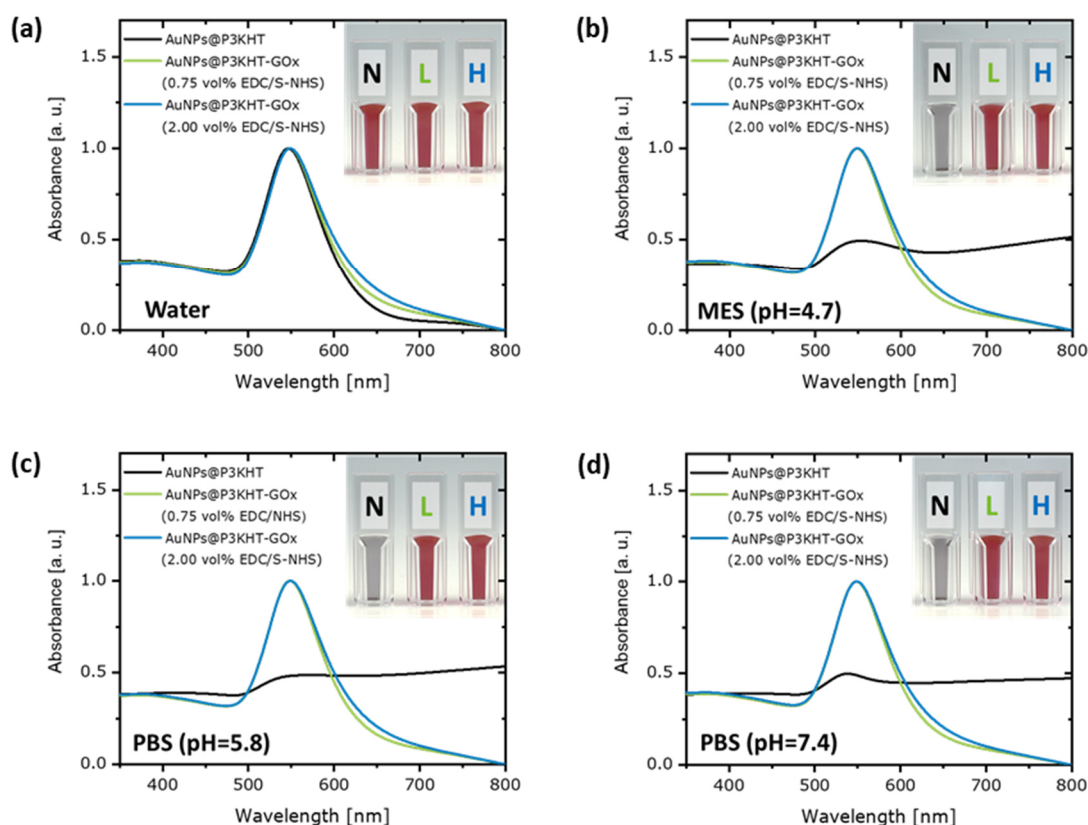


Figure 3-36: UV-vis absorption spectra and photographs of non-functionalized AuNPs@P3KHT and enzyme-functionalized AuNPs@P3KHT-GOx in (a) Milli-Q water, (b) MES buffer (0.1 M, pH=4.7), (c) PBS buffer (0.1 M, pH=5.8) and (d) PBS buffer (0.1 M, pH=7.4). Bioconjugation of glucose oxidase GOx was performed in solution using EDC/S-NHS_{low} (0.75 vol%) or EDC/S-NHS_{high} (2.00 vol%), respectively. (N) denotes non-functionalized AuNPs@P3KHT, (L) enzyme-functionalized AuNPs@P3KHT-GOx activated with EDC/S-NHS_{low} and (H) enzyme-functionalized AuNPs@P3KHT-GOx activated with EDC/S-NHS_{high}.

3.4.2 Structural analysis of bioconjugated gold-P3KHT hybrid nanoparticles

TEM was applied to analyze if the bioconjugation with GOx influenced the morphology of the biofunctionalizable gold-polythiophene hybrid nanoparticles. TEMs of enzyme-modified AuNPs@P3KHT-GOx are shown in Figure 3-37a and b. There were no distinct differences in the morphology of the gold nanoparticles after functionalization with GOx

(Figure 3-26b). The AuNPs@P3KHT-GOx were still quasi-spherical with a large variety of polyhedral shapes as illustrated in Figure 3-37a and b.

The average core diameter of AuNPs@P3KHT-GOx activated by EDC/S-NHS_{low} (0.75 vol%) was 71.3 nm determined by size analysis with enclosing circles of 300 AuNPs in TEMs (Figure 3-37c). Similar investigations of 289 AuNPs in TEMs revealed a mean diameter of 71.8 nm for AuNPs@P3KHT-GOx activated with EDC/S-NHS_{high} (2.00 vol%) as depicted in Figure 3-37d. In the range of experimental error, enzyme-functionalized AuNPs@P3KHT-GOx were similar in size to the native biofunctionalizable hybrid particles AuNPs@P3KHT ($d_o=73.3$ nm, Figure 3-26d in section 3.3.1). Thus, TEM characterization clearly showed that the bioconjugation of glucose oxidase to AuNPs@P3KHT did not affect the morphology and dimensions of the gold cores.

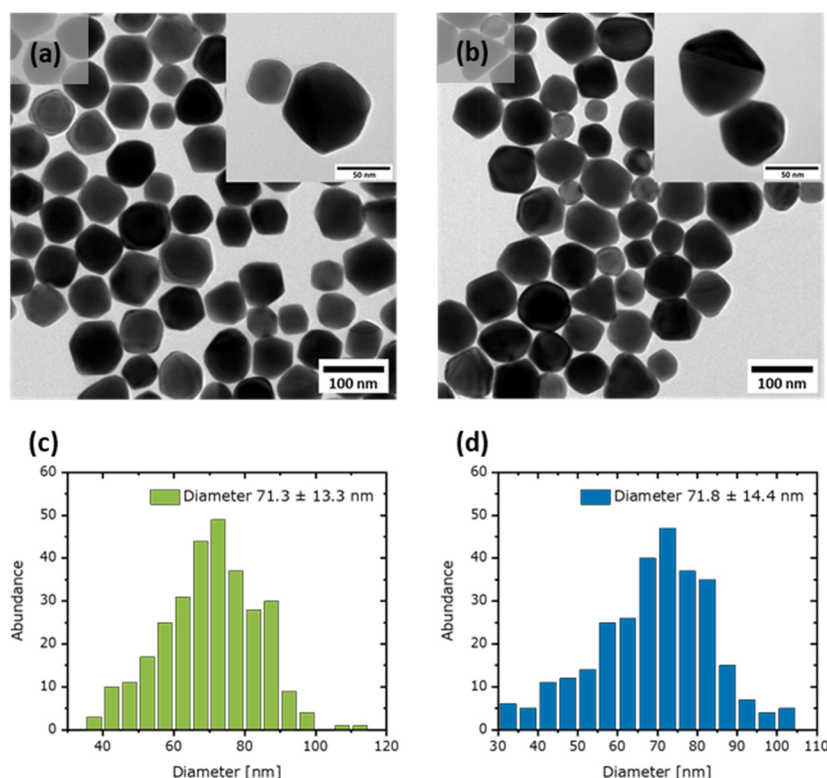


Figure 3-37: Transmission electron micrographs and particle size distribution from TEM analysis of enzyme-functionalized AuNPs@P3KHT-GOx (a, c) using EDC/S-NHS_{low} (0.75 vol%) and (b, d) using EDC/S-NHS_{high} (2.00 vol%) for bioconjugation. TEMs were taken after purification of the nanoparticle dispersions.

3.4.3 Characterization of bioconjugation in gold-P3KHT hybrids by Raman spectroscopy

Raman spectroscopy was employed to assess if amine-containing molecules can be covalently linked to AuNPs@P3KHT via amide bond formation during the bioconjugation process. Successful conjugation via EDC/NHS coupling should result in an amide signal in the Raman spectra of the functionalized gold-polythiophene hybrid nanoparticles. Many biomolecules contain amide bonds in their internal structure. In order to assess whether the observed amide bands in the Raman spectra are caused by the newly formed amide bonds upon bioconjugation or originate from the biomolecule itself, I used aminated PEG as a reference system (Figure 3-38). PEG-NH₂ was covalently attached to the AuNPs@P3KHT by surface and solution bioconjugation applying the same protocols as for the bioconjugation of glucose oxidase (section 6.2.3).

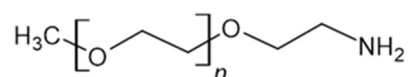


Figure 3-38: Molecular structure of aminated PEG (*O*-(2-Aminoethyl)-*O'*-methylpolyethylene glycol).

The Raman spectra of AuNPs@P3KHT-PEG-NH₂ functionalized with different methods are illustrated in Figure 3-39a. The range between 1600 cm⁻¹ to 1700 cm⁻¹ is of importance, since there the amide I bands should appear.^{555–559} The main contribution to the amide I mode is the C=O stretching and to a small extent also the N-H bending of the amide bond.^{555–557,559} Other known amide modes (II: 1500-1580 cm⁻¹, III: 1230-1300 cm⁻¹)^{556,559} overlap with the distinct Raman peaks of the polythiophene ligand shell (1000-1550 cm⁻¹) and may not be visible in the spectra. I focused my analysis on the amide I band region.

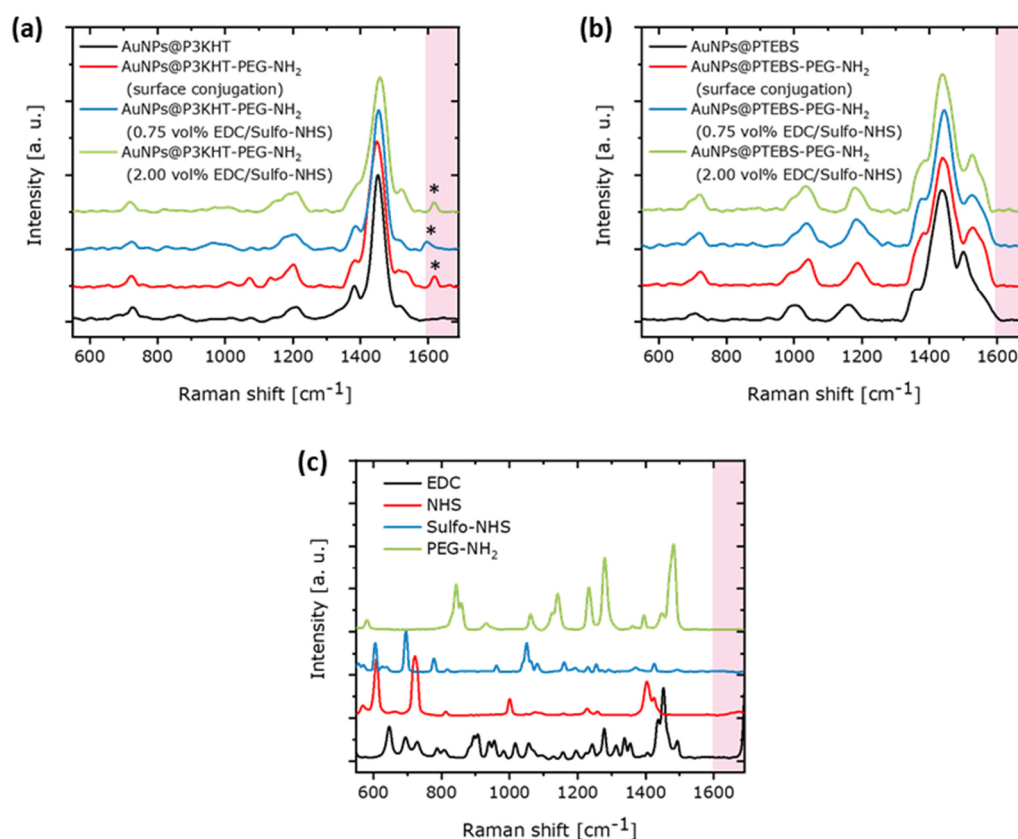


Figure 3-39: (a) Raman spectra of functionalized AuNPs@P3KHT-PEG-NH₂. Conjugation of aminated PEG was done after film deposition (surface conjugation) or in solution using EDC/S-NHS_{low} (0.75 vol%) or EDC/S-NHS_{high} (2.00 vol%). (b) Raman spectra of functionalized AuNPs@PTEBS-PEG-NH₂. Conjugation of aminated PEG was done after film deposition (surface conjugation) or in solution using EDC/S-NHS_{low} (0.75 vol%) or EDC/S-NHS_{high} (2.00 vol%). (c) Raman spectra of EDC, NHS, Sulfo-NHS and PEG-NH₂. The area (1600-1700 cm⁻¹) where amide bands can appear are highlighted in red and detected amide I modes are marked with *.

Small amide I mode peaks between 1610-1620 cm⁻¹ were visible in all Raman spectra of functionalized AuNPs@P3KHT-PEG-NH₂ (Figure 3-39a), which were not present in the Raman spectra of the original AuNPs@P3KHT and of the reactive compounds (EDC, (Sulfo-)NHS and PEG-NH₂, light red area in Figure 3-39c). These amides I mode peaks, indicated that the covalent linkage of PEG-NH₂ to AuNPs@P3KHT was realized via amide bond formation. Compared to the signals of the polythiophene ligand shell (intra-ring C-C and symmetric and asymmetric C=C stretch modes in the range of 1300 cm⁻¹ to 1550 cm⁻¹), the detected amide I peaks were small, suggesting that only little amounts of PEG-NH₂ were coupled to the AuNPs@P3KHT. This was probably based on

the low amount of terminal primary amine groups (loading ≥ 0.4 mmol/g) present in the PEG chains. It is also possible that only a fraction of the carboxylate groups in the polythiophene ligand shell were activated by EDC/NHS activation. Since there were no significant differences in the amide I peaks for samples activated by EDC/S-NHS_{low} (0.75 vol%) and EDC/S-NHS_{high} (2.00 vol%), I conclude that the amine loading of the PEG chains was the limiting factor.

Non-biofunctionalizable AuNPs@PTEBS were also functionalized with PEG-NH₂ using the same procedures as for AuNPs@P3KHT (section 6.2.3). The Raman spectra of functionalized AuNPs@PTEBS-PEG-NH₂ had no peaks in the amide I band region (light red area of Figure 3-39b), suggesting that there was no covalent conjugation of the aminated PEG chains to AuNPs@PTEBS. These results further supported the hypothesis that in case of the AuNPs@P3KHT-PEG-NH₂ the conjugation of the PEG chains was based on amide bond formation and not due to other unspecific adsorption mechanisms, which would be also present in AuNPs@PTEBS-PEG-NH₂.

The amide I peaks provide additional information about the conformational structure of free enzymes and proteins, which can be used to characterize their secondary structure.^{555–559} Structures with α -helix conformation result in amide I modes at about 1650 cm⁻¹, while β -sheet conformations possess amide I modes at about 1670 cm⁻¹.^{555–558} It should be noted that the amide I peaks of AuNPs@PTEBS-PEG-NH₂ were located at lower wavenumbers (1610–1620 cm⁻¹). Such blue-shifting of the amide peaks was also observed for dry powders of peptides, which can be attributed to stronger hydrogen bonds between adjacent amide groups in dry forms than in hydrated structures in solution.^{560,561} Since Raman spectra were recorded of dry AuNPs@P3KHT-PEG-NH₂ layers, similar effects likely caused the observed blue-shift of the detected amide I modes.

3.4.4 Electrical conductivity of bioconjugated gold-P3KHT hybrid nanoparticle films

AuNPs@P3KHT-GOx films prepared by surface and solution bioconjugation were analyzed regarding their electrical features. Surface bioconjugation is based on the

covalent attachment of GOx to dried AuNPs@P3KHT layers. Solution bioconjugation yielded enzyme-functionalized AuNPs@P3KHT-GOx dispersions, which were deposited on glass substrates by drop-casting to obtain appropriate hybrid films. All deposited films were line-shaped (experimental details in sections 6.2.3 and 6.2.4). I contacted these line patterns by silver paste and measured current-voltage (I - V) curves of four individual samples of each bioconjugation procedure (surface vs. solution bioconjugation). AuNPs@P3KHT-GOx films were directly conductive after deposition, independent of the bioconjugation method and the amount of EDC/NHS reagent (0.75 vol% and 2.00 vol%). The current was normalized to the film thickness and the appropriate linear average I - V curves are depicted in Figure 3-40a and c, indicating ohmic behavior (metal-like electrical conductivities).

Width and length of the line patterns were determined by optical transmission microscopy and thickness by confocal microscopy (sections 6.3.3 and 6.3.5). I used the detected geometrical dimension to calculate the material resistivity ρ according to equation 3-1 presented in section 3.1.2. The determined average material resistivity ρ of surface-bioconjugated AuNPs@P3KHT-GOx layers was $9.18 \cdot 10^{-6} \Omega\text{m} \pm 0.02 \cdot 10^{-6} \Omega\text{m}$ (mean \pm one standard deviation), two orders of magnitude above bulk gold ($2.35 \cdot 10^{-8} \Omega\text{m}$)¹⁶⁰ and only slightly above bare AuNPs@P3KHT ($8.84 \cdot 10^{-6} \Omega\text{m} \pm 0.11 \cdot 10^{-6} \Omega\text{m}$, section 3.3.4). The mean material resistivity ρ of AuNPs@P3KHT-GOx films obtained by solution bioconjugation of GOx was $9.30 \cdot 10^{-5} \Omega\text{m} \pm 0.05 \cdot 10^{-5} \Omega\text{m}$ using EDC/S-NHS_{low} (0.75 vol%) and $2.14 \cdot 10^{-4} \Omega\text{m} \pm 0.01 \cdot 10^{-4} \Omega\text{m}$ employing EDC/S-NHS_{high} (2.00 vol%).

I attributed the differences in material resistivity ρ to an increase in the inter-particle distances upon the bioconjugation of GOx. Glucose oxidase has dimensions of $60 \times 52 \times 77 \text{ \AA}^3$ and a hydrodynamic diameter of 8.9 nm.^{550,551} The GOx molecules act as insulating barriers between adjacent AuNPs in the hybrid films. In surface bioconjugation GOx molecules were only bioconjugated to AuNPs at or just below the surface of the films due to porosity, while the underlying bulk remained unaffected. Hence, the electrical conductivity was less affected than in films obtained by solution bioconjugation, where the entire bulk of the hybrid films was altered by the GOx molecules.

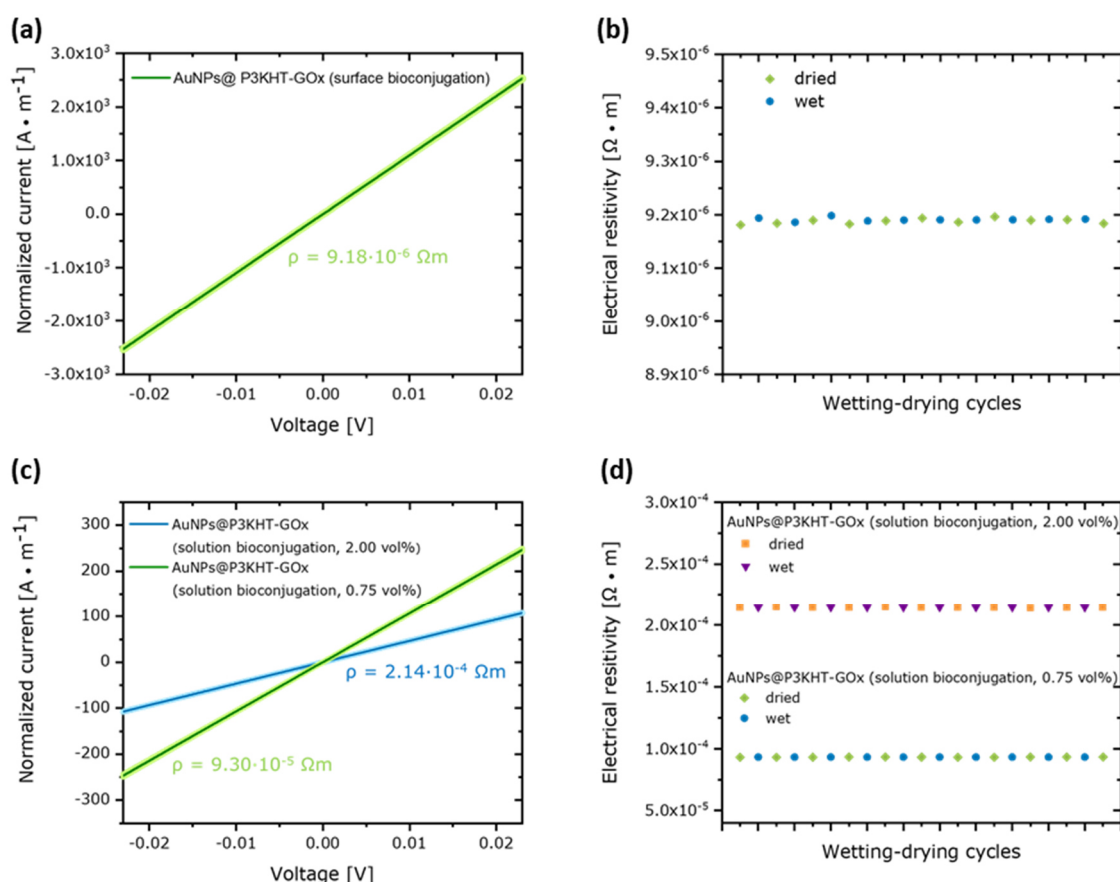


Figure 3-40: Average $I-V$ curves with normalized currents to film thicknesses and the corresponding error ranges (light blue and light green areas) of AuNPs@P3KHT-GOx films obtained by (a) surface bioconjugation after film deposition and (c) solution bioconjugation prior film deposition using EDC/S-NHS_{low} (0.75 vol%) or EDC/S-NHS_{high} (2.00 vol%). Material resistivity ρ upon ten wetting-drying cycles in Milli-Q water of AuNPs@P3KHT-GOx films prepared by (b) surface bioconjugation and (d) solution bioconjugation using EDC/S-NHS_{low} (0.75 vol%) or EDC/S-NHS_{high} (2.00 vol%). All experiments were conducted under ambient conditions.

The amount of bioconjugated GOx molecules determined the thickness of the insulating GOx shell and directly correlated with the concentrations of the EDC/Sulfo-NHS reagent. This was visible in the increase of hydrodynamic diameters d_h upon GOx bioconjugation (section 3.4.1) and in TGA results (Appendix A, Figure A-1c). I detected organic weight fractions of 4.8 wt% and 8.8 wt% for solution-bioconjugated AuNPs@P3KHT-GOx using EDC/S-NHS_{low} (0.75 vol%) or EDC/S-NHS_{high} (2.00 vol%), respectively. Thus, the results show that there is always a trade-off between electrical conductivity and bioactivity of the hybrid films, which can be tailored by the choice of bioconjugation

method (surface vs. solution) and the concentration of the EDC/Sulfo-NHS reagent. The biofunctionalizable gold-polythiophene hybrid nanoparticles AuNPs@P3KHT are suitable for electrodes, where bioactivity and electrical conductivity are required at the same time.

Since many biological applications are conducted in liquids, I investigated how AuNPs@P3KHT-GOx films behave under wet conditions, following the procedure described in section 3.3.4. I characterized four individual samples of AuNPs@P3KHT-GOx layers obtained by different bioconjugation procedures and monitored their average material resistivity ρ under dry and wet conditions. All films retained their electrical properties after ten wetting-drying cycles in Milli-Q water. Furthermore, I did not observe macroscopically or in SEM (Figure 3-41) any delamination or cracking of the hybrid layers within the ten wetting-drying cycles due to e.g. swelling of the GOx enzyme shell. SEMs also illustrate that the morphology and shape of the particles were unaffected by the repeated wetting and drying processes.

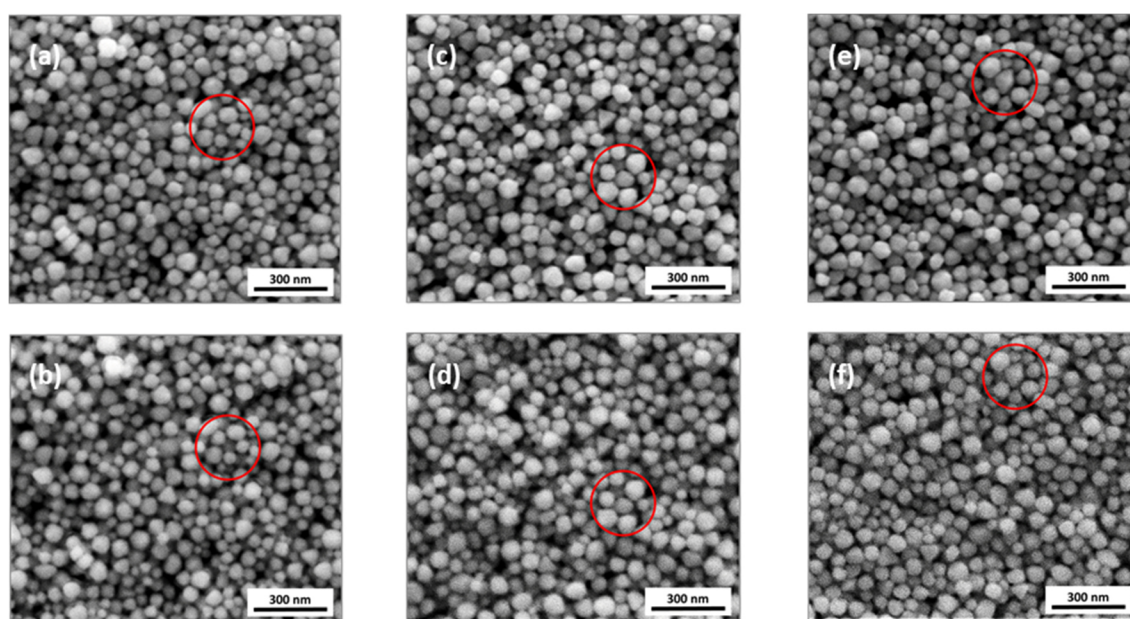


Figure 3-41: Scanning electron micrographs of enzyme-functionalized AuNPs@P3KHT-GOx (a, c, e) before and (b, d, f) after water exposure. The films in (a) and (b) were bioconjugated with GOx after film deposition. Layers presented in (c, d, e, f) consisted of AuNPs@P3KHT-GOx, which were bioconjugated in solution using (c, d) EDC/S-NHS_{low} (0.75 vol%) or (e, f) EDC/S-NHS_{high} (2.00 vol%). The SEMs were recorded at nearly identical positions of the films before and after water exposure. The red circles mark areas to illustrate that water exposure caused no significant structural changes in the layer morphology.

3.4.5 Enzymatic activity of bioconjugated gold-P3KHT hybrid nanoparticles

Immobilization and encapsulation can reduce the enzymatic activity of glucose oxidase.^{562–568} I tested whether the covalent linkage of glucose oxidase to AuNPs impacts the catalytic activity of the enzyme in colorimetric bioassays. The dye 2,2'-azino-bis(3-ethylbenzothiazoline-6-sulfonic acid) (ABTS) is sensitive to hydrogen peroxide (H₂O₂), a byproduct in the enzymatic oxidation of glucose by GOx (equation 3-2). With the catalytic aid of horseradish peroxidase (HRP) the colorless ABTS reacts with H₂O₂, yielding an ABTS^{•+} radical possessing a significant blue-green color (equation 3-3). The formation of the ABTS^{•+} radical directly correlates with the concentration of glucose and can be monitored by UV-vis spectroscopy.

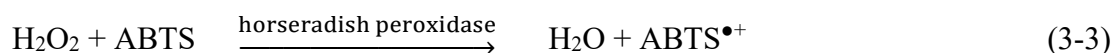
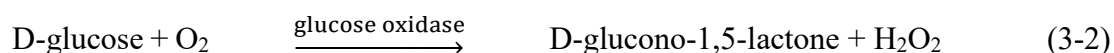


Figure 3-42a illustrates the absorption maximum of reduced ABTS at about 340 nm^{569,570} and the characteristic absorption peaks of the stable ABTS^{•+} radical at 415, 635 and 734 nm.^{569,569,571} The absorption of the ABTS^{•+} radical at about 415 nm is usually chosen to monitor the oxidation of ABTS and to correlate this to the glucose concentration.^{570,572} Figure 3-42a clearly illustrates that the plasmonic absorption maxima of AuNPs@P3KHT-GOx at 550 nm do not interfere with the ABTS/ABTS^{•+} radical absorption signals, enabling the usage of AuNPs@-GOx in colorimetric bioassays. The reaction scheme of a bioassay with incorporated AuNPs@P3KHT-GOx is illustrated in Figure 3-42b. I used the appropriate diammonium salt of ABTS for all my bioassay experiments. UV-vis absorption spectra of bioassays at different time points after glucose addition are shown in Appendix D (Figure D-1). The presence of the AuNPs@P3KHT-GOx did not inhibit the monitoring of the ABTS^{•+} radical formation, since the absorption of ABTS/ABTS^{•+} radical was much stronger than the gold plasmon band. The overall absorption increase at 415 nm was much faster and more pronounced for AuNPs@P3KHT-GOx activated with EDC/S-NHS_{high} (2.00 vol%) (Appendix D, Figure D-1a and b). This corresponds to a faster oxidation of glucose due to the enhanced number

of bioconjugated GOx molecules. Photographs of bioassays containing AuNPs@P3KHT-GOx at different time points after glucose addition (Appendix D, Figure D-1c), illustrate a gradual color change from pinkish-red to blue-green upon proceeding glucose oxidation and ABTS^{•+} radical formation.

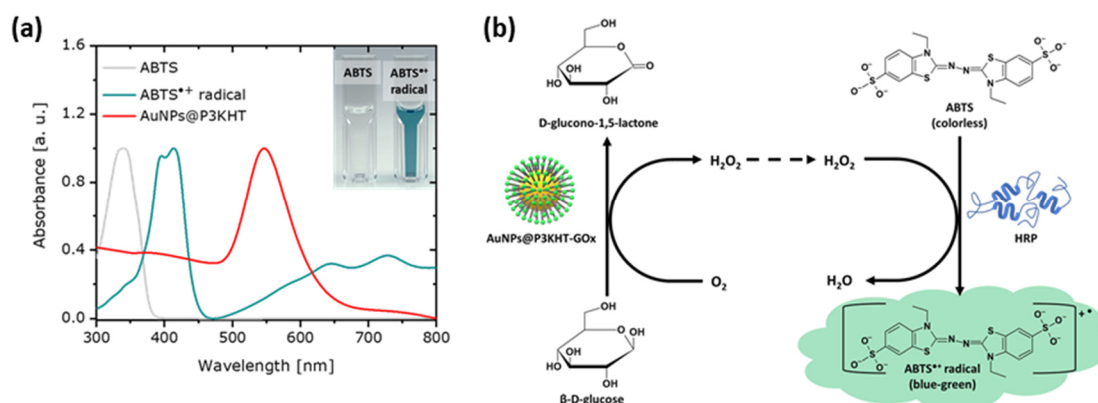


Figure 3-42: (a) UV-vis absorption spectra of ABTS, ABTS^{•+} radical and AuNPs@P3KHT. The photograph illustrates the transition from the colorless ABTS to the blue-green ABTS^{•+} radical upon enzymatic oxidation. (b) Reaction scheme of a glucose bioassay with AuNPs@P3KHT-GOx replacing the free enzyme GOx in the first reaction step.

I performed calibration studies of bioassays with different gold concentrations to determine optimal working conditions. The results are presented in Table 3-17. Important parameters determining the quality of a colorimetric glucose bioassay are the liner range, in which the colorimetric signal is proportional to the glucose concentration and the sensitivity S . For biological sensors and assays, the sensitivity S is usually defined by the slope of the calibration line.^{573–577} For all tested bioassays, I applied a reaction time of 10 min after which the colorimetric signal was detected. The chosen time range corresponds to the reaction times of most commercial colorimetric glucose assays, which require, depending on the system, reaction times between 10 min to 30 min.^{578–580} The best working conditions (comparable broad linear ranges and good sensitivity) for both types of bioconjugated AuNPs@P3KHT-GOx (EDC/S-NHS_{low} and EDC/S-NHS_{high}) were achieved in colorimetric assays containing gold concentrations of 12.5 $\mu\text{g}\cdot\text{mL}^{-1}$ (Table 3-17). The results for these bioassays are depicted in Figure 3-43. The data of the other bioassays with different gold concentrations are given in Appendix D (Figure D-2). The calibration studies revealed that at a given gold concentration, AuNPs@P3KHT-GOx

activated by EDC/S-NHS_{high} (2.00 vol%) yielded higher assay sensitivities, indicating faster glucose conversion (Table 3-17). This effect correlates with the increased number of bioconjugated GOx molecules with increasing concentration of EDC/S-NHS reagent.

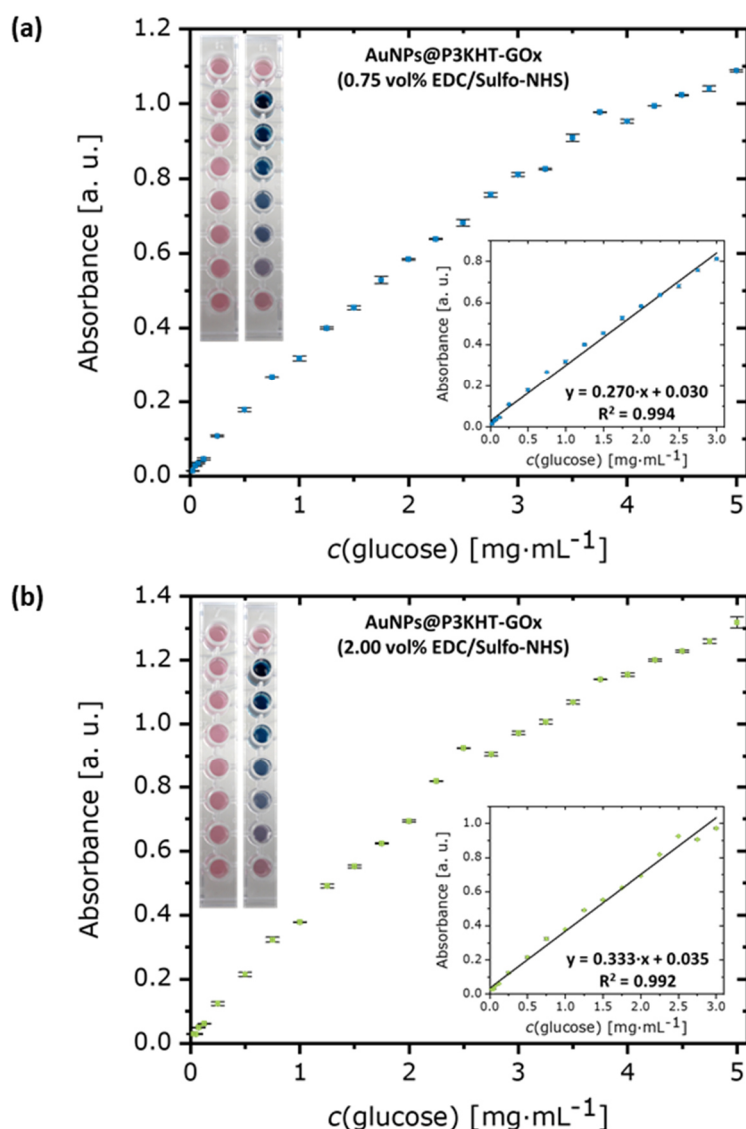


Figure 3-43: Absorption intensities at 415 nm for different glucose concentrations in bioassays based on AuNPs@P3KHT-GOx ($c[\text{Au}] = 12.5 \mu\text{g} \cdot \text{mL}^{-1}$). The insets show calibration curves in the linear range where the absorption signal is proportional to the glucose concentration. Error bars are the standard deviation (mean \pm standard deviation) of three individual measurements for each glucose concentration. The photographs show the colorimetric assays based on AuNPs@P3KHT-GOx before (left) and after 10 min of glucose addition (right) for different glucose concentrations (up to down: blank, $2 \text{ mg} \cdot \text{mL}^{-1}$, $1 \text{ mg} \cdot \text{mL}^{-1}$, $0.5 \text{ mg} \cdot \text{mL}^{-1}$, $0.25 \text{ mg} \cdot \text{mL}^{-1}$, $0.125 \text{ mg} \cdot \text{mL}^{-1}$, $75 \mu\text{g} \cdot \text{mL}^{-1}$, $25 \mu\text{g} \cdot \text{mL}^{-1}$). The data belong to bioassays with AuNPs@P3KHT-GOx activated by (a) EDC/S-NHS_{low} (0.75 vol%) and (b) EDC/S-NHS_{high} (2.00 vol%).

Table 3-17: Linear ranges and sensitivities S (defined as slope of calibration line^{578–580}) of colorimetric glucose bioassays with different gold concentrations. The assays contained AuNPs@P3KHT-GOx, which were bioconjugated in solution using EDC/S-NHS_{low} (0.75 vol%) or EDC/S-NHS_{high} (2.00 vol%).

	AuNPs@P3KHT-GOx EDC/S-NHS _{low} (0.75 vol%)		AuNPs@P3KHT-GOx EDC/S-NHS _{high} (2.00 vol%)	
$c(\text{Au})$	Linear range [mg·mL ⁻¹]	Sensitivity S [mL·mg ⁻¹]	Linear range [mg·mL ⁻¹]	Sensitivity S [mL·mg ⁻¹]
5 µg·mL ⁻¹	0.025-5.00	0.110	0.025-3.50	0.155
12.5 µg·mL ⁻¹	0.025-3.00	0.270	0.025-3.00	0.333
25 µg·mL ⁻¹	0.025-2.75	0.454	0.025-2.25	0.627
50 µg·mL ⁻¹	0.025-1.75	0.959	0.025-1.00	1.480

IUPAC defines the limit of detection (LOD) as the smallest concentration or quantity of an analyte that can be detected with sufficient reliability.^{581,582} I used a method introduced by Demchenko (equation 3-4),⁵⁸³ which is often employed to determine the LOD of colorimetric glucose sensors.^{584–588}

$$c_{\text{LOD}} = \frac{3 \cdot S_{\text{BL}}}{S} \quad (3-4)$$

S_{BL} is the standard deviation of the blank value and S the sensitivity defined by the slope of the calibration line. The LOD was 32 µM (5.8 µg·mL⁻¹) for AuNPs@P3KHT-GOx activated by EDC/S-NHS_{low} (0.75 vol%) and 15 µM (2.7 µg·mL⁻¹) for AuNPs@P3KHT-GOx activated by EDC/S-NHS_{high} (2.00 vol%). Table 3-18 lists characteristics of published colorimetric sensors for glucose detection, where the enzymes GOx or HRP were immobilized, encapsulated or covalently linked to an inorganic biosensing material. Bioassays composed of enzyme-functionalized AuNPs@P3KHT-GOx possessed comparable or even lower LOD levels than the reported systems. Additionally, the colorimetric bioassays of this work showed linearity over a wider glucose range. Furthermore, the LOD of a commercial colorimetric glucose assay containing free non-bioconjugated GOx molecules in solution is more than 7 times higher (LOD=110 µM) than the LOD of bioassays based on AuNPs@P3KHT-GOx. This indicates that the attachment of GOx to AuNPs can enhance the sensitivity of the enzymatic glucose detection beyond those of commercial assay kits.

It should be noted, that today's research focuses on further lowering LOD levels for the colorimetric detection of glucose by replacing HRP with nanoparticles mimicking enzyme-activity.^{589–591} These nanoenzymes often show an improved enzymatic performance compared to natural enzymes.⁵⁹² Hence, such nanoenzyme-based bioassays will always be superior to the AuNPs@P3KHT-GOx assays introduced in this work.

Table 3-18: Limit of detection (LOD) levels of different colorimetric glucose sensors, where the enzymes glucose oxidase (GOx) or horseradish peroxidase (HRP) were immobilized, entrapped or covalently linked to an inorganic supporting material. *Immobilization in these reports describes physisorption of enzymes due to weak interactions such as hydrogen bonds or van der Waals interactions, as well as ionic bonds.^{593–595} †Entrapment/Encapsulation defines the confinement of enzymes in polymer matrices, fiber networks or porous materials.^{593–595} In addition, the equivalent data of a commercial glucose assay kit (Sigma Aldrich) is shown.

Supporting material	Type of enzyme binding	Linear range [μM]	LOD [μM]	Reference
AuNPs	Immobilization	400-80000	400	596
Magnetic cellulose nanocrystals	Immobilization	250-2500	83	597
Magnetic nanoparticles	Immobilization	500-3500	50	598
Mesoporous silica	Entrapping	832-13877	416	599
Cu-hemin metal-organic frameworks	Entrapping	30-800	10	600
Graphene oxide/MnO ₂	Covalent binding	1388-16652	172	601
Au nanostars	Covalent binding	200-1800	40	602
AuNPs@P3KHT-GOx (0.75 vol% EDC/S-NHS)	Covalent binding	139-16700	32	This work
AuNPs@P3KHT-GOx (2.00 vol% EDC/S-NHS)	Covalent binding	139-16700	15	This work
commercial colorimetric glucose assay (Sigma Aldrich)		1-10000	110	603

The enzyme activity of the AuNPs@P3KHT-GOx could be ascertained using colorimetric assays with optimized conditions ($c[\text{Au}] = 12.5 \mu\text{g}\cdot\text{mL}^{-1}$ and linear range $25 \mu\text{g}\cdot\text{mL}^{-1}$ to $3.0 \text{ mg}\cdot\text{mL}^{-1}$). Determination of the enzymatic activity of glucose oxidase using colorimetric ABTS bioassays is possible, since the co-enzyme HRP involved in the enzymatic cascade reaction has faster reaction rates and much higher substrate turnover rates.^{536,604,605} Hence, the glucose oxidation by GOx is the rate limiting enzymatic reaction and the overall reaction kinetics in the bioassay is mainly determined by the GOx reaction rate. As a reference, I determined the enzymatic activity of free GOx in solution by

varying the glucose concentration at constant ABTS, HRP and GOx concentrations. I estimated the reaction velocity v_0 by the change in the absorption signal at 415 nm over time. The reaction kinetics of free GOx revealed a typical Michaelis-Menten behavior^{606–609} (Figure 3-44a), where the reaction velocity constantly increased until a plateau at a maximal reaction velocity v_{\max} was reached. This plateau indicates the saturation of the catalytic sites of GOx or the complete consumption of glucose in the solution.^{536,610}

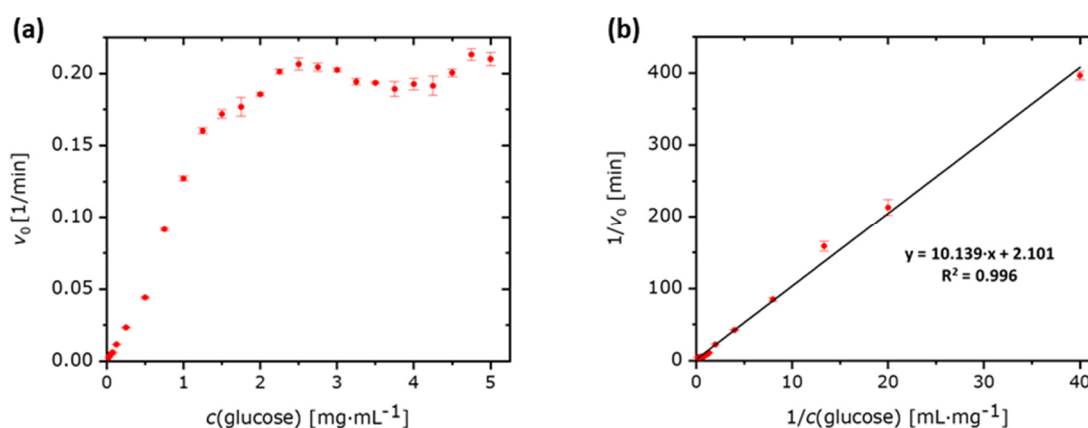


Figure 3-44: (a) Reaction rate v_0 against glucose concentration of free glucose oxidase. (b) Lineweaver–Burk plot of free GOx in PBS buffer (0.1 M, pH 5.8). Error bars in (a) and (b) are standard deviation (mean \pm standard deviation) obtained of three individual measurements. Data were collected from colorimetric bioassays containing GOx, HRP and ABTS in PBS buffer (0.1 M, pH 5.8).

The two most important kinetic parameters in the Michaelis-Menten model are the Michaelis-Menten constant K_m and the maximal reaction velocity v_{\max} . Small values of K_m suggest high binding affinity between substrate and enzyme, leading to faster reactions reaching v_{\max} at lower substrate concentrations.^{608,609} Both parameters (K_m and v_{\max}) can be determined by converting the data of Figure 3-44a to a double reciprocal plot, yielding a linear Lineweaver–Burk plot (Figure 3-44b). This plot depends on substrate concentration $[S]$ and can be fitted by a linear version of the Michaelis-Menten equation.^{608,611}

$$\frac{1}{v_0} = \frac{K_m}{v_{\max} \cdot [S]} + \frac{1}{v_{\max}} \quad (3-5)$$

Figure 3-44b indicates a K_m value of 26.8 mM (4.8 mg·mL⁻¹) for the free GOx enzyme, consistent with reported K_m values of 25 mM to 27 mM for pure glucose oxidase in

solution.^{612–614} The same glucose assays with AuNPs@P3KHT-GOx showed similar Michaelis-Menten behavior (Figure 3-45a). The corresponding Lineweaver–Burk plots (Figure 3-45b) suggested K_m values of 17.8 mM (3.2 mg·mL⁻¹) for AuNPs@P3KHT-GOx bioconjugated with EDC/S-NHS_{low} (0.75 vol%) and 14.8 mM (2.7 mg·mL⁻¹) for AuNPs@P3KHT-GOx bioconjugated with EDC/S-NHS_{high} (2.00 vol%). The K_m constant correlated with the density of bioconjugated GOx molecules which is proportional to the concentration of the EDC/Sulfo-NHS reagent. The lower K_m values indicated a higher enzymatic affinity of AuNPs@P3KHT-GOx towards glucose than free GOx.

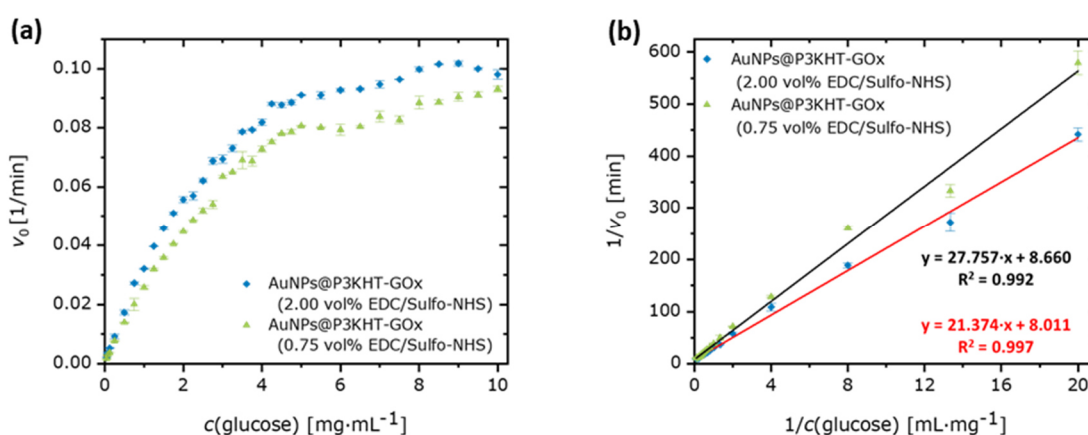


Figure 3-45: (a) Reaction rate v_0 against glucose concentration of enzyme-functionalized AuNPs@P3KHT-GOx. Bioconjugation was done in solution using EDC/S-NHS_{low} (0.75 vol%) or EDC/S-NHS_{high} (2.00 vol%), respectively. (b) Lineweaver–Burk plot of AuNPs@P3KHT-GOx in PBS (0.1 M, pH 5.8). Error bars in (a) and (b) are standard deviation (mean \pm standard deviation) obtained of three individual measurements.

The conformation of enzymes, can affect their enzymatic activity. It is possible that in certain conformations the active sides of the enzymes are masked, making them inaccessible for the substrate and limiting the overall enzymatic activity. It is likely that attached GOx molecules on gold-polythiophene hybrid nanoparticles spread over the whole particle surface, creating a more open structure that reveals the active sides.^{615–617} This conformational change upon bioconjugation could cause the observed increase in enzyme activity for AuNPs@P3KHT-GOx. In addition, several studies showed that the attachment of enzymes to small nanoparticles can reduce the diffusional resistance, enhancing the transport of the substrate to the active sites.^{618,619}

According to literature, immobilization and encapsulation of glucose oxidase often lead to loss in enzymatic activity and an increased Michaelis Menten constant K_m .^{562–568} This originates from a reduced conformational flexibility of GOx molecules upon attachment to a support material, reducing the accessibility of the active sides of the enzymes. The enhancement in enzymatic activity observed for AuNPs@P3KHT-GOx is a rare phenomenon. Table 3-19 compares the enzymatic properties of AuNPs@P3KHT-GOx with various other nano- or micro-materials containing GOx in immobilized, encapsulated or covalently bound form. At an enhancement in enzymatic activity of up to 44.8%, the AuNPs@P3KHT-GOx developed in this work are among the materials with the largest activity improvement compared to free GOx. Only glucose oxidase immobilized on CoFe₂O₄/SiO₂ nanoparticles reported by Wang *et al.* showed a slightly larger increase (+46.1%) in enzymatic activity.⁶¹⁸

I further investigated how long the AuNPs@P3KHT-GOx preserved their enzymatic activity upon storage in a refrigerator (4 °C) by analyzing the colorimetric signal for a defined glucose concentration (1 mg·mL⁻¹). Figure 3-46a and b indicate no significant decrease in enzymatic activity over a time period of six months, since the detected absorption signal at 415 nm remained nearly constant. AuNPs@P3KHT-GOx activated by EDC/S-NHS_{low} (0.75 vol%) retained over 99% and AuNPs@P3KHT-GOx activated by EDC/S-NHS_{high} (2.00 vol%) over 95% of their initial activity. The data suggest a shelf life of at least 6 months, consistent with published data on GOx-functionalized AuNPs.⁶²⁰

Figure 3-46c and d reveal no distinct differences in the absorption behavior of the bioassays containing different batches of AuNPs@P3KHT-GOx. Hence, the developed bioconjugation process is highly reproducible, yielding AuNPs@P3KHT-GOx with similar enzymatic activities after each bioconjugation. Additionally, the results demonstrated that the designed bioassay composed of AuNPs@P3KHT-GOx, ABTS and HRP is also resistant against experimental errors, providing reliable and reproducible glucose detection. Furthermore, I characterized the selectivity of the developed colorimetric assay by analyzing the colorimetric signal at 415 nm caused by different sugars (fructose, maltose, sucrose). Figure 3-46e and f clearly show that other sugars led to one order of magnitude lower absorption signals than glucose, suggesting high selectivity of the bioassays containing AuNPs@P3KHT-GOx towards glucose. Glucose

oxidase is also able to oxidize other saccharides, but with much slower speed compared to glucose.^{621–625} For that reason, the other sugars also generated small absorption signals.

Table 3-19: Michaelis Menten K_m constants of free GOx and nano- or micro-materials containing GOx in immobilized, encapsulated or covalently bound form. The relative change in enzyme activity upon binding is also added. All K_m values were obtained by colorimetric glucose detection. *Immobilization in these reports describes physisorption of enzymes due to weak interactions such as hydrogen bonds or van der Waals interactions, as well as ionic bonds.^{593–595} †Entrapment/Encapsulation defines the confinement of enzymes in polymer matrices, fiber networks or porous materials.^{593–595}

Supporting material	Type of enzyme binding	K_m [mM]		Change in enzymatic activity upon binding	Reference
		free	bound		
Carbon nanoparticles (CNPs)	Immobilization*	13	42	-223%	605
CoFe ₂ O ₄ nanoparticles	Immobilization*	28	50.05	-79%	564
Graphene oxide	Immobilization*	22.55	27.19	-20.6%	626
Calcium phosphate (CaP) nanoparticles	Immobilization*	34.22	35.51	-3.8%	562
Au@PDA@CaP core shell nanoparticles	Immobilization*	34.22	34.23	-0.03%	562
Magnetic cellulose nanocrystals (CNCs)	Immobilization*	9.03	6.38	+29.3%	597
Metal-organic frameworks (MIL-125)	Immobilization*	22.352	14.93	+33.2%	627
CoFe ₂ O ₄ /SiO ₂ nanoparticles	Immobilization*	27.1	14.6	+46.1%	618
Tragacanth gel capsules	Encapsulation†	9	12.375	-37.5%	628
Poly(St-GMA-NaSS) microspheres	Covalent binding	21.35	29.98	-40.4%	565
Ni-Co ferrite/SiO ₂ nanocomposites	Covalent binding	45.28	58.29	-28.7%	563
Fe ₃ O ₄ nanoparticles	Covalent binding	6.2	6.8	-9.7%	629
AuNPs	Covalent binding	5.85	3.74	+36.1%	620
AuNPs@P3KHT-GOx (0.75 vol% EDC/S-NHS)	Covalent binding	26.8	17.8	+33.6%	This work
AuNPs@P3KHT-GOx (2.00 vol% EDC/S-NHS)	Covalent binding	26.8	14.8	+44.8%	This work

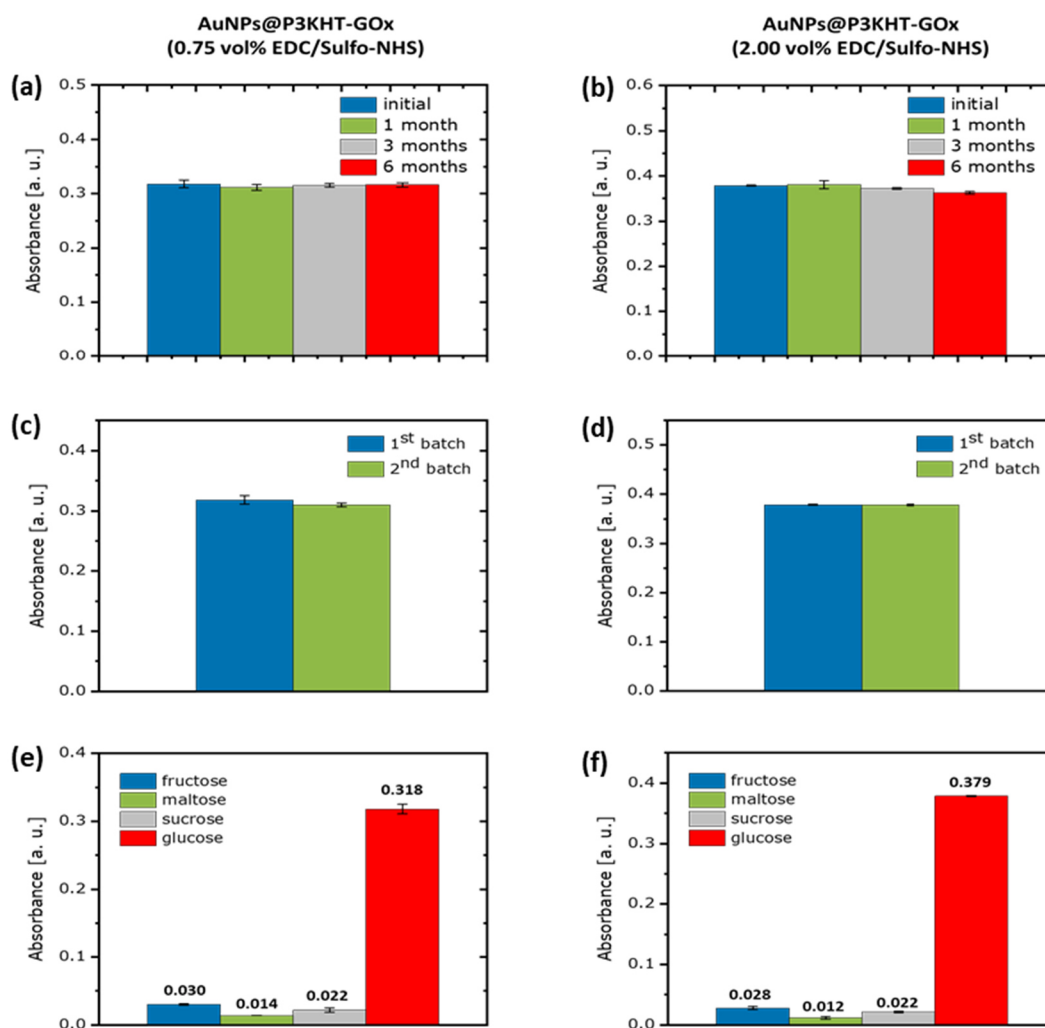


Figure 3-46: (a, b) Optical absorption at 415 nm caused by 1 mg·mL⁻¹ glucose in bioassays containing AuNPs@P3KHT-GOx samples, which were stored at 4 °C for one, two and six months. (c, d) Optical absorption at 415 nm caused by 1 mg·mL⁻¹ glucose in bioassays containing two different batches of enzyme-functionalized AuNPs@P3KHT-GOx. (e, f) Optical absorption at 415 nm caused by different sugars in colorimetric bioassays containing AuNPs@P3KHT-GOx. The concentration of the sugars was 1 mg·mL⁻¹. Bioconjugation of GOx molecules to AuNPs@P3KHT was performed in solution using (a, c, e) EDC/S-NHS_{low} (0.75 vol%) and (b, d, f) EDC/S-NHS_{high} (2.00 vol%). Error bars illustrate standard deviation (mean ± standard deviation) obtained by three individual measurements. All measurements were performed 10 min after the addition of the sugars.

Colorimetric glucose bioassays containing non-biofunctionalizable gold-polythiophene hybrid nanoparticles (AuNPs@PTEBS-GOx and AuNPs@PEDOT:PSS-GOx) yielded absorption signals at 415 nm, which were two orders of magnitude lower than those of bioassays containing AuNPs@P3KHT-GOx (Appendix D, Figure D-3c). The UV-vis spectra of these bioassays showed no absorption signals of $\text{ABTS}^{\bullet+}$ radicals, indicating that no GOx molecules were present and no glucose oxidation occurred (Appendix D, Figure D-3a and b). This is consistent with Raman data (section 3.4.3), revealing that bioconjugation of GOx is not possible for non-biofunctionalizable AuNPs@PTEBS and AuNPs@PEDOT:PSS, that lack active carboxylate groups.

In conclusion, this section revealed that bioconjugation of glucose oxidase to AuNPs@P3KHT enhanced its enzymatic activity up to 44%. Colorimetric bioassays containing bioconjugated AuNPs@P3KHT possessed low LODs down to 15 μM and broad linear ranges. Additionally, the bioconjugated AuNPs@P3KHT-GOx also had a long shelf life of at least six months and high selectivity towards glucose. Furthermore, the developed bioconjugation process yielded AuNPs@P3KHT-GOx with reproducible enzymatic activity.

3.4.6 Electrochemical glucose sensing using bioconjugated gold-P3KHT hybrids

AuNPs@P3KHT-GOx combine good electrical conductivity with biofunctionality, which make them suitable for electrical biosensors. I fabricated flexible amperometric glucose sensors by inkjet printing on PET foils. The working electrodes (WEs) were prepared by printing inks based on enzyme-functionalized AuNPs@P3KHT-GOx or non-functionalized AuNPs@P3KHT. In the latter case, enzyme-functionalization of the WEs was performed after inkjet printing (surface bioconjugation). The reference (REs) and counter electrodes (CEs) of the amperometric biosensors were obtained by inkjet printing of a commercial silver nanoparticle ink SicrysTM I40DM-106 (PV Nano Cell Ltd, Israel), consistent with several studies reporting inkjet-printed silver pseudo-reference electrodes.^{630–633} Experimental details are given in the sections 6.2.3 and 6.2.5, respectively. I adapted the design of reported inkjet-printed biosensors, which contain a

circular active part of the WE.^{630–634} For financial reasons, I decided to print only the active area of the WE using hybrid gold nanoparticle inks. A scheme of the biosensor is shown in Figure 3-48.

Successful inkjet printing requires inks with stable drop formation and good jettability.⁶³⁵ Escudero *et al.* fabricated electrical circuits by inkjet printing of inks containing gold-polythiophene hybrid nanoparticles (AuNPs@PEDOT:PSS),⁶³⁶ similar to the biofunctionalizable AuNPs@P3KHT introduced in this work. They used a PiXDRO LP50 inkjet printer operating with the a Dimatix Material Cartridge printhead (drop volume 10 pL, nozzle diameter 21.5 μm) and reported an Ohnesorge number of 0.24 (Z value of 4.17, Z = inverse Ohnesorge number) for inks composed of AuNPs@PEDOT:PSS, indicating stable drop formation during inkjet printing, since stable drop formation requires a Z value between 1 and 10.⁶³⁷ I used the same printing setup as Escudero *et al.* and concluded that their results are also valid for aqueous inks containing AuNPs@P3KHT-GOx or AuNPs@P3KHT, suggesting their suitability for inkjet printing. Optimized printing waveforms (section 6.2.5) led to single drop formation for inks containing AuNPs@P3KHT-GOx and AuNPs@P3KHT as presented in sequences of stroboscopic images in Appendix E (Figure E-1). The absence of satellite drops in these stroboscopic images indicated good printability of inks based on biofunctionalizable gold-polythiophene hybrid nanoparticles. Figure 3-47a and b show the final inkjet-printed biosensors on flexible PET foils, providing them with good bendability. The dimensions of the biosensor were 2 cm x 1 cm with a WE diameter of 3mm and widths of the RE and CE being 1 mm.

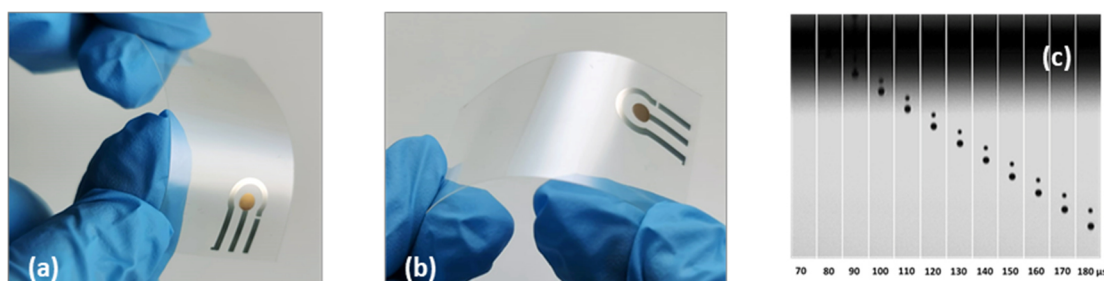


Figure 3-47: (a, b) Photographs of inkjet-printed amperometric biosensors on flexible PET foils. (c) Sequence of stroboscopic images illustrating drop ejection and satellite drop formation of inks containing enzyme-functionalized hybrid nanoparticles AuNPs@P3KHT-GOx.

Scanning electron micrographs of the different parts of the amperometric biosensors are illustrated in Figure 3-48. The SEMs revealed that the printed silver structures of the WE, RE and CE possessed wavy edges from the coalescence of liquid drops during inkjet printing. These types of printing defects are called “scalloped” edges/structures. In contrast to classical graphics printing, the printing of conductive patterns requires continuous structures.^{104,638,639} This can be achieved if adjacent drops overlap and coalesce, which leads to the formation of a continuous liquid film.^{104,638,639} If the drop spacing (distance between centers of two neighboring drops) exceeds the drop diameter, there is no overlap of the adjacent drops and the printed structure consists of isolated drops.^{104,638–640} At drop spacings which are slightly smaller than the drop diameter, the drops start to merge and “scalloped” structures are produced.^{104,638–640} By further decreasing the drop spacing, patterns with straight edges can be achieved.^{104,638–640} The drop spacing is defined by the given dpi (dots per inch) during the printing process. The higher the dpi number, the smaller the drop spacing. Additionally, the printing speed has also an impact on the printed pattern.^{638,639}

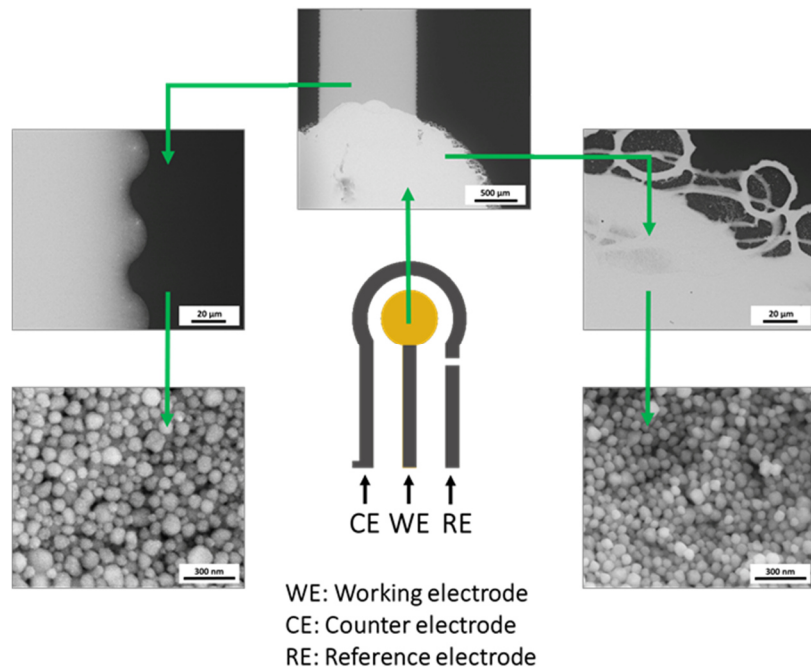


Figure 3-48: Scheme of the biosensor design and scanning electron micrographs (SEMs) of the inkjet-printed WE containing enzyme-functionalized hybrid nanoparticles AuNPs@P3KHT-GOx and of the inkjet-printed RE/CE composed of commercial silver ink. The sensor was printed on PET foil.

I tried to minimize “scalloped” edges of the printed silver structures by adjusting printing speed and dpi settings and by manipulating the wetting via plasma treating the PET substrate with oxygen plasma or argon plasma before inkjet printing. The SEMs in Figure 3-48 illustrate the biosensors with the least printing defects, which still possessed “scalloped” edges of the printed silver structures. Since I was able to fabricate defect-free silver structures with flat parallel edges on glass substrates using the same printing parameters and ink, I assumed that the interactions between the PET substrate and the commercial silver ink were the main reasons for the “scalloped” structures.

Optical micrographs (Appendix E, Figure E-2) revealed small gold-colored circular splashes around the inkjet-printed gold WE. Scanning electron micrographs (Figure 3-48) resolved these structures as circles with diameters of 30 μm to 50 μm , which likely formed during drying of the hybrid nanoparticle ink due to coffee ring effects. These circular features probably originated from satellite drops, that do not merge with the leading drop or travel in different angle from the leading drop. Optimized waveforms reduced satellite drops, but they occurred occasionally as depicted in Figure 3-47c. I optimized the utilized waveforms for printing at the beginning of each printing session. Changes in ambient temperature and humidity during printing can affect the rheological properties of the hybrid nanoparticle inks, causing satellite drop formation. Hence, continuous readjustment of the waveforms during printing sessions could help to eliminate satellite drops. Since the observed circular features due to satellite drops were sparse and did not form connecting pathways between the individual electrodes, they had no impact on the functionality of the inkjet-printed biosensors. SEMs (Figure 3-48) also revealed that the inkjet-printed biosensors were composed of individual silver nanoparticles (RE, CE and parts of WE) or gold nanoparticles (circular part of WE), respectively. No distinct neck formation between adjacent nanoparticles was visible, illustrating that sintering (150 $^{\circ}\text{C}$ for 30 min, section 6.2.5) of the printed silver structures mainly removed the insulating ligand shell and did not cause merging of the AgNPs.

I characterized the inkjet-printed biosensors containing enzyme-functionalized AuNPs@P3KHT-GOx regarding their suitability for electrochemical glucose detection. The detected output signal in amperometric sensors is the current between the working (WE) and counter electrode (CE).^{641–643} I used chronoamperometry, where a constant

square-wave potential is applied to the WE and the resulting current is detected over time.^{644,645} To ensure a stable potential, no or only small amounts of current flow through the RE.^{643,646} In amperometric biosensors the current is generated by the electron transfer between the electrodes and the biological system.^{647–649} In the case of the inkjet-printed biosensors, electrons are exchanged between the gold-polythiophene hybrid nanoparticles of the WE and the glucose oxidase molecules, which are covalently linked to the AuNPs. In general, amperometric sensors operate in the diffusion-limited mode,^{641,650–652} where the mass transport of the analyte through the solution to the electrode is slower than the electrochemical reaction at the electrode.^{641,651,652} Hence, the detected current is only influenced by the diffusion of the analyte, which results in a linear relation between the measured current and the concentration of the analyte.^{641,650,651}

Many parameters such as the degree of enzyme loading, the pH value of the electrolyte and the applied potential can influence the performance of amperometric glucose sensors.^{653–659,660} In order to obtain the maximum current response, I optimized the working electrode potential and the pH value before calibration. For the optimization studies, I utilized sensors containing AuNPs@P3KHT-GOx, which were bioconjugated in solution using EDC/S-NHS_{high} (2.00 vol%). The activity of glucose oxidase strongly depends on pH value. I tested buffer solutions with pH from 3.4 to 8.0 in order to identify the optimal working conditions. Citrate-phosphate buffers (0.1 M) with pH between 3.4 and 5.0 and PBS buffers (0.1 M) with pH from 5.8 to 8.0 were utilized for the studies. As shown in Figure 3-49a, the current response of the biosensor towards 5 mM glucose increased with increasing pH until a maximum was reached at pH 6.6. This result is consistent with different studies of GOx-containing biosensors that reported optimal performance in the pH range from 6.5 to 7.0.^{653–659} The optimal pH value of the inkjet-printed biosensor was less acidic than the ideal pH of 5.5 for free glucose oxidase in solution,^{661,662} probably due to bioconjugation. Covalent linkage of the GOx molecules to hybrid AuNPs likely caused a change in the surrounding microenvironment and the conformation of the enzyme, which altered the kinetics of the enzymatic reaction and affected the optimal reaction conditions.^{653,663–665}

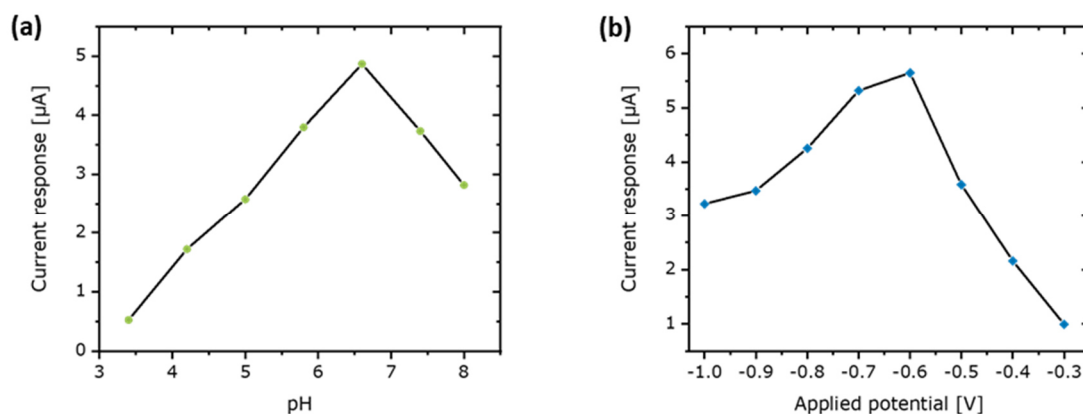


Figure 3-49: (a) Effect of buffer pH and (b) applied potential on the current response of the inkjet-printed biosensors containing AuNPs@P3KHT-GOx towards 5 mM glucose. The pH optimization experiments were conducted at a constant applied potential of -0.5 V against the printed silver reference electrode, while optimization studies of the applied potential were performed in a PBS buffer (0.1 M) with pH of 6.6. The WE of the investigated sensors was composed of enzyme-functionalized AuNPs@P3KHT-GOx. The bioconjugation of GOx was conducted prior to printing using EDC/S-NHS_{high} (2.00 vol%).

The applied potential affects the selectivity and sensitivity of printed glucose sensors.⁶⁶⁰ I evaluated potentials at the WE from -0.3 V to -1.0 V against the printed silver nanoparticle RE (Figure 3-49b). The detected current response towards glucose (5 mM) had a maximum at -0.6 V. The increase of current response with increasing potential can be attributed to an enhanced driving force for the enzymatic glucose oxidation.^{658,666} The optimal working conditions with the maximal current response for the printed amperometric glucose sensors containing AuNPs@P3KHT-GOx were determined at an applied potential of -0.6 V using a PBS buffer (0.1 M) with pH 6.6 as electrolyte. These conditions were applied for all further electrochemical glucose sensing studies.

I calibrated two types of biosensors, which differ in the bioconjugation of GOx to AuNPs@P3KHT (surface vs. solution bioconjugation), by means of the successive addition of glucose solution (2 mM in PBS buffer with pH 6.6) every 30 seconds (experimental details in section 6.3.15). The insets in Figure 3-50a and b illustrate typical amperometric current-time responses of the tested biosensors. The detected current increased steeply with the subsequent addition of glucose. Both types of biosensors showed a fast response to glucose addition. The steady-state current was reached in less than 5s, which is in conformity with reports of other amperometric glucose biosensors

containing immobilized GOx^{653,656,658} and which is faster than reported enzyme-free glucose sensors composed of metallic nanoparticles.^{667,668}

The calibration curves were obtained by characterizing three different printed biosensors of each biosensor type. The results in Figure 3-50a and b revealed linear behavior in the glucose range from 2 mM to 14 mM for both types of biosensors. Fits showed high linearity with R^2 values above 0.99 (Figure 3-50a and b). This linear detection range of the printed biosensors is suitable to monitor blood sugar concentration, since the normal blood glucose level of a healthy human is between 4 mM and 6 mM and diabetic blood glucose levels are larger than 7 mM.^{669–671} Different sensors of the same biosensor type possessed similar current responses (range of error bars), illustrating good reproducibility.

I calculated the limit of detections (LODs) for the two different types of inkjet-printed amperometric glucose biosensors using equation 3-4 (section 3.4.5).

$$C_{LOD} = \frac{3 \cdot S_{BL}}{S} \quad (3-4)$$

S_{BL} is the standard deviation of the detected blank current (pure PBS buffer without glucose) obtained by analyzing three different sensors of each biosensor type. The parameter S denotes the slope of the particular calibration line (Figure 3-50a and b) and defines the sensitivity of the biosensors.^{573–577} Sensors containing AuNPs@P3KHT-GOx obtained by solution bioconjugation were over two times more sensitive towards glucose ($1.351 \mu A \cdot mM^{-1}$) than sensors with surface-bioconjugated AuNPs@P3KHT-GOx ($0.626 \mu A \cdot mM^{-1}$).

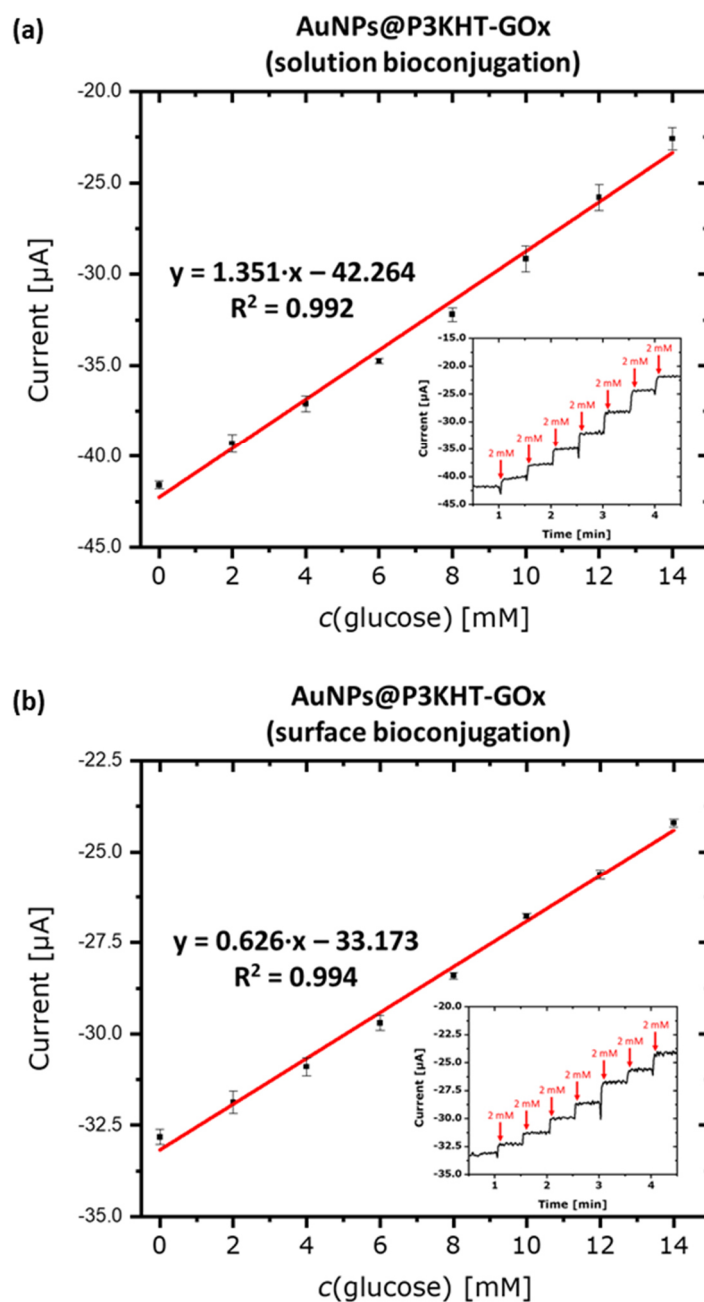


Figure 3-50: Calibration curves and amperometric current response signals (insets) towards successive glucose addition (2 mM in PBS buffer with pH 6.6) of biosensors containing enzyme-functionalized AuNPs@P3KHT-GOx as WEs. The bioconjugation of the GOx to AuNPs@P3KHT was conducted (a) before printing in solution using EDC/S-NHS_{high} (2.00 vol%) and (b) after printing on the surface of the inkjet-printed WEs. Error bars are the standard deviation (mean \pm standard deviation) of three individual sensors for each biosensor type.

The higher sensitivity also resulted in lower LOD (0.465 mM) of amperometric biosensors containing solution-bioconjugated AuNPs@P3KHT-GOx. The LOD of biosensors with WEs composed of surface-bioconjugated AuNPs@P3kHT-GOx was more than double (LOD=0.975 mM). The differences in sensitivity and LOD of the two types of amperometric biosensors probably originated from the different amounts of GOx molecules covalently linked to the hybrid AuNPs. Since surface bioconjugation was conducted after printing of the biosensor, it modified only the surface of the printed WE with GOx molecules. In contrast, GOx molecules were bioconjugated through the whole bulk of the WE if enzyme-functionalization of AuNPs was done prior to printing. Porosity of the printed structures likely enabled reactions between GOx molecules below the surface and glucose. Thus, in the case of WEs with solution-bioconjugated AuNPs@P3KHT-GOx, more GOx were available, leading to faster glucose oxidation and increased sensitivity of the printed biosensors. Although the larger enzyme density reduced the electrical conductivity of hybrid layers composed of solution-bioconjugated AuNPs@P3KHT-GOx (section 3.4.4), the increased sensitivity apparently outweighs this effect, causing improved performance of this type of inkjet-printed amperometric biosensor.

Table 3-20 summarizes linear detection ranges and LODs of different published electrochemical glucose sensors containing gold nanostructures and glucose oxidase. According to the data in Table 3-20, lower LODs of electrochemical glucose sensors are often accompanied by a reduction of the linear range. A broad linear detection regime is important for monitoring human glucose blood levels. Healthy humans have blood glucose levels between 4 mM and 6 mM, while diabetic blood glucose levels are larger than 7 mM.^{669–671} Since the inkjet-printed biosensors possessed linear current responses in the glucose range of 2 mM to 14 mM, they are suitable for detection of human blood glucose levels. Compared to other glucose sensors based on AuNPs that fulfill these requirements, the biosensors of this work had similar or only slightly higher LODs (Table 3-20). Since this thesis was the first study using gold-polythiophene hybrid nanoparticles for electrochemical glucose sensing, there is still optimization potential for improving the performance and lowering the LOD of this type of amperometric glucose sensors.

Table 3-20: Linear detection ranges and limits of detection (LODs) of different electrochemical glucose sensors containing gold nanostructures and glucose oxidase. The enzyme glucose oxidase was attached to the sensing material with different techniques. *Immobilization in these reports describes physisorption of enzymes due to weak interactions such as hydrogen bonds or van der Waals interactions, as well as ionic bonds.^{593–595} †Entrapment/Encapsulation defines the confinement of enzymes in polymer matrices or fiber networks.^{593–595}

Biosensing material	Type of enzyme binding	Linear range [mM]	LOD [mM]	Reference
Fe ₃ O ₄ -CS-Au magnetic nanoparticles	Immobilization*	5-30	0.55	672
AuNPs coated with nafion	Immobilization*	2-20	2.03	671
AuNPs coated with polypyrrole	Immobilization*	0.99 -19.9	0.2	673
AuNPs/graphene nanosheet hybrid	Immobilization*	2-16	0.2	674
AuNPs@P3KHT	Covalent (EDC/NHS) on surface	2-14	0.975	This work
AuNPs@P3KHT	Covalent (EDC/NHS) in solution	2-14	0.465	This work
AuNPs/rGO nanocomposite	Protein-cross-linking	1-11	0.640	675
AuNPs capped with tannic acid	Electro-cross-linking	0.3-10	0.3	610
AuNPs/CNTs composite	Immobilization*	0.5-8	0.2	676
Dendritic gold nanostructures	Cross-linking	0.1-10	0.022	677
AuNPs	Immobilization*	0.1-5	0.063	678
AuNPs/graphene nanocomposite	Covalent (EDC/NHS)	0.17-2.78	0.11-0.17	679
Pt nanowire array coated with AuNPs	Covalent (EDC/NHS)	0.015-2.5	0.015	680
Polystyrene/Polyaniline/AuNPs composite	Entrapped [†]	0.04-2.04	0.012	681
AuNPs/polypyrrole nanocomposite	Entrapped [†]	0.1-0.7	0.10	682

Many studies revealed that bulk gold and gold nanostructures have the electroactivity to oxidize glucose by electro-oxidation under certain conditions.^{630,683–686} Hence, I investigated if the detected glucose oxidation is caused by an enzymatic reaction due to the covalently bound GOx molecules or if the hybrid AuNPs themselves have the potential to react with glucose. I fabricated biosensors by inkjet printing using inks composed of non-functionalized AuNPs@P3KHT and investigated the activity of these biosensors at an applied potential of -0.6 V in PBS buffer with pH 6.6 As illustrated in Figure 3-51a, I did not detect a significant current response towards glucose, indicating

that the signal of the AuNPs@P3KHT-GOx biosensors (Figure 3-50) only originated from the enzymatic reaction between glucose oxidase and glucose. Thus, the covalent bioconjugation of GOx to the gold-polythiophene hybrid nanoparticles is crucial for the development of amperometric glucose biosensors.

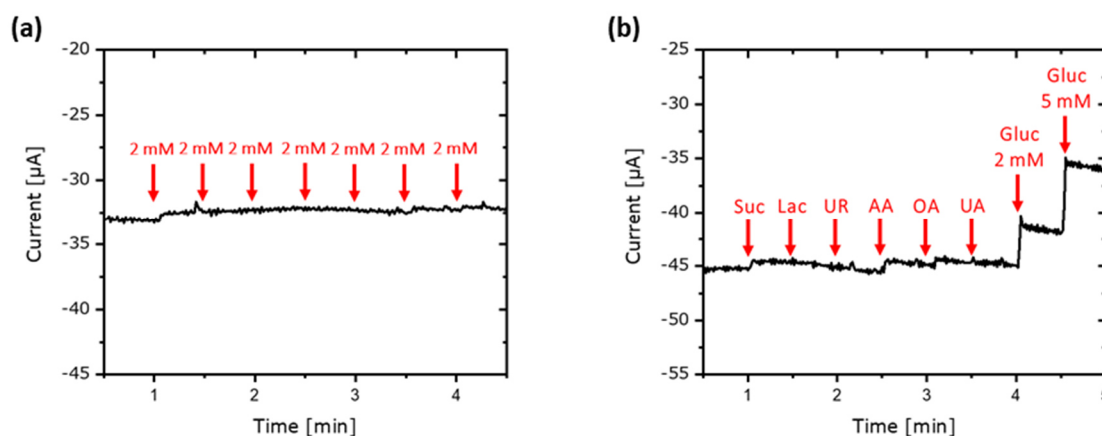


Figure 3-51: (a) Detected current response of biosensors containing WEs composed of non-functionalized AuNPs@P3KHT upon the gradual addition of glucose solution (2 mM). (b) Detected current response of biosensors containing WEs composed of enzyme-functionalized AuNPs@P3KHT-GOx (solution bioconjugation using EDC/S-NHS_{high}) upon the gradual addition of different interferents (AA=ascorbic acid, OA=oxalic acid, UA=uric acid, Suc=sucrose, Lac=lactose and UR=urea) and glucose (2 mM and 5 mM). The concentration of all interferents in the added stock solutions was 20 mM.

Electroactive and non-electroactive compounds present in biological and clinical samples (e.g. blood serum) can interfere with the electrochemical glucose response. Electroactive interferents such as ascorbic acid (AA), oxalic acid (OA) and uric acid (UA) can also be oxidized at the working electrode, falsifying the current response.^{655,660} Non-electroactive species such as sucrose (Suc), lactose (Lac) and urea (UR) can foul the WE, blocking the surface of the electrode, which inhibits further glucose oxidation and lowers current response.^{655,660} Although the concentration of glucose is much higher (over 30 times higher) compared to the interferents in biological samples, these interferants can cause a significant error in the current signal.^{687–689} Thus, it is very important that the amperometric sensors show a high selectivity towards glucose under the chosen working conditions.

I analyzed the selectivity of the inkjet-printed biosensors by investigating the current response in the presence of different interferents. I tested biosensors with WEs composed of AuNPs@P3KHT-GOx, which were bioconjugated in solution prior to printing using EDC/S-NHS_{high} (2.00 vol%). I injected stock solutions of different non-electroactive and electroactive interferents to the electrolyte and recorded the current response of the amperometric biosensors. The concentration of the interferents in the added stock solutions was 20 mM. As illustrated in Figure 3-51b, there were no significant changes in the detected current upon the addition of various interferents. Ascorbic acid (20 mM) caused the most intense current response, which was only about 25% of the current response induced by glucose (2 mM). Figure 3-51b shows that the amperometric biosensors containing AuNPs@P3KHT-GOx had a well-defined glucose current response signal even in the presence of the six interferents, demonstrating the good selectivity of the inkjet-printed biosensors towards glucose.

I did not observe any delamination of the hybrid gold working electrode from the PET substrate during the electrochemical glucose detection. At long measurement times (> 30 min), delamination of the printed silver components (RE, CE) started. Additionally, at high applied voltages (< -0.8 V) and long measurement times (> 30 min), the printed silver parts turned black, indicating partial oxidation of the printed silver structures. Hence, there is still potential to optimize the design and working conditions of the amperometric biosensors containing AuNPs@P3KHT-GOx. The problems of delamination and oxidation could perhaps be overcome by replacing the silver nanoparticles with carbon materials. Inkjet-printable carbon inks^{690–693} already exist and different carbon materials have already been successfully incorporated into different types of biosensors.^{694–697} Alternatively, replacing the silver reference electrode with an Ag/AgCl reference electrode could likely further improve the performance and stability of the biosensors. Experimental studies already revealed that stable Ag/AgCl electrodes can be produced by inkjet printing.^{698,699}

3.4.7 Cell growth supporting features of bioconjugated gold-P3KHT hybrid nanoparticles[§]

The affinity of AuNPs@P3KHT towards biomolecules is not limited to enzymes. The carboxylate groups in the polythiophene ligand shell of AuNPs@P3KHT enable the interaction with various biological species containing primary amines. I bioconjugated several cell-growth promoting peptides to hybrid films made of AuNPs@P3KHT and used these as cell growth platforms. If the underlying substrate possesses low or no interactions with cells, only the hybrid films can affect cell growth.

Nexterion slides H are thin glass slides (d=1 mm) with a hydrophilic polymer coating that is resistant against non-specific binding of biomolecules and possesses low interactions with cells. The coating consists of a cross-linked three-dimensional hydrogel network to which activated NHS esters are attached via long and flexible spacer molecules. I used these NHS esters to covalently attach the hybrid gold nanoparticle films to the Nexterion substrates (Figure 3-52). First, I transferred the NHS esters of the Nexterion slides H to amine groups by a reaction with diamine linkers. The primary amine groups of the linkers and the NHS esters form stable covalent amide bonds. Subsequently, I deposited films made of AuNPs@P3KHT on these aminated Nexterion substrates by drop-casting. The amine groups of the Nexterion substrate reacted with the carboxylate groups of the AuNPs@P3KHT via EDC/NHS activation (Figure 3-52, experimental details in section 6.2.8). As a result, the hybrid nanoparticle films were covalently attached to the underlying Nexterion substrate by stable amide bonds. This improved the mechanical integrity of the films.

Different cell growth promoting peptides were bioconjugated to these hybrid films using EDC/NHS chemistry. I assumed that not all carboxyl/carboxylate groups of the AuNPs@P3KHT reacted with the Nexterion substrate and were still available for further reactions with the primary amine groups of the peptides, yielding stable covalent amide bonds between the hybrid layers and the peptides. Since the aminated Nexterion slides H

[§] All experiments regarding fibroblast and neurosphere cells including cell culturing, cell growth, staining and imaging by fluorescence microscopy were performed by Dr. Aleeza Farrukh and Dr. Shifang Zhao from the Dynamic Biomaterials group of Prof. Dr. Aránzazu del Campo (INM-Leibniz Institute for New Materials, Saarbrücken, Germany).

lacked carboxyl groups, the peptides cannot react with these slides and the covalent attachment of the peptides was limited to the hybrid layers.

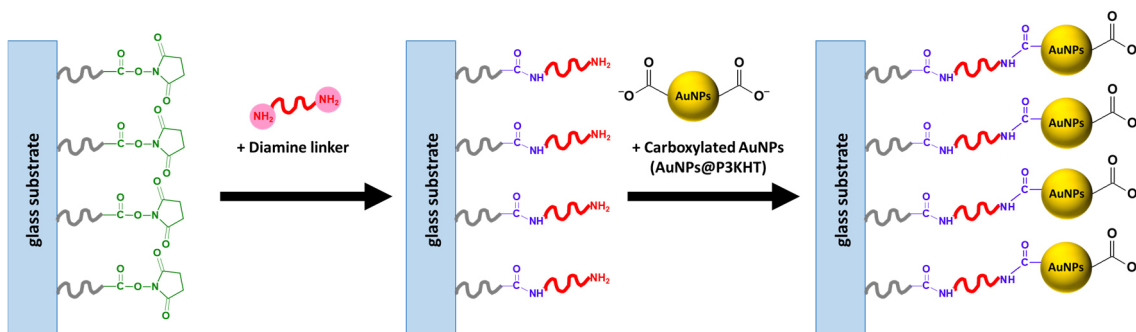


Figure 3-52: Scheme of the covalent coupling of carboxylated gold-polythiophene hybrid nanoparticles to Nexterion slides H. In a first step, a diamine linker reacts with the active NHS ester at the surface of the Nexterion slides H upon amide bond formation. In a second step, the carboxylate groups of the gold-polythiophene hybrid nanoparticles react with the diamine linker via EDC/NHS coupling. Finally, the gold-polythiophene hybrid nanoparticles are covalently linked to the substrate via stable amide bonds.

Based on the procedure described above, cell-growth promoting peptidomimetics containing RGD or IKVAV motifs were anchored to the drop-cast hybrid films. Peptidomimetics are short peptide sequences mimicking the functional elements (e.g. active sites) and the three-dimensional space of particular proteins, while still maintaining the interaction with the biological target.^{700–702} Since peptidomimetics are smaller than bulky proteins, they enable improved control over coating densities and binding chemistry in the design of biomaterials.⁷⁰³ Compared to bulky proteins, short peptide sequences are more stable, less sterically hindered, easier to handle and to synthesize.^{704,705,706} I employed a commercially available cyclic RGD peptide (cyclo[RGDf]). RGD is a tripeptide motif consisting of arginine (R), glycine (G) and aspartic acid (D) as shown in Figure 3-53 and this peptide sequence is one of the most common and most efficient cell adhesion promoters on surfaces.^{706–710} Proper cell attachment is crucial for functionality, proliferation and differentiation of cells.^{706–708} Cells that have lost their adhesion are prone to anoikis, a special form of apoptosis.⁷⁰⁶ Adhesive proteins and peptides can also promote cell migration.⁷⁰⁸

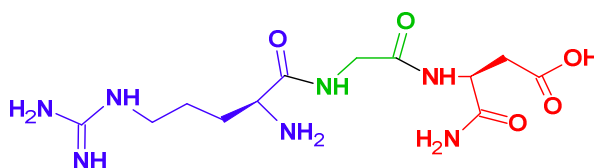


Figure 3-53: Molecular structure of the RGD sequence consisting of arginine (blue), glycine (green) and aspartic acid (red) motifs.

Fibroblasts were grown on films composed of AuNPs@P3KHT with and without RGD functionalization. After 3 days, the cells were fixed and stained. Fluorescence microscopy images of the cells (Figure 3-54) revealed clear differences in cell growth. Fibroblasts on non-functionalized AuNPs@P3KHT layers showed no significant cell spreading and the cells retained their rounded morphology (Figure 3-54a). This behavior was also observed for the fibroblast grown on aminated Nexterion slides H acting as negative control (Figure 3-54c). Fibroblast on RGD-functionalized AuNPs@P3KHT films showed proliferation, elongation and spreading (Figure 3-54b). The higher and faster cell spreading on the functionalized hybrid films can only be explained by the higher density of RGD peptides on these layers.

In contrast, there should be no covalent attachment of the RGD peptides on the negative controls (aminated Nexterion slides H) due to leakage of carboxylate groups. It is always possible that some peptides adsorb nonspecifically on the Nexterion substrates. However, the fluorescence microscopy images clearly illustrated that such non-specific absorption of RGD peptides did not cause a pronounced cell growth of fibroblast on the aminated Nexterion slide H. Additionally, I did not observe delamination of the hybrid nanoparticle layers from the underlying Nexterion slides H during the 3 days of fibroblast cell culture. This result demonstrated successful covalent linkage between the hybrid nanoparticle layers and the Nexterion slides H due to EDC/NHS coupling as depicted in Figure 3-52.

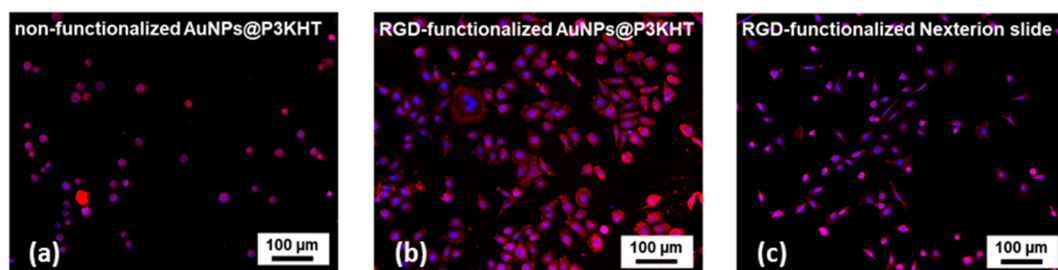


Figure 3-54: Fluorescence microscopy images of fibroblasts grown on (a) a non-functionalized hybrid film made of AuNPs@P3KHT, (b) a RGD-functionalized hybrid film made of AuNPs@P3KHT and (c) a Nexterion slide H functionalized with a diamine linker (surface is amine-terminated) and RGD functionalization. Actin fibers were stained with phalloidin (red) and the nucleus was stained with DAPI (blue). Images were taken after 3 days of cell culture.

I further investigated how the amount of covalently attached RGD peptides affected the fibroblast growth on hybrid nanoparticle films. Therefore, I prepared various inks by mixing biofunctionalizable AuNPs@P3KHT dispersions with dispersions containing non-biofunctionalizable gold-polythiophene hybrid nanoparticles AuNPs@PTEBS in different volume ratios. These mixed inks yielded hybrid surfaces which can only be partially modified with RGD peptides, since AuNPs@PTEBS lacked carboxyl groups for covalent peptide attachment. The different hybrid films were covalently coupled to the underlying Nexterion H substrates (Figure 3-52) and fibroblasts were grown on them for 3 days. Fluorescence microscopy images of the fixed and stained cells on the various gold-polythiophene hybrid nanoparticle layers are depicted in Figure 3-55.

While the fibroblast developed elongated morphologies and showed high cell spreading on films made from pure AuNPs@P3KHT (Figure 3-55a), the fibroblasts on films made of AuNPs@PTEBS retained their round morphology (Figure 3-55e), indicating no cell attachment and growth. With increasing degree (20% to 80%) of non-biofunctionalizable gold-polythiophene hybrid nanoparticles AuNPs@PTEBS, the degree of cell proliferation and spreading on the partially RGD-modified hybrid films decreased due to reduction in functional RGD density (Figure 3-55b-d). The results clearly showed that the biofunctionality of the AuNPs@P3KHT due to the carboxylate groups in the polythiophene ligand shell was crucial for the covalent attachment of the RGD peptides. Note that on all hybrid layers including AuNPs@PTEBS films additional non-specific adsorption of RGD peptides can occur. Since there was no distinct cell growth on non-

biofunctionalizable AuNPs@PTEBS layers, I conclude that the cell growth of fibroblasts on AuNPs@P3KHT films was solely caused by covalently attached RGD peptides.

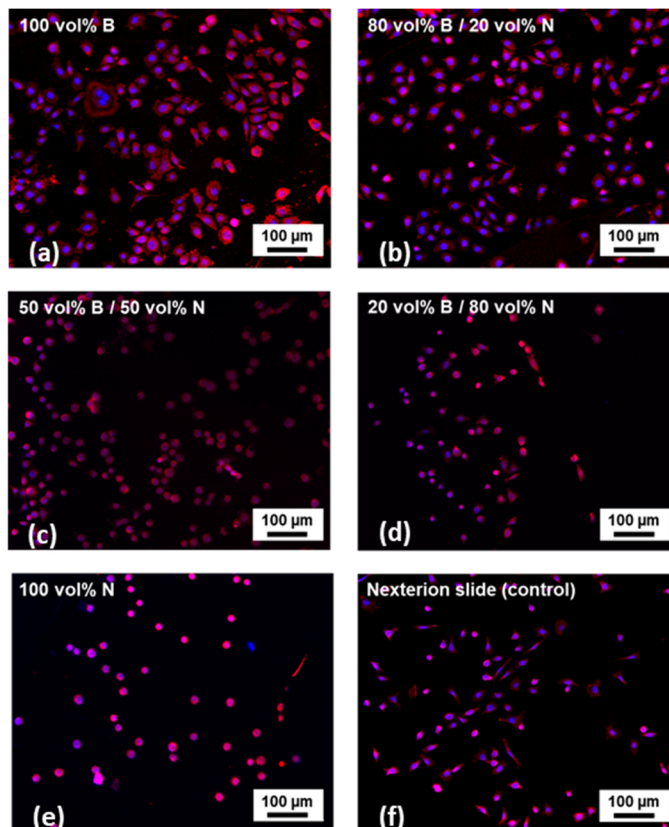


Figure 3-55: Fluorescence microscopy images of fibroblasts grown on partially RGD-functionalized gold-polythiophene hybrid nanoparticle films, which contained different degrees of biofunctionalizable AuNPs@P3KHT (B) and non-biofunctionalizable AuNPs@PTEBS (N). As a control, fibroblasts were also grown on an aminated and RGD-functionalized Nexterion slide H. Actin fibers were stained with phalloidin (red) and the nucleus was stained with DAPI (blue). Images were taken after 3 days of cell culture.

The applicability of gold-polythiophene hybrid nanoparticle films as platforms for cell growth was further explored with neurospheres. Neurospheres are free-floating clusters of stem cells, which can be cultured *in vivo* and *in vitro*.^{711–713} Compared to neural progenitor cells (NPCs), neurospheres are easier to handle and since neurospheres are a source of undifferentiated stem cells, they are often used to monitor the development of neurons in biomaterials.^{703,714–716}

Since neural cells do not react to RGD, growth of neurospheres requires other growth supporting peptides. The adhesive protein laminin promotes neural cell adhesion,

differentiation and migration.^{703,717–719} The cell growth stimulating properties are based on special peptide sequences present in laminin. One important peptide sequence present in the α -laminin chain,^{704,705,720,721} is the pentapeptide motif IKVAV consisting of the amino acids isoleucine (Ile), lysine (Lys), valine (Val) and alanine (Ala) as illustrated in the structure of Figure 3-56. Several studies revealed that the IKVAV sequence stimulated cell adhesion, migration, collagenase IV production, angiogenesis, tumor growth and neurite outgrowth.^{722–726} The most commonly used peptidomimetic containing the IKVAV sequence is a 19-mer peptide IK-19 (sequence CSRARKQAASIKVAVSADR), which was first identified by Tashiro and co-workers.^{722,724} IK-19 is commercially available and besides the IKVAV sequence it contains positively charged tails, which increase the water solubility of the hydrophobic IKVAV motif and avoid aggregation of the peptide.⁷⁰³ Silva *et al.* showed that biomaterials with incorporated peptidomimetics containing the IKVAV motif promoted selective differentiation of cells into neurons.⁷²⁷

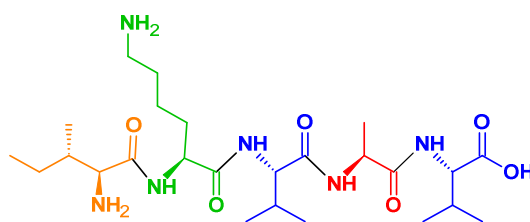


Figure 3-56: Molecular structure of the pentapeptide IKVAV consisting of isoleucine (orange), lysine (green), valine (blue) and alanine (red) motifs.

I functionalized the hybrid nanoparticle films made of AuNPs@P3KHT with IK-19 using the same EDC/NHS coupling method as for the RGD functionalization described above (Figure 3-52). The primary amine groups of the IK-19 peptides should only react with the carboxylate groups of the AuNPs@P3KHT yielding a covalent attachment. In contrast, the IK-19 should not be able to react with the amine-terminated surface of the Nexterion slide H, resulting in a selective IK-19 functionalization of the gold-polythiophene hybrid nanoparticle films.

Neurospheres were seeded on hybrid layers made of AuNPs@P3KHT and on aminated Nexterion slides H, which were all functionalized by the IK-19. After 3 days, the cells were fixed and stained. Due to the covalent attachment of the hybrid layers to the underlying Nexterion slide H (Figure 3-52), I did not observe delamination of the hybrid

nanoparticle films during the 3 days of neurosphere cell culture, similar to the fibroblast studies. Fluorescence microscopy images of the neurospheres on the two different substrates are shown in Figure 3-57. The images revealed that the neurospheres selectively attached to the gold-polythiophene hybrid nanoparticle layers. The population of the neurospheres was much higher on the hybrid films (Figure 3-57b, darker areas in Figure 3-57a and c) than on the bare aminated Nexterion slide H (lighter areas in Figure 3-57a and c). This observation can be attributed to the higher density of IK-19 on the hybrid nanoparticle layers. Furthermore, some neurospheres seeded on the IK-19-modified AuNPs@P3KHT layers also showed cell proliferation, spreading and elongation, since they did not retain their rounded morphology (Figure 3-57). This further demonstrated the cell growth supporting effect of IK-19.

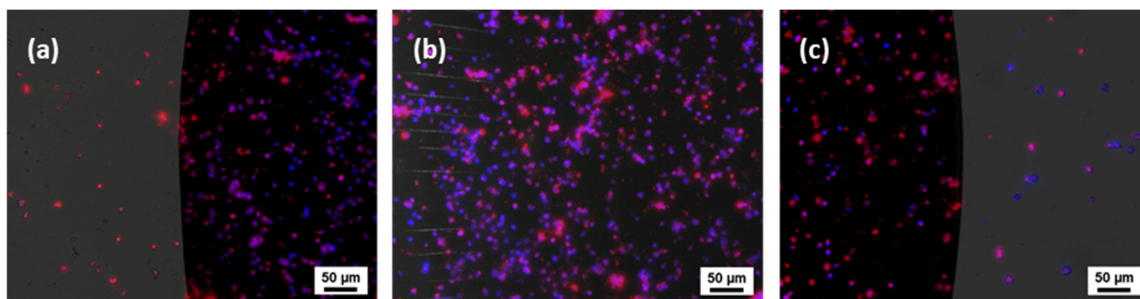


Figure 3-57: Fluorescence microscopy images of neurospheres grown on (b, darker areas in a and c) IK-19-functionalized films made of AuNPs@P3KHT and (lighter areas in a and c) IK-19-functionalized aminated Nexterion slide H. Actin fibers were stained with phalloidin (red) and the nucleus was stained with DAPI (blue). Images were taken after 3 days of cell culture.

There was no neural differentiation of the neurospheres. They did not develop elongated axons, secondary branches or dendritic filopodia within the 3 days of cell culture on the hybrid nanoparticle layers. The observed low cell spreading and the non-existing neural differentiation of the neurospheres can likely be attributed to the low quality of used neurospheres. There was already a low number of neurospheres with limited viability present in the cell culture medium before seeding the cells on the hybrid layers and the Nexterion slide H. Although neurosphere culture was performed according to an established protocol,⁷⁰³ there were problems in growing sufficient number of vital cells. Compared to neural progenitor cells (NPCs), neurospheres require higher cell densities for neural differentiation.⁷²⁸ High cell densities enhance the cell-cell contacts and

facilitate neurite formation in the case of neurospheres.⁷²⁸ Thus, it is likely that there was no neural differentiation on the hybrid nanoparticle films due to the low number of seeded neurospheres. Since NPCs are much more active and the actual benchmark for the investigation of neural behavior,⁷⁰³ it would be worthwhile repeating the experiments, replacing the neurospheres with NPCs. Studies with NPCs could provide further information about the effects of IK-19-functionalized gold-polythiophene hybrid nanoparticle films on neural differentiation.

The results of this section show that films made of biofunctionalizable AuNPs@P3KHT can be used as platforms for cell growth. Cell attachment and proliferation can be further enhanced by covalent linkage of cell growth supporting peptides to the hybrid layers by EDC/NHS coupling. The carboxylate groups in the ligand shell enable the covalent coupling of various primary amine-containing growth factors (peptides and proteins). Thus, the gold-polythiophene hybrid nanoparticles AuNPs@P3KHT developed in this work are ideal platforms for the growth of various cells, since they can be modified to match the different growth conditions for each cell type.

3.4.8 Summary

This chapter deals with the covalent bioconjugation of primary amine-containing molecules to biofunctionalizable AuNPs@P3KHT using EDC/NHS coupling chemistry.^{384–386} Bioconjugation was successfully conducted implementing two different methods, referred to as surface and solution bioconjugation. In surface bioconjugation amine-containing molecules were covalently attached on the surface of the deposited dry hybrid nanoparticle films. Solution bioconjugation was conducted in solution prior to film deposition by a new one-step protocol. Raman spectroscopy revealed that bioconjugation led to the formation of stable amide bonds between primary amines and the carboxylate groups of AuNPs@P3KHT for both bioconjugation methods. Colloidal characterization demonstrated that bioconjugation with glucose oxidase increased the colloidal stability of the gold-polythiophene hybrid nanoparticles, even in different buffers (MES and PBS buffer) with varying pH (pH 4.7 to 7.4) and high ionic strength.

Electrical characterization showed that bioconjugation of GOx to AuNPs@P3KHT caused a drop in the electrical conductivity of hybrid gold films. Solution bioconjugation yielded enzyme-functionalized AuNPs@P3KHT-GOx that possessed an up to two orders of magnitude higher material resistivity ρ ($2.14 \cdot 10^{-4} \Omega\text{m} \pm 0.01 \cdot 10^{-4} \Omega\text{m}$) compared to non-functionalized AuNPs@P3KHT ($8.84 \cdot 10^{-6} \Omega\text{m} \pm 0.11 \cdot 10^{-6} \Omega\text{m}$). In contrast, enzyme-functionalized hybrid films obtained by surface bioconjugation had a lower material resistivity ρ ($9.18 \cdot 10^{-6} \Omega\text{m} \pm 0.02 \cdot 10^{-6} \Omega\text{m}$), probably due to smaller inter-particle distances within these films. There is a trade-off between the electrical conductivity and the biofunctionality of the gold-polythiophene hybrid nanoparticles.

Enzyme-functionalized hybrid nanoparticles (AuNPs@P3KHT-GOx) were suitable for glucose monitoring. Within the scope of this application filed, AuNPs@P3KHT-GOx were successfully used in colorimetric bioassays for glucose detection. These assays had a low LOD of $15 \mu\text{M}$ ($2.7 \mu\text{g} \cdot \text{mL}^{-1}$) over a broad linear optical output range of $25 \mu\text{g} \cdot \text{mL}^{-1}$ to $3.0 \text{ mg} \cdot \text{mL}^{-1}$. Enzymatic activity of GOx increased upon covalent attachment to AuNPs, resulting in an over 40% lower Michaelis Menten constant K_m of AuNPs@P3KHT-GOx (14.8 mM [$2.7 \text{ mg} \cdot \text{mL}^{-1}$]) compared to free GOx in solution (26.8 mM [$4.8 \text{ mg} \cdot \text{mL}^{-1}$]). I also fabricated flexible amperometric biosensors on PET substrates by inkjet printing colloidal inks containing AuNPs@P3KHT-GOx. The printed sensors showed a linear current response in the glucose range of 2 mM to 14 mM . This makes the inkjet-printed biosensors suitable for the detection of blood glucose concentrations, since the glucose level of a healthy human is between 4 mM and 6 mM and diabetic blood glucose levels are greater than 7 mM .^{669–671} The printed amperometric biosensors possessed high selectivity towards glucose, even in the presence of electroactive and non-electroactive interferents, which are often contained in real biological and clinical samples, such as blood serum, saliva or sweat.

I further exploited the bioconjugation by covalently attaching different cell growth supporting peptidomimetics (RGD- or IKVAV-containing peptides) to AuNPs@P3KHT using EDC/NHS chemistry. Hybrid films functionalized by RGD peptides enhanced the cell growth of fibroblasts, while AuNPs@P3KHT layers functionalized with IKVAV-containing peptides supported cell attachment of neurospheres.

Further studies should explore the applicability of the gold-polythiophene hybrid nanoparticles as a sensing material for different targets besides glucose. For example, as an alternative, the enzyme horseradish peroxidase (HRP) could be linked to the AuNPs@P3KHT. There are several studies indicating that AuNPs with immobilized HRP can be successfully used for electrochemical detection of hydrogen peroxide.^{729–731} Furthermore, antibodies are an interesting group of biomolecules to be bioconjugated to AuNPs@P3KHT, since several AuNPs-antibodies composite materials were already successfully utilized for the electrochemical sensing of various biological processes.^{732–734} Additionally, oligonucleotides are an inserting molecule class for bioconjugation. Electrochemical DNA sensors were already realized by covalent linkage of oligonucleotides with sulfur-containing anchoring groups to AuNPs.^{735,736} This approach could be transferred to the hybrid nanoparticles AuNPs@P3KHT using amino-functionalized oligonucleotides,^{737–739} which could react with carboxylate groups present in the polythiophene ligand shell. Oligonucleotide-functionalized AuNPs could also be used for the colorimetric detection of complementary oligonucleotides.^{740,741} Due to the unique combination of biofunctionality and plasmonic properties of AuNPs@P3KHT, further studies should also investigate the applicability of the hybrid nanoparticles in new optical biosensors. Aptasensors detect the SPR shift of plasmonic nanoparticles, which was caused by the reaction of the aptamers with the target molecules. Colorimetric aptasensors based on AuNPs have already been used to detect bacteria, peptides and proteins.^{742–744} Thus, upcoming work should exploit the utilization of AuNPs@P3KHT in modern aptasensors.

Electrical stimulation of neural stem cells is a novel method in tissue engineering for regeneration medicine, which recently gained much attention.^{745–748} Several studies demonstrated that electrical stimulation can increase the differentiation and proliferation of stem cells, the growth and elongation of neurites and it can further lead to guided cell migration.^{749–755} Suitable conductive biomaterials for electrical stimulation of stem cells should have a good biocompatibility and produce no side effects or byproducts when in contact with the cells. The main material classes used as conductive biomaterials for tissue engineering are noble metals (gold and platinum), conductive polymers and carbon materials.^{745–748,756} Metallic biomaterials offer good electrical conductivity, high

mechanical strength, excellent long-term stability and great biocompatibility.^{745,746} Conductive polymers also allow electrical stimulation of neural cells and can further be functionalized with cell growth supporting peptides.^{757–760} The gold-polythiophene hybrid nanoparticles AuNPs@P3KHT combine the advantages of both material types. They possess sufficient electrical conductivity and they can be modified with IKVAV-containing peptidomimetics, which support proliferation and differentiation of neural stem cells. Further studies should explore if AuNPs@P3KHT can be used for electrical stimulation of neural stem cells and if they can guide neurite growth along printed structures. As a consequence, gold-polythiophene hybrid nanomaterials would offer new opportunities in the development of functional biomaterials. Biomaterials promoting directed neural growth could enable new treatment options against neurological injuries and neurological disorders such as Parkinson's and Alzheimer's disease.

4. Conclusion

This thesis deals with the development and characterization of electrically conductive gold-polythiophene hybrid nanocrystals. Spherical and rod-shaped gold cores with different sizes were functionalized with polythiophene ligands by ligand exchange reactions. Films made of these gold-polythiophene hybrid nanocrystals were directly conductive after drying and did not require any post-treatment (e.g. thermal sintering) to enhance electrical conductivity.^{69,423} The most conductive hybrid layers in this work (AuNRs@PTEBS and AuNPs@PFS-Na) possessed material resistivities ρ in the range of $4 \cdot 10^{-6} \Omega\text{m}$, which is only two orders of magnitude larger than the resistivity of bulk gold ($2.35 \cdot 10^{-8} \Omega\text{m}$).¹⁶⁰

Interactions between the gold cores and the surrounding polythiophene ligands strongly affect the electrical properties of the hybrid materials. The following features of these interactions were investigated systematically in this thesis:

- The molecular orientation of the polythiophene chains in the polymer ligand shell.
- The energy level alignment of gold's Fermi level E_F with the HOMO and LUMO of the polythiophenes at the inorganic-organic interface.

The molecular orientation of polythiophene ligands is important, since polythiophenes have the highest electrical conductivities along the conjugated polymer backbone and in π - π stacking direction.⁷⁰⁻⁷⁴ Raman spectroscopy and XPS revealed that the polythiophene PTEBS arranged differently on spherical gold nanoparticles AuNPs and gold nanorods AuNRs. While in the case of AuNRs@PTEBS, the polythiophene chains arranged in a pure face-on configuration, some PTEBS chains (25%) adopted an edge-on orientation in AuNPs@PTEBS. Hybrid films made of AuNRs@PTEBS were over 40% more electrically conductive. The molecular face-on orientation originated from energetic interactions between PTEBS chains and high-energy $\{110\}$ facets, which are only present on the surface of the AuNRs, as well as from the low local surface curvature on the sidewalls of the AuNRs. The rigid PTEBS chains align along the long axis of the AuNRs

by face-on binding more easily than to the curved surfaces of the gold nanorod tips and AuNPs.

This work clearly demonstrates that a face-on orientation of polythiophene ligands is beneficial for the inter-particle charge carrier transport along the π - π stacking direction,^{325,79} resulting in higher electrical conductivities of gold-polythiophene hybrid nanocrystals. To the best of my knowledge, this thesis is the *first study* characterizing the molecular arrangement of polythiophenes on the curved surfaces of metallic nanocrystals. Previous studies focused on molecular orientation of polythiophenes on surfaces of planar substrates,⁷⁴⁻⁷⁶ nano-confined spaces (e.g. produced by nanoimprinting),⁷⁷⁻⁸⁰ carbon nanomaterials^{71,302,278,331,334} and ceramic nanocrystals.^{81,82}

Organic-inorganic interfaces are present in many modern opto-electronic devices such as LEDs and solar cells. These devices mostly contain planar inorganic/organic interfaces. and research was mainly focused on these planar systems. Little is known about the energy level alignment at highly curved inorganic/organic interfaces, which are common in hybrid nanocrystals. This work investigated how the energetic alignment on highly curved gold-polythiophene interfaces affects the electrical properties of the appropriate hybrid materials. In general, an energetic match between the metal's Fermi level E_F and the molecular orbitals (HOMO and LUMO) of an organic compound is required to achieve sufficient charger carrier transport across metal-organic interfaces.⁸³⁻⁸⁶ Thus, the electrical conductivity of gold-polythiophene hybrid nanocrystals can be enhanced by tailored conductive polymer ligands, that align well with the Fermi level E_F of gold (-5.1 eV). Replacing PTEBS by the polythiophene derivate PFS-Na (E_{HOMO} -5.4 eV), resulted in hybrid gold nanoparticles (AuNPs@PFS-Na) with an over 40% higher electrical conductivity. Improved energy level alignment at the gold-PFS-Na interfaces yielded lower charge carrier injection barriers and facilitated electron flow from the gold cores to the PFS-Na ligand shell.

Additional features can be introduced to gold-polythiophene hybrid nanoparticles by modifying the polythiophene ligand shell. I created biofunctionalizable hybrid nanomaterials (AuNPs@P3KHT) by modifying gold nanoparticles with carboxylated polythiophenes, which enable bioconjugation of amine-containing biomolecules such as

enzymes, peptides or antibodies. These biomolecules were covalently bound to AuNPs@P3KHT via stable amide bonds as proven by Raman spectroscopy.

Glucose oxidase (GOx), a commercially available and highly stable enzyme with widespread usage in glucose sensing,^{531–539} was chosen as a model system to investigate the biofunctionality of the biofunctionalizable hybrid nanoparticles. Enzyme-functionalized gold hybrid nanocrystals (AuNPs@P3KHT-GOx) were successfully utilized for the colorimetric and electrochemical detection of glucose. Bioconjugation of GOx to AuNPs@P3KHT increased the enzymatic activity of the enzyme in colorimetric bioassays. Inkjet-printed amperometric biosensors containing AuNPs@P3KHT-GOx enabled electrochemical glucose detection with linear current response signals in the glucose range of 2 mM to 14 mM, suitable for monitoring human blood glucose concentrations.^{669–671} I further demonstrated the bioconjugation of several cell growth supporting peptidomimetics with RGD or IKVAV sequences to hybrid AuNPs@P3KHT films. These layers were successfully used as platforms for cell growth of fibroblast and neurosphere cells. In contrast, layers made of non-biofunctionalizable AuNPs@PTEBS did not support cell growth.

The gold-polythiophene hybrid nanoparticles introduced in this work were colloidally stable in aqueous media and different water-organic solvent mixtures. This excellent colloidal stability likely originated from the strong Au-S bonds (Au-S bond dissociation energy is $418 \text{ kJ}\cdot\text{mol}^{-1}$),²³⁰ indicated in Raman and X-ray photoelectron spectroscopy. Additionally, the charged polythiophene ligand chains lent the gold-polythiophene hybrid nanocrystals sufficient electrosteric stabilization. This excellent colloidal stability enabled the formulation of highly concentrated inks based on AuNPs@P3KHT, which were suitable for inkjet printing. The hybrid inks possessed good jettability and led to stable drop formation without satellite drop generation during the inkjet printing process, which is important to create high-quality printed products without defects and with high resolution. The sinter-free nature of the gold-polythiophene hybrid nanoparticle inks facilitated the production of flexible and bendable amperometric biosensors on PET foils using inkjet printing. In contrast, most commercial metallic nanoparticle inks require thermal sintering at elevated temperatures (200°C to 350°C),^{1,5} which often impedes the production of flexible, bendable and wearable electronics using temperature-sensitive

substrates such as paper or common polymers (e.g. polyethylene and polycarbonate) with low glass transition temperatures T_g .

In summary, the results of this thesis show that a precise control over the gold-polythiophene interactions allows the targeted adjustment of the electrical properties of gold-polythiophene hybrid nanocrystals. The right combination of gold nanocrystal and polythiophene can alter the energy level alignment at the gold-polythiophene interfaces and the molecular orientations of the polythiophene ligands. Suitable combinations between diverse gold nanocrystals (different sizes and shapes) and various polythiophene ligands with desired electronic structure enable the development of highly conductive hybrid nanomaterials.

Compared to commercial state-of-the-art metal nanoparticle inks for printed electronics, gold-polythiophene hybrid nanocrystals possess several advantages. Their sinter-free nature permits printing on various flexible substrates without any limitations. Besides electrical conductivity, the gold-polythiophene hybrid nanoparticles deliver additional functionalities such as biofunctionality due to the option to modify the polythiophene ligand shell. Their unique features make gold-polythiophene hybrid nanocrystals attractive for soft electronics used in human-machine interfaces and health monitors, where good electrical conductivity, high mechanical flexibility and biocompatibility is required.^{761–765}

5. Outlook

Gold has large electrical conductivity ($\sigma=4.42 \cdot 10^7 \text{ } \Omega^{-1} \cdot \text{m}^{-1}$),^{1,5} stability against oxidation and excellent biocompatibility, but it is expensive. Therefore, it would be interesting to transfer the concept of sinter-free conductive hybrid nanoparticles with polythiophene ligand shells to less expensive metals. In particular, silver nanoparticles (AgNPs) are attractive, since bulk silver has the highest electrical conductivity ($\sigma=6.3 \cdot 10^7 \text{ } \Omega^{-1} \cdot \text{m}^{-1}$)^{1,5} of all metals at room temperature and it is resistant against oxidation. The room-temperature conductivity of bulk copper is only 6% lower ($\sigma=5.96 \cdot 10^7 \text{ } \Omega^{-1} \cdot \text{m}^{-1}$)^{1,5} compared to bulk silver, but copper nanoparticles (CuNPs) easily oxidize and long-term stable CuNPs require coatings with dense ligand shells, preventing oxygen migration to the copper cores.^{766–768} Hence, further studies should also explore if polythiophene ligands are suitable to protect CuNPs from oxidation. I demonstrated in this work, that polythiophenes preferentially bind to gold nanocrystals via sulfur species. Compared to gold, silver and copper have less affinity towards sulfur, which is reflected in the decrease of bond dissociation energy from Au-S ($418 \text{ kJ} \cdot \text{mol}^{-1}$)²³⁰ via Cu-S ($276 \text{ kJ} \cdot \text{mol}^{-1}$)²³⁰ through to Ag-S ($217 \text{ kJ} \cdot \text{mol}^{-1}$).⁴²⁶ The covalent character of the metal-sulfur bond increases $\text{Ag} < \text{Cu} < \text{Au}$.⁷⁶⁹ Due to the reduced affinity of silver and copper towards sulfur, it could perhaps be challenging to produce stable AgNPs and CuNPs with dense polythiophene ligand shells.

Silver and copper possess a slightly higher affinity towards oxygen illustrated by the larger bond dissociation energies of Cu-O ($343 \text{ kJ} \cdot \text{mol}^{-1}$)²³⁰ and Ag-O ($220 \text{ kJ} \cdot \text{mol}^{-1}$).⁴²⁶ Polythiophenes with oxygen-containing functional groups could enhance the interactions between AgNPs and CuNPs, since these polythiophene ligands may coordinate to the metal cores via oxygen species. Thus, promising ligands are the carboxylated polythiophenes (P3KBT, P3KPT, P3KHT and P3KHepT) and the sulfonate-containing polythiophenes (PTEBS and PEDOT:PSS). Further studies could also investigate if other conductive polymers with oxygen-containing groups beyond polythiophenes such as carboxylated polypyrrole^{760,770} or carboxylated polyaniline^{771,772} are suitable for the stabilization of AgNPs and CuNPs. Since silver and copper nanocrystals with various

shapes, including spherical nanoparticles, nanorods, nanocubes, nanowires and nanoplates can be synthesized with CTAB as a capping agent,^{773–779} upcoming studies should explore if similar ligand exchange reactions⁶⁹ used in this work are appropriate preparation methods for conductive hybrid AgNPs and CuNPs.

Due to ionic interactions, aqueous synthesis of gold nanocrystals is often limited to dilute gold concentrations, while synthesis routes in organic (nonpolar) solvents overcome this problem and yield dispersions with higher gold concentrations.^{780,781} This could be beneficial for the formulation of printable AuNPs inks, since the commercial large-scale printing of conductive patterns requires inks with high metal loading (20–80%).^{1,5,29} Furthermore, the synthesis of AuNPs in organic media enables a better control over nanoparticle size and yields narrow particle size distributions,^{780,782} e.g. very small nanoparticles (2–10 nm) can be obtained from Brust-Schiffrin method.^{110,111,783} Since the dimensions of the nanoparticles should be less than 0.1–0.01 of the diameter of the printing nozzle,¹ AuNPs inks with smaller particle size may enable the utilization of smaller printing nozzles, which could improve the resolution of the inkjet-printed structures. Hence, future studies should explore if AuNPs synthesized in organic media are suitable for the preparation of printable gold-polythiophene hybrid inks.

The usage of organic solvents also broadens the range of suitable conductive polymer ligands for the production of sinter-free gold polythiophene hybrid nanoparticles, since derivatives of classical conductive polymers such as polyacetylene, polypyrrole or polyaniline are only soluble in organic media. There is also a large variety of commercially available conducting polythiophenes, which are soluble in organic solvents, including poly-(3-butylthiophene-2,5-diyl) (P3BT), poly(3-hexylthiophene-2,5-diyl) (P3HT), poly(3-octylthiophene-2,5-diyl) (P3OT), poly(3-decylthiophene-2,5-diyl) (P3DT) and poly(3-dodecylthiophene-2,5-diyl) (P3DDT). This could open up new opportunities in the development of sinter-free gold-polythiophene hybrid nanoparticles. Thus, further studies should functionalize gold nanocrystals with different shapes by various organic-solvent-soluble conductive polymer ligands and characterize the resulting gold- polythiophene hybrid nanocrystals regarding their colloidal stability and electrical properties.

Recently, the production of complex electrically conductive structures by 3D printing gained much interest.^{5,784–787} 3D printing of (metallic) nanoparticles requires the formulation of suitable nanocomposites by incorporating the nanocrystals into 3D printable polymer matrices such as thermoplastic polymers.^{5,786,787} For example, Li and co-workers produced flexible three-dimensional electrical circuits by 3D printing of a nanocomposite based on polylactic acid (PLA) with reduced graphene oxide (rGOx).⁷⁸⁸ Possible applications of such 3D printed electrically conductive nanocomposites are sensors,^{789,790} actuators,^{791,792} batteries,^{793,794} supercapacitors^{795,796} and wearable electronics.^{797,798} Hydrogels are promising matrices for nanocomposites in biological applications due to their non-toxicity, biocompatibility, self-healing and mechanical characteristics similar to human native tissue.^{799–802} 3D printed electrically conductive nanocomposites based on hydrogels have been successfully used in sensors,^{803,804} flexible electronics,^{805,806} energy storage devices,^{807,808} bioelectronics^{809,810} and tissue engineering.^{811–813}

Future studies should investigate if the sinter-free gold-polythiophene hybrid nanoparticles developed in this work can also be used to formulate 3D printable inks. The hybrid nanoparticles should be incorporated in diverse 3D printable polymer matrices. Suitable inks require gold-polythiophene hybrid nanoparticle contents above the percolation threshold and excellent dispersibility of the nanocrystals in the appropriate matrix material. According to percolation theory, percolation threshold describes the transition point between an insulating and an electrically conductive state of a nanocomposite.^{179,180} Commonly, nanocrystals in nanocomposites are randomly dispersed in the polymer matrix. At nanocrystal concentrations below the percolation threshold the particles are separated in the matrix, yielding an electrically insulating nanocomposite, while at nanocrystal concentrations above the percolation threshold the nanoparticles form percolating networks inside the polymer matrix, which result in an electrically conductive nanocomposite.^{186,814,815,816,817} The percolation threshold depends on parameters such as the size and shape of the nanocrystals, the nanocrystal assembly, the polarity of the matrix and the processing of the composite.^{815,786,818–820} The concentration of nanocrystals can also affect the rheological properties and thus the printability of the ink. A first step in the formulation of 3D printable inks should be the

determination of the percolation threshold of gold-polythiophene hybrid nanoparticles in various polymer matrices. Hydrogels could be attractive 3D printable matrices for the biofunctionalizable gold-polythiophene hybrid nanoparticles (e.g. AuNPs@P3KHT) devised in this work. The resulting nanocomposites could be applied for different biological and biomedical applications. I demonstrated the compatibility of the biofunctionalizable gold-polythiophene hybrid nanoparticles with different cell types. 3D printing of hydrogel-based nanocomposites containing such hybrid nanoparticles could open up new options in modern tissue engineering by printing electrically conductive scaffolds to facilitate cell growth.

6. Experimental part and characterization

6.1 Materials

All materials and chemicals listed in Table 6-1 were used as provided by the supplier without further purification. All aqueous solutions were prepared using ultrapure Milli-Q water ($18.2 \text{ M}\Omega\cdot\text{cm}^{-1}$), which was obtained by a water purification system Elix 20 (Merck Millipore, Burlington, USA). Chloroauric acid ($\text{HAuCl}_4\cdot 3 \text{ H}_2\text{O}$) was produced by dissolving gold bars (999.9 Degussa, München, Germany) in aqua regia according to an established protocol.⁸²¹

Table 6-1: List of used chemicals and materials.

Chemical/Material	Abbreviation	Purity	Supplier
Cetyltrimethylammonium bromide	CTAB	99%	Sigma Aldrich (Steinheim, Germany)
Sodium oleate	NaOL	$\geq 99\%$	Sigma Aldrich (Steinheim, Germany)
Silver nitrate	AgNO_3	$> 99\%$	Sigma Aldrich (Steinheim, Germany)
Sodium borohydride	NaBH_4	99%	Sigma Aldrich (Steinheim, Germany)
Hydrochloric acid	HCl	37 wt% in water	Sigma Aldrich (Steinheim, Germany)
Poly[2-(3-thienyl)-ethyloxy-4-butylsulfonate] (average $M_w=40 \text{ kDa}$ -70 kDa)	PTEBS	n/a	Solaris Chem Inc. (Quebec, Canada)
Poly(3,4-ethylenedioxythiophene) polystyrene sulfonate (aqueous solution Clevios P)	PEDOT:PSS	1.3 wt% in water	Heraeus (Hanau, Germany)
Poly[3-(potassium-4-butanoate)thiophene-2,5-diyl] (average $M_w=12 \text{ kDa}$ -16 kDa)	P3KBT	n/a	Rieke Metals (Lincoln, USA)
Poly[3-(potassium-5-pentanoate)thiophene-2,5-diyl] (average $M_w=30 \text{ kDa}$ -40 kDa)	P3KPT	n/a	Rieke Metals (Lincoln, USA)
Poly[3-(potassium-6-hexanoate)thiophene-2,5-diyl] (average $M_w=55 \text{ kDa}$ -65 kDa)	P3KHT	n/a	Rieke Metals (Lincoln, USA)
Poly[3-(potassium-7-heptanoate)thiophene-2,5-diyl] (average $M_w=55 \text{ kDa}$ -65 kDa)	P3KHepT	n/a	Rieke Metals (Lincoln, USA)
Polyoxyethylene-20-sorbitan monolaurate	Tween 20	n/a	Sigma Aldrich (Steinheim, Germany)

1-Ethyl-3-(3-dimethylaminopropyl)carbodiimide hydrochloride	EDC	≥99%	Sigma Aldrich (Steinheim, Germany)
N-Hydroxysuccinimide	NHS	98%	Sigma Aldrich (Steinheim, Germany)
N-Hydroxysulfosuccinimide sodium salt	Sulfo-NHS/S-NHS	>95%	Sigma Aldrich (Steinheim, Germany)
Glucose oxidase from <i>Aspergillus niger</i> 100,000-250,000 units/g solid (without added oxygen)	GOx	Protein, ≥65%	Thermo Fisher Scientific (Waltham, USA)
O-(2-Aminoethyl)-O'-methylpolyethylene glycol, ($M_w=5$ kDa, extent of labeling: ≥0.17 mmol/g NH ₂ loading)	PEG-NH ₂	n/a	Sigma Aldrich (Steinheim, Germany)
2,2'-azino-bis(3-ethylbenzothiazoline-6-sulfonic acid) diammonium salt	ABTS	≥98%	Sigma Aldrich (Steinheim, Germany)
Peroxidase from horseradish (≈150 U/mg)	HRP	n/a	Sigma Aldrich (Steinheim, Germany)
D-glucose	Gluc	≥99.5%	Sigma Aldrich (Steinheim, Germany)
D-fructose	Fruc	≥99%	Sigma Aldrich (Steinheim, Germany)
D-sucrose	Suc	≥99.5%	Sigma Aldrich (Steinheim, Germany)
D-maltose monohydrate	Mal	≥99%	Sigma Aldrich (Steinheim, Germany)
Lactose tested according to Ph. Eur.	Lac	n/a	Sigma Aldrich (Steinheim, Germany)
Uric acid	UA	≥99%	Sigma Aldrich (Steinheim, Germany)
L-Ascorbic acid	AA	≥99%	Sigma Aldrich (Steinheim, Germany)
Oxalic acid	OA	98%	Sigma Aldrich (Steinheim, Germany)
Urea	UR	≥98%	Sigma Aldrich (Steinheim, Germany)
RGD cyclo(Arg-Gly-Asp-phe-Cys)	c(RGDfC) or RGD	n/a	Vivitide (Gardner, USA)
IK-19 peptide (J65640 Laminin A Chain [2091-2108])	IK-19	n/a	Alfa Aesar (Haverhill, USA)
4,7,10-Trioxa-1,13-tridecanediamine	Diamine linker	97%	Sigma Aldrich (Steinheim, Germany)
Ethanolamine	/	≥99%	Sigma Aldrich (Steinheim, Germany)
Gibco RPMI 1640 medium (61870-010, Scotland facility)	/	n/a	Thermo Fisher Scientific (Waltham, USA)
Fetal bovine serum (Brazil, 10270)	FBS	n/a	Thermo Fisher Scientific (Waltham, USA)
Triton X-100	/	laboratory grade	Sigma Aldrich (Steinheim, Germany)
Bovine serum albumin	BSA	≥98%	Sigma Aldrich (Steinheim, Germany)
DMEM/F12 medium (Invitrogen, 31331093)	/	n/a	Thermo Fisher Scientific (Waltham, USA)
N-2 Supplement (Invitrogen)	N2	n/a	Thermo Fisher Scientific (Waltham, USA)

Heparin (Invitrogen)	/	n/a	Thermo Fisher Scientific (Waltham, USA)
Epidermal growth factors (Invitrogen)	EFGs	n/a	Thermo Fisher Scientific (Waltham, USA)
Basic fibroblast growth factors	FGFs-2/bFGFs	n/a	Thermo Fisher Scientific (Waltham, USA)
Penicillin-Streptomycin (10.000 u/mL) (Invitrogen, 15140-122)	P/S	n/a	Thermo Fisher Scientific (Waltham, USA)
Tetramethylrhodamine B isothiocyanate-phalloidin	TRITC-phalloidin	n/a	Thermo Fisher Scientific (Waltham, USA)
4',6-diamidino-2-phenylindole (Life Technology)	DAPI	n/a	Thermo Fisher Scientific (Waltham, USA)
Citric acid monohydrate (for citrate phosphate buffer)	CA	≥99%	Sigma Aldrich (Steinheim, Germany)
Disodium hydrogen phosphate dihydrate (for citrate-phosphate and PBS buffer)	Na ₂ HPO ₄ ·2 H ₂ O	≥99%	Carl Roth (Karlsruhe, Germany)
Potassium dihydrogen phosphate (for PBS buffer)	KH ₂ PO ₄	≥99%	Carl Roth (Karlsruhe, Germany)
2-(N-morpholino)ethanesulfonic acid	MES	≥99%	Sigma Aldrich (Steinheim, Germany)
Sodium chloride	NaCl	≥99.8%	Carl Roth (Karlsruhe, Germany)
Sodium hydroxide (pellets)	NaOH	≥97%	Sigma Aldrich (Steinheim, Germany)
Nexterion slide H	/	/	Schott AG (Mainz, Germany)
Silver paste (Acheson, G3692)	/	/	Plano GmbH (Wetzlar, Germany)

6.2 Experimental procedures

6.2.1 Synthesis of gold nanocrystals

Synthesis of gold nanorods (AuNRs)

Gold nanorods (AuNRs@CTAB) were synthesized according to a reported procedure by Ye *et al.*¹⁵⁰ The synthesis is based on a seed-mediated growth. In a first step, a seed solution was prepared by mixing 5 mL of aqueous CTAB solution (0.2 M) with 5 mL of aqueous HAuCl₄ solution (0.5 mM). Subsequently, 1 mL of a freshly prepared NaBH₄ (6 mM) solution was added to the mixture under vigorous stirring (1200 rpm). After NaBH₄ addition, the yellow solution turned brown, indicating the formation of gold seeds. The seed solution was stirred for 2 min and aged in an oven at 30 °C for 30 min.

Additionally, a growth solution was prepared by dissolving 7.0 g CTAB and 1.23 g NaOL in 475 mL warm Milli-Q water (40 °C to 50 °C). After complete dissolution of the solid materials, the solution was cooled down to 30 °C. Subsequently, 12 mL of aqueous AgNO₃ solution (8 mM) was added to the stirred solution (300 rpm). The growth solution was kept undisturbed at 30 °C for 15 min. Afterwards 25 mL of aqueous HAuCl₄ solution (10 mM) was added under vigorous stirring (700 rpm) and the solution was stirred (700 rpm) for 90 min. During this time period the orange growth solution became colorless. The pH of the solution was adjusted by adding 2.1 mL HCl (37 wt% in water, 12.1 M) under stirring (400 rpm). The solution was stirred at 400 rpm for 15 min. In the next step, 1.25 mL of aqueous ascorbic acid solution (0.064 M) was added and the solution was vigorously stirred (700 rpm) for 30 s. Finally, 400 µL of the freshly prepared seed solution was added to the growth solution and the solution was stirred (900 rpm) for 30 s. In the last step, the solution was aged by keeping it undisturbed for 12 h in an oven at 30 °C. The final products (AuNRs@CTAB) were collected by centrifugation at 3700 rpm for 38 min. The centrifugation step in Milli-Q water (18.2 MΩ·cm⁻¹) was repeated twice to remove remaining educts from the solution. The washed AuNRs@CTAB were kept in aqueous CTAB solution (5 mM).

Synthesis of spherical gold nanoparticles (AuNPs)

I synthesized spherical gold nanoparticles (AuNPs@CTAB) by slightly modifying the protocol of the AuNRs synthesis established by Ye *et al.*¹⁵⁰ The synthesis was also based on a seed-mediated growth. The required seed solution was produced in the same way as for synthesis of AuNRs described above.

A growth solution was prepared by dissolving 10.0 g CTAB and 1.23 g NaOL in 480 mL warm Milli-Q water (40 °C to 50 °C). After complete dissolution of the solid materials, the solution was cooled down to 30 °C. Subsequently, 12 mL of aqueous AgNO₃ solution (4 mM) was added under stirring (300 rpm). In the next step, 4 mL of aqueous HAuCl₄ solution (0.5 M) was added and the solution was vigorously stirred (900 rpm) for 10 min at 30 °C. Afterwards, 4 mL of the seed solution was added to the stirred (900 rpm) growth solution. In the last reaction step, 10 mL of aqueous ascorbic acid solution (0.064 M) was added dropwise to the solution and the solution was vigorously stirred (900 rpm) for 12 h. The final products (AuNPs@CTAB) were collected by centrifugation at 3000 rpm for 30 min. The centrifugation step in Milli-Q water (18.2 MΩ·cm⁻¹) was repeated twice to remove remaining educts from the solution. The washed AuNPs@CTAB were kept in CTAB solution (5 mM).

Hybrid gold nanoparticle inks for inkjet printing required dispersions with high gold contents (100-200 mg·mL⁻¹). Such high gold concentrations could not be achieved by the laboratory synthesis described above. Hence, our group upscaled the synthesis to produce AuNPs@CTAB in the gram-scale. Large-scale synthesis was conducted in a 10 L reactor and each batch yielded approximately 10 g of AuNPs@CTAB. Details about the upscaling process and the nanoparticle synthesis in the 10 L reactor are given in a recently published report of our group.⁶³⁶ Synthesis of AuNPs@CTAB in the upscaled setup was performed by Anja Colbus and Maria Rodríguez Jiménez. Both, the AuNPs@CTAB obtained from the laboratory and the large-scale synthesis, were functionalized with conductive polythiophene ligands according to the procedures described in the upcoming section 6.2.2.

6.2.2 Surface modification of gold nanocrystals with conductive polythiophene ligands

The surface modification of as-synthesized gold nanocrystals (AuNPs@CTAB and AuNRs@CTAB) with different conductive polythiophenes was done by ligand exchange reaction. The as-synthesized nanocrystals were stored in aqueous CTAB solution (5 mM). However, successful ligand exchange requires excess CTAB concentration of 100 μM or even below.⁸²² Hence, the as-synthesized gold nanocrystals were centrifuged in Milli-Q water ($18.2 \text{ M}\Omega\cdot\text{cm}^{-1}$) for three times to gradually reduce the CTAB concentration. After the third centrifugation step, a CTAB concentration of about 80 μM was achieved. Centrifugation of AuNRs@CTAB was done at 3700 rpm for 38 min, while AuNPs@CTAB were centrifuged at 3000 rpm for 30 min.

Ligand exchange with PTEBS and PEDOT:PSS

Ligand exchange was conducted to replace CTAB by polythiophenes. I slightly modified an established protocol to functionalize gold nanocrystals with PTEBS and PEDOT:PSS.⁶⁹

In short, the conductive polymers PTEBS and PEDOT:PSS were dissolved in Milli-Q water ($18.2 \text{ M}\Omega\cdot\text{cm}^{-1}$). Purified nanocrystals (excess CTAB concentration below 100 μM) were added to the polymer solutions and incubated for 3 days under stirring (700 rpm). It is important that the washed nanocrystals were immediately combined with the polymer solution after purification, since the AuNPs@CTAB and AuNRs@CTAB are prone to agglomeration in solutions with CTAB concentrations below the critical micelle concentration, which is 1 mM.⁸²³ In the ligand exchange solution the mass ratio of polythiophene to gold was 1:1. In other words, 15 mg of polythiophene needed to be dissolved if the total amount of gold was also 15 mg. After ligand exchange, the polythiophene-stabilized gold nanocrystals were purified three times by centrifugation in Milli-Q water ($18.2 \text{ M}\Omega\cdot\text{cm}^{-1}$) again to remove excess polythiophene ligands. The same parameters (centrifugation speed and time) as for the washing of the CTAB-stabilized gold nanocrystals were also applied for the purification of the polythiophene-functionalized nanocrystals (AuNRs@PTEBS, AuNPs@PTEBS, AuNRs@PEDOT:PSS,

AuNPs@PEDOT:PSS). According to a published protocol, ligand exchange should lead to a surface coverage of polythiophenes that is in the range of 9-10 mg/m² (equivalent to Au:polythiophene mass ratio of 1:0.8) as determined via TGA and UV-vis spectroscopy).⁶⁹

Ligand exchange with carboxylated polythiophenes

Surface modification of gold nanocrystals with carboxylated polythiophenes P3KBT, P3KPT, P3KHT and P3KHepT was also performed by slightly modifying an established ligand exchange protocol.⁶⁹ In this work, I only functionalized spherical AuNPs@CTAB with various carboxylated polythiophenes. However, the used ligand exchange procedure is also valid for other CTAB-stabilized gold nanocrystals, including AuNRs@CTAB.

In short, solutions of the different carboxylated polythiophenes were prepared by dissolving the solid polymers in Milli-Q water (18.2 MΩ·cm⁻¹). In a common ligand exchange reaction, 100 mg of the desired carboxylated polythiophene was dissolved in 250 mL Milli-Q water (18.2 MΩ·cm⁻¹). Complete dissolution required vigorous stirring (700 rpm) of the solution at a slightly evaluated temperature of 30 °C overnight (12-14 h). The washed AuNPs@CTAB (excess CTAB concentration below 100 μM) were added to the polythiophene solution and incubated for 7 days under vigorous stirring (700 rpm) of the solution at a constant temperature of 30 °C. In the ligand exchange solution, the mass ratio of polythiophene to gold was 1:1. In other words, if 100 mg of carboxylated polythiophene was dissolved, 100 mg of gold in the form of AuNPs@CTAB also needed to be added to the solution.

The final products (AuNPs@P3KBT, AuNPs@P3KPT, AuNPs@P3KHT and AuNPs@P3HepT) were washed by centrifugation to remove excessive polythiophenes from the solution. The purification process was either performed in Milli-Q water (18.2 MΩ·cm⁻¹) or in aqueous Tween 20 (0.05 vol%) solution. To do so, the ligand exchange solution was transferred to centrifuge tubes (maximal volume 50 mL). The tubes were filled half-way (22.5 mL) with this solution and filled up (additional 22.5 mL) with Milli-Q water or aqueous Tween 20 solution (0.05 vol%). Hence, the volume ratio of

ligand exchange solution to Milli-Q water/Tween 20 solution was 1:1 inside the tubes. Since the biofunctionalizable gold-polythiophene hybrid nanoparticles are prone to agglomeration, mild centrifugation conditions were applied. In a first centrifugation step, the gold-polythiophene hybrid nanoparticles were purified at 2000 rpm for 3 h. After centrifugation the supernatant was removed and the residues were dissolved in small amounts (1-2 mL) of Milli-Q water or aqueous Tween 20 solution (0.05 vol%). Subsequently, the dissolved residues were filtered through syringe filters with polyethersulfone (PES) membranes (pore size 0.22 μm). Filtered residues of two centrifugation tubes were combined and transferred to one new centrifugation tube. The tubes were again filled with either Milli-Q water or aqueous Tween 20 solution (0.05 vol%) until a total volume of 45 mL was reached. The biofunctionalizable hybrid particles were centrifuged for a second time at 2000 rpm for 3 h. Afterwards, the supernatant was discarded and the residues were redispersed in small amounts (1-2 mL) of Milli-Q water or aqueous Tween 20 solution (0.05 vol%) solution again. The redispersed residues of two centrifugation tubes were combined again in one new tube and the tubes were filled up to 45 mL with the appropriate solvent (Milli-Q water or aqueous Tween 20 solution) and centrifugation was repeated for a third time at 2000 rpm for 3 h.

After the third centrifugation step, the supernatant was removed again and the residues were dissolved in as little Milli-Q water as possible (maximal 1 mL). All redispersed residues were transferred to small silanized glass vials (volume 1.5 mL). Usually, all residues fitted into two or three vials. No aqueous Tween 20 solution (0.05 vol%) was used for dispersing the residues, even if it was used in the prior washing steps, since the last centrifugation step was applied to remove the maximal amount of Tween 20 surfactant. However, Tween 20 was also responsible for an enhanced nanoparticle stability during centrifugation. On account of the fact that the surfactant is missing in the last purification step, milder centrifugation conditions were applied to prevent nanoparticle agglomeration. The fourth centrifugation step was performed at only 580 rpm overnight (12-14 h). Subsequently, the supernatant was discarded and the residues were dissolved in small amounts of Milli-Q water. The final volume of the

washed biofunctionalizable gold-polythiophene hybrid nanoparticle dispersion was between 1 mL and 1.5 mL.

I took samples for colloidal (DLS and ζ potential measurements) and UV-vis characterization of all gold-polythiophene hybrid nanoparticles (AuNPs@P3KBT, AuNPs@P3KPT, AuNPs@P3KHT and AuNPs@P3HepT) after each centrifugation step in Milli-Q water and aqueous Tween 20 solution (0.05 vol%). DLS and ζ potential analysis of the samples were performed with constant gold concentrations of $1 \text{ mg}\cdot\text{mL}^{-1}$. Further experimental details about DLS and zeta characterization are given in sections 6.3.9 and 6.3.10

I prepared suitable samples for UV-vis analysis by diluting the original samples with the appropriate solvent (Milli-Q water or aqueous Tween 20 solution). All samples obtained after the first centrifugation step were diluted 1:2 with the respective solvent. After the second centrifugation step, I diluted the obtained samples 1:4 and after the third washing step 1:8 with the particular solvent. Finally, after the last purification step, I prepared UV-vis samples by diluting the highly concentrated gold-polythiophene hybrid nanoparticle dispersions 1:500 with the appropriate solvent.

Ligand exchange with PFS-Na

In this work, I only functionalized spherical AuNPs@CTAB with the polythiophene ligand PFS-Na. However, the used ligand exchange procedure is also applicable for other CTAB-stabilized gold nanocrystals, including AuNRs@CTAB.

Since the conductive polymer PFS-Na is sensitive to light and oxygen, the ligand exchange was conducted under argon atmosphere and in the dark. Appropriate amounts of PFS-Na were dissolved in Milli-Q water ($18.2 \text{ M}\Omega\cdot\text{cm}^{-1}$) under vigorous stirring (700 rpm) at 80°C and under reflux conditions. To avoid loss of water, a Dimroth condenser was mounted on a Schlenk flask. Complete dissolution of PFS-Na in Milli-Q water required stirring for 4 days under the previously mentioned conditions. In a common ligand exchange reaction, 30 mg of PFS-Na was dissolved in 20 mL of Milli-Q water. After total dissolution of the solid PFS-Na polymer, the washed AuNPs@CTAB

(excess CTAB concentration below 100 μM) were added to the polythiophene solution and incubated for 14 days under argon atmosphere and reflux conditions. In the ligand exchange solution, the mass ratio of PFS-Na to gold was 1:1. In other words, if 30 mg of PFS-Na was dissolved, 30 mg of gold in the form of AuNPs@CTAB also needed to be added to the solution. During ligand exchange, the solution was vigorously stirred (700 rpm) at a constant temperature of 70 $^{\circ}\text{C}$.

After ligand exchange, the final products AuNPs@PFS-Na were purified by centrifugation. In contrast to the pure polymer, the produced AuNPs@PFS-Na were not sensitive to light and oxygen. Thus, the purification procedure was conducted in air at ambient conditions. The ligand exchange solution was transferred to centrifugation tubes. However, each tube was only filled to one quarter of the maximal volume by the ligand exchange solution. Subsequently, all centrifugation tubes were filled up to the maximal volume using Milli-Q water and centrifugation was conducted at 1700 rpm for 45 min. The supernatant was removed and the residues were redispersed in small amounts of Milli-Q water (0.5-1 mL). The dissolved residues of two centrifuge tubes were combined and transferred to one new centrifugation tube.

Centrifugation with the same parameters (centrifugation speed and time) was repeated twice. After each centrifugation step, redispersions of the residues and combination of the residues were conducted according to the procedure described above. After the third centrifugation step, the redispersed and combined residues were filtered through syringe filters with polyethersulfone (PES) membranes (pore size 0.22 μm). The filtered residues were transferred to new centrifugation tubes and purification was performed in a last centrifugation step at 1700 rpm for 45 min. Finally, the supernatant was removed again and the residues were dissolved in small amounts of Milli-Q water. The final volume of the purified AuNPs@PFS-Na dispersion was between 0.5 mL and 1 mL.

6.2.3 Bioconjugation of biofunctionalizable gold-polythiophene hybrid nanoparticles

Glucose oxidase (GOx), a commercially available and highly stable enzyme with widespread usage in glucose sensing,^{531–539} was used as a model system to perform bioconjugation of biomolecules to biofunctionalizable gold-polythiophene hybrid nanoparticles AuNPs@P3KHT via EDC/NHS coupling. In addition, aminated polyethylene glycol (PEG-NH₂) was also covalently linked to AuNPs@P3KHT using EDC/NHS chemistry. Bioconjugation can be conducted after film deposition, further referred to as surface bioconjugation or in solution prior to film formation, denoted as solution bioconjugation. The bioconjugation protocols described below were used to couple both molecules, GOx and PEG-NH₂, to AuNPs@P3KHT.

Surface bioconjugation

In order to perform bioconjugation after film deposition, I adapted and modified a protocol which was originally developed for the bioconjugation between carboxyl groups of hydrogels with primary amine groups of peptides via EDC/NHS coupling.^{529,530}

Gold layers were deposited by drop-casting on glass substrates or inkjet-printed on PET foils (central part of the working electrode in the biosensor design) according to the procedures described in sections 6.2.4 and 6.2.5. Activation solution was prepared by dissolving 60 mg of 1-Ethyl-3-(3-dimethylaminopropyl)carbodiimide hydrochloride (EDC) and 20 mg *N*-Hydroxysuccinimide (NHS) in 2 mL MES buffer (0.1 M, pH 4.7) containing 0.5 M NaCl. The final EDC and NHS concentrations were 156.5 mM and 86.9 mM, respectively. Since EDC and NHS react immediately with each other, it is important to prepare the activation solution fresh for every bioconjugation process.

The hybrid nanoparticle films to be bioconjugated were placed in a plastic petri dish, which had been lined with parafilm beforehand. Subsequently, small volumes (100–200 μ L) of EDC/NHS reagent were pipetted onto the parafilm and the hybrid gold films on glass substrates or PET foils were placed on the liquid. Due to capillary forces, the complete area of the substrate, including the hybrid nanoparticle layers, was covered with EDC/NHS reagent. A wet paper towel was placed next to the samples inside the petri dish and the petri dish was sealed. The wet paper towel was used to maintain sufficient

humidity inside the petri dish, preventing evaporation of the EDC/NHS reagent. The sealed petri dish was placed in the refrigerator at 4 °C overnight.

The next day, the samples were taken out of the petri dish and were rinsed three times with Milli-Q water ($18.2 \text{ M}\Omega\cdot\text{cm}^{-1}$). Subsequently, all gold-polythiophene hybrid nanoparticles layers on glass or PET substrates were blow-dried with nitrogen (N_2) gas. Coupling solutions were prepared by dissolving glucose oxidase GOx ($c[\text{GOx}]=0.1 \text{ mg}\cdot\text{mL}^{-1}$) or PEG- NH_2 ($c[\text{GOx}]=0.1 \text{ mg}\cdot\text{mL}^{-1}$) in PBS buffer (0.1 M, pH 7.4). I lined a plastic petri dish with parafilm again and pipetted small volumes (100–200 μL) of coupling solution onto the parafilm. The hybrid nanoparticle layers on glass and PET foils were again placed on the liquid. In doing so, the whole area was covered by the coupling solution due to capillary forces. According to the procedure described previously, a wet paper towel was placed again in the petri dish and the sealed dish was stored in the refrigerator at 4 °C overnight.

The following day, the samples were taken out of the petri dish. Finally, all specimens were washed three times with Milli-Q water ($18.2 \text{ M}\Omega\cdot\text{cm}^{-1}$) and blow-dried with nitrogen (N_2) gas. With this procedure, GOx and PEG- NH_2 were covalently bioconjugated to the surface of the gold-polythiophene hybrid nanoparticle films using EDC/NHS chemistry.

Solution bioconjugation

I also covalently linked glucose oxidase (GOx) and aminated PEG (PEG- NH_2) in solution to AuNPs@P3KHT using EDC/NHS chemistry. Instead of neutral NHS, I used *N*-Hydroxysulfosuccinimide sodium salt (Sulfo-NHS), which introduces additional charges to the nanoparticles during bioconjugation and helps to prevent nanoparticle agglomeration. An activation solution was fabricated by dissolving EDC and Sulfo-NHS in Milli-Q water ($18.2 \text{ M}\Omega\cdot\text{cm}^{-1}$), obtaining a final concentration of each component of 100 mM.

The enzyme GOx or respectively PEG- NH_2 were dissolved in Milli-Q water to obtain aqueous solutions with concentrations of $0.4 \text{ mg}\cdot\text{mL}^{-1}$. Aqueous dispersions of gold-polythiophene nanoparticles AuNPs@P3KHT were added to these solutions under

vigorous stirring (700 rpm) to obtain dispersions with a gold concentration of $1 \text{ mg}\cdot\text{mL}^{-1}$. The dispersions were vigorously stirred at 700 rpm for 10 min. Subsequently, different amounts of prepared EDC/Sulfo-NHS solutions were added while stirring the dispersions (700 rpm). I tested the addition of 0.50 vol%, 0.75 vol%, 1.00 vol%, 1.50 vol%, 2.00 vol% and 3.00 vol%. The added amounts are related to the total reaction volume. For example, a typical reaction volume was 10 mL. The addition of 0.75 vol% EDC/Sulfo-NHS reagent (S-NHS_{low}) was realized by adding 75 μL of the EDC/NHS solution to 9.925 mL of the dispersion containing AuNPs@P3KHT and GOx or PEG-NH₂ ($c[\text{Au}]=1 \text{ mg}\cdot\text{mL}^{-1}$, $c[\text{GOx/PEG-NH}_2]=0.4 \text{ mg}\cdot\text{mL}^{-1}$). Analogously, the addition of 2.00 vol% EDC/Sulfo-NHS reagent (S-NHS_{high}) was achieved by adding 200 μL of EDC/NHS solution to 9.800 mL of the gold hybrid nanoparticle dispersion ($c[\text{Au}]=1 \text{ mg}\cdot\text{mL}^{-1}$, $c[\text{GOx/PEG-NH}_2]=0.4 \text{ mg}\cdot\text{mL}^{-1}$). All other EDC/Sulfo-NHS concentrations were obtained by adjusting the amounts of the EDC/Sulfo-NHS solutions using the same procedure. After addition of the EDC/Sulfo-NHS reagent, the complete solution was vigorously stirred (700 rpm) for 3 days to ensure successful bioconjugation. Most bioconjugation protocols require shorter times (from a few minutes to several hours). However, in these procedures bioconjugation is performed in buffer solutions (MES or PBS buffers) with adequate pH. Most protocols suggest pH values between 7 and 9 to form stable amide bonds between carboxyl and primary amine groups. Since AuNPs@P3KHT were not stable in such buffers with appropriate pH (data presented in section 3.4.1), I decided to perform the bioconjugation in Milli-Q water ($18.2 \text{ M}\Omega\cdot\text{cm}^{-1}$). I measured a pH of 6.8 for the Milli-Q water ($18.2 \text{ M}\Omega\cdot\text{cm}^{-1}$) in our laboratory. Since the bioconjugation rate decreases with decreasing pH (due to decreased half-life time of the intermediate NHS ester),^{824,825,826,384} I chose a reaction time of 3 days to guarantee sufficient time for amide bond formation between AuNPs@P3KHT and GOx or PEG-NH₂.

After 3 days, the bioconjugated AuNPs@P3KHT-GOx or AuNPs@P3KHT-PEG-NH₂ were purified and collected by centrifugation. Purification was applied to remove excess of unreacted EDC, Sulfo-NHS, GOx and PEG-NH₂. The dispersions were transferred to centrifuge tubes and centrifuged for 30 min at 3000 rpm. Subsequently, the supernatant was removed and the residue was redispersed in Milli-Q water ($18.2 \text{ M}\Omega\cdot\text{cm}^{-1}$). Washing

with the same centrifugation parameters (speed and time) was repeated three times. Finally, the residues were dispersed in Milli-Q water ($18.2 \text{ M}\Omega\cdot\text{cm}^{-1}$) or PBS buffer (0.1 M, pH 5.8). The samples were stored in the refrigerator at 4°C until further use.

6.2.4 Deposition of hybrid layers by drop-casting

Aqueous dispersions containing different gold-polythiophene hybrid nanocrystals (AuNRs@PTEBS, AuNPs@PTEBS, AuNPs@PFS-Na, AuNPs@P3KHT and AuNPs@P3KHT-GOx) were utilized to fabricate films possessing line shape on glass substrates. In the deposition process, PDMS strips were used as templates to achieve well-defined lines. Two PDMS strips were placed on a glass substrate and aligned parallel with a spacing of 1-2 mm. This gap defined the width of the deposited line structure. Small amounts (10 μl) of the nanoparticle dispersions were filled into the gap and dried at ambient conditions and room temperature. In order to achieve sufficient layer thickness ($\geq 0.9 \text{ }\mu\text{m}$), this procedure was repeated 5-7 times. The dispersions contained gold concentrations of about $30 \text{ mg}\cdot\text{mL}^{-1}$ for AuNPs@PTEBS, AuNRs@PTEBS and AuNPs@PFS-Na, while the gold concentration of the dispersions containing the biofunctionalizable gold-polythiophene hybrid nanoparticles AuNPs@P3KHT and AuNPs@P3KHT-GOx (bioconjugation in solution with EDC/S-NHS_{low} 0.75 vol% or EDC/S-NHS_{high} 2.00 vol%) was approximately $50 \text{ mg}\cdot\text{mL}^{-1}$.

The precise lateral dimensions (widths and lengths) of the hybrid films were determined by optical microscopy. Details about the microscopic analysis are given in section 6.3.3. The accurate thickness was characterized by 3D confocal microscopy. The determined film thicknesses and the exact lateral dimensions obtained by optical microscopy were used for calculating the resistivity of each deposited line pattern composed of various gold-polythiophene hybrid nanoparticles. Further information about 3D confocal microscopy and about the electrical characterization are given in sections 6.3.5 and 6.3.12, respectively.

6.2.5 Inkjet printing of amperometric biosensors

I fabricated biosensors by inkjet printing on PET substrates using a high-precision inkjet printer PiXDRO LP50 (Meyer Burger, Switzerland), working with the drop-on-demand (DoD) printing technique. The printer has five-axis motion and operates with an accuracy of below 20 μm (3σ) and with a precision of below 5 μm (3σ). As printhead a Dimatix Material Cartridge (FujiFilm, Santa Clara, California, USA) was utilized, containing 16 nozzles (nozzle diameter 21.5 μm) with a spacing of 254 μm in a single row. The printhead is a piezo-based jetting instrument, which releases drops with a nominal volume of 10 pL.

The design of the biosensor is illustrated in Figure 6-1. Each sensor is composed of a working (WE), counter (CE) and reference electrode (RE). Only the center of the working electrode (circle) was composed of the biofunctionalizable gold nanoparticles (AuNPs@P3KHT or AuNPs@P3KHT-GOx), the other parts of the sensor were made of a commercial silver ink Sicrys™ I40DM-106 (PV Nano Cell Ltd, Israel). The commercial ink is a dispersion of silver nanoparticles ($d_{90}=115\text{ nm}$) in diethylene glycol monomethyl ether (DGME). The total concentration of silver in the ink is 40 wt%.

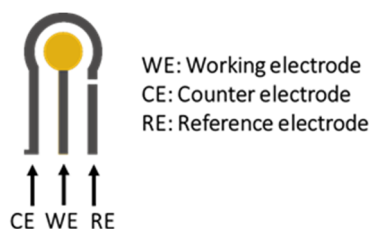


Figure 6-1: Design of inkjet-printed biosensor. Only the central part of the working electrode (orange circle) was composed of biofunctionalizable gold nanoparticles (AuNPs@P3KHT or AuNPs@P3KHT-GOx). Residual parts of the sensor were fabricated using a commercial silver ink Sicrys™ I40DM-106 (PV Nano Cell Ltd, Israel).

In a first printing step, all parts composed of the commercial silver ink were printed on PET foil. Subsequently, the printed silver pattern was sintered at 150 °C for 30 min. The printed silver structures remained nonconductive without sintering. In a second printing step, the aqueous gold ink containing AuNPs@P3KHT or AuNPs@P3KHT-GOx was printed. However, the gold ink showed limited wettability on the PET substrate leading

to low printing quality. Therefore, the PET substrate was exposed to an O₂ plasma prior to printing, which improved the wetting of the gold ink on the polymer substrate. In order to avoid oxidation of the inkjet-printed silver pattern, I covered the structures with a mask made of Scotch tape. The mask contained a hole ($\varnothing=3$ mm), which corresponded to the dimensions of the circular working electrode ($\varnothing=3$ mm) of the biosensor. Hence, only the part of the PET substrate became plasma-activated where the gold ink should be printed on. Immediately after O₂ plasma exposure, the mask was removed and the circular working electrode was produced by inkjet printing of the aqueous gold ink (AuNPs@P3KHT or AuNPs@P3KHT-GOx). Further details about the plasma treatment are given in 6.2.6. The complete fabrication process of the biosensor is illustrated in Figure 6-2.

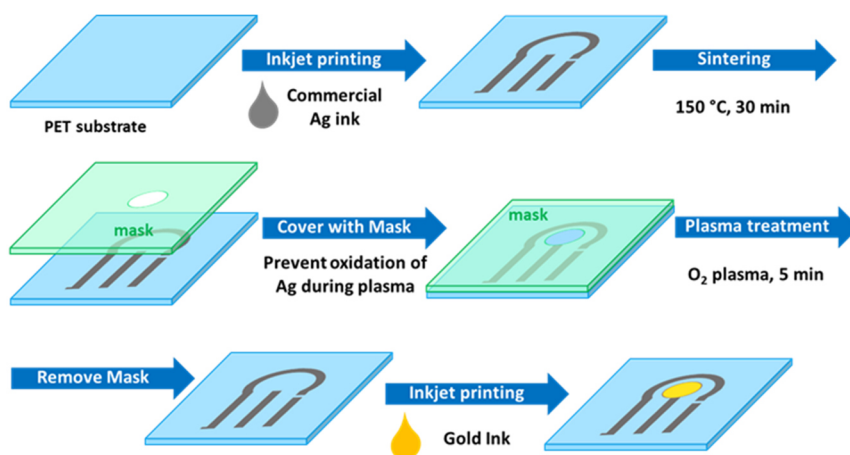


Figure 6-2: Fabrication process of the biosensor by inkjet printing. Only the central part (orange circle) of the working electrode was produced by inkjet printing an aqueous gold-polythiophene hybrid nanoparticle ink (AuNPs@P3KHT or AuNPs@P3KHT-GOx). Commercial silver ink was inkjet-printed to produce the other parts of the biosensor. In order to improve the wettability of the aqueous gold ink on the PET substrate, O₂ plasma was applied. Oxidation of the printed silver pattern was avoided by protecting the silver structures with a mask made of Scotch tape.

For inkjet printing the commercial silver ink and the gold-polythiophene hybrid nanoparticle inks, I applied custom voltage profiles actuating the piezo printhead. Optimized waveforms possessed a trapezoidal shape and were similar for both hybrid nanoparticle inks, containing AuNPs@P3KHT-GOx and AuNPs@P3KHT, respectively. However, successful drop ejection of inks composed of enzyme-functionalized AuNPs@P3KHT-GOx required slightly higher actuating voltages. Since glucose oxidase

molecules are not compatible with organic solvents and many additives such as surfactants, optimization of the used waveforms was the only possibility to optimize drop formation and to avoid satellite generation during inkjet printing of inks containing AuNPs@P3KHT-GOx. The used waveforms, which were implemented to the software of the LP50 printing device, are depicted in Figure 6-3. During inkjet printing of the commercial silver ink, the printhead moved with a speed of $100 \text{ mm}\cdot\text{s}^{-1}$ and deposited droplets at a density of 1000 dpi. To inkjet print the gold hybrid nanoparticle ink, I chose a printing speed of $150 \text{ mm}\cdot\text{s}^{-1}$ and a printing density of 2000 dpi.

I used enzyme-functionalized AuNPs@P3KHT-GOx (bioconjugation with 2.00 vol% EDC/Sulfo-NHS as described in section 6.2.3) and non-functionalized AuNPs@P3KHT to inkjet print the central region of the working electrode. In the case of non-functionalized AuNPs@P3KHT, I bioconjugated glucose oxidase GOx after printing of the working electrode according to the protocol of surface bioconjugation described in section 6.2.3. The gold concentration of all hybrid nanoparticle inks was about $150 \text{ mg}\cdot\text{mL}^{-1}$. Higher gold concentration led to nozzle clogging of the printhead during inkjet printing. In order to achieve sufficient film thickness of the working electrode, I printed two gold layers on top of each other using the same printing parameters mentioned above. Printing of the commercial silver ink only required the deposition of one single layer to obtain adequate thickness of the printed structures.

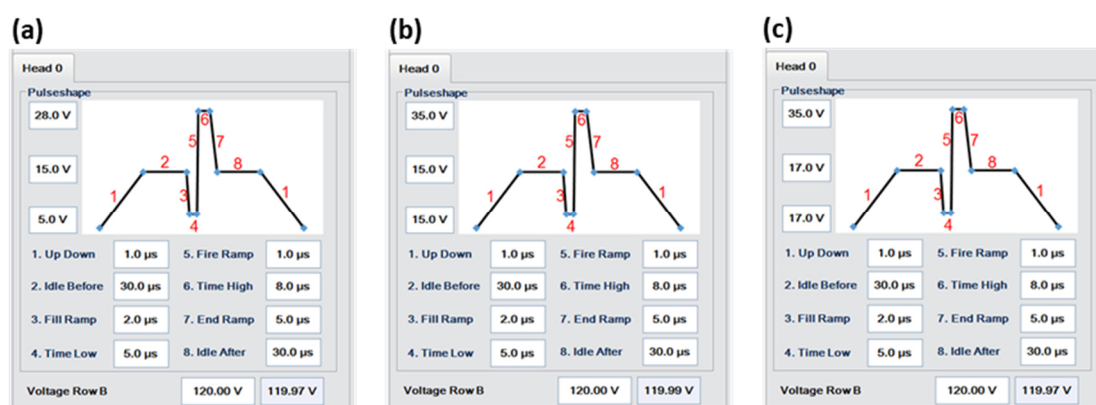


Figure 6-3: Custom voltage profiles (waveforms) driving the piezo printhead during inkjet printing of (a) commercial silver ink, (b) gold-polythiophene hybrid nanoparticle ink AuNPs@P3KHT and (c) enzyme-functionalized gold-polythiophene hybrid nanoparticle ink AuNPs@P3KHT-GOx. Bioconjugation was conducted in solution using EDC/S-NHS_{high} (2.00 vol%).

6.2.6 Plasma treatments

Deposited films of gold-polythiophene hybrid nanocrystals (AuNPs@PTEBS and AuNRs@PTEBS) on glass substrates were exposed to a plasma of 5% hydrogen in argon (Ar/H₂ plasma) for 30 min. Additionally, polyethylene terephthalate (PET) substrates were also subjected for 5 min to an oxygen (O₂) plasma or to an Ar/H₂ plasma in order to change the wetting properties of the gold hybrid inks and of the commercial silver ink Sicrys™ I40DM-106 (PV Nano Cell Ltd, Israel) on PET. Plasma treatment with O₂ plasma increased the hydrophilicity of the PET foils and improved the wetting of the aqueous inks containing AuNPs@P3KHT or AuNPs@P3KHT-GOx on these substrates during inkjet printing. Both plasma types, Ar/H₂ and O₂ plasma, had no impact on the wetting behavior of the commercial silver ink Sicrys™ I40DM-106 (PV Nano Cell Ltd, Israel) on PET substrates. Further experimental details about the inkjet printing process are given in section 6.2.5. All plasma treatments (Ar/H₂ and O₂ plasma) were conducted at 100 W RF power (13.56 MHz) and a gas pressure of 0.3 mbar in a RF PICO plasma system (Diener electronic, Ebhausen, Germany).

6.2.7 Preparation of colorimetric bioassays for glucose detection

All bioassays were fabricated in 96 well half-area microplates with flat bottom made of polystyrene (PS) (Corning, New York, USA). PBS buffer (0.1 M, pH 5.8) was used as a solvent for all samples. The colorimetric detection of glucose was conducted by UV-vis spectroscopy. Details about the UV-vis measurements are described in section 6.3.11. As a byproduct in the oxidation of glucose by glucose oxidase (GOx), hydrogen peroxide (H₂O₂) is formed, which can react with the colorless dye ABTS, resulting in the formation of an ABTS[•] radical. This radical has a characteristic blue-green color, corresponding to an absorption maximum at about 415 nm. Thus, I chose the absorption signal at 415 nm as the output signal for the colorimetric glucose detection in the different developed bioassays.

For the calibration measurements, the bioassays contained enzyme-functionalized hybrid nanoparticles AuNPs@P3KHT-GOx, which were bioconjugated in solution using

EDC/S-NHS_{low} (0.75 vol%) or EDC/S-NHS_{high} (2.00 vol%). Details about the bioconjugation processes are described in section 6.2.3. The gold concentration in the samples for bioassay calibration were 50 $\mu\text{g}\cdot\text{mL}^{-1}$, 25 $\mu\text{g}\cdot\text{mL}^{-1}$, 12.5 $\mu\text{g}\cdot\text{mL}^{-1}$ and 5 $\mu\text{g}\cdot\text{mL}^{-1}$, respectively. Each sample also contained a constant concentration of the dye ABTS being 500 $\mu\text{g}\cdot\text{mL}^{-1}$ and a constant concentration of the enzyme horseradish peroxidase (HRP) being 15 $\mu\text{g}\cdot\text{mL}^{-1}$. Calibration measurements of the colorimetric bioassays containing AuNPs@P3KHT-GOx were performed by varying the glucose concentration in the range of 25 $\mu\text{g}\cdot\text{mL}^{-1}$ to 5 $\text{mg}\cdot\text{mL}^{-1}$. The resulting colorimetric signals at 415 nm due to ABTS[•] radical formation were always taken 10 min after the addition of the various glucose solutions to the different bioassays. For reason of reproducibility, I characterized three individual samples of each glucose concentration and determined the average absorption signals and the corresponding standard deviations.

Kinetic studies were only performed for bioassays with a total gold concentration of 12.5 $\mu\text{g}\cdot\text{mL}^{-1}$ containing AuNPs@P3KHT-GOx, which were bioconjugated in solution using EDC/S-NHS_{low} (0.75 vol%) or EDC/S-NHS_{high} (2.00 vol%). The samples for the kinetic studies also contained constant ABTS concentrations of 500 $\mu\text{g}\cdot\text{mL}^{-1}$ and constant HRP amounts of 15 $\mu\text{g}\cdot\text{mL}^{-1}$. Analysis of the enzymatic kinetics inside the bioassays containing AuNPs@P3KHT-GOx were conducted by varying the glucose concentrations in the samples from 50 $\mu\text{g}\cdot\text{mL}^{-1}$ to 10 $\text{mg}\cdot\text{mL}^{-1}$.

In addition, enzyme kinetics were also investigated for colorimetric bioassays containing only the free enzyme glucose oxidase (GOx). Each sample contained constant concentrations of GOx, HRP and ABTS being 3.125 $\mu\text{g}\cdot\text{mL}^{-1}$, 5 $\mu\text{g}\cdot\text{mL}^{-1}$ and 250 $\mu\text{g}\cdot\text{mL}^{-1}$. Enzymatic kinetics were studied by varying the glucose concentration in the range of 25 $\mu\text{g}\cdot\text{mL}^{-1}$ to 5 $\text{mg}\cdot\text{mL}^{-1}$.

For each glucose concentration, I detected the variation of the absorption signal in the colorimetric bioassays containing AuNPs@P3KHT-GOx or free GOx over a time range of 5 min (step interval 1 min). I estimated the reaction velocity v_0 by the change in the absorption signal at 415 nm over time ($\frac{dAbs}{dt}$). Thus, I fitted the measured absorption data by linear regressions and obtained the reaction velocities v_0 from the slopes m of the regression lines. Exemplary measurement data with corresponding fits of colorimetric

bioassays with free GOx or AuNPs@P3KHT-GOx (bioconjugation in solution with EDC/S-NHS_{low} 0.75 vol% or EDC/S-NHS_{high} 2.00 vol%) are presented in Figure 6-4. I characterized three individual samples of each glucose concentration and the data shown in Figure 6-4 represent the determined average absorption values with the corresponding standard deviations. The experimental data matched well the linear fits ($R^2 \geq 0.99$) as shown in Figure 6-4.

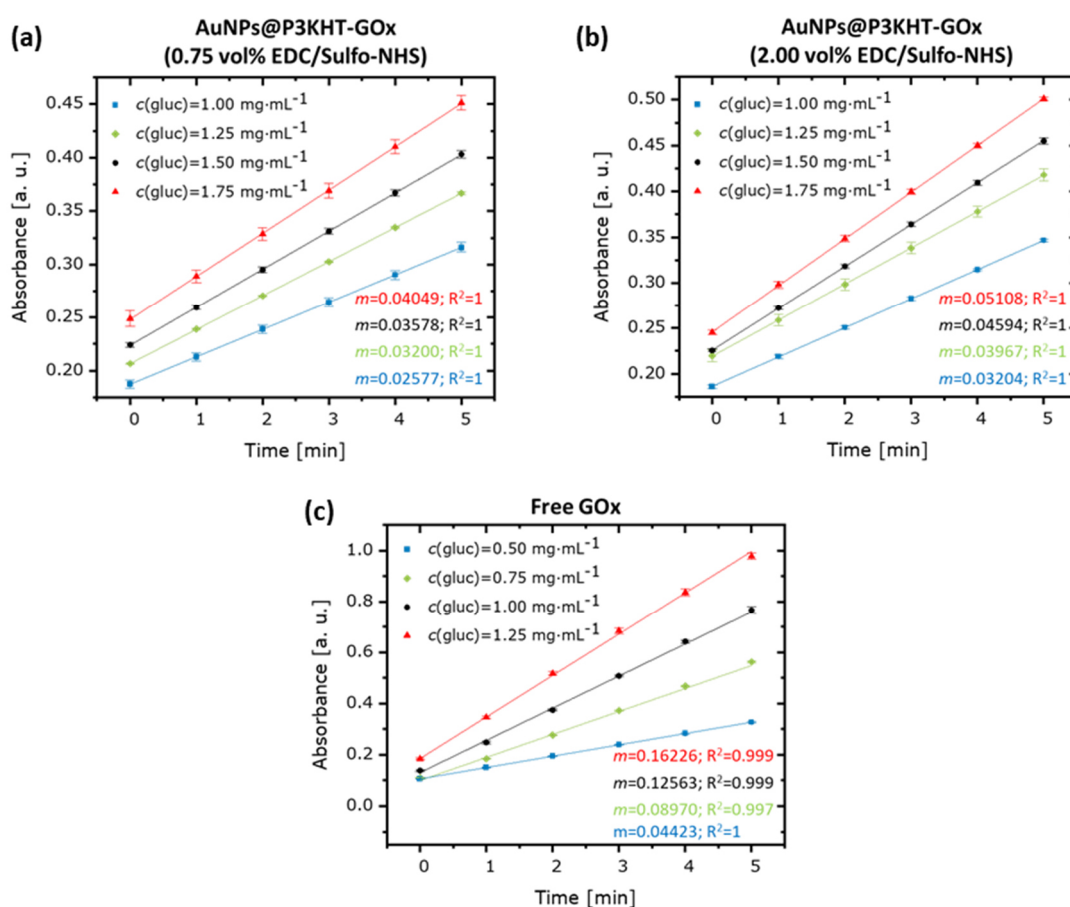


Figure 6-4: Detected absorption change at 415 nm of the colorimetric bioassays containing (a, b) AuNPs@P3KHT-GOx, which were bioconjugated in solution using EDC/S-NHS_{low} (0.75 vol%) or EDC/S-NHS_{high} (2.00 vol%) and (c) free glucose oxidase GOx after addition of glucose solutions with different concentrations. All investigated bioassays based on AuNPs@P3KHT-GOx contained a constant gold concentration of $12.5 \mu\text{g} \cdot \text{mL}^{-1}$. The absorption signals at 415 nm were recorded over a time period of 5 min with a step interval of 1 min. The measurement data were fitted by liner regression and the reaction velocities v_0 were derived from the slopes m of the regression lines. For reason of reproducibility, three different samples of each glucose concentration were characterized. The shown data represent the average absorption signals with corresponding standard deviations.

6.2.8 Preparation of gold-polythiophene hybrid platforms for cell growth

I used Nexterion slides H as substrates to prepare hybrid nanoparticle layers as platforms for cell growth. According to the supplier Schott (Mainz, Germany), Nexterion slides H are very thin glass slides ($d=1$ mm), which are coated with a hydrophilic polymer film. This coating is resistant against non-specific binding of biomolecules. This makes Nexterion slides H the ideal substrate to test the applicability of the gold-polythiophene hybrid nanoparticle layers as platforms for cell growth, since there should be no or negligible interactions between the cells and the Nexterion slides H. Hence, detected cell growth supporting features can be solely attributed to the gold-polythiophene hybrid nanoparticle layers. The coating of the Nexterion slides H is composed of a cross-linked three-dimensional hydrogel network to which activated NHS esters are linked via long and flexible spacer molecules. Biomolecules containing primary amines can react with these reactive NHS ester groups, resulting in stable and covalent amine bonds. Covalent linkage of biomolecules to the Nexterion slides H maintain the conformation of the biomolecules, while non-specific interactions between the substrate and the biomolecules are suppressed.

Nexterion slides H need to be stored in the freezer (-20 °C) under inert gas atmosphere in a sealed package to retain the activity of the NHS ester groups. Before opening the package and exposing the Nexterion slides H to atmospheric conditions (exposure to moisture), the slides should be completely equilibrated at room temperature. Otherwise, condensation will immediately occur on the surface of the Nexterion slides H, resulting in reduced activity of the NHS ester groups. The package should be opened and the Nexterion slides H should be uncased just before starting the experiments. Unused slides should be immediately sealed in the package again under inert gas atmosphere and stored in the freezer (-20 °C).

In the first step, I lined a plastic petri dish with parafilm and prepared a solution of the diamine linker (0.1 mg·mL⁻¹) in PBS buffer (0.1 M, pH 7.4). Subsequently, small volumes (100 - 200 µL) of the diamine linker solution were pipetted onto the parafilm. The Nexterion slide H was placed on the liquid. Due to capillary forces, the complete surface of the Nexterion slide H was covered by the liquid. Since Nexterion slides H possess the

hydrogel coating with the reactive NHS ester groups only on one side, it is important that the coated side faces the liquid. The coated side of the Nexterion H slide has a cut edge on the top left and bottom right. A wet paper towel was placed next to the Nexterion slide H inside the petri dish and the petri dish was sealed. The wet paper towel was used to maintain sufficient humidity inside the petri dish, preventing evaporation of the diamine linker solution. The sealed petri dish was placed in the refrigerator at 4 °C overnight.

The next day, the Nexterion slide H was taken out of the petri dish, rinsed with Milli-Q water ($18.2 \text{ M}\Omega\cdot\text{cm}^{-1}$) and blow-dried with nitrogen gas. Due to the reaction of the NHS ester groups with the diamine linker molecules, the surface of the Nexterion slide H was converted to amine groups. Hybrid nanoparticle films were prepared by drop-casting dispersions containing AuNPs@P3KHT onto the aminated Nexterion slide H. After complete drying of the hybrid nanoparticle layers, covalent linkage of the films to the underlying Nexterion slide H was conducted using EDC/NHS chemistry. In the following process yielding hybrid layers as platforms for cell growth experiments, all individual EDC/NHS coupling steps were performed according to the surface bioconjugation protocol, already described in section 6.2.3. I prepared an activation solution by dissolving 60 mg EDC and 20 mg NHS in 2 mL of MES buffer (0.1 M, pH 4.7) containing 0.5 M NaCl. The final EDC and NHS concentrations were 156.5 mM and 86.9 mM, respectively. Since EDC and NHS react immediately with each other, it is important to prepare the activation solution fresh for every conjugation reaction.

Again, a plastic petri dish was lined with parafilm and small volumes (100-200 μL) of EDC/NHS reactive solution were pipetted onto the parafilm. The Nexterion H slide with the deposited gold-polythiophene hybrid nanoparticle films was placed on the liquid. Due to capillary forces, the whole Nexterion H slide, including the hybrid nanoparticle layers, was covered completely by the EDC/NHS solution. According to the procedure described above, a wet paper towel was placed again in the petri dish and the sealed dish was stored in the refrigerator at 4 °C overnight. Due to EDC/NHS chemistry the carboxylate groups in the ligand shell of the hybrid AuNPs@P3KHT should react with the amine groups present at the surface of the Nexterion slide H, forming stable amide bonds. This reaction should lead to a covalent attachment of the hybrid nanoparticle layers to the underlying

Nexterion slide H. The covalent bonding between the hybrid films and the substrate can prevent delamination of the hybrid gold layers during cell growth experiments.

The following day, the Nexterion slide H with the deposited films made of AuNPs@P3KHT were rinsed with Milli-Q water ($18.2 \text{ M}\Omega\cdot\text{cm}^{-1}$) and blow-dried with nitrogen gas. In order to enhance growth of fibroblasts and neurospheres, I functionalized the hybrid nanoparticle films with RGD- or IKVAV-containing peptidomimetics. I used the commercially available cyclo(RGDfC) and the 19-mer peptide IK-19 for the functionalization. I prepared solutions of the different peptidomimetics ($c[\text{IK-19/cyclo(RGDfC)}]=0.1 \text{ mg}\cdot\text{mL}^{-1}$) in PBS buffer (0.1 M, pH 7.4). It is important to use freshly prepared peptidomimetics solutions for each experiment. A plastic petri dish was again lined with parafilm and small volumes (100-200 μL) of the solutions containing the peptidomimetics were pipetted onto the parafilm. Subsequently, the Nexterion slide H with the deposited gold-polythiophene hybrid nanoparticle films was placed on the liquid. It is important that the whole surface of the slide, including the complete area of the hybrid nanoparticle films, was covered by the liquid. A wet paper towel was placed again in the petri dish and the sealed dish was stored in the refrigerator at 4 °C overnight. Not all of the carboxylate groups in the ligand shell of AuNPs@P3KHT should have reacted with the diamine linker present at the surface of the Nexterion slide H. Hence, the remaining carboxylate groups of AuNPs@P3KHT can react with the amine groups of the peptidomimetics, forming stable amide bonds. This leads to a covalent attachment of the peptidomimetics on the surface of the hybrid nanoparticle layers.

The next day, the Nexterion slide H coated with the gold-polythiophene hybrid nanoparticle layers was taken out of the petri dish, rinsed with Milli-Q water ($18.2 \text{ M}\Omega\cdot\text{cm}^{-1}$) and blow-dried with nitrogen gas. In a last step, the remaining carboxylate groups present in the hybrid nanoparticle films were blocked by reacting with ethanolamine. For this purpose, an ethanolamine solution (50 mM) in PBS buffer (0.1 M, pH 7.4) was prepared. The solution was pipetted onto the hybrid nanoparticle films, covering the whole area of the films. The reaction between the remaining carboxylate groups of AuNPs@P3KHT and ethanolamine was conducted at room temperature under atmospheric conditions. The reaction time was at least 30 min and maximal 60 min. After the reaction, the Nexterion slide H with the deposited hybrid nanoparticle films was rinsed

with Milli-Q water ($18.2 \text{ M}\Omega\cdot\text{cm}^{-1}$) and subsequently wetted with PBS buffer (0.1 M, pH 7.4) to prevent drying. The wet Nexterion slide H coated with the hybrid nanoparticle films was stored in the refrigerator at 4 °C until the start of the cell growth experiments. Cell experiments were always started on the same day as the functionalization process of the hybrid nanoparticle layers with peptidomimetics was finished to ensure a short storage time.

6.2.9 Cell experiments

All cell experiments were performed by Dr. Aleeza Farrukh and Dr. Shifang Zhao from the Dynamic Biomaterials group of Prof. Dr. Aránzazu del Campo (INM-Leibniz Institute for New Materials, Saarbrücken, Germany).

Fibroblast experiments

Fibroblast cells were cultured according to published procedures.^{827–829} Fibroblast L929 cell line (ATCC) was cultivated at 37 °C and 5% CO₂ in RPMI 1640 medium (Gibco, 61870–010) supplemented with 10% FBS (Gibco, 10270) and 1% P/S (Invitrogen).

The cultured fibroblasts were placed on the deposited gold-polythiophene hybrid nanoparticle films with and without RGD functionalization and on aminated Nexterion slides H. The samples were stored in the cell culture incubator for 3 days, while the cell culture medium was replaced by fresh medium every day.

Fixation and staining of fibroblasts

Cultivated fibroblast cells were fixed and stained according to published protocols.^{828,829} Fibroblasts were fixed with 4% paraformaldehyde (PFA) solution for 2 h at room temperature and subsequently washed with PBS (0.1 M, pH 7.4). Samples were blocked with 1% BSA solution and permeabilized with 0.5% Triton X-100 for 1 h.

Actin fibers were stained using TRITC-phalloidin (1:200 in water, Thermo Fisher Scientific) and the nucleus was stained with 4',6-diamidino-2-phenylindole (DAPI) (1:500 in water, Life Technology).

Neurosphere experiments

Neurospheres were cultured according to a reported protocol.^{703,830} All animal experiments were conducted in accordance with the policies on the use of animals approved by Saarland University. Cells were isolated from the cerebral cortex of an embryonic mouse (E14.5) obtained from C57BL/6 mice. Further information about the isolation process can be found in the PhD thesis of Dr. Shifang Zhao.⁸³⁰ The isolated cells were centrifuged at 100 rpm (123g) for 5 min. Subsequently, the collected cell pellets were redispersed in DMEM/F12 medium containing N2 (Invitrogen, 1%), heparin (0.1%), basic fibroblast growth factors (bFGFs, Invitrogen, 20 ng/mL⁻¹), epidermal growth factors (EGFs, Invitrogen, 20 ng/mL⁻¹) and penicillin/streptomycin (N2 complete medium).^{831,832} Afterwards, the dissociated cells were seeded in 6-well plates and maintained as undifferentiated neurospheres. The neurospheres were collected and separated mechanically with a pipette (maximal volume 1 mL). In the next step, the medium was changed from N2 complete media to differentiation media (DMEM-F12/glutamax, 2% B27, penicillin-streptomycin). In the final step, the dissociated neurospheres were seeded on the IK-19-functionalized hybrid films made of AuNPs@P3KHT and on the aminated the Nexterion slides H. Samples were cultured for 3 days in the cell culture incubator.

Fixation and staining of neurospheres

Fixation was performed according to a published procedure.^{703,830} Neurospheres were fixed with paraformaldehyde (PFA) solution (4%) for 10 min and subsequently washed three times with PBS (pH 7.4). Afterwards blocking and permeabilization were conducted by incubating for 45 min with bovine serum albumin (BSA, 2%) and Triton X-100 (0.2%) in PBS (0.1 M, pH 7.4) at room temperature.

Staining was conducted analogously to reported protocols.^{828–830,833} F-actin staining was performed using TRITC-phalloidin (1:200 in water, Thermo Fisher Scientific). Finally, the cells were mounted and the nucleus was stained using an immunoselect antifading mounting medium with DAPI (SCR-038448, Dianova).

6.3 Characterization methods

6.3.1 Transmission electron microscopy (TEM)

Sizes and shapes of the as-synthesized gold nanocrystals, polythiophene-stabilized hybrid gold nanocrystals after ligand exchange and bioconjugated gold-polythiophene hybrid nanocrystals were investigated by TEM (JEM 2010, JEOL, Japan) working at 200 kV. Therefore, dispersions containing the respective nanocrystals were deposited on carbon-coated copper grids by drop-casting and air-dried under ambient conditions. The mean diameters of quasi-spherical AuNPs, as well as the average widths and lengths of AuNRs were evaluated by image analysis using FIJI software.⁸³⁴ For quasi-spherical AuNPs size analysis with enclosing circles was performed. The results of the image analysis were also used to determine size distributions of the nanocrystals. Table 6-2 summarizes how many nanocrystals of each system were analyzed.

Table 6-2: Number of nanocrystals evaluated by TEM image analysis, where for quasi-spherical AuNPs size analysis with enclosing circles was conducted using FIJI software.

Type of nanocrystal	Number of analyzed nanocrystals
AuNPs@CTAB	274 (1 st batch), 278 (2 nd batch)
AuNRs@PTEBS	219
AuNPs@PTEBS	264
AuNPs@PFS-Na	243
AuNPs@P3KHT	253
AuNPs@P3KHT-GOx (0.75 vol% EDC/Sulfo-NHS reagent)	300
AuNPs@P3KHT-GOx (2.00 vol% EDC/Sulfo-NHS reagent)	289

6.3.2 Scanning electron microscopy (SEM)

Scanning electron micrographs of dried deposited films made of different gold-polythiophene hybrid nanocrystals on glass substrates and inkjet-printed biosensors on PET foils were recorded with a Quanta 400 ESEM (FEI, Germany). Details about the film deposition and the inkjet printing are described in sections 6.2.4 and 6.2.5.

6.3.3 Optical microscopy

The lateral dimensions (width and length) of the deposited line patterns made of various gold-polythiophene hybrid nanocrystals on glass substrates were characterized by optical microscopy using an Olympus microscope SZX16 (Olympus, Shinjuku, Japan). The measured dimension ranges of the different hybrid nanocrystal films are summarized in Table 6-3. Additionally, optical micrographs of inkjet-printed biosensors on PET substrates were recorded using an optical microscope Axio Scope A1 (Zeiss, Jena, Germany).

Table 6-3: Lateral dimensions of deposited line patterns composed of different gold-polythiophene hybrid nanocrystals on glass substrates determined by optical microscopy.

Type of nanocrystal	Width [μm]	Length [μm]
AuNRs@PTEBS	0.9-1.3	2.0-2.9
AuNPs@PTEBS	1.1-1.3	1.7-2.3
AuNPs@PFS-Na	0.9-1.4	1.5-4.2
AuNPs@P3KHT	0.7-1.7	2.3-3.3
AuNPs@P3KHT-GOx (surface bioconjugation)	0.9-1.3	1.7-2.3
AuNPs@P3KHT-GOx (solution bioconjugation 0.75 vol% EDC/Sulfo-NHS)	0.8-1.5	1.8-2.6
AuNPs@P3KHT-GOx (solution bioconjugation 2.00 vol% EDC/Sulfo-NHS)	0.8-1.2	2.0-2.6

6.3.4 Fluorescence microscopy

Fluorescence images of the fixed and stained fibroblasts and neurospheres on deposited gold-polythiophene hybrid films (substrates were Nexterion slides H) were recorded with a Zeiss Axio Observer epi-fluorescence microscope (Zeiss, Jena, Germany).

6.3.5 3D Confocal microscopy

The thicknesses of the deposited gold-polythiophene hybrid films on glass substrates were determined by 3D confocal microscope using a MarSurf CM explorer (Mahr, Göttingen, Germany). The measured topography data were transferred to histograms, which were fitted by Gaussian functions to obtain the average layer thickness and the corresponding standard deviations.

By way of example, the detected topography data of films made of AuNPs@PTEBS, AuNRs@PTEBS, as well as AuNPs@PFS-Na and the corresponding fitted data are depicted in Figure 6-5a, b and c. Each topography data contained two maxima, corresponding to the relative heights of the glass substrate and the hybrid layer. The thickness of the film was determined as the difference between the height positions of the two maxima. The positions of the maxima were obtained by Gaussian fits. For all analyzed samples Gaussian fits matched well with the measuring data ($R^2 \geq 0.990$).

Additionally, the average height profiles of the different hybrid films obtained by the *MarSurf* software are also shown in Figure 6-5d, e and f. To determine the mean height profiles, the device measured 2000 individual profiles over the complete sample area and averaged them. The software further calculated a mean and maximum film thickness by analyzing the average height profiles. The mean film thicknesses determined by the device software corresponded well to the results obtained from the Gaussian fit method. The differences were below 2%. Since the fitting method analyzed the complete topography data of the sample and not only limited number of profiles, I chose to work with the results obtained by the fitting method.

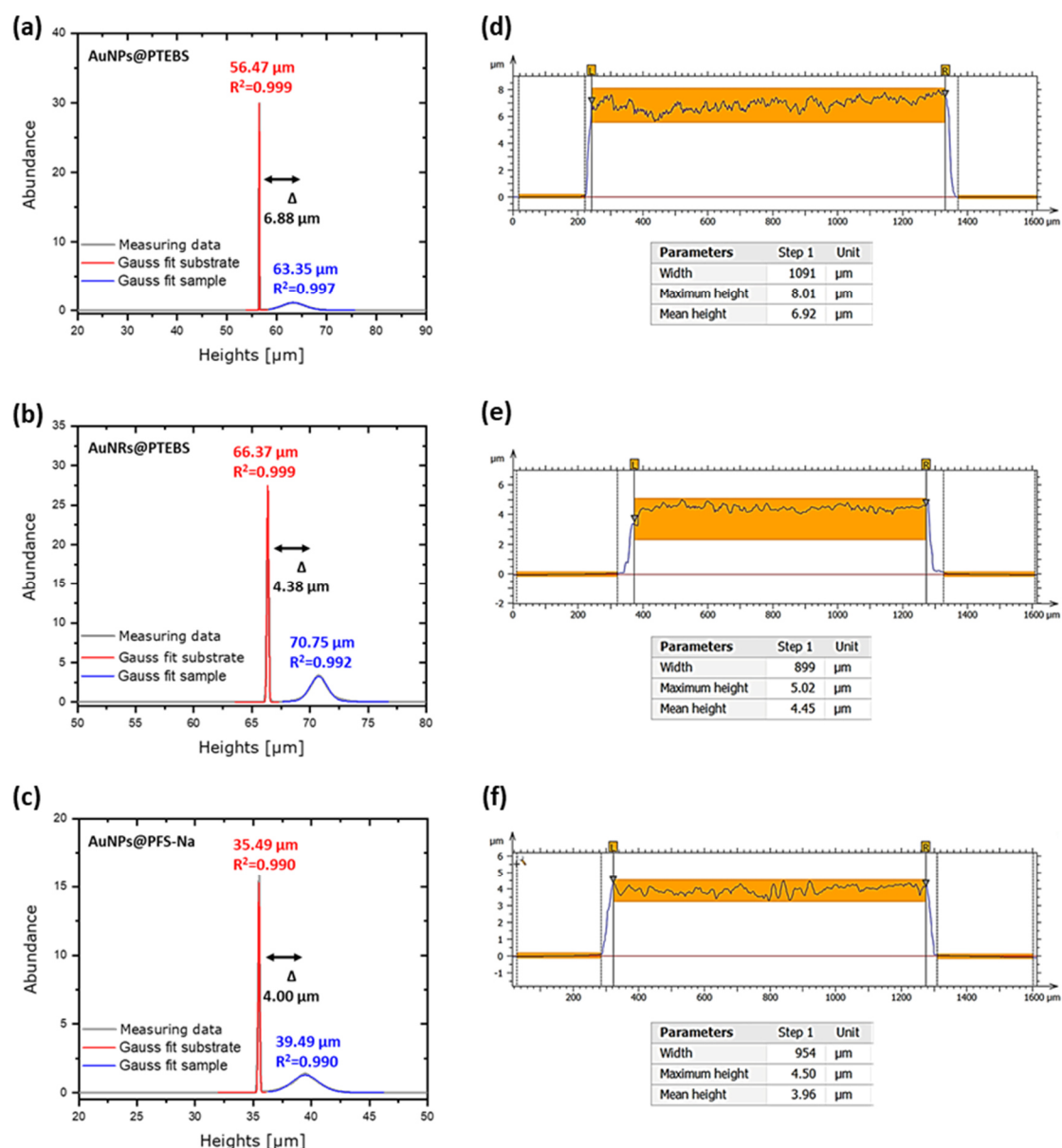


Figure 6-5: (a, c, e) Topography data and corresponding Gaussian fits of gold-polythiophene hybrid films. Maxima of the topography data were determined by Gaussian fits and the thicknesses of the gold-polythiophene hybrid layers were determined by the difference of the height positions of the maxima. (d, e, f) Average height profiles, mean and maximum thicknesses of the gold-polythiophene hybrid films obtained by the *MarSurf* software. The average height profiles were calculated based on 2000 individual profiles over the complete sample area. The data belong to layers made of (a, d) AuNPs@PTEBS, (b, e) AuNRs@PTEBS and (c, f) AuNPs@PFS-Na.

The mean profiles in Figure 6-5d, e and f illustrate that the thickness variations within one film (ratio between mean and maximal thickness) were below 30%. The determined thickness ranges of the analyzed samples of the different gold-polythiophene hybrid nanocrystals are listed in Table 6-4. Further exemplary topography data with corresponding Gaussian fits and height profiles of AuNPs@P3KHT and AuNPs@P3KHT-GOx are shown in Appendix B (Figure B-1).

Table 6-4: Determined ranges of film thicknesses of gold-polythiophene hybrid films obtained by 3D confocal microscopy.

Type of nanocrystal	Average film thickness [μm]
AuNRs@PTEBS	3.6-10.0
AuNPs@PTEBS	2.6-11.4
AuNPs@PFS-Na	0.9-4.0
AuNPs@P3KHT	1.4-2.8
AuNPs@P3KHT-GOx (surface bioconjugation)	1.5-2.1
AuNPs@P3KHT-GOx (0.75 vol% EDC/Sulfo-NHS reagent)	1.4-1.6
AuNPs@P3KHT-GOx (2.00 vol% EDC/Sulfo-NHS reagent)	1.9-4.1

6.3.6 Raman spectroscopy

Suitable samples for characterization by Raman spectroscopy were fabricated by drop-casting dispersions containing various gold-polythiophene hybrid nanocrystals (AuNRs@PTEBS, AuNPs@PTEBS, AuNPs@PFS-Na, AuNPs@P3KHT and AuNPs@P3KHT-GOx) onto steel substrates. Films made of pure polymers PTEBS, P3KBT, P3KPT, P3KHT and P3KHepT were also produced by deposition of aqueous polymer solutions onto steel substrates. Only dried films were analyzed by Raman spectroscopy. In addition, powder samples of EDC, NHS, Sulfo-NHS and aminated PEG (PEG-NH₂) were placed on steel substrates to be investigated by Raman spectroscopy.

Raman analysis was conducted with a confocal Raman microscope inVia (Renishaw, Wotton-under-Edge, United Kingdom), using a laser excitation wavelength of 633 nm.

Only films of pure PTEBS irradiated by laser light with this excitation wavelength possessed considerable photoluminescence overlaying the actual Raman signal. To suppress photoluminescence of this PTEBS sample, I used a near-infrared (NIR) laser with an excitation wavelength of 782 nm in a Labram HR Evolution confocal Raman microscope (Horiba, Kyōto, Japan). Quenching effects in the case of AuNPs@PTEBS and AuNRs@PTEBS suppressed the photoluminescence of the pure polymer and Raman characterization could be performed with lasers of higher energy (633 nm). All other samples (gold-polythiophene hybrid nanoparticles or pure polymers) showed no distinct photoluminescence during Raman investigation.

The averaged area in each Raman measurement was about 1 mm² to 4 mm². For each sample, Raman spectra at five different positions were recorded. The detected local Raman spectra did not show significant differences, verifying the homogeneity of the investigated samples. By way of example, the Raman spectra detected at two different spots of films composed of AuNPs@PTEBS and AuNRs@PTEBS are depicted in Figure 6-6. Since the Raman spectra of the analyzed samples did not depend on the exact positions, the Raman data shown in this work were always representative for the complete sample area.

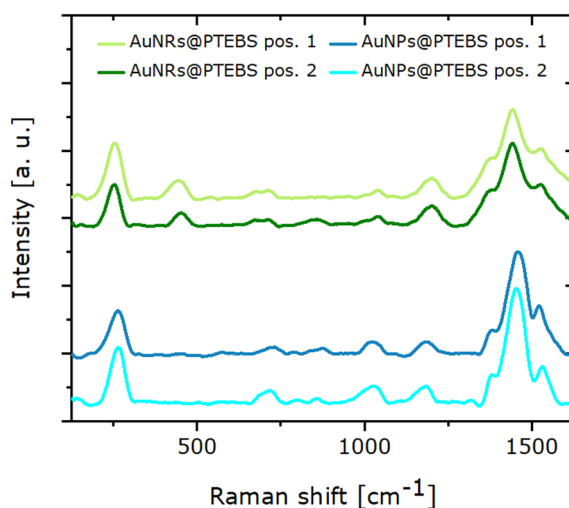


Figure 6-6: Raman spectra taken at two different positions of films made of AuNRs@PTEBS and AuNPs@PTEBS, respectively. The spectra are similar, illustrating the homogeneity of the characterized samples.

6.3.7 X-ray photoelectron spectroscopy (XPS)

All XPS measurements of AuNPs@PTEBS, AuNRs@PTEBS and pure PTEBS were performed by Dr. Frank Müller (group of Prof. Jacobs, Experimental Physics and Center for Biophysics, Saarland University, Saarbrücken, Germany).

XPS investigations of AuNPs@PTEBS, AuNRs@PTEBS and pure PTEBS were conducted with an ESCA MkII photoelectron spectrometer by Vacuum Generators using non-monochromatized Al-K α radiation ($\hbar\omega=1486.6$ eV) in normal emission geometry, i.e. spectra were recorded with the surface normal of the sample parallel to the entrance axis of the 150°-type hemispherical analyzer. Survey spectra were recorded at a pass energy of 50 eV, while detail spectra were taken at a pass energy of 20 eV. For quantitative analysis, spectra were corrected with Shirley backgrounds⁸³⁵ and peak areas were weighted with the photoemission cross sections by Yeh and Lindau.⁸³⁶ All measurements were conducted on dry films, which were obtained by drop-casting of aqueous dispersions containing AuNPs@PTEBS, AuNRs@PTEBS or PTEBS.

6.3.8 Scanning tunneling microscopy (STM) and spectroscopy (STS)

All STM and STS investigations of AuNPs@PTEBS and AuNRs@PTEBS were performed by Dr. Frank Müller (group of Prof. Jacobs, Experimental Physics and Center for Biophysics, Saarland University, Saarbrücken, Germany) and Dr. Anne Holtsch (group of Prof. Jacobs, Experimental Physics and Center for Biophysics, Saarland University, Saarbrücken, Germany).

STM^{837,838} and STS^{839,840} measurements of AuNPs@PTEBS and AuNRs@PTEBS were conducted with a VT-STM by Scienta Omicron in ultra-high vacuum with a base pressure below $5\cdot 10^{-9}$ mbar at room temperature. An etched, sharp tungsten tip was utilized for the measurements. The lower potential was on the tip. All measurements were conducted on dry films, which were obtained by drop-casting of aqueous dispersions containing AuNPs@PTEBS, AuNRs@PTEBS or PTEBS.

6.3.9 Zeta potential measurements

Zeta potentials ζ of various nanoparticle dispersions were performed using a Litesizer 500 instrument (Anton Paar, Ostfildern, Germany). The measurements were performed in an Omega cuvette (Anton Paar, Ostfildern, Germany) and the sample volume of each zeta measurement was 600 μL . The gold concentration was kept constant at 1 $\text{mg}\cdot\text{mL}^{-1}$ for all analyzed samples. All measurements were performed at 20 °C and the collected data were analyzed according to the Smoluchowski model. The characterized samples were dispersed in Milli-Q water (18.2 $\text{M}\Omega\cdot\text{cm}^{-1}$) or in aqueous mixtures with different solvents. For the aqueous samples the viscosity η , refractive index n and relative permittivity ϵ_r parameters implemented in the measurement software *Kalliope* of the Litesizer 500 device were used. Measurements in water-solvent mixtures required manual input of the respective parameters to the *Kalliope* software. The appropriate viscosity η , refractive index n and relative permittivity ϵ_r were taken from reported literature. All used parameters are listed in Table 6-5.

Table 6-5: Viscosity η , refractive index n and relative permittivity ϵ_r parameters of various water-organic solvent mixtures according to published literature. The numbers in the superscripts refer to the corresponding references.

	η [mPa·s]	n	ϵ_r
water/methanol (60/40, w/w)	1.837 ⁴²⁶	1.3425 ⁴²⁶	61.24 ⁸⁴¹
water/ethanol (60/40, w/w)	2.846 ⁴²⁶	1.3583 ⁴²⁶	56.49 ⁸⁴¹
water/n-propanol (60/40, w/w)	3.010 ⁴²⁶	1.3635 ⁴²⁶	51.68 ⁸⁴¹
water/acetone (80/20, w/w)	1.4077 ⁸⁴²	1.34498 ⁸⁴³	68.58 ⁸⁴¹

6.3.10 Dynamic light scattering (DLS)

Hydrodynamic diameters and particle size distributions of quasi-spherical AuNPs were evaluated by DLS using a Litesizer 500 device (Anton Paar, Ostfildern, Germany). The instrument was operated in a 175° backscatter mode and a laser diode was used as light source ($\lambda=658$ nm). Analyzed samples were transferred to disposable poly(methyl methacrylate) (PMMA) cuvettes. For all DLS measurements, the sample volume was 1.5 mL and the gold concentration was kept constant at 1 $\text{mg}\cdot\text{mL}^{-1}$. All measurements were conducted at 20 °C. Hydrodynamic diameters were determined by the *Kalliope*

software of the Litesizer 500 instrument based on Z-average diameters obtained from cumulant analysis. The polydispersity index (PDI) was also determined using the *Kalliope* software, quantifying the polydispersity of the individual AuNPs samples.

Measurements were performed of AuNPs dispersion in Milli-Q water ($18.2 \text{ M}\Omega\cdot\text{cm}^{-1}$), various buffers and different water-organic solvent mixtures. For the aqueous samples the viscosity η and refractive index n parameters implemented in the measurement software *Kalliope* of the Litesizer 500 device were used. The used buffers, PBS (pH 7.4 or 5.8, both 0.1 M) and MES (pH 4.7, 0.1 M), were fabricated by diluting appropriate amounts of salts in water. Experimental studies showed that the optical and rheological parameters of such buffers did not differ significantly from those of pure water.^{844–846} Hence, I assumed that the refractive index n and viscosity η of water implemented in the *Kalliope* software were also valid for the DLS measurements of AuNPs in the different buffers. In contrast, DLS characterization of samples in various water-organic solvent mixtures required manual input of the respective parameters to the *Kalliope* software. The appropriate viscosity η and refractive index n parameters of the different water-organic solvent mixtures were taken from literature (Table 6-5), corresponding the zeta potential measurements.

6.3.11 UV-vis spectroscopy

All UV-vis measurements were conducted in transmission mode. Besides the calibration and kinetic measurements of the colorimetric bioassays, all samples were characterized using a UV-vis/NIR spectrophotometer Cary 5000 (Agilent, California, USA). Disposable polystyrene (PS) cuvettes were used for sample and reference measurements.

Calibration and kinetic measurements of the colorimetric bioassays were performed using a Spectramax 190 microplate reader (Molecular Devices, California, USA). Therefore, the samples were pipetted into 96-well half area microplates with flat bottom made of polystyrene (Corning, New York, USA). Details about the bioassay preparation are given in section 6.2.7. For bioassay characterization the UV-vis absorption signal at 415 nm

was investigated over time to detect the formation of $\text{ABTS}^{\bullet+}$ radical upon glucose oxidation.

6.3.12 Electrical characterization

Electrical properties of the deposited line patterns made of various gold-polythiophene hybrid nanocrystals (AuNRs@PTEBS, AuNPs@PTEBS, AuNPs@PFS-Na, AuNPs@P3KHT and AuNPs@P3KHT-GOx) on glass substrates were investigated with a 2450 sourcemeter (Keithley Instruments, Ohio, USA) using a 2-point probe setup. Current-voltage (I - V) curves were taken of several samples of each gold-polythiophene hybrid nanocrystal system. The exact number of analyzed samples of each system is listed in Table 6-6. The measured current was normalized to the thickness of each individual gold-polythiophene hybrid layer and an average I - V curve was determined for each type of gold-polythiophene hybrid nanomaterial. Further information about the thickness determination by 3D confocal microscopy are given in section 6.3.5.

Table 6-6: Number of electrically characterized deposited films on glass substrates made of different gold-polythiophene hybrid nanocrystals.

Type of nanocrystal	Number of analyzed samples
AuNRs@PTEBS	6
AuNPs@PTEBS	6
AuNPs@PFS-Na	6
AuNPs@P3KHT	6
AuNPs@P3KHT (surface bioconjugation)	4
AuNPs@P3KHT-GOx (0.75 vol% EDC/Sulfo-NHS reagent)	4
AuNPs@P3KHT-GOx (2.00 vol% EDC/Sulfo-NHS reagent)	4

The inverse of the I - V curve's slope ($R \cdot t$, R =resistance, t =thickness) was multiplied by the ratio of width to length (w/l) to determine the resistivity ρ of each gold-polythiophene hybrid nanomaterial according to equation 6-1. The lateral dimensions (width w and length l) were analyzed by optical microscopy as described in section 6.3.3. Based on the

varying number of investigated samples of each gold-polythiophene hybrid nanocrystal system, the mean resistivity ρ and the corresponding standard deviation were calculated for each hybrid nanomaterial.

$$\rho = R \cdot t \cdot \frac{w}{l} \quad (6-1)$$

ρ : resistivity

R : resistance

t : thickness of the line patterns

w : width of the line patterns

l : length of the line patterns

6.3.13 Thermogravimetric analysis (TGA)

TGA measurements were conducted using a TGA 8000 instrument (PerkinElmer, Massachusetts, USA). Various washed gold-polythiophene hybrid nanocrystal dispersions (AuNPs@PTEBS, AuNRs@PTEBS, AuNPs@PFS-Na, AuNPs@P3KHT and AuNPs@P3KHT-GOx) were dried inside aluminum oxide (Al_2O_3) crucibles. The mass of each sample was between 8-20 mg. Every sample was heated from 50 °C to 1000 °C with a heating rate of 10 °C·min⁻¹ under nitrogen atmosphere.

6.3.14 Density measurements

The density of the PTEBS powder (as obtained from the supplier) was determined using a gas pycnometer AccuPyc 1330 (Micromeritics, Unterschleißheim, Germany), which operated with helium as the displacement medium. At least 500 mg of PTEBS powder was used for each measurement. One measurement consisted of 25 runs, providing an average value and its standard deviation.

6.3.15 Electrochemical characterization of inkjet-printed amperometric biosensors

I characterized the inkjet-printed biosensors containing enzyme-functionalized AuNPs@P3KHT-GOx using chronoamperometry. In this method, I applied a constant potential at the working electrode and detected the resulting current as a function of time. All measurements were performed using a VSP-300 multi-channel potentiostat/galvanostat from Bio-Logic (Seyssinet-Pariset, France). The device was equipped with *EC-Lab* software.

The inkjet-printed biosensors on PET foils were mounted on glass slides using double-sided adhesive tape. PDMS wells were super-glued on top of the biosensors to confine the electrolyte. The PDMS wells were fabricated by cutting out holes (diameter=12 mm) from a PDMS layer (height \approx 5 mm). This complete setup was fixed on a shaker MS 3 digital from IKA (Staufen, Germany) as shown in the photographs of Figure 6-7.

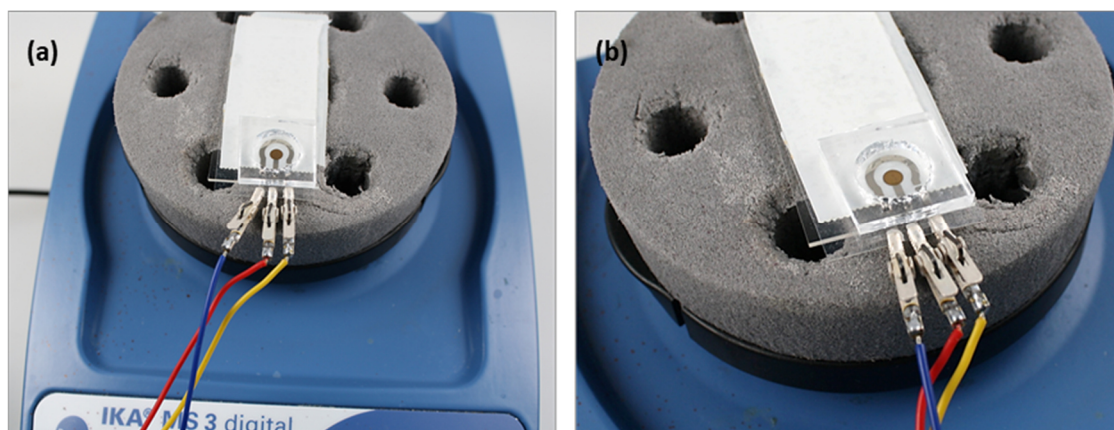


Figure 6-7: (a, b) Photographs of the setup used for the electrochemical characterization of the inkjet-printed biosensors. The printed biosensors on PET foils were glued on glass slides and the slides were mounted to a shaker (IKA MS 3 digital). PDMS wells were glued on top of the biosensors to confine the space of the electrolyte. The photographs show the golden WE (circle) and the silver CE and RE. The different electrodes were contacted with silver paste and crocodile clamps were used to connect the sensor with the potentiostat via wires (blue=CE, red=WE and yellow=RE). (b) Close-up image of the measurement unit composed of biosensor, PDMS well and wire connections.

Within each measurement the shaker was moved with a constant speed of 300 rpm to ensure sufficient mixing of the electrolyte. During all measurements a stable baseline current (current caused by pure electrolyte) was ensured before the injection of the

analytes (glucose or interferents). The counter (CE), reference (RE) and working (WE) electrodes were contacted with silver paste providing a better contact to the crocodile clamps, which were used to connect the electrodes via wires (blue=CE, red=WE and yellow=RE) to the potentiostat.

Optimization studies

I used a biosensor with a working electrode composed of enzyme-functionalized AuNPs@P3KHT-GOx for all optimization studies. The bioconjugation of the gold-polythiophene hybrid nanoparticles was conducted in solution prior to printing using EDC/S-NHS_{high} (2.00 vol%). Further details about bioconjugation are described in section 6.2.3.

Optimization of pH

For all measurements the applied potential was set to -0.5 V vs. the printed silver nanoparticle electrode. I prepared citrate-phosphate buffers (pH 3.4, pH 4.2. and pH 5.0) and PBS buffers (pH 5.8, pH 6.6, pH 7.4 and pH 8.0). All buffers had a concentration of 0.1 M. I always added 180 μ L of the respective buffer to the PDMS well and detected the stable baseline current of each buffer. Subsequently, I added 20 μ L of glucose solution (5 mM in the corresponding buffer) and detected the current response of the biosensor.

Optimization of working potential

All measurements were conducted using a PBS buffer (0.1 M) with pH 6.6 as the electrolyte. The volume of the electrolyte for the detection of the baseline current was 180 μ L. I varied the applied potential against the printed silver nanoparticle reference electrode from -1.0V to -0.3 V and detected the baseline current for each applied working potential. At each applied potential I added 20 μ L of glucose solution (5 mM) in PBS buffer (pH 6.6) and measured the current response towards glucose.

Calibration studies

For the calibration of the biosensors I used an applied working potential of -0.6 V and a PBS buffer (0.1 M, pH 6.6) as the electrolyte. Firstly, I detected the baseline current by adding 180 μL of pure PBS buffer to the PDMS well. Subsequently, I calibrated the inkjet-printed amperometric biosensors by seven successive additions of 20 μL glucose solution (2 mM) in PBS buffer (0.1 M, pH 6.6) every 30 sec and detected the current response for each glucose injection step. The glucose range for calibration was between 2 mM and 14 mM.

I calibrated two different sets of printed amperometric biosensors with working electrodes composed of enzyme-functionalized AuNPs@P3KHT-GOx. Each set contained three individual samples in order to gain information about the reproducibility of the printed biosensor. Bioconjugation with glucose oxidase was conducted in solution before printing with EDC/S-NHS_{high} (2.00 vol%) for all biosensors of the first set. In contrast, the second set contained biosensors with working electrodes, which were functionalized with glucose oxidase after printing (surface bioconjugation). Additional information about the different bioconjugation procedures is given in section 6.2.3.

I also calibrated one biosensor containing a working electrode composed of non-functionalized AuNPs@P3KHT according to the same procedure described above.

Selectivity measurements

I tested the selectivity of the inkjet-printed amperometric biosensors towards glucose. In this process, I used a biosensor with a working electrode composed of enzyme-functionalized AuNPs@P3KHT-GOx. The bioconjugation of the gold-polythiophene hybrid nanoparticles was conducted in solution prior to printing using EDC/S-NHS_{high} (2.00 vol%). All measurements were performed using an applied potential of -0.6 V and a PBS buffer (0.1 M, pH 6.6) as the electrolyte. I prepared solutions of different interferents by dissolving the respective interferent in PBS buffer (0.1 M, pH 6.6). The concentration of the interferents was always 20 mM. I tested ascorbic acid (AA), oxalic

acid (OA), uric acid (UA), sucrose (Suc), lactose (Lac) and urea (UR) regarding their interfering properties.

Before starting the selectivity studies, I detected the baseline current by adding 180 μL of pure electrolyte to the PDMS well. Subsequently, I injected successively 20 μL of each interferent solution and detected the current response. Finally, I added consecutively 20 μL of 2 mM and 5 mM glucose solutions in PBS buffer (0.1 M, pH 6.6) and detected the current response. The current signal of the biosensor towards glucose in the presence of the various interferents determined the selectivity of the inkjet-printed biosensors for glucose.

Appendix

A Thermogravimetric analysis of gold-polythiophene hybrid nanoparticles

I performed TGA measurements of various gold-polythiophene hybrid nanoparticles in the range of 50 °C to 1000 °C. Further experimental details are given in section 6.3.13. The detected TGA curves are presented in Figure A-1.

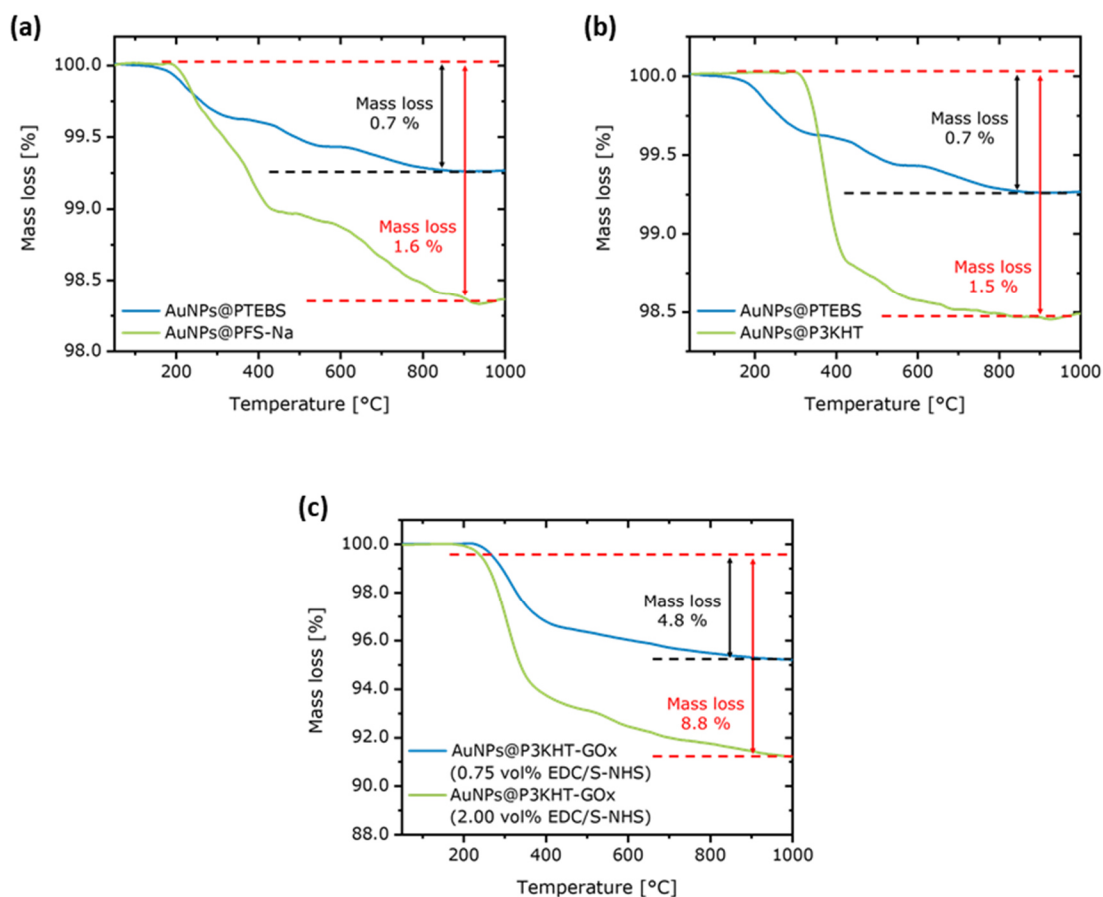


Figure A-1: TGA curves obtained from dried samples of (a) AuNPs@PTEBS and AuNPs@PFS-Na, (b) AuNPs@PTEBS and biofunctionalizable AuNPs@P3KHT and (c) enzyme-functionalized AuNPs@P3KHT-GOx. Bioconjugation with glucose oxidase GOx was conducted in solution using EDC/S-NHS_{low} (0.75 vol%) or EDC/S-NHS_{high} (2.00 vol%). The samples were heated from 50 °C to 1000 °C under nitrogen atmosphere with a heating rate of 10 °C·min⁻¹.

TGA revealed organic weight fractions of 0.7 wt% for AuNPs@PTEBS and 1.6 wt% for AuNPs@PFS-Na, as illustrated in Figure A-1a. The larger organic weight fraction of AuNPs@PFS-Na indicated thicker polythiophene ligand shells for AuNPs@PFS-Na, since the core dimensions were similar for both types of gold-polythiophene hybrid nanoparticles. A detailed discussion of the TGA curve of AuNPs@PTEBS is given in section 3.1.1. The TGA curve of AuNPs@PFS-Na possessed two distinct mass loss steps in the range of 300 °C to 425 °C and from about 425 °C to 900 °C. The first mass loss step led to a loss of about 1 wt%, while in the second mass loss step additional 0.6 wt% of organic mass decomposed. I attributed these two mass loss regimes to the molecular structure of PFS-Na containing thiophene and fluorene units in the polymer backbone. According to reported literature, the thermal decomposition of classical polythiophenes starts at about 300°C,^{847–849} while polymers with fluorene units possess enhanced thermal stability and decompose at a temperature of 400 °C or even above.^{850–852} In conclusion, the first mass loss step in the TGA curve of Figure A-1a likely originated from the decomposition of the thiophene units of PFS-Na, while the second mass loss step arose from the degradation of the thermally more stable fluorene units.

Figure A-1b illustrates the TGA curve of biofunctionalizable AuNPs@P3KHT, which revealed an organic weight fraction of 1.5 wt%. This is comparable to the organic weight fraction of AuNPs@PFS-Na presented in Figure A-1a. The TGA curve of AuNPs@P3KHT also possessed two pronounced weight loss steps. The first one was in the temperature region of 300 °C to 420 °C, corresponding to 1.1 wt% weight loss. In the second mass loss step (420 °C to 900 °C), additional 0.4 wt% of organic components, mainly P3KHT, decomposed. Compared to the weight loss of AuNPs@PTEBS (0.7 wt%), the organic amount was much more in the case of AuNPs@P3KHT, which indicated thicker polythiophene ligand shells for AuNPs@P3KHT, since the core dimensions were similar for both types of gold-polythiophene hybrid nanoparticles. Additionally, the TGA curves in Figure A-1b clearly demonstrated that the decomposition of PTEBS started at much lower temperatures of about 200 °C, while P3KHT just degraded at temperatures above 300 °C, which is typical of classical polythiophenes.^{847–849} The low decomposition temperature of PTEBS can be attributed to sulfonate groups in the side chain of the polymer, which have lower thermal stability than the

polythiophene backbone. This corresponds to reported TGA data of PEDOT:PSS, a polythiophene which also possesses sulfonate groups and which decomposes at temperatures even far below 300 °C due to the degradation of the sulfonate groups.^{853,854}

The TGA curves of biofunctionalizable gold-polythiophene hybrid nanoparticles bioconjugated with the enzyme glucose oxidase GOx are depicted in Figure A-1c. The bioconjugation was performed in solution using different concentrations of EDC/Sulfo-NHS reagent, namely 0.75 vol% and 2.00 vol%. Further experimental details about the bioconjugation process are given in section 6.2.3. The two TGA curves possessed similar shape with two distinct mass loss steps. The first mass loss step was in the range of 220 °C to 400 °C, which led to a mass loss of 3.2 wt% for AuNPs@P3KHT-GOx (bioconjugated with EDC/S-NHS_{low} 0.75 vol%) and 6.2 wt% for AuNPs@P3KHT-GOx (bioconjugated with EDC/S-NHS_{high} 2.00 vol%). In the second mass loss step from 400 °C to 900 °C, additional 1.6 wt% of organic mass decomposed for AuNPs@P3KHT-GOx (bioconjugated with EDC/S-NHS_{low} 0.75 vol%) and additional 2.6 wt% for (bioconjugated with EDC/S-NHS_{high} 2.00 vol%). Thus, based on TGA measurements the overall organic weight fractions of AuNPs@P3KHT-GOx (bioconjugated with EDC/S-NHS_{low} 0.75 vol%) and AuNPs@P3KHT-GOx (bioconjugated with EDC/S-NHS_{high} 2.00 vol%) were 4.8 wt% and 8.8 wt%, respectively. This result corresponds to the fact that with the increasing concentration of EDC/Sulfo-NHS reagent, more carboxylate groups in the polythiophene ligand shell become activated, which means that more GOx molecules can be covalently linked to the gold-polythiophene hybrid nanoparticles. Thus, with the increasing amount of bioconjugated GOx molecules, the organic weight fraction and as revealed in section 3.4.1 the hydrodynamic radius of the hybrid nanoparticles increased.

While for non-functionalized AuNPs@P3KHT the decomposition of the organic components started at 300 °C (Figure A-1b), the degradation of enzyme-functionalized AuNPs@P3KHT-GOx began at a lower temperature of about 220 °C. This can be related to the degradation of glucose oxidase, which is not as thermally stable as polythiophenes. TGA characterization of glucose oxidase immobilized on metal-organic frameworks and nanoparticles also determined a decomposition temperature of GOx in the range of 180 °C to 250 °C,^{564,855,856} which corresponds very well to the detected degradation

temperature of about 220 °C for AuNPs@P3KHT-GOx (Figure A-1c). Thus, it is likely, that firstly the GOx molecules bioconjugated to the gold-polythiophene hybrid nanoparticles decomposed, before the actual P3KHT ligand shell degraded at temperatures above 300 °C.

B Thickness determination of hybrid gold-polythiophene films

I detected topography data using 3D confocal microscopy as discussed in section 6.3.5. The measured topography data were transferred to histograms which are shown in Figure B-1a-d

The topography data of each tested hybrid film contained two maxima, corresponding to the relative heights of the glass substrate and the gold-polythiophene hybrid layer. The height positions of the maxima were obtained by Gaussian fits and the thicknesses of the layers were determined as the difference between the height positions of the two maxima. Further details about the data processing are given in section 6.3.5. In addition, the average height profiles of the different gold-polythiophene hybrid films determined by 3D confocal microscopy are also shown in Figure B-1e-h. The software of the 3D confocal microscope (*MarSurf* software) calculated the maximum and mean heights of the gold-polythiophene hybrid layers. Details about the determination of the average height profiles are also provided in section 6.3.5.

As illustrated in Figure B-1, the average layer thicknesses determined by the device software corresponded well to the results derived from the Gaussian fit method. The mean profiles in Figure B-1e-h, revealed that the thickness variations within one film (differences between mean and maximal thickness) were below 30%.

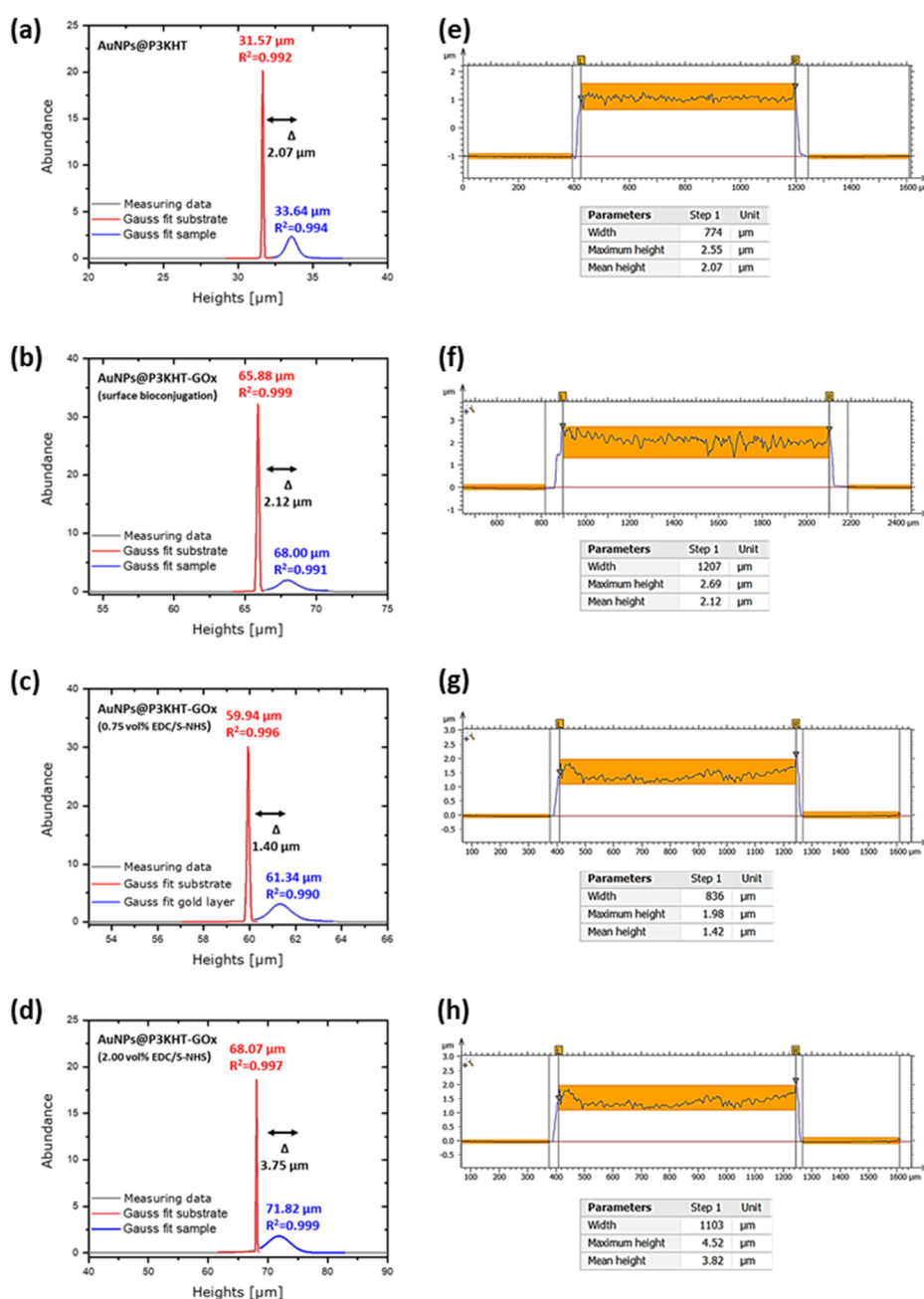


Figure B-1: (a, b, c, d) Topography data and corresponding Gaussian fits of gold-polythiophene hybrid films. Maxima of the topography data were determined by Gaussian fits and the thicknesses of the gold-polythiophene hybrid layers were determined by the differences of the maxima height positions. (e, f, g, h) Average height profiles, mean and maximum thickness of the gold-polythiophene hybrid films obtained by the *MarSurf* software. The average height profiles were calculated based on 2000 individual profiles over the complete sample area. The data belong to layers made of (a, e) AuNPs@P3KHT, (b, f) AuNPs@P3KHT-GOx (surface bioconjugation), (c, g) AuNPs@P3KHT-GOx (solution bioconjugation with EDC/S-NHS_{low} 0.75 vol%) and (d, h) AuNPs@P3KHT-GOx (solution bioconjugation with EDC/S-NHS_{high} 2.00 vol%).

C Characterization of agglomerated gold-polythiophene hybrid nanoparticles by DLS

Centrifugation of biofunctionalizable gold-polythiophene hybrid nanoparticles in pure Milli-Q water ($18.2 \text{ M}\Omega\cdot\text{cm}^{-1}$) caused nanoparticle agglomeration and lead to residues, which could not be redispersed completely. I sonicated the agglomerated samples for 30 min in an ultrasonic bath to bring some of the agglomerates to solution and to gain information about the dimensions of these agglomerates by DLS. The measured DLS data after different centrifugation steps are summarized in Table C-1. The agglomerates of all biofunctionalizable gold-polythiophene hybrid nanoparticles had dimensions of several hundreds of nanometers, which continuously increased with proceeding centrifugation steps. Hence, DLS characterization clearly showed that washing in pure Milli-Q water is no appropriate purification method, since the biofunctionalizable gold-polythiophene nanoparticles possessed limited colloidal stability in this media and were prone to agglomeration.

Table C-1: Hydrodynamic diameters d_h and polydispersity indexes (PDI) obtained by DLS for the agglomerated biofunctionalizable gold-polythiophene hybrid nanoparticles AuNPs@P3KBT, AuNPs@P3KPT, AuNPs@P3KHT and AuNPs@P3KHepT after different centrifugation steps in pure Milli-Q water ($18.2 \text{ M}\Omega\cdot\text{cm}^{-1}$).

	2 nd step		3 rd step		4 th step	
	d_h [nm]	PDI [%]	d_h [nm]	PDI [%]	d_h [nm]	PDI [%]
AuNPs@P3KBT	158.2	26.7	689.2	28.5	916.6	33.9
AuNPs@P3KPT	203.0	25.3	717.6	22.5	1214.7	28.2
AuNPs@P3KHT	153.3	26.4	618.7	22.5	890.1	26.9
AuNPs@P3KHepT	328.2	24.9	744.9	29.1	1319.9	22.2

D Colorimetric glucose bioassays containing gold-polythiophene hybrid nanoparticles

Implementation of gold-P3KHT hybrid nanoparticles in colorimetric bioassays

UV-vis absorption spectra of the bioassays containing AuNPs@P3KHT-GOx at different time points after glucose addition are depicted in Figure D-1a and b. The bioconjugation of GOx was done in solution using different concentrations of EDC/Sulfo-NHS reagent (0.75 vol% and 2.00 vol%). The UV-vis absorption spectra illustrated an increase in the absorption peak of the ABTS^{•+} radical at 415 nm, while simultaneously the ABTS absorption peak decreased with increasing time after glucose addition. Under the chosen *reaction* conditions the absorption signal of ABTS/ABTS^{•+} radical was much stronger than the plasmon band of the gold nanoparticles and both peaks did not interfere. Since the transformation of ABTS to the ABTS^{•+} radical with the accompanied color change occurred, I concluded that AuNPs@P3KHT-GOx provided sufficient glucose oxidase to transfer D-glucose to D-glucono-1,5-lactone under the chosen reaction conditions of the bioassays. The overall increase of absorption at 415 nm was much faster and more pronounced for AuNPs@P3KHT-GOx activated with EDC/S-NHS_{high} (2.00 vol%) (Figure D-1b), which corresponded to the increasing amount of bioconjugated GOx molecules with increasing concentration of EDS/Sulfo-NHS reagent as proven by TGA (Appendix A, Figure A-1c). The enhanced number of bioconjugated GOx molecules finally resulted in faster glucose oxidation and ABTS^{•+} radical formation.

Photographs of dispersions containing AuNPs@P3KHT-GOx bioconjugated with EDC/S-NHS_{low} (0.75 vol%) or EDC/S-NHS_{high} (2.00 vol%) at different time points after glucose addition are shown in Figure D-1c. For better comparability, equivalent samples without glucose are also illustrated. The red AuNPs@P3KHT-GOx dispersions gradually changed their color to blue-green, indicating the formation of ABTS^{•+} radicals. The blue-green color was intensified with increasing time after glucose addition as more and more ABTS molecules are oxidized upon the enzymatic reactions. Even after 10 min, there was already an obvious difference between the red color of the blank samples and the purple color of the samples containing glucose. Hence, the characteristic absorption properties

of the AuNPs@P3KHT-GOx (red color of colloidal gold due to SPR) did not inhibit the colorimetric monitoring of ABTS oxidation. This makes AuNPs@P3KHT-GOx suitable to replace free glucose oxidase in colorimetric bioassays for glucose detection.

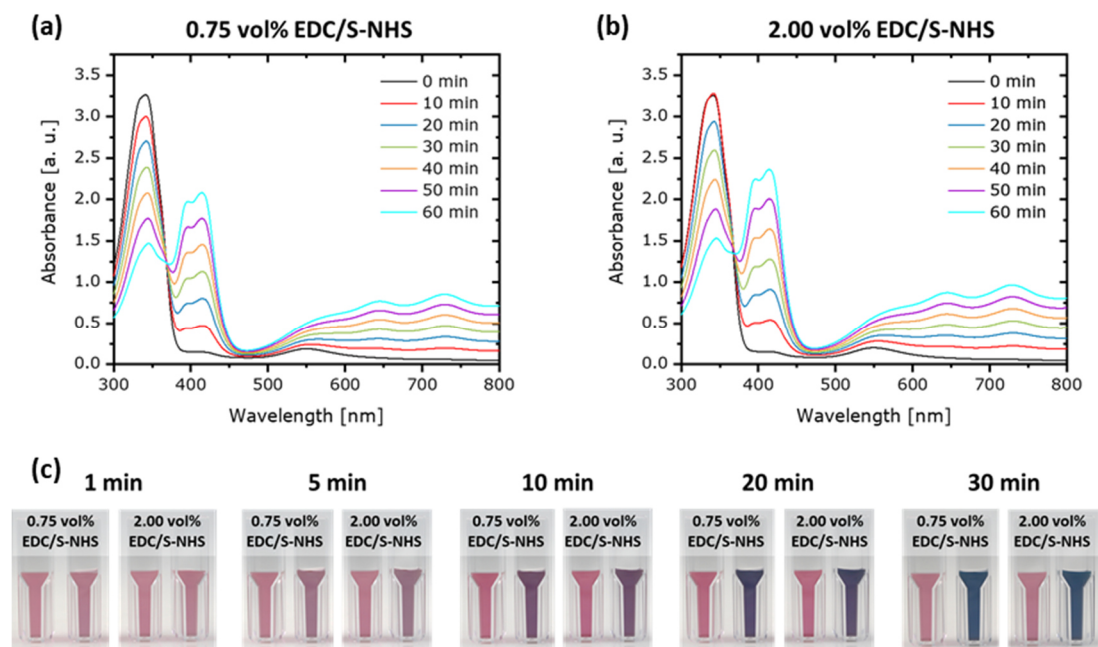


Figure D-1: UV-vis absorption spectra of colorimetric assays containing ABTS ($c[\text{ABTS}] = 500 \mu\text{g}\cdot\text{mL}^{-1}$), horseradish peroxidase ($c[\text{HRP}] = 15 \mu\text{g}\cdot\text{mL}^{-1}$) and AuNPs@P3KHT-GOx ($c[\text{Au}] = 12.5 \mu\text{g}\cdot\text{mL}^{-1}$) at different time points after glucose addition ($c[\text{gluc}] = 1.0 \text{ mg}\cdot\text{mL}^{-1}$). The gold-polythiophene hybrid nanoparticles were bioconjugated in solution with (a) EDC/S-NHS_{low} (0.75 vol%) and (b) EDC/S-NHS_{high} (2.00 vol%). (c) Photographs of AuNPs@P3KHT-GOx dispersions at various time points after glucose addition ($c[\text{gluc}] = 1.0 \text{ mg}\cdot\text{mL}^{-1}$). For comparison, photographs of the blank samples without glucose at different time points are also shown.

Calibration of colorimetric glucose bioassays containing gold-P3KHT hybrid nanoparticles

I prepared different colorimetric bioassays for glucose detection with various concentrations of enzyme-functionalized AuNPs@P3KHT-GOx. The gold concentrations in the bioassays were $50 \mu\text{g}\cdot\text{mL}^{-1}$, $25 \mu\text{g}\cdot\text{mL}^{-1}$, $12.5 \mu\text{g}\cdot\text{mL}^{-1}$ and $5 \mu\text{g}\cdot\text{mL}^{-1}$, respectively. The best results regarding signal-to-noise ratio, linearity and limit of detection (LOD) were obtained for colorimetric bioassays containing gold

concentrations of $12.5 \mu\text{g}\cdot\text{mL}^{-1}$. The data of these particular colorimetric bioassays are discussed extensively in section 3.4.5. The calibration data of the other colorimetric bioassays with gold concentrations of $50 \mu\text{g}\cdot\text{mL}^{-1}$, $25 \mu\text{g}\cdot\text{mL}^{-1}$ and $5 \mu\text{g}\cdot\text{mL}^{-1}$ are illustrated in Figure D-2. I always produced bioassays with the same gold concentration of two different types of enzyme-functionalized gold-polythiophene hybrid nanoparticles AuNPs@P3KHT-GOx. All hybrid nanoparticles were bioconjugated with glucose oxidase GOx in solution. However, two different concentrations of EDC/Sulfo-NHS reagent, EDC/S-NHS_{low} (0.75 vol%) and EDC/S-NHS_{high} (2.00 vol%), were used to conduct the bioconjugation between AuNPs@P3KHT and the enzyme GOx. Details about the bioconjugation procedure are given in section 6.2.3. I performed calibration measurements in the glucose range of $25 \mu\text{g}\cdot\text{mL}^{-1}$ to $5 \text{mg}\cdot\text{mL}^{-1}$.

Different trends can be distinguished from the calibration data shown in Figure D-2. The higher the gold concentration was, the more intense was the detected absorption signal. This is not surprising, since higher gold concentrations were always accompanied with larger amounts of glucose oxidase GOx covalently linked to the gold-polythiophene hybrid nanoparticles. More GOx molecules can oxidize greater amounts of glucose in a shorter time. Thus, more ABTS is converted faster to blue-green ABTS^{•+} radicals, yielding a more intense colorimetric signal.

Colorimetric assays with the same gold concentration, possessed a larger linear range in the case of enzyme-functionalized AuNPs@P3KHT-GOx, which were bioconjugated with EDC/S-NHS_{low} (0.75 vol%). This is consistent with the results presented in section 3.4.5. Higher amounts of EDC/Sulfo-NHS reagent increased the number of GOx molecules attached to AuNPs@P3KHT. More GOx molecules caused a faster oxidation of glucose and a more pronounced colorimetric signal. Hence, due to the faster glucose conversion, the linear ranges were smaller for colorimetric bioassays containing enzyme-functionalized AuNPs@P3KHT-GOx, which were bioconjugated by EDC/S-NHS_{high} (2.00 vol%). Additionally, the faster glucose oxidation in the case of AuNPs@P3KHT-GOx (2.00 vol% EDC/Sulfo-NHS), yielded larger slopes of the fitted regression lines compared to AuNPs@P3KHT-GOx (0.75 vol% EDC/Sulfo-NHS) at identical gold concentrations (Figure D-2).

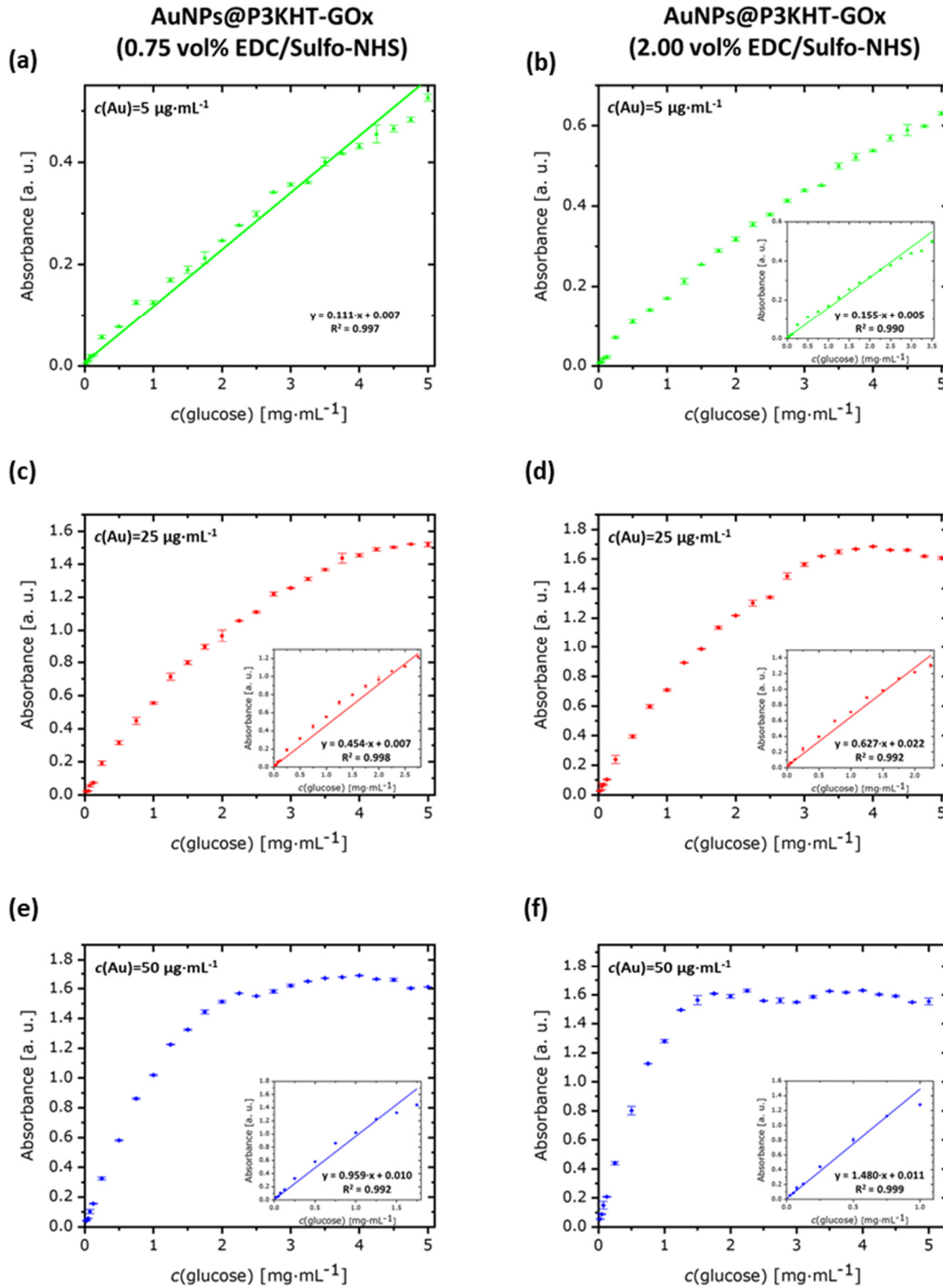


Figure D-2: Absorption intensities at 415 nm obtained by UV-vis spectroscopy for different glucose concentrations of bioassays based on AuNPs@P3KHT-GOx with various gold concentrations: (a, b) $c(\text{Au}) = 5 \mu\text{g}\cdot\text{mL}^{-1}$, (c, d) $c(\text{Au}) = 25 \mu\text{g}\cdot\text{mL}^{-1}$, (e, f) $c(\text{Au}) = 50 \mu\text{g}\cdot\text{mL}^{-1}$. The insets show calibration curves in the linear range where the absorption signal is proportional to the glucose concentration. Error bars are the standard deviation (mean \pm standard deviation) of three individual measurements for each glucose concentration. Bioconjugation between AuNPs@P3KHT and GOx was conducted in solution using (a, c, e) EDC/S-NHS_{low} (0.75 vol%) or (b, d, f) EDC/S-NHS_{high} (2.00 vol%).

As revealed in Figure D-2a, only colorimetric assays based on AuNPs@P3KHT-GOx (0.75 vol% EDC/Sulfo-NHS) and gold concentration of $5 \mu\text{g}\cdot\text{mL}^{-1}$ yielded conditions in which the detected absorption signal at 415 nm of the $\text{ABTS}^{\bullet+}$ radicals is proportional to the glucose concentration over the whole investigated glucose range from $25 \mu\text{g}\cdot\text{mL}^{-1}$ to $5 \text{mg}\cdot\text{mL}^{-1}$. However, the intensity of the detected colorimetric output signal is very low under this condition, resulting in low-signal-to noise ratios, especially for low glucose concentrations. Therefore, I decided to use higher gold concentrations of $12.5 \mu\text{g}\cdot\text{mL}^{-1}$ for colorimetric glucose detection. Bioassays with this gold concentration yielded the best conditions for colorimetric glucose detection with intense absorption signals (even at low glucose concentrations) and broad linear ranges from $25 \mu\text{g}\cdot\text{mL}^{-1}$ to $3.0 \text{mg}\cdot\text{mL}^{-1}$ as discussed in section 3.4.5.

Colorimetric glucose bioassays based on non-biofunctionalizable gold-polythiophene hybrid nanocrystals

I also implemented enzyme-modified non-biofunctionalizable gold-polythiophene hybrid nanoparticles AuNPs@PTEBS-GOx and AuNPs@PEDOT:PSS-GOx into colorimetric bioassays. Bioconjugation of amine-containing species to these hybrid nanomaterials should not be possible as proven by Raman spectroscopy (section 3.4.3). UV-vis absorption spectra of these colorimetric bioassays at different time points after glucose addition are depicted in FigureD-3a and b. Even 1 h after glucose addition, there were no differences in the UV-vis absorption spectra compared to the initial state, indicating that no GOx molecules were present in the colorimetric bioassay, which could oxidize glucose and cause a colorimetric signal due to $\text{ABTS}^{\bullet+}$ radical formation.

FigureD-3c compares the measured UV-vis absorption signal at 415 nm of the colorimetric bioassays containing AuNPs@PTEBS-GOx, AuNPs@PEDOT:PSS-GOx and AuNPs@P3KHT-GOx. The signal caused by $1 \text{mg}\cdot\text{mL}^{-1}$ glucose in bioassays with non-biofunctionalizable gold-polythiophene hybrid nanoparticles was two orders of magnitude lower than that of bioassays with AuNPs@P3KHT-GOx. This result clearly demonstrates that hybrid nanoparticles require carboxyl groups in the polythiophene ligand shell to be biofunctionalizable and to interact with biological species. Thus,

AuNPs@PTEBS and AuNPs@PEDOT:PSS are not suitable for implementation in colorimetric bioassays, since they lack biofunctionality.

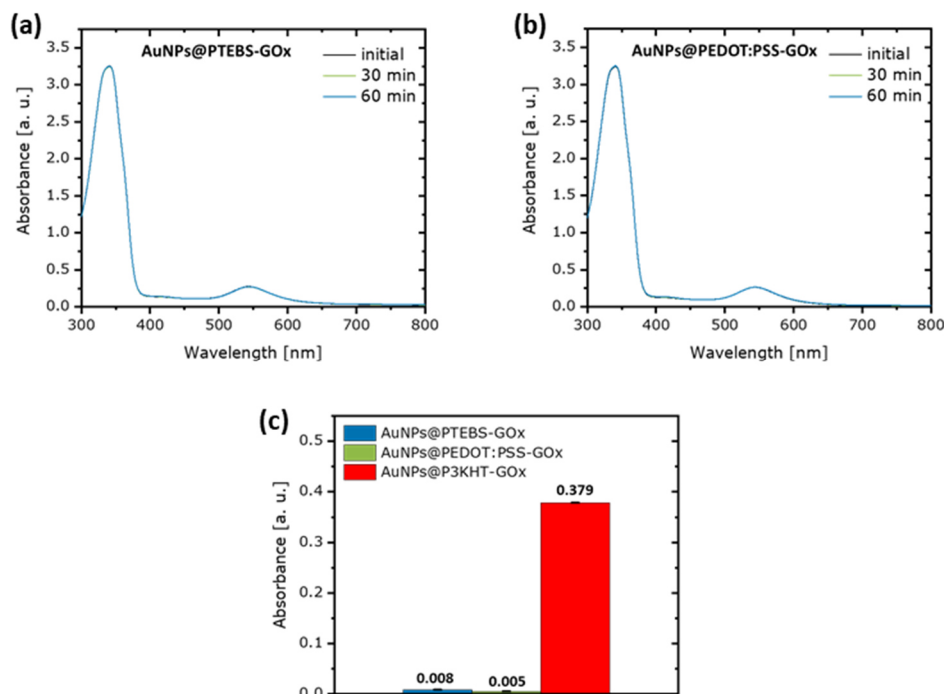


Figure D-3: UV-vis absorption spectra of colorimetric bioassays containing (a) AuNPs@PTEBS-GOx and (b) AuNPs@PEDOT:PSS-GOx at different time points after glucose addition. The concentration of glucose was $1 \text{ mg}\cdot\text{mL}^{-1}$. (c) Detected UV-vis absorption signal at 415 nm caused by $1 \text{ mg}\cdot\text{mL}^{-1}$ glucose in the bioassays containing AuNPs@PTEBS-GOx, AuNPs@PEDOT:PSS-GOx and AuNPs@P3KHT-GOx. Bioconjugation of all gold-polythiophene hybrid nanoparticles was conducted in solution using EDC/S-NHS_{high} (2.00 vol%). Error bars illustrate standard deviation obtained by three individual measurements. All measurements were performed 10 min after the addition of glucose.

E Inkjet printing of amperometric biosensors for electrochemical glucose detection

Figure E-1 shows sequences of stroboscopic images of drop formation using inks containing AuNPs@P3KHT-GOx and AuNPs@P3KHT. The images were recorded with the internal camera of the PiXDRO LP50 inkjet printer by increasing the delay time of

the camera in steps of $10\ \mu\text{s}$. The distance, which the drop moved between each image is proportional to the velocity of the drop.⁸⁵⁷

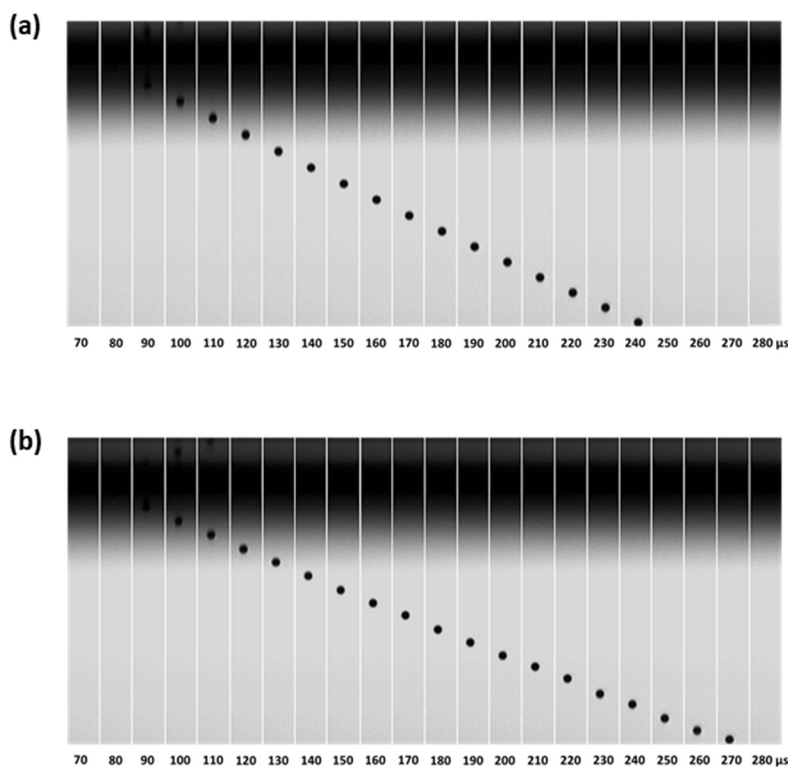


Figure E-1: Sequence of stroboscopic images illustrating drop ejection of inks containing (a) enzyme-functionalized gold-polythiophene hybrid nanoparticles AuNPs@P3KHT-GOx and (b) non-functionalized gold-polythiophene hybrid nanoparticles AuNPs@P3KHT. The images were recorded with a $10\ \mu\text{s}$ delay increment.

Both inks possessed similar drop formation processes. The drop creation started at a delay time of $90\ \mu\text{s}$ (Figure E-1). At this point the liquid was pushed out of the nozzle and a ligament with a round head was created. At a delay time of $100\ \mu\text{s}$ the formed filaments already ruptured near the edge of the nozzle (black area on the top of the stroboscopic images), creating a single drop. Due to surface tensions, the tail of the filaments retracted to the nozzle, while the drops traveled towards the substrate. Drops formed by inks containing enzyme-functionalized AuNPs@P3KHT-GOx moved faster and disappeared from the area visible by the camera at a delay time of $250\ \mu\text{s}$. In contrast, drops created by inks composed of non-functionalized AuNPs@P3KHT were slower and disappeared from the visible area at a longer delay time of $280\ \mu\text{s}$. This observation corresponded to the higher actuating voltage in the optimal waveform of inks containing

AuNPs@P3KHT-GOx (section 6.2.5). In general, the drop velocity enhances with increasing actuating voltage.⁸⁵⁷

Small gold-colored circular splashes were visible around the gold WE in the optical micrographs of the inkjet-printed biosensors (Figure E-2), which likely originated from satellite drops. If satellite drops occur during inkjet printing, the leading drop has a higher velocity compared to the single-drop case. This means that the leading drop travels a larger distance in the sequence of stroboscopic images in a shorter time (Figure 3-47c, section 3.4.6). The faster movement is based on the smaller volume of the leading drop, since two drops were developed from the same amount of ejected liquid as in the case of single drop formation.

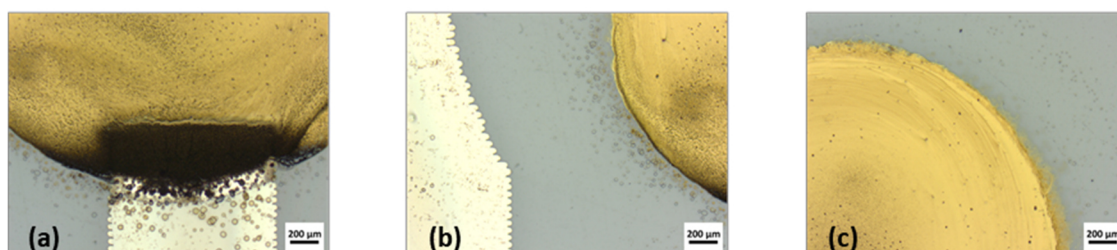


Figure E-2: (a, b, c) Optical micrographs of inkjet-printed amperometric biosensors on flexible PET foils. The CE and RE were printed using a commercial silver ink Sicrys™ I40DM-106 (PV Nano Cell Ltd, Israel) and the WE was printed using an ink containing enzyme-functionalized AuNPs@P3KHT-GOx.

Optical microscope images in Figure E-2 also revealed that the edges of the gold WE were blurry and not sharp. This likely originated from the two layers which have been printed on top of each other to produce sufficient film thickness of the WE. It is likely that the drops were not deposited on the exact same position in the second printing step. Actually, the PiXDRO LP50 inkjet printer should be able to print with high accuracy. However, it is also possible that the substrate slipped out of place during printing. Prior to printing, the substrate is placed on a vacuum table and fixed by the emerging vacuum. Temporary problems in vacuum generation could cause a small shift in the substrate's position.

Bibliography

1. Kamyshny, A. & Magdassi, S. Conductive nanomaterials for printed electronics. *Small* **10**, 3515–3535 (2014).
2. Wu, W. Inorganic nanomaterials for printed electronics: a review. *Nanoscale* **9**, 7342–7372 (2017).
3. Huang, Q. & Zhu, Y. Printing conductive nanomaterials for flexible and stretchable electronics: a review of materials, processes, and applications. *Adv. Mater. Technol.* **4**, 1800546(1–41) (2019).
4. Park, S., Kim, H., Kim, J.-H. & Yeo, W.-H. Advanced nanomaterials, printing processes, and applications for flexible hybrid electronics. *Materials (Basel)*. **13**, 3587(1–34) (2020).
5. Kamyshny, A. & Magdassi, S. Conductive nanomaterials for 2D and 3D printed flexible electronics. *Chem. Soc. Rev.* **48**, 1712–1740 (2019).
6. Perelaer, J. *et al.* Printed electronics: the challenges involved in printing devices, interconnects, and contacts based on inorganic materials. *J. Mater. Chem.* **20**, 8446–8453 (2010).
7. Tekin, E., Smith, P. J. & Schubert, U. S. Inkjet printing as a deposition and patterning tool for polymers and inorganic particles. *Soft Matter* **4**, 703–713 (2008).
8. Singh, M., Haverinen, H. M., Dhagat, P. & Jabbour, G. E. Inkjet printing-process and its applications. *Adv. Mater.* **22**, 673–685 (2010).
9. Caironi, M., Gili, E., Sakanoue, T., Cheng, X. & Sirringhaus, H. High yield, single droplet electrode arrays for nanoscale printed electronics. *ACS Nano* **4**, 1451–1456 (2010).
10. Li, B. *et al.* Inkjet printed chemical sensor array based on polythiophene conductive polymers. *Sensors Actuators B Chem.* **123**, 651–660 (2007).
11. Dua, V. *et al.* All-organic vapor sensor using inkjet-printed reduced graphene oxide. *Angew. Chemie Int. Ed.* **49**, 2154–2157 (2010).
12. Jang, J., Ha, J. & Cho, J. Fabrication of water-dispersible polyaniline-poly(4-styrenesulfonate) nanoparticles for inkjet-printed chemical-sensor applications. *Adv. Mater.* **19**, 1772–1775 (2007).
13. Sekitani, T., Noguchi, Y., Zschieschang, U., Klauk, H. & Someya, T. Organic transistors manufactured using inkjet technology with subfemtoliter accuracy. *PNAS* **105**, 4976–4980 (2008).
14. Noh, Y. Y., Zhao, N., Caironi, M. & Sirringhaus, H. Downscaling of self-aligned, all-printed polymer thin-film transistors. *Nat. Nanotechnol.* **2**, 784–789 (2007).
15. Nogi, M., Komoda, N., Otsuka, K. & Suganuma, K. Foldable nanopaper antennas for origami electronics. *Nanoscale* **5**, 4395–4399 (2013).

16. Song, L., Myers, A. C., Adams, J. J. & Zhu, Y. Stretchable and reversibly deformable radio frequency antennas based on silver nanowires. *ACS Appl. Mater. Interfaces* **6**, 4248–4253 (2014).
17. Kim, B. H. *et al.* High-resolution patterns of quantum dots formed by electrohydrodynamic jet printing for light-emitting diodes. *Nano Lett.* **15**, 969–973 (2015).
18. Sandstrom, A., Dam, H. F., Krebs, F. C. & Edman, L. Ambient fabrication of flexible and large-area organic light-emitting devices using slot-die coating. *Nat. Commun.* **3**, 1002(1–5) (2012).
19. Cao, X. *et al.* Fully screen-printed, large-area, and flexible active-matrix electrochromic displays using carbon nanotube thin-film transistors. *ACS Nano* **10**, 9816–9822 (2016).
20. Krebs, F. C., Fyenbo, J. & Jørgensen, M. Product integration of compact roll-to-roll processed polymer solar cell modules: methods and manufacture using flexographic printing, slot-die coating and rotary screen printing. *J. Mater. Chem.* **20**, 8994–9001 (2010).
21. Hwang, K. *et al.* Toward large scale roll-to-roll production of fully printed perovskite solar cells. *Adv. Mater.* **27**, 1241–1247 (2015).
22. Kumar, R. *et al.* All-Printed, stretchable Zn-Ag₂O rechargeable battery via hyperelastic binder for self-powering wearable electronics. *Adv. Energy Mater.* **7**, 1602096(1–8) (2017).
23. Gaikwad, A. M., Steingart, D. A., Nga Ng, T., Schwartz, D. E. & Whiting, G. L. A flexible high potential printed battery for powering printed electronics. *Appl. Phys. Lett.* **102**, 233302 (1–5) (2013).
24. Zhang, H., Qiao, Y. & Lu, Z. Fully printed ultraflexible supercapacitor supported by a single-textile substrate. *ACS Appl. Mater. Interfaces* **8**, 32317–32323 (2016).
25. Choi, K. H., Yoo, J. T., Lee, C. K. & Lee, S. Y. All-inkjet-printed, solid-state flexible supercapacitors on paper. *Energy Environ. Sci.* **9**, 2812–2821 (2016).
26. Schlatter, S., Grasso, G., Rosset, S. & Shea, H. Inkjet printing of complex soft machines with densely integrated electrostatic actuators. *Adv. Intell. Syst.* **2**, 2000136(1–14) (2020).
27. Zhang, Y. *et al.* All-printed strain sensors: building blocks of the aircraft structural health monitoring system. *Sensors Actuators A Phys.* **253**, 165–172 (2017).
28. Ali, S., Khan, S. & Bermak, A. Inkjet-Printed human body temperature sensor for wearable electronics. *IEEE Access* **7**, 163981–163987 (2019).
29. Kamyshny, A., Steinke, J. & Magdassi, S. Metal-based inkjet inks for printed electronics. *Open Appl. Phys. J.* **4**, 19–36 (2011).
30. Nir, M. M. *et al.* Electrically conductive inks for inkjet printing. in *The Chemistry of Inkjet Inks* (ed. Magdassi, S.) 225–254 (World Scientific, 2009).
31. Calvert, P. Inkjet printing for materials and devices. *Chem. Mater.* **13**, 3299–3305 (2001).

32. Kamyshny, A., Ben-Moshe, M., Aviezer, S. & Magdassi, S. Ink-jet printing of metallic nanoparticles and microemulsions. *Macromol. Rapid Commun.* **26**, 281–288 (2005).
33. Xin, Z. *et al.* Sustainable production of highly conductive multilayer graphene ink for wireless connectivity and IoT applications. *Nat. Commun.* **9**, 5197 (2018).
34. Huang, L., Huang, Y., Liang, J., Wan, X. & Chen, Y. Graphene-based conducting inks for direct inkjet printing of flexible conductive patterns and their applications in electric circuits and chemical sensors. *Nano Res.* **4**, 675–684 (2011).
35. Capasso, A. *et al.* Ink-jet printing of graphene for flexible electronics: an environmentally-friendly approach. *Solid State Commun.* **224**, 53–63 (2015).
36. Kordás, K. *et al.* Inkjet printing of electrically conductive patterns of carbon nanotubes. *Small* **2**, 1021–1025 (2006).
37. Song, J. W. *et al.* The production of transparent carbon nanotube field emitters using inkjet printing. *Phys. E* **41**, 1513–1516 (2009).
38. Park, S., Vosguerichian, M. & Bao, Z. A review of fabrication and applications of carbon nanotube film-based flexible electronics. *Nanoscale* **5**, 1727–1752 (2013).
39. Sirringhaus, H. *et al.* High-resolution inkjet printing of all-polymer transistor circuits. *Science* (80-). **290**, 2123–2126 (2000).
40. Weng, B., Shepherd, R. L., Crowley, K., Killard, A. J. & Wallace, G. G. Printing conducting polymers. *Analyst* **135**, 2779–2789 (2010).
41. Vacca, A. *et al.* Preparation and characterisation of transparent and flexible PEDOT:PSS/PANI electrodes by ink-jet printing and electropolymerisation. *RSC Adv.* **5**, 79600–79606 (2015).
42. Vuorinen, T., Niittynen, J., Kankkunen, T., Kraft, T. M. & Mäntysalo, M. Inkjet-printed graphene PEDOT:PSS temperature sensors on a skin-conformable polyurethane substrate. *Sci. Rep.* **6**, 35289(1–8) (2016).
43. Liu, Z. *et al.* Transparent conductive electrodes from graphene/PEDOT:PSS hybrid inks for ultrathin organic photodetectors. *Adv. Mater.* **27**, 669–675 (2015).
44. Xiong, Z., Dong, C., Cai, H., Liu, C. & Zhang, X. Composite inks of poly (3,4-ethylenedioxythiophene)/poly(styrenesulfonate)/silver nanoparticles and electric/optical properties of inkjet-printed thin films. *Mater. Chem. Phys.* **141**, 416–422 (2013).
45. Choi, S. *et al.* Highly conductive, stretchable and biocompatible Ag–Au core–sheath nanowire composite for wearable and implantable bioelectronics. *Nat. Nanotechnol.* **13**, 1048–1056 (2018).
46. Rajan, K. *et al.* Silver nanoparticle ink technology: state of the art. *Nanotechnol. Sci. Appl.* **9**, 1–13 (2016).

47. Shariq, M., Chattopadhyaya, S., Rudolf, R. & Rai Dixit, A. Characterization of AuNPs based ink for inkjet printing of low cost paper based sensors. *Mater. Lett.* **264**, 127332(1–4) (2020).
48. Shen, W., Zhang, X., Huang, Q., Xu, Q. & Song, W. Preparation of solid silver nanoparticles for inkjet printed flexible electronics with high conductivity. *Nanoscale* **6**, 1622–1628 (2014).
49. Huang, D., Liao, F., Moles, S., Redinger, D. & Subramanian, V. Plastic-compatible low resistance printable gold nanoparticle conductors for flexible electronics. *J. Electrochem. Soc.* **150**, G412–G417 (2003).
50. Cui, Z. *et al.* Design and operation of silver nanowire based flexible and stretchable touch sensors. *J. Mater. Res.* **30**, 79–85 (2014).
51. Yang, C. *et al.* Silver nanowires: from scalable synthesis to recyclable foldable electronics. *Adv. Mater.* **23**, 3052–3056 (2011).
52. Buffat, P. & Borel, J. P. Size effect on the melting temperature of gold particles. *Phys. Rev. A* **13**, 2287–2298 (1976).
53. Dick, K., Dhanasekaran, T., Zhang, Z. & Meisel, D. Size-dependent melting of silica-encapsulated gold nanoparticles. *J. Am. Chem. Soc.* **124**, 2312–2317 (2002).
54. Kim, H. S., Dhage, S. R., Shim, D. E. & Hahn, H. T. Intense pulsed light sintering of copper nanoink for printed electronics. *Appl. Phys. A Mater. Sci. Process.* **97**, 791–798 (2009).
55. Ko, S. H. *et al.* All-inkjet-printed flexible electronics fabrication on a polymer substrate by low-temperature high-resolution selective laser sintering of metal nanoparticles. *Nanotechnology* **18**, 345202(1–8) (2007).
56. Bieri, N. R., Chung, J., Poulikakos, D. & Grigoropoulos, C. P. Manufacturing of nanoscale thickness gold lines by laser curing of a discretely deposited nanoparticle suspension. *Superlattices Microstruct.* **35**, 437–444 (2004).
57. Tsumaki, M., Nitta, K., Jeon, S., Terashima, K. & Ito, T. Development of plasma-assisted inkjet printing and demonstration for direct printing of conductive silver line. *J. Phys. D: Appl. Phys.* **51**, 30LT01(1–5) (2018).
58. Reinhold, I. *et al.* Argon plasma sintering of inkjet printed silver tracks on polymer substrates. *J. Mater. Chem.* **19**, 3384–3388 (2009).
59. Wünscher, S. *et al.* Localized atmospheric plasma sintering of inkjet printed silver nanoparticles. *J. Mater. Chem.* **22**, 24569–24576 (2012).
60. Perelaer, J., Klokkenburg, M., Hendriks, C. E. & Schubert, U. S. Microwave flash sintering of inkjet-printed silver tracks on polymer substrates. *Adv. Mater.* **21**, 4830–4834 (2009).
61. Perelaer, J., De Gans, B. J. & Schubert, U. S. Ink-jet printing and microwave sintering of conductive

- silver tracks. *Adv. Mater.* **18**, 2101–2104 (2006).
62. Jung, S., Chun, S. J. & Shon, C. H. Rapid cellulose-mediated microwave sintering for high-conductivity Ag patterns on paper. *ACS Appl. Mater. Interfaces* **8**, 20301–20308 (2016).
63. Alastalo, A. T. *et al.* Rapid electrical sintering of nanoparticle structures. *MRS Proc.* **1113**, 1113–F02-07 (2009).
64. Allen, M. L. *et al.* Electrical sintering of nanoparticle structures. *Nanotechnology* **19**, 175201(1–4) (2008).
65. Jang, S., Lee, D. J., Lee, D. & Oh, J. H. Electrical sintering characteristics of inkjet-printed conductive Ag lines on a paper substrate. *Thin Solid Films* **546**, 157–161 (2013).
66. Grouchko, M., Kamyshny, A., Mihailescu, C. F., Anghel, D. F. & Magdassi, S. Conductive inks with a ‘built-in’ mechanism that enables sintering at room temperature. *ACS Nano* **5**, 3354–3359 (2011).
67. Magdassi, S., Grouchko, M., Berezin, O. & Kamyshny, A. Triggering the sintering of silver nanoparticles at room temperature. *ACS Nano* **4**, 1943–1948 (2010).
68. Coutts, M. J., Cortie, M. B., Ford, M. J. & McDonagh, A. M. Rapid and controllable sintering of gold nanoparticle inks at room temperature using a chemical agent. *J. Phys. Chem. C* **113**, 1325–1328 (2009).
69. Reiser, B., González-García, L., Kannelidis, I., Maurer, J. H. M. & Kraus, T. Gold nanorods with conjugated polymer ligands: sintering-free conductive inks for printed electronics. *Chem. Sci.* **7**, 4190–4196 (2016).
70. Acevedo-Cartagena, D. E. *et al.* Selective nucleation of poly(3-hexyl thiophene) nanofibers on multilayer graphene substrates. *ACS Macro Lett.* **4**, 483–487 (2015).
71. Skrypnichuk, V. *et al.* Enhanced vertical charge transport in a semiconducting P3HT thin film on single layer graphene. *Adv. Funct. Mater.* **25**, 664–670 (2015).
72. Yao, Y., Dong, H. & Hu, W. Ordering of conjugated polymer molecules: Recent advances and perspectives. *Polym. Chem.* **4**, 5197–5205 (2013).
73. Agbolaghi, S. *et al.* Conversion of face-on orientation to edge-on/flat-on in induced-crystallization of poly(3-hexylthiophene) via functionalization/grafting of reduced graphene oxide with thiophene adducts. *Macromol. Chem. Phys.* **219**, 1700484(1–15) (2018).
74. Tremel, K. & Ludwigs, S. Morphology of P3HT in thin films in relation to optical and electrical properties. in *P3HT Revisited – From Molecular Scale to Solar Cell Devices* (ed. Ludwigs, S.) 39–82 (Springer, 2014). doi:10.1007/12_2014_288.
75. Osaka, I. & Takimiya, K. Backbone orientation in semiconducting polymers. *Polymer (Guildf)*. **59**,

- A1–A15 (2015).
76. Sirringhaus, H. *et al.* Two-dimensional charge transport in self-organized, high-mobility conjugated polymers. *Nature* **401**, 685–688 (1999).
77. Hlaing, H. *et al.* Nanoimprint induced molecular orientation in semiconducting polymer nanostructures. *ACS Nano* **5**, 7532–7538 (2011).
78. Ko, J. *et al.* Enhanced vertical charge transport of homo- and blended semiconducting polymers by nanoconfinement. *Adv. Mater.* **32**, 1908087(1–7) (2020).
79. Aryal, M., Trivedi, K. & Hu, W. Nano-confinement induced chain alignment in ordered P3HT nanostructures defined by nanoimprint lithography. *ACS Nano* **3**, 3085–3090 (2009).
80. Coakley, K. M. *et al.* Enhanced hole mobility in regioregular polythiophene infiltrated in straight nanopores. *Adv. Funct. Mater.* **15**, 1927–1932 (2005).
81. Zhang, S. *et al.* Directed self-assembly of hybrid oxide/polymer core/shell nanowires with transport optimized morphology for photovoltaics. *Adv. Mater.* **24**, 82–87 (2012).
82. Briseno, A. L. *et al.* Oligo- and polythiophene/ZnO hybrid nanowire solar cells. *Nano Lett.* **10**, 334–340 (2010).
83. Goiri, E., Borghetti, P., El-Sayed, A., Ortega, J. E. & De Oteyza, D. G. Multi-component organic layers on metal substrates. *Adv. Mater.* **28**, 1340–1368 (2016).
84. Braun, S., Salaneck, W. R. & Fahlman, M. Energy-level alignment at organic/metal and organic/organic interfaces. *Adv. Mater.* **21**, 1450–1472 (2009).
85. Ishii, H., Sugiyama, K., Ito, E. & Seki, K. Energy level alignment and interfacial electronic structures at organic/metal and organic/organic interfaces. *Adv. Mater.* **11**, 605–625 (1999).
86. Otero, R., Vázquez de Parga, A. L. & Gallego, J. M. Electronic, structural and chemical effects of charge-transfer at organic/inorganic interfaces. *Surf. Sci. Rep.* **72**, 105–145 (2017).
87. Li, P. & Lu, Z.-H. Interface engineering in organic electronics: energy-level alignment and charge Transport. *Small Sci.* **1**, 2000015(1–20) (2021).
88. Liu, R. Hybrid organic/inorganic nanocomposites for photovoltaic cells. *Materials (Basel)*. **7**, 2747–2771 (2014).
89. Gruber, M., Stickler, B. A., Trimmel, G., Schürer, F. & Zojer, K. Impact of energy alignment and morphology on the efficiency in inorganic-organic hybrid solar cells. *Org. Electron.* **11**, 1999–2011 (2010).
90. Hu, Z. *et al.* Energy-level alignment at the organic/electrode interface in organic optoelectronic devices. *Adv. Funct. Mater.* **26**, 129–136 (2016).

91. Kawamura, S. *et al.* Effects of energy-level alignment on characteristics of inverted organic light-emitting diodes. *ACS Appl. Mater. Interfaces* **11**, 21749–21755 (2019).
92. Khan, S., Ali, S. & Bermak, A. Recent developments in printing flexible and wearable sensing electronics for healthcare applications. *Sensors* **19**, 1230(1–34) (2019).
93. Kim, K., Kim, B. & Lee, C. H. Printing flexible and hybrid electronics for human skin and eye-interfaced health monitoring systems. *Adv. Mater.* **32**, 1902051(1–22) (2020).
94. Kim, J., Kumar, R., Bandodkar, A. J. & Wang, J. Advanced materials for printed wearable electrochemical devices: a review. *Adv. Electron. Mater.* **3**, 1600260(1–15) (2017).
95. Sreenilayam, S. P., Ahad, I. U., Nicolosi, V., Acinas Garzon, V. & Brabazon, D. Advanced materials of printed wearables for physiological parameter monitoring. *Mater. Today* **32**, 147–177 (2020).
96. Bandodkar, A. J. & Wang, J. Wearable biofuel cells: a review. *Electroanalysis* **28**, 1188–1200 (2016).
97. Jia, W. *et al.* Wearable textile biofuel cells for powering electronics. *J. Mater. Chem. A* **2**, 18184–18189 (2014).
98. Jia, W., Valdés-Ramírez, G., Bandodkar, A. J., Windmiller, J. R. & Wang, J. Epidermal biofuel cells: energy harvesting from human perspiration. *Angew. Chemie Int. Ed.* **52**, 7233–7236 (2013).
99. Kim, J. *et al.* Wearable salivary uric acid mouthguard biosensor with integrated wireless electronics. *Biosens. Bioelectron.* **74**, 1061–1068 (2015).
100. Sekine, T. *et al.* Fully printed wearable vital sensor for human pulse rate monitoring using ferroelectric polymer. *Sci. Rep.* **8**, 4442(1–10) (2018).
101. Malzahn, K., Windmiller, J. R., Valdés-Ramírez, G., Schöning, M. J. & Wang, J. Wearable electrochemical sensors for in situ analysis in marine environments. *Analyst* **136**, 2912–2917 (2011).
102. Bandodkar, A. J. *et al.* Tattoo-based noninvasive glucose monitoring: a proof-of-concept study. *Anal. Chem.* **87**, 394–398 (2015).
103. Jia, W. *et al.* Electrochemical tattoo biosensors for real-time noninvasive lactate monitoring in human perspiration. *Anal. Chem.* **85**, 6553–6560 (2013).
104. Lemarchand, J. *et al.* Challenges, prospects, and emerging applications of inkjet-printed electronics : a chemist ' point of view. *Angew. Chemie Int. Ed.* **61**, e202200166(1-26) (2022).
105. Borchers, K., Schönhaar, V., Hirth, T., Tovar, G. E. M. & Weber, A. Ink formulation for inkjet printing of streptavidin and streptavidin functionalized nanoparticles. *J. Dispers. Sci. Technol.* **32**, 759–1764 (2011).
106. Kang, T. H. *et al.* All-inkjet-printed flexible nanobio-devices with efficient electrochemical coupling

- using amphiphilic biomaterials. *ACS Appl. Mater. Interfaces* **12**, 24231–24241 (2020).
107. Yun, Y. H. *et al.* A glucose sensor fabricated by piezoelectric inkjet printing of conducting polymers and bienzymes. *Anal. Sci.* **27**, 375–379 (2011).
108. Hou, M., Zhao, H., Feng, Y. & Ge, J. Synthesis of patterned enzyme–metal–organic framework composites by ink-jet printing. *Bioresour. Bioprocess.* **4**, 40(1–8) (2017).
109. Alex, S. & Tiwari, A. Functionalized gold nanoparticles: synthesis, properties and applications-a review. *J. Nanosci. Nanotechnol.* **15**, 1869–1894 (2015).
110. Daruich De Souza, C., Ribeiro Nogueira, B. & Rostelato, M. E. C. M. Review of the methodologies used in the synthesis gold nanoparticles by chemical reduction. *J. Alloys Compd.* **798**, 714–740 (2019).
111. Zhao, P., Li, N. & Astruc, D. State of the art in gold nanoparticle synthesis. *Coord. Chem. Rev.* **257**, 638–665 (2013).
112. Turkevich, J., Stevenson, P. C. & Hillier, J. A study of the nucleation and growth processes in the synthesis of colloidal gold. *Discuss. Faraday Soc.* **11**, 55–75 (1951).
113. Frens, G. Controlled nucleation for the regulation of the particle size in monodisperse gold suspensions. *Nat. Phys. Sci.* **241**, 20–22 (1973).
114. Perrault, S. D. & Chan, W. C. W. Synthesis and surface modification of highly monodispersed, spherical gold nanoparticles of 50-200 nm. *J. Am. Chem. Soc.* **131**, 17042–17043 (2009).
115. Nikoobakht, B. & El-Sayed, M. A. Preparation and growth mechanism of gold nanorods (NRs) using seed-mediated growth method. *Chem. Mater.* **15**, 1957–1962 (2003).
116. Inoue, Y. *et al.* Stepwise preparation of spherical gold nanoparticles passivated with cationic amphiphiles. *Anal. Sci.* **32**, 875–880 (2016).
117. Rodríguez-Fernández, J., Pérez-Juste, J., García De Abajo, F. J. & Liz-Marzán, L. M. Seeded growth of submicron Au colloids with quadrupole plasmon resonance modes. *Langmuir* **22**, 7007–7010 (2006).
118. Koczur, K. M., Mourdikoudis, S., Polavarapu, L. & Skrabalak, S. E. Polyvinylpyrrolidone (PVP) in nanoparticle synthesis. *Dalt. Trans.* **44**, 17883–17905 (2015).
119. Khanna, P. K. *et al.* PVA stabilized gold nanoparticles by use of unexplored albeit conventional reducing agent. *Mater. Chem. Phys.* **92**, 229–233 (2005).
120. Wu, B. H., Yang, H. Y., Huang, H. Q., Chen, G. X. & Zheng, N. F. Solvent effect on the synthesis of monodisperse amine-capped Au nanoparticles. *Chinese Chem. Lett.* **24**, 457–462 (2013).
121. Brust, M., Walker, M., Bethell, D., Schiffrin, D. J. & Whyman, R. Synthesis of thiol-derivatised gold nanoparticles in two-phase liquid-liquid system. *J. Chem. Soc. Chem. Commun.* 801–802

- (1994).
122. Busbee, B. D., Obare, S. O. & Murphy, C. J. An improved synthesis of high-aspect-ratio gold nanorods. *Adv. Mater.* **15**, 414–416 (2003).
 123. Jana, N. R., Gearheart, L. & Murphy, C. J. Wet chemical synthesis of high aspect ratio cylindrical gold nanorods. *J. Phys. Chem. B* **105**, 4065–4067 (2001).
 124. Gao, J., Bender, C. M. & Murphy, C. J. Dependence of the gold nanorod aspect ratio on the nature of the directing surfactant in aqueous solution. *Langmuir* **19**, 9065–9070 (2003).
 125. Nikoobakht, B. & El-Sayed, M. A. Evidence for bilayer assembly of cationic surfactants on the surface of gold nanorods. *Langmuir* **17**, 6368–6374 (2001).
 126. Almora-Barrios, N., Novell-Leruth, G., Whiting, P., Liz-Marzán, L. M. & López, N. Theoretical description of the role of halides, silver, and surfactants on the structure of gold nanorods. *Nano Lett.* **14**, 871–875 (2014).
 127. Si, S., Leduc, C., Delville, M. H. & Lounis, B. Short gold nanorod growth revisited: the critical role of the bromide counterion. *ChemPhysChem* **13**, 193–202 (2012).
 128. Scarabelli, L., Sánchez-Iglesias, A., Pérez-Juste, J. & Liz-Marzán, L. M. A ‘tips and tricks’ practical guide to the synthesis of gold nanorods. *J. Phys. Chem. Lett.* **6**, 4270–4279 (2015).
 129. Garg, N., Scholl, C., Mohanty, A. & Jin, R. The role of bromide ions in seeding growth of Au nanorods. *Langmuir* **26**, 10271–10276 (2010).
 130. Sau, T. K. & Murphy, C. J. Role of ions in the colloidal synthesis of gold nanowires. *Philos. Mag.* **87**, 2143–2158 (2007).
 131. Liu, X. H., Luo, X. H., Lu, S. X., Zhang, J. C. & Cao, W. L. A novel cetyltrimethyl ammonium silver bromide complex and silver bromide nanoparticles obtained by the surfactant counterion. *J. Colloid Interface Sci.* **307**, 94–100 (2007).
 132. Grzelczak, M. *et al.* Influence of iodide ions on the growth of gold nanorods: Tuning tip curvature and surface plasmon resonance. *Adv. Funct. Mater.* **18**, 3780–3786 (2008).
 133. Hubert, F., Testard, F. & Spalla, O. Cetyltrimethylammonium bromide silver bromide complex as the capping agent of gold nanorods. *Langmuir* **24**, 9219–9222 (2008).
 134. Torigoe, K. & Esumi, K. Preparation of monodispersed colloidal gold by reduction of AuCl_4^- - cationic surfactant complexes. *Colloids and Surfaces* **63**, 337–340 (1992).
 135. Rodríguez-Fernández, J., Pérez-Juste, J., Mulvaney, P. & Liz-Marzán, L. M. Spatially-directed oxidation of gold nanoparticles by Au(III)-CTAB complexes. *J. Phys. Chem. B* **109**, 14257–14261 (2005).
 136. Khan, Z., Singh, T., Hussain, J. I. & Hashmi, A. A. Au(III)-CTAB reduction by ascorbic acid:

- preparation and characterization of gold nanoparticles. *Colloids Surfaces B Biointerfaces* **104**, 11–17 (2013).
137. Zümreoglu-Karan, B. A rationale on the role of intermediate Au(III)-vitamin C complexation in the production of gold nanoparticles. *J. Nanoparticle Res.* **11**, 1099–1105 (2009).
138. Pérez-Juste, J., Pastoriza-Santos, I., Liz-Marzán, L. M. & Mulvaney, P. Gold nanorods: synthesis, characterization and applications. *Coord. Chem. Rev.* **249**, 1870–1901 (2005).
139. Pérez-Juste, J., Liz-Marzán, L. M., Carnie, S., Chan, D. Y. C. & Mulvaney, P. Electric-field-directed growth of gold nanorods in aqueous surfactant solutions. *Adv. Funct. Mater.* **14**, 571–579 (2004).
140. Johnson, C. J., Dujardin, E., Davis, S. A., Murphy, C. J. & Mann, S. Growth and form of gold nanorods prepared by seed-mediated, surfactant-directed synthesis. *J. Mater. Chem.* **12**, 1765–1770 (2002).
141. Liu, M. & Guyot-Sionnest, P. Mechanism of silver(I)-assisted growth of gold nanorods and bipyramids. *J. Phys. Chem. B* **109**, 22192–22200 (2005).
142. Wang, Z. L., Gao, R. P., Nikoobakht, B. & El-Sayed, M. A. Surface reconstruction of the unstable {110} surface in gold nanorods. *J. Phys. Chem. B* **104**, 5417–5420 (2000).
143. Wang, Z. L., Mohamed, M. B., Link, S. & El-Sayed, M. A. Crystallographic facets and shapes of gold nanorods of different aspect ratios. *Surf. Sci.* **440**, L809–L814 (1999).
144. Murphy, C. J. *et al.* Gold nanorod crystal growth: from seed-mediated synthesis to nanoscale sculpting. *Curr. Opin. Colloid Interface Sci.* **16**, 128–134 (2011).
145. Grzelczak, M., Pérez-Juste, J., Mulvaney, P. & Liz-Marzán, L. M. Shape control in gold nanoparticle synthesis. *Chem. Soc. Rev.* **37**, 1783–1791 (2008).
146. Jana, N. R., Gearheart, L. & Murphy, C. J. Seed-mediated growth approach for shape-controlled synthesis of spheroidal and rod-like gold nanoparticles using a surfactant template. *Adv. Mater.* **13**, 1389–1393 (2001).
147. Orendorff, C. J. & Murphy, C. J. Quantitation of metal content in the silver-assisted growth of gold nanorods. *J. Phys. Chem. B* **110**, 3990–3994 (2006).
148. Ye, X. *et al.* Seeded growth of monodisperse gold nanorods using bromide-free surfactant mixtures. *Nano Lett.* **13**, 2163–2171 (2013).
149. Ye, X. *et al.* Improved size-tunable synthesis of monodisperse gold nanorods through the use of aromatic additives. *ACS Nano* **6**, 2804–2817 (2012).
150. Ye, X., Zheng, C., Chen, J., Gao, Y. & Murray, C. B. Using binary surfactant mixtures to simultaneously improve the dimensional tunability and monodispersity in the seeded growth of gold nanorods. *Nano Lett.* **13**, 765–771 (2013).

151. Yu, Y.-Y., Chang, S.-S., Lee, C.-L. & Wang, C. R. C. Gold nanorods: electrochemical synthesis and optical properties. *J. Phys. Chem. B* **101**, 6661–6664 (1997).
152. Chang, S.-S., Shih, C.-W., Chen, C.-D., Lai, W.-C. & Wang, C. R. C. The shape transition of gold nanorods. *Langmuir* **15**, 701–709 (1999).
153. Kim, F., Song, J. H. & Yang, P. Photochemical synthesis of gold nanorods. *J. Am. Chem. Soc.* **124**, 14316–14317 (2002).
154. Niidome, Y., Nishioka, K., Kawasaki, H. & Yamada, S. Rapid synthesis of gold nanorods by the combination of chemical reduction and photoirradiation processes; morphological changes depending on the growing processes. *Chem. Commun.* **3**, 2376–2377 (2003).
155. Martin, C. R. Membrane-based synthesis of nanomaterials. *Chem. Mater.* **8**, 1739–1746 (1996).
156. Foss, C. A., Hornyak, G. L., Stockert, J. A. & Martin, C. R. Optical properties of composite membranes containing arrays of nanoscopic gold cylinders. *J. Phys. Chem.* **96**, 7497–7499 (1992).
157. Cepak, V. M. & Martin, C. R. Preparation and stability of template-synthesized metal nanorod sols in organic solvents. *J. Phys. Chem. B* **102**, 9985–9990 (1998).
158. Van Der Zande, B. M. I., Böhmer, M. R., Fokkink, L. G. J. & Schönenberger, C. Colloidal dispersions of gold rods: synthesis and optical properties. *Langmuir* **16**, 451–458 (2000).
159. Martin, C. R. Nanomaterials : a membrane-based synthetic approach. *Science (80-.)*. **266**, 1961–1966 (1994).
160. Cardarelli, F. Less common nonferrous metals. in *Materials Handbook* (ed. Cardarelli, F.) 317–695 (Springer International Publishing, 2018). doi:10.1007/978-3-319-38925-7_4.
161. Zabet-Khosousi, A. & Dhirani, A.-A. Charge transport in nanoparticle assemblies. *Chem. Rev.* **108**, 4072–4124 (2008).
162. Beecher, P., Quinn, A. J., Shevchenko, E. V., Weller, H. & Redmond, G. Insulator-to-metal transition in nanocrystal assemblies driven by in situ mild thermal annealing. *Nano Lett.* **4**, 1289–1293 (2004).
163. Zabet-Khosousi, A., Trudeau, P. E., Suganuma, Y., Dhirani, A.-A. & Statt, B. Metal to insulator transition in films of molecularly linked gold nanoparticles. *Phys. Rev. Lett.* **96**, 2–5 (2006).
164. Kanelidis, I. & Kraus, T. The role of ligands in coinage-metal nanoparticles for electronics. *Beilstein J. Nanotechnol.* **8**, 2625–2639 (2017).
165. Polavarapu, L. *et al.* Alkylamine capped metal nanoparticle ‘inks’ for printable SERS substrates, electronics and broadband photodetectors. *Nanoscale* **3**, 2268–2274 (2011).
166. Gupta, A., Mandal, S., Katiyar, M. & Mohapatra, Y. N. Film processing characteristics of nano gold suitable for conductive application on flexible substrates. *Thin Solid Films* **520**, 5664–5670 (2012).

167. Moreira, H. *et al.* Electron transport in gold colloidal nanoparticle-based strain gauges. *Nanotechnology* **24**, 095701(1–9) (2013).
168. Gerber, R. W., Leonard, D. N. & Franzen, S. Conductive thin film multilayers of gold on glass formed by self-assembly of multiple size gold nanoparticles. *Thin Solid Films* **517**, 6803–6808 (2009).
169. Kovalenko, M. V., Bodnarchuk, M. I., Zaumseil, J., Lee, J. S. & Talapin, D. V. Expanding the chemical versatility of colloidal nanocrystals capped with molecular metal chalcogenide ligands. *J. Am. Chem. Soc.* **132**, 10085–10092 (2010).
170. Stansfield, G. L. & Thomas, P. J. Substituent effects on charge transport in films of Au nanocrystals. *J. Am. Chem. Soc.* **134**, 11888–11891 (2012).
171. Wang, G. R. *et al.* Correlation between nanostructural parameters and conductivity properties for molecularly-mediated thin film assemblies of gold nanoparticles. *J. Mater. Chem.* **17**, 457–462 (2007).
172. Joseph, Y. *et al.* Self-assembled gold nanoparticle/alkanedithiol films: preparation, electron microscopy, charge transport and vapor-sensing properties. *J. Phys. Chem. B* **107**, 7406–7413 (2003).
173. Schlicke, H. *et al.* Freestanding films of crosslinked gold nanoparticles prepared via layer-by-layer spin-coating. *Nanotechnology* **22**, 305303(1–9) (2011).
174. Schlicke, H., Leib, E. W., Petrov, A., Schröder, J. H. & Vossmeier, T. Elastic and viscoelastic properties of cross-linked gold nanoparticles probed by AFM bulge tests. *J. Phys. Chem. C* **118**, 4386–4395 (2014).
175. Zotti, G., Vercelli, B. & Berlin, A. Gold nanoparticles linked by pyrrole- and thiophene-based thiols. Electrochemical, optical, and conductive properties. *Chem. Mater.* **20**, 397–412 (2008).
176. Saitou, K. I., Nishiyabu, R., Iyoda, M. & Kubo, Y. Gold nanoparticle-templated assembly of oligothiophenes: preparation and film properties. *Tetrahedron* **67**, 9685–9689 (2011).
177. Ahn, H., Chandekar, A., Kang, B., Sung, C. & Whitten, J. E. Electrical conductivity and vapor-sensing properties of ω -(3-thienyl)alkanethiol-protected gold nanoparticle films. *Chem. Mater.* **16**, 3274–3278 (2004).
178. Min, S. H. *et al.* Simulation of electrical conductivity for nanoparticles and nanotubes composite sensor according to geometrical properties of nanomaterials. *Compos. Part B Eng.* **174**, 107003 (2019).
179. Stauffer, D. & Aharony, A. *Introduction to percolation theory*. (Taylor & Francis, 1992). doi:10.1201/9781315274386.

-
180. Sahimi, M. *Applications of percolation theory*. (CRC Press, 1994). doi:10.1201/9781482272444.
181. Lefferts, M. J., Murugappan, K., Wu, C. & Castell, M. R. Electrical percolation through a discontinuous Au nanoparticle film. *Appl. Phys. Lett.* **112**, 251602(1–3) (2018).
182. Hu, L., Hecht, D. S. & Gruner, G. Percolation in transparent and conducting carbon nanotube networks. *Nano Lett.* **4**, 2513–2517 (2004).
183. Keblinski, P. & Cleri, F. Contact resistance in percolating networks. *Phys. Rev. B* **69**, 184201(1–4) (2004).
184. Li, J. & Östling, M. Conductivity scaling in supercritical percolation of nanoparticles - not a power law. *Nanoscale* **7**, 3424–3428 (2015).
185. Foygel, M., Morris, R. D., Anez, D., French, S. & Sobolev, V. L. Theoretical and computational studies of carbon nanotube composites and suspensions: electrical and thermal conductivity. *Phys. Rev. B* **71**, 104201(1–8) (2005).
186. Mutiso, R. M. & Winey, K. I. Electrical properties of polymer nanocomposites containing rod-like nanofillers. *Prog. Polym. Sci.* **40**, 63–84 (2015).
187. Powell, M. J. Site percolation in randomly packed spheres. *Phys. Rev. B* **20**, 4194–4198 (1979).
188. Ziff, R. M. & Torquato, S. Percolation of disordered jammed sphere packings. *J. Phys. A Math. Theor.* **50**, 085001(1–8) (2017).
189. Lin, J., Chen, H. & Xu, W. Geometrical percolation threshold of congruent cuboidlike particles in overlapping particle systems. *Phys. Rev. E* **98**, 012134(1–17) (2018).
190. Xu, W., Su, X. & Jiao, Y. Continuum percolation of congruent overlapping spherocylinders. *Phys. Rev. E* **94**, 032122(1–8) (2016).
191. Rintoul, M. D. & Torquato, S. Precise determination of the critical threshold and exponents in a three-dimensional continuum percolation model. *J. Phys. A Math. Gen.* **30**, L585–L592 (1997).
192. Corsi, A. & Gujrati, P. D. Percolation of particles on recursive lattices using a nanoscale approach. III. Percolation of polydisperse particles in the presence of a polymer matrix. *Phys. Rev. E* **74**, 061123(1–15) (2006).
193. Ogata, R., Odagaki, T. & Okazaki, K. Effects of poly-dispersity on continuum percolation. *J. Phys. Condens. Matter* **17**, 4531–4538 (2005).
194. Balberg, I., Anderson, C. H., Alexander, S. & Wagner, N. Excluded volume and its relation to the onset of percolation. *Phys. Rev. B* **30**, 3933–3943 (1984).
195. Zhang, B. *et al.* Percolation threshold of graphene nanosheets as conductive additive in $\text{Li}_4\text{Ti}_5\text{O}_{12}$ anodes of Li-ion batteries. *Nanoscale* **5**, 2100–2106 (2013).

196. Hijjawi, R. S., Asad, J. H., Sakaji, A. J., Al-Sabayleh, M. & Khalifeh, J. M. Infinite simple 3D cubic lattice of identical resistors (two missing bonds). *Eur. Phys. J. Appl. Phys.* **41**, 111–114 (2008).
197. Asad, J. H., Diab, A. A., Hijjawi, R. S. & Khalifeh, J. M. Infinite face-centered-cubic network of identical resistors: application to lattice Green's function. *Eur. Phys. J. Plus* **128**, 1–5 (2013).
198. Song, T. Bin *et al.* Nanoscale joule heating and electromigration enhanced ripening of silver nanowire contacts. *ACS Nano* **8**, 2804–2811 (2014).
199. Mutiso, R. M., Sherrott, M. C., Rathmell, A. R., Wiley, B. J. & Winey, K. I. Integrating simulations and experiments to predict sheet resistance and optical transmittance in nanowire films for transparent conductors. *ACS Nano* **7**, 7654–7663 (2013).
200. Lee, J. Y., Connor, S. T., Cui, Y. & Peumans, P. Solution-processed metal nanowire mesh transparent electrodes. *Nano Lett.* **8**, 689–692 (2008).
201. Garnett, E. C. *et al.* Self-limited plasmonic welding of silver nanowire junctions. *Nat. Mater.* **11**, 241–249 (2012).
202. Hu, L., Kim, H. S., Lee, J. Y., Peumans, P. & Cui, Y. Scalable coating and properties of transparent, flexible, silver nanowire electrodes. *ACS Nano* **4**, 2955–2963 (2010).
203. Stewart, I. E., Kim, M. J. & Wiley, B. J. Effect of morphology on the electrical resistivity of silver nanostructure films. *ACS Appl. Mater. Interfaces* **9**, 1870–1879 (2017).
204. Nirmalraj, P. N., Lyons, P. E., De, S., Coleman, J. N. & Boland, J. J. Electrical connectivity in single-walled carbon nanotube networks. *Nano Lett.* **9**, 3890–3895 (2009).
205. Lyons, P. E. *et al.* The relationship between network morphology and conductivity in nanotube films. *J. Appl. Phys.* **104**, 044302(1–8) (2008).
206. Ye, S., Rathmell, A. R., Chen, Z., Stewart, I. E. & Wiley, B. J. Metal nanowire networks: the next generation of transparent conductors. *Adv. Mater.* **26**, 6670–6687 (2014).
207. Sorel, S., Lyons, P. E., De, S., Dickerson, J. C. & Coleman, J. N. The dependence of the optoelectrical properties of silver nanowire networks on nanowire length and diameter. *Nanotechnology* **23**, 185201(1–9) (2012).
208. Patil, P., Patil, S., Kate, P. & Kulkarni, A. A. Inkjet printing of silver nanowires on flexible surfaces and methodologies to improve the conductivity and stability of the printed patterns. *Nanoscale Adv.* **3**, 240–248 (2021).
209. Tokuno, T. *et al.* Fabrication of silver nanowire transparent electrodes at room temperature. *Nano Res.* **4**, 1215–1222 (2011).
210. Chen, C. *et al.* Necking growth and mechanical properties of sintered Ag particles with different shapes under air and N₂ atmosphere. *J. Mater. Sci.* **54**, 13344–13357 (2019).

-
211. Chen, C. & Suganuma, K. Microstructure and mechanical properties of sintered Ag particles with flake and spherical shape from nano to micro size. *Mater. Des.* **162**, 311–321 (2019).
212. Fujii, S. *et al.* Microwave sintering of Ag-nanoparticle thin films on a polyimide substrate. *AIP Adv.* **5**, 127226(1–11) (2015).
213. Ma, S. *et al.* Low temperature plasma sintering of silver nanoparticles. *Appl. Surf. Sci.* **293**, 207–215 (2014).
214. Li, Z. & Suslick, K. S. Chemically induced sintering of nanoparticles. *Angew. Chemie Int. Ed.* **58**, 14193–14196 (2019).
215. Hui, Z. *et al.* Chemical sintering of direct-written silver nanowire flexible electrodes under room temperature. *Nanotechnology* **28**, 285703(1–12) (2017).
216. Niittynen, J., Sowade, E., Kang, H., Baumann, R. R. & Mäntysalo, M. Comparison of laser and intense pulsed light sintering (IPL) for inkjet-printed copper nanoparticle layers. *Sci. Rep.* **5**, 8832(1–10) (2015).
217. Shankar, A., Salcedo, E., Berndt, A., Choi, D. & Ryu, J. E. Pulsed light sintering of silver nanoparticles for large deformation of printed stretchable electronics. *Adv. Compos. Hybrid Mater.* **1**, 193–198 (2018).
218. Hwang, H. J. *et al.* Rapid pulsed light sintering of silver nanowires on woven polyester for personal thermal management with enhanced performance, durability and cost-effectiveness. *Sci. Rep.* **8**, 17159(1–12) (2018).
219. Terrill, R. H. *et al.* Monolayers in three dimensions: NMR, SAXS, thermal, and electron hopping studies of alkanethiol stabilized gold clusters. *J. Am. Chem. Soc.* **117**, 12537–12548 (1995).
220. Wuelfing, W. P., Green, S. J., Pietron, J. J., Cliffel, D. E. & Murray, R. W. Electronic conductivity of solid-state, mixed-valent, monolayer-protected Au clusters. *J. Am. Chem. Soc.* **122**, 11465–11472 (2000).
221. Wuelfing, W. P. & Murray, R. W. Electron hopping through films of arenethiolate monolayer-protected gold clusters. *J. Phys. Chem. B* **106**, 3139–3145 (2002).
222. Wessels, J. M. *et al.* Optical and electrical properties of three-dimensional interlinked gold nanoparticle assemblies. *J. Am. Chem. Soc.* **126**, 3349–3356 (2004).
223. Tao, N. J. Electron transport in molecular junctions. *Nat. Nanotechnol.* **1**, 173–181 (2006).
224. Wold, D. J. & Frisbie, C. D. Fabrication and characterization of metal-molecule-metal junctions by conducting probe atomic force microscopy. *J. Am. Chem. Soc.* **123**, 5549–5556 (2001).
225. Kahn, A. Fermi level, work function and vacuum level. *Mater. Horizons* **3**, 7–10 (2016).
226. Abas, Z., Kim, H. S., Zhai, L., Kim, J. & Kim, J.-H. Electrode effects of a cellulose-based electro-

- active paper energy harvester. *Smart Mater. Struct.* **23**, 074003(1–7) (2014).
227. Michaelson, H. B. The work function of the elements and its periodicity. *J. Appl. Phys.* **48**, 4729–4733 (1977).
228. Eastman, D. E. Photoelectric work functions of transition, rare-earth, and noble metals. *Phys. Rev. B* **2**, 1–2 (1970).
229. Ulman, A. Formation and structure of self-assembled monolayers. *Chem. Rev.* **96**, 1533–1554 (1996).
230. Speight, J. G. Chap. 1.7 Bond lengths and strengths. in *Lange's Handbook of Chemistry* (ed. Speight, J. G.) 166–187 (McGraw-Hill Education, 2017).
231. Dubois, L. H. & Nuzzo, R. G. Synthesis, structure, and properties of model organic surfaces. *Annu. Rev. Phys. Chem.* **43**, 437–463 (1992).
232. Shirakawa, H., Louis, E. J., MacDiarmid, A. G., Chiang, C. K. & Heeger, A. J. Synthesis of electrically conducting organic polymers: halogen derivatives of polyacetylene, (CH)_x. *J. Chem. Soc. Chem. Commun.* 578–580 (1977).
233. Shirakawa, H. Nobel lecture: The discovery of polyacetylene film - the dawning of an era of conducting polymers. *Rev. Mod. Phys.* **73**, 713–718 (2001).
234. Heeger, A. J. Semiconducting and metallic polymers: the fourth generation of polymeric materials (Nobel lecture). *Angew. Chemie Int. Ed.* **40**, 2591–2611 (2001).
235. Naveen, M. H., Gurudatt, N. G. & Shim, Y. B. Applications of conducting polymer composites to electrochemical sensors: a review. *Appl. Mater. Today* **9**, 419–433 (2017).
236. Nezakati, T., Seifalian, A., Tan, A. & Seifalian, A. M. Conductive polymers: opportunities and challenges in biomedical applications. *Chem. Rev.* **118**, 6766–6843 (2018).
237. Kaur, G., Adhikari, R., Cass, P., Bown, M. & Gunatillake, P. Electrically conductive polymers and composites for biomedical applications. *RSC Adv.* **5**, 37553–37567 (2015).
238. Mike, J. F. & Lutkenhaus, J. L. Recent advances in conjugated polymer energy storage. *J. Polym. Sci. Part B Polym. Phys.* **51**, 468–480 (2013).
239. Balint, R., Cassidy, N. J. & Cartmell, S. H. Conductive polymers: towards a smart biomaterial for tissue engineering. *Acta Biomater.* **10**, 2341–2353 (2014).
240. Forrest, S. R. The path to ubiquitous and low-cost organic electronic appliances on plastic. *Nature* **428**, 911–918 (2004).
241. Tsutsui, T. & Fujita, K. The shift from ‘hard’ to ‘soft’ electronics. *Adv. Mater.* **14**, 949–952 (2002).
242. Mehmood, U., Al-Ahmed, A. & Hussein, I. A. Review on recent advances in polythiophene based

- photovoltaic devices. *Renew. Sustain. Energy Rev.* **57**, 550–561 (2016).
243. Kuei, B. & Gomez, E. D. Chain conformations and phase behavior of conjugated polymers. *Soft Matter* **13**, 49–67 (2017).
244. Tummala, N. R., Risko, C., Bruner, C., Dauskardt, R. H. & Brédas, J. L. Entanglements in P3HT and their influence on thin-film mechanical properties: insights from molecular dynamics simulations. *J. Polym. Sci. Part B Polym. Phys.* **53**, 934–942 (2015).
245. McCulloch, B. *et al.* Polymer chain shape of poly(3-alkylthiophenes) in solution using small-angle neutron scattering. *Macromolecules* **46**, 1899–1907 (2013).
246. Scherlis, D. A. & Marzari, N. π -stacking in thiophene oligomers as the driving force for electroactive materials and devices. *J. Am. Chem. Soc.* **127**, 3207–3212 (2005).
247. Qu, S. *et al.* Highly anisotropic P3HT films with enhanced thermoelectric performance via organic small molecule epitaxy. *NPG Asia Mater.* **8**, e292(1-11) (2016).
248. Alberga, D. *et al.* Morphological and charge transport properties of amorphous and crystalline P3HT and PBTTT: insights from theory. *Phys. Chem. Chem. Phys.* **17**, 18742–18750 (2015).
249. Wang, T., Pearson, A. J. & Lidzey, D. G. Correlating molecular morphology with optoelectronic function in solar cells based on low band-gap copolymer:fullerene blends. *J. Mater. Chem. C* **1**, 7266–7293 (2013).
250. Melis, C., Colombo, L. & Mattoni, A. Self-assembling of poly(3-hexylthiophene). *J. Phys. Chem. C* **115**, 576–581 (2011).
251. Colle, R., Grosso, G., Ronzani, A. & Zicovich-Wilson, C. M. Structure and X-ray spectrum of crystalline poly(3-hexylthiophene) from DFT-van der Waals calculations. *Phys. Status Solidi B* **1368**, 1360–1368 (2011).
252. Dai, L. Conjugated and fullerene-containing polymers for electronic and photonic applications: advanced syntheses and microlithographic fabrications. *J. Macromol. Sci. Part C* **39**, 273–387 (1999).
253. Bredas, J. L. & Street, G. B. Polarons, bipolarons, and solitons in conducting polymers. *Acc. Chem. Res.* **18**, 309–315 (1985).
254. Heinze, J., Frontana-Uribe, B. A. & Ludwigs, S. Electrochemistry of conducting polymers - persistent models and new concepts. *Chem. Rev.* **110**, 4724–4771 (2010).
255. Armes, S. P. Optimum reaction conditions for the polymerization of pyrrole by iron(III) chloride in aqueous solution. *Synth. Met.* **20**, 365–371 (1987).
256. Tan, Y. & Ghandi, K. Kinetics and mechanism of pyrrole chemical polymerization. *Synth. Met.* **175**, 183–191 (2013).

257. Kaneto, K., Yoshino, K. & Inuishi, Y. Electrical and optical properties of polythiophene prepared by electrochemical polymerization. *Solid State Communications* **46**, 389–391 (1983).
258. Guimard, N. K., Gomez, N. & Schmidt, C. E. Conducting polymers in biomedical engineering. *Prog. Polym. Sci.* **32**, 876–921 (2007).
259. Zheng, Y., Zeng, H., Zhu, Q. & Xu, J. Recent advances in conducting poly(3,4-ethylenedioxythiophene):polystyrene sulfonate hybrids for thermoelectric applications. *J. Mater. Chem. C* **6**, 8858–8873 (2018).
260. Hu, L., Song, J., Yin, X., Su, Z. & Li, Z. Research progress on polymer solar cells based on PEDOT:PSS electrodes. *Polymers (Basel)*. **12**, 145(1–19) (2020).
261. Sun, K. *et al.* Review on application of PEDOTs and PEDOT:PSS in energy conversion and storage devices. *J. Mater. Sci. Mater. Electron.* **26**, 4438–4462 (2015).
262. Thomas, C. A., Zong, K., Schottland, P. & Reynolds, J. R. Poly(3,4-alkylenedioxythiophene)s as highly stable aqueous-compatible conducting polymers with biomedical implications. *Adv. Mater.* **12**, 222–225 (2000).
263. Simpson, J., Kirchmeyer, S. & Reuter, K. Advances and applications of inherently conductive polymer technologies based on poly(3,4-ethylenedioxythiophene). in *AIMCAL Fall Technical Conference and 19th International Vacuum Web Coating Conference*. Myrtle Beach, South Carolina 1–10 (2005).
264. Zhou, D. D., Cui, X. T., Hines, A. & Greenberg, R. J. Conducting polymers in neural stimulation application. in *Implantable Neural Prostheses 2. Biological and Medical Physics, Biomedical Engineering* (eds. Zhou, D. & Greenbaum, E.) 217–252 (Springer New York, 2010). doi:10.1007/978-0-387-98120-8_8.
265. Pandey, M., Kumari, N., Nagamatsu, S. & Pandey, S. S. Recent advances in the orientation of conjugated polymer for organic field-effect transistors. *J. Mater. Chem. C* **7**, 13323–13351 (2019).
266. Gargi, D. *et al.* Charge transport in highly face-on poly(3-hexylthiophene) films. *J. Phys. Chem. C* **117**, 17421–17428 (2013).
267. Maddison, D. S. & Tansley, T. L. Variable range hopping in polypyrrole films of a range of conductivities and preparation methods. *J. Appl. Phys.* **72**, 4677–4682 (1992).
268. Bajpai, M., Srivastava, R., Dhar, R. & Tiwari, R. S. Review on optical and electrical properties of conducting polymers. *Indian J. Mater. Sci.* **2016**, 5842763(1–8) (2016).
269. Essaleh, L. *et al.* Mott type variable range hopping conduction and magnetoresistance in p-type CuIn₃Te₅ semiconductor compound. *J. Appl. Phys.* **122**, 015702(1–5) (2017).
270. Kline, R. J., McGehee, M. D., Kadnikova, E. N., Liu, J. & Fréchet, J. M. J. Controlling the field-

- effect mobility of regioregular polythiophene by changing the molecular weight. *Adv. Mater.* **15**, 1519–1522 (2003).
271. Kline, R. J. *et al.* Dependence of regioregular poly(3-hexylthiophene) film morphology and field-effect mobility on molecular weight. *Macromolecules* **38**, 3312–3319 (2005).
272. Verilhac, J. M. *et al.* Effect of macromolecular parameters and processing conditions on supramolecular organisation, morphology and electrical transport properties in thin layers of regioregular poly(3-hexylthiophene). *Synth. Met.* **156**, 815–823 (2006).
273. Hiroshige, Y., Ookawa, M. & Toshima, N. High thermoelectric performance of poly(2,5-dimethoxyphenylenevinylene) and its derivatives. *Synth. Met.* **156**, 1341–1347 (2006).
274. Yao, Q., Chen, L., Xu, X. & Wang, C. The high thermoelectric properties of conducting polyaniline with special submicron-fibre structure. *Chem. Lett.* **34**, 522–523 (2005).
275. Yao, Q., Chen, L., Zhang, W., Liufu, S. & Chen, X. Enhanced thermoelectric performance of single-walled carbon nanotubes/polyaniline hybrid nanocomposite. *ACS Nano* **4**, 2445–2451 (2010).
276. Jaroch, T., Knor, M., Nowakowski, R., Zagórska, M. & Proń, A. Effect of molecular mass on supramolecular organisation of poly(4,4''-dioctyl-2,2':5',2''-terthiophene). *Phys. Chem. Chem. Phys.* **10**, 6182–6189 (2008).
277. Reiss, P., Couderc, E., De Girolamo, J. & Pron, A. Conjugated polymers/semiconductor nanocrystals hybrid materials - preparation, electrical transport properties and applications. *Nanoscale* **3**, 446–489 (2011).
278. Boulanger, N., Yu, V., Hilke, M., Toney, M. F. & Barbero, D. R. Graphene induced electrical percolation enables more efficient charge transport at a hybrid organic semiconductor/graphene interface. *Phys. Chem. Chem. Phys.* **20**, 4422–4428 (2018).
279. Le, T., Kim, Y. & Yoon, H. Electrical and electrochemical properties of conducting polymers. *Polymers (Basel)* **9**, 159 (2017).
280. Moliton, A. & Hiorns, R. C. Review of electronic and optical properties of semiconducting π -conjugated polymers: applications in optoelectronics. *Polym. Int.* **53**, 1397–1412 (2004).
281. Kim, N. *et al.* Highly conductive PEDOT:PSS nanofibrils induced by solution-processed crystallization. *Adv. Mater.* **26**, 2268–2272 (2014).
282. Basescu, N. *et al.* High electrical conductivity in doped polyacetylene. *Nature* **327**, 403–405 (1987).
283. Kaynak, A., Rintoul, L. & George, G. A. Change of mechanical and electrical properties of polypyrrole films with dopant concentration and oxidative aging. *Mater. Res. Bull.* **35**, 813–824 (2000).
284. Bäessler, H. & Köhler, A. Charge transport in organic semiconductors. in *Unimolecular and*

- Supramolecular Electronics I. Topics in Current Chemistry*, vol 312 (ed. Metzger, R. M.) 1–65 (Springer Berlin Heidelberg, 2011). doi:10.1007/128_2011_218.
285. Culebras, M., Gómez, C. M. & Cantarero, A. Review on polymers for thermoelectric applications. *Materials (Basel)*. **6**, 6701–6732 (2014).
286. Dietmueller, R. *et al.* Light-induced charge transfer in hybrid composites of organic semiconductors and silicon nanocrystals. *Appl. Phys. Lett.* **94**, 113301(1–3) (2009).
287. Al-Ibrahim, M. *et al.* The influence of the optoelectronic properties of poly(3-alkylthiophenes) on the device parameters in flexible polymer solar cells. *Org. Electron.* **6**, 65–77 (2005).
288. Chirvase, D. *et al.* Electrical and optical design and characterisation of regioregular poly(3-hexylthiophene-2,5-diyl)/fullerene-based heterojunction polymer solar cells. *Synth. Met.* **138**, 299–304 (2003).
289. Khlyabich, P. P., Burkhart, B., Rudenko, A. E. & Thompson, B. C. Optimization and simplification of polymer-fullerene solar cells through polymer and active layer design. *Polymer (Guildf)*. **54**, 5267–5298 (2013).
290. Qiao, Q., Su, L., Beck, J. & McLeskey, J. T. Characteristics of water-soluble polythiophene: TiO₂ composite and its application in photovoltaics. *J. Appl. Phys.* **98**, 094906(1–7) (2005).
291. Wang, D. *et al.* Trap-assisted charge injection into large bandgap polymer semiconductors. *Materials (Basel)*. **12**, 2427 (2019).
292. Kamarulzaman, N. H. *et al.* Enhanced hybrid solar cells efficiency by plant wastes (terminalia cattapa) as a sensitizer to titanium dioxide TiO₂) combined with PEDOT:PSS. *Int. J. Eng. Technol.* **7**, 177–181 (2018).
293. Ahn, S., Yabumoto, K., Jeong, Y. & Akagi, K. Low bandgap poly(thienylenemethine) derivatives bearing terarylene moieties in the side chains. *Polym. Chem.* **5**, 6977–6989 (2014).
294. Hwang, J., Tanner, D. B., Schwendeman, I. & Reynolds, J. R. Optical properties of nondegenerate ground-state polymers: three dioxythiophene-based conjugated polymers. *Phys. Rev. B* **67**, 115205(1–10) (2003).
295. Chandrasekhar, P. *Conducting polymers, fundamentals and applications*. (Springer New York, 1999). doi:10.1007/978-1-4615-5245-1.
296. Viehe, H. G., Janousek, Z., Merényi, R. & Stella, L. The captodative effect. *Acc. Chem. Res.* **18**, 148–154 (1985).
297. Brédas, J. L., Beljonne, D., Coropceanu, V. & Cornil, J. Charge-transfer and energy-transfer processes in π -conjugated oligomers and polymers: a molecular picture. *Chem. Rev.* **104**, 4971–5003 (2004).

-
298. Giri, D. & Kundu, K. Theoretical study of the evolution of electronic band structure of polythiophene due to bipolaron doping. *Phys. Rev. B* **53**, 4340–4350 (1996).
299. Liu, C., Wang, K., Gong, X. & Heeger, A. J. Low bandgap semiconducting polymers for polymeric photovoltaics. *Chem. Soc. Rev.* **45**, 4825–4846 (2016).
300. Kitamura, C., Tanaka, S. & Yamashita, Y. Design of narrow-bandgap polymers. Syntheses and properties of monomers and polymers containing aromatic-donor and o-quinoid-acceptor units. *Chem. Mater.* **8**, 570–578 (1996).
301. Hu, X., Chen, G., Wang, X. & Wang, H. Tuning thermoelectric performance by nanostructure evolution of a conducting polymer. *J. Mater. Chem. A* **3**, 20896–20902 (2015).
302. Agbolaghi, S. & Abbaspour, S. Nano-hybrids based on surface modified reduced graphene oxide nanosheets and carbon nanotubes and a regioregular polythiophene. *J. Ultrafine Grained Nanostructured Mater.* **51**, 60–70 (2018).
303. Liu, J. *et al.* Oriented poly(3-hexylthiophene) nanofibril with the π - π stacking growth direction by solvent directional evaporation. *Langmuir* **27**, 4212–4219 (2011).
304. Baker, J. L. *et al.* Quantification of thin film crystallographic orientation using X-ray diffraction with an area detector. *Langmuir* **26**, 9146–9151 (2010).
305. Yang, H., Wang, L., Zhang, J., Yu, X. & Geng, Y. Molecular packing and orientation transition of crystalline poly(2, 5-dihexyloxy-p-phenylene). *Macromol. Chem. Phys.* **215**, 405–411 (2014).
306. Chu, C. W. *et al.* Control of the nanoscale crystallinity and phase separation in polymer solar cells. *Appl. Phys. Lett.* **92**, 103306(1–3) (2008).
307. Choi, S. Y. *et al.* Highly ordered poly(3-hexylthiophene) rod polymers via block copolymer self-assembly. *Macromolecules* **44**, 1771–1774 (2011).
308. Rogers, J. T., Schmidt, K., Toney, M. F., Kramer, E. J. & Bazan, G. C. Structural order in bulk heterojunction films prepared with solvent additives. *Adv. Mater.* **23**, 2284–2288 (2011).
309. Yang, H., Lefevre, S. W., Ryu, C. Y. & Bao, Z. Solubility-driven thin film structures of regioregular poly(3-hexyl thiophene) using volatile solvents. *Appl. Phys. Lett.* **90**, 2–4 (2007).
310. Breiby, D. W. & Samuelsen, E. J. Quantification of preferential orientation in conjugated polymers using X-ray diffraction. *J. Polym. Sci. Part B Polym. Phys.* **41**, 2375–2393 (2003).
311. Aasmundtveit, K. E. *et al.* Structural anisotropy of poly(alkylthiophene) films. *Macromolecules* **33**, 3120–3127 (2000).
312. Kim, D. H., Jang, Y., Park, Y. D. & Cho, K. Surface-induced conformational changes in poly(3-hexylthiophene) monolayer films. *Langmuir* **21**, 1999–2002 (2005).
313. Obata, S. & Shimoi, Y. Control of molecular orientations of poly(3-hexylthiophene) on self-

- assembled monolayers: molecular dynamics simulations. *Phys. Chem. Chem. Phys.* **15**, 9265–9270 (2013).
314. Chang, J. F. *et al.* Enhanced mobility of poly(3-hexylthiophene) transistors by spin-coating from high-boiling-point solvents. *Chem. Mater.* **16**, 4772–4776 (2004).
315. Yang, H. *et al.* Effect of mesoscale crystalline structure on the field-effect mobility of regioregular poly(3-hexyl thiophene) in thin-film transistors. *Adv. Funct. Mater.* **15**, 671–676 (2005).
316. DeLongchamp, D. M. *et al.* Variations in semiconducting polymer microstructure and hole mobility with spin-coating speed. *Chem. Mater.* **17**, 5610–5612 (2005).
317. Hartmann, L. *et al.* 2D versus 3D crystalline order in thin films of regioregular poly(3-hexylthiophene) oriented by mechanical rubbing and epitaxy. *Adv. Funct. Mater.* **21**, 4047–4057 (2011).
318. Nagamatsu, S. *et al.* Backbone arrangement in ‘friction-transferred’ regioregular poly(3-alkylthiophene)s. *Macromolecules* **36**, 5252–5257 (2003).
319. Park, Y. D. *et al.* Energy-level alignment at interfaces between gold and poly(3-hexylthiophene) films with two different molecular structures. *Electrochem. Solid-State Lett.* **9**, G317–G319 (2006).
320. Zen, A. *et al.* Effect of molecular weight on the structure and crystallinity of poly(3-hexylthiophene). *Macromolecules* **39**, 2162–2171 (2006).
321. Kim, J. S. *et al.* Tuning mechanical and optoelectrical properties of poly(3-hexylthiophene) through systematic regioregularity control. *Macromolecules* **48**, 4339–4346 (2015).
322. Kim, D. H. *et al.* Enhancement of field-effect mobility due to surface-mediated molecular ordering in regioregular polythiophene thin film transistors. *Adv. Funct. Mater.* **15**, 77–82 (2005).
323. Bulgarevich, K. *et al.* Polymer-based organic field-effect transistors with active layers aligned by highly hydrophobic nanogrooved surfaces. *Adv. Funct. Mater.* **29**, 1905365(1–9) (2019).
324. Wang, G., Swensen, J., Moses, D. & Heeger, A. J. Increased mobility from regioregular poly(3-hexylthiophene) field-effect transistors. *J. Appl. Phys.* **93**, 6137–6141 (2003).
325. Tumbleston, J. R. *et al.* The influence of molecular orientation on organic bulk heterojunction solar cells. *Nat. Photon.* **8**, 385–391 (2014).
326. Savikhin, V. *et al.* Impact of polymer side chain modification on OPV morphology and performance. *Chem. Mater.* **30**, 7872–7884 (2018).
327. Brinkmann, M. & Wittmann, J. C. Orientation of regioregular poly(3-hexylthiophene) by directional solidification: a simple method to reveal the semicrystalline structure of a conjugated polymer. *Adv. Mater.* **18**, 860–863 (2006).
328. Boulanger, N., Yu, V., Hilke, M., Toney, M. F. & Barbero, D. R. In situ probing of the crystallization

- kinetics of rr-P3HT on single layer graphene as a function of temperature. *Phys. Chem. Chem. Phys.* **19**, 8496–8503 (2017).
329. Kim, D. H. *et al.* Graphene surface induced specific self-assembly of poly(3-hexylthiophene) for nanohybrid optoelectronics: from first-principles calculation to experimental characterizations. *Soft Matter* **9**, 5355–5360 (2013).
330. Agbolaghi, S. Core-shell super-structures via smart deposition of naphthothiadiazole and benzodithiophene-possessing polymer backbones onto carbon nanotubes and photovoltaic applications thereof. *J. Mater. Sci. Mater. Electron.* **30**, 832–841 (2019).
331. Charoughchi, S., Agbolaghi, S., Aghapour, S., Sarvari, R. & Abbasi, F. Polymer wrapping: versus well-oriented crystal growth of polythiophenes onto multi-wall carbon nanotubes via surface chemical modification and regioregularity deliberation. *New J. Chem.* **42**, 14469–14480 (2018).
332. Boon, F. *et al.* Synthesis and characterization of nanocomposites based on functional regioregular poly(3-hexylthiophene) and multiwall carbon nanotubes. *Macromol. Rapid Commun.* **31**, 1427–1434 (2010).
333. Misra, R. D. K., Depan, D., Challa, V. S. A. & Shah, J. S. Supramolecular structures fabricated through the epitaxial growth of semiconducting poly(3-hexylthiophene) on carbon nanotubes as building blocks of nanoscale electronics. *Phys. Chem. Chem. Phys.* **16**, 19122–19129 (2014).
334. Charoughchi, S., Agbolaghi, S., Sarvari, R. & Aghapour, S. Purposive assembling of poly(3-hexylthiophene) onto chemically treated multi-wall cCarbon nanotube versus reduced graphene oxide. *Macromol. Res.* **26**, 1200–1211 (2018).
335. Geng, J. & Zeng, T. Influence of single-walled carbon nanotubes induced crystallinity enhancement and morphology change on polymer photovoltaic devices. *J. Am. Chem. Soc.* **128**, 16827–16833 (2006).
336. Nanko, M. Definitions and categories of hybrid materials. *Adv. Technol. Mater. Mater. Process. J.* **11**, 1–8 (2009).
337. Singh, A., Verma, N. & Kumar, K. Chapter 2 - Hybrid composites: a revolutionary trend in biomedical engineering. in *Materials for Biomedical Engineering* (eds. Grumezescu, A. M. & Grumezescu, V.) 33–46 (Elsevier, 2019). doi:10.1016/B978-0-12-818431-8.00002-7.
338. Yamada, A., Sasabe, H., Osada, Y. & Shiroda, Y. *Concepts of Hybrid Materials, Hybrid Materials - Concept and Case Studies*. (ASM International, 1989).
339. Gómez-Romero, P. & Sanchez, C. Hybrid materials, functional applications. An Introduction. in *Functional Hybrid Materials* (eds. Gómez-Romero, P. & Sanchez, C.) 1–14 (Wiley-VCH, 2003). doi:10.1002/3527602372.ch1.
340. Ashby, M. F. & Bréchet, Y. J. M. Designing hybrid materials. *Acta Mater.* **51**, 5801–5821 (2003).

341. Alemán, J. *et al.* Definitions of terms relating to the structure and processing of sols, gels, networks, and inorganic-organic hybrid materials (IUPAC recommendations 2007). *Pure Appl. Chem.* **79**, 1801–1829 (2007).
342. Kickelbick, G. Introduction to hybrid materials. in *Hybrid Materials* (ed. Kickelbick, G.) 1–48 (Wiley-VCH, 2007). doi:10.1002/9783527610495.ch1.
343. Judeinstein, P. & Sanchez, C. Hybrid organic-inorganic materials: a land of multidisciplinary. *J. Mater. Chem.* **6**, 511–525 (1996).
344. Drisko, G. L. & Sanchez, C. Hybridization in materials science - evolution, current state, and future aspirations. *Eur. J. Inorg. Chem.* **2012**, 5097–5105 (2012).
345. Faustini, M., Nicole, L., Ruiz-Hitzky, E. & Sanchez, C. History of organic–inorganic hybrid materials: prehistory, art, science, and advanced applications. *Adv. Funct. Mater.* **28**, 1704158(1–30) (2018).
346. Saveleva, M. S. *et al.* Hierarchy of hybrid materials - the place of inorganics-in-organics in it, their composition and applications. *Front. Chem.* **7**, 179(1–21) (2019).
347. Sanchez, C. & Soler-Illia, G. J. A. A. Hybrid materials (organic-inorganic). in *Encyclopedia of Chemical Processing* (ed. Lee, S.) 1267–1280 (CRC Press, 2005). doi:10.1201/NOE0824755638.
348. Pope, E. J. A., Asami, M. & Mackenzie, J. D. Transparent silica gel-PMMA composites. *J. Mater. Res.* **4**, 1018–1026 (1989).
349. Nishida, F. *et al.* Incorporation of polyaniline into a silica gel via the sol-gel technique. *MRS Online Proc. Libr.* **180**, 747–752 (1990).
350. Dunn, B. & Zink, J. I. Optical properties of sol-gel glasses doped with organic molecules. *J. Mater. Chem.* **1**, 903–913 (1991).
351. Chanana, M. & Liz-Marzán, L. M. Coating matters: the influence of coating materials on the optical properties of gold nanoparticles. *Nanophotonics* **1**, 199–220 (2012).
352. Erathodiyil, N. & Ying, J. Y. Functionalization of inorganic nanoparticles for bioimaging applications. *Acc. Chem. Res.* **44**, 925–935 (2003).
353. Heuer-Jungemann, A. *et al.* The role of ligands in the chemical synthesis and applications of inorganic nanoparticles. *Chem. Rev.* **119**, 4819–4880 (2019).
354. Zhang, Z. & Lin, M. Fast loading of PEG-SH on CTAB-protected gold nanorods. *RSC Adv.* **4**, 17760–17767 (2014).
355. Kim, H. J. *et al.* Controlled synthesis of multi-armed P3HT star polymers with gold nanoparticle core. *RSC Adv.* **6**, 49206–49213 (2016).
356. Lu, K. Hybrid materials – a review on co-dispersion, processing, patterning, and properties. *Int.*

- Mater. Rev.* **65**, 463–501 (2020).
357. Chou, C.-H., Wang, H.-S., Wei, K.-H. & Huang, J. Y. Thiophenol-modified CdS nanoparticles enhance the luminescence of benzoxyl dendron-substituted polyfluorene copolymers. *Adv. Funct. Mater.* **16**, 909–916 (2006).
358. Wang, S., Li, C. & Shi, G. Photoresponsive properties of multilayers of conductive polymer and CdSe nanoparticles. *Sol. Energy Mater. Sol. Cells* **92**, 543–549 (2008).
359. De Girolamo, J., Reiss, P. & Pron, A. Supramolecularly assembled hybrid materials via molecular recognition between diaminopyrimidine-functionalized poly(hexylthiophene) and thymine-capped CdSe nanocrystals. *J. Phys. Chem. C* **111**, 14681–14688 (2007).
360. Coleman, B. R. & Moffitt, M. G. Amphiphilic inorganic nanoparticles with mixed polymer brush layers of variable composition: bridging the paradigms of block copolymer and nanoparticle self-assembly. *Chem. Mater.* **30**, 2474–2482 (2018).
361. Wu, L., Glebe, U. & Böker, A. Surface-initiated controlled radical polymerizations from silica nanoparticles, gold nanocrystals, and bionanoparticles. *Polym. Chem.* **6**, 5143–5184 (2015).
362. Minko, S. Grafting on solid surfaces: “grafting to” and “grafting from” methods. in *Polymer Surfaces and Interfaces* (ed. Stamm, M.) 215–234 (Springer Berlin Heidelberg, 2008). doi:10.1007/978-3-540-73865-7_11.
363. Li, N. & Binder, W. H. Click-chemistry for nanoparticle-modification. *J. Mater. Chem.* **21**, 16717–16734 (2011).
364. Fournier, D., Hoogenboom, R. & Schubert, U. S. Clicking polymers: a straightforward approach to novel macromolecular architectures. *Chem. Soc. Rev.* **36**, 1369–1380 (2007).
365. Zhang, Q., Russell, T. P. & Emrick, T. Synthesis and characterization of CdSe nanorods functionalized with regioregular poly(3-hexylthiophene). *Chem. Mater.* **19**, 3712–3716 (2007).
366. Aldakov, D. *et al.* Oligothiophene-functionalized CdSe nanocrystals: preparation and electrochemical properties. *Microchim. Acta* **160**, 335–344 (2008).
367. Macchione, M. A., Biglione, C. & Strumia, M. Design, synthesis and architectures of hybrid Nanomaterials for therapy and diagnosis applications. *Polymers (Basel)*. **10**, 527(1–34) (2018).
368. Ranjan, R. & Brittain, W. J. Synthesis of high density polymer brushes on nanoparticles by combined RAFT polymerization and click chemistry. *Macromol. Rapid Commun.* **29**, 1104–1110 (2008).
369. Ohno, K. *et al.* Surface-initiated reversible addition-fragmentation chain transfer (RAFT) polymerization from fine particles functionalized with trithiocarbonates. *Macromolecules* **44**, 8944–8953 (2011).

370. Jin, J., Liu, J., Lian, X., Sun, P. & Zhao, H. Dynamic polymer brushes on the surface of silica particles. *RSC Adv.* **3**, 7023–7029 (2013).
371. Sunday, D., Curras-Medina, S. & Green, D. L. Impact of initiator spacer length on grafting polystyrene from silica nanoparticles. *Macromolecules* **43**, 4871–4878 (2010).
372. Lin, Y.-C., Chen, H.-L., Hashimoto, T. & Chen, S.-A. Mechanism of hierarchical structure formation of polymer/nanoparticle hybrids. *Macromolecules* **49**, 7535–7550 (2016).
373. Tanaka, H. *et al.* Combined in situ and time-resolved SANS and SAXS studies of chemical reactions at specific sites and self-assembling processes of reaction products: reduction of palladium ions in self-assembled polyamidoamine dendrimers as a template. *Macromolecules* **40**, 4327–4337 (2007).
374. Sakamoto, N., Harada, M. & Hashimoto, T. In situ and time-resolved SAXS studies of Pd nanoparticle formation in a template of block copolymer microdomain structures. *Macromolecules* **39**, 1116–1124 (2006).
375. Saunders, B. R. Hybrid polymer/nanoparticle solar cells: preparation, principles and challenges. *J. Colloid Interface Sci.* **369**, 1–15 (2012).
376. Liao, H.-C., Chen, S.-Y. & Liu, D.-M. In-situ growing CdS single-crystal nanorods via P3HT polymer as a soft template for enhancing photovoltaic performance. *Macromolecules* **42**, 6558–6563 (2009).
377. Dowland, S. *et al.* Direct growth of metal sulfide nanoparticle networks in solid-state polymer films for hybrid inorganic-organic solar cells. *Adv. Mater.* **23**, 2739–2744 (2011).
378. Avelino, K. Y. P. S. *et al.* Atomolar electrochemical detection of the BCR/ABL fusion gene based on an amplifying self-signal metal nanoparticle-conducting polymer hybrid composite. *Colloids Surfaces B Biointerfaces* **148**, 576–584 (2016).
379. Singh, R., Bajpai, A. K. & Shrivastava, A. K. CdSe nanorod-reinforced poly(thiophene) composites in designing energy storage devices: study of morphology and dielectric behavior. *Polym. Bull.* **78**, 115–131 (2021).
380. Ogurtsov, N. A. *et al.* Synthesis and properties of hybrid poly(3-methylthiophene)-CdSe nanocomposite and estimation of its photovoltaic ability. *Mol. Cryst. Liq. Cryst.* **536**, 33–40 (2011).
381. Jaimes, W. *et al.* Effect of CdS nanoparticle content on the in-situ polymerization of 3-hexylthiophene-2,5-diyl and the application of P3HT-CdS products in hybrid solar cells. *Mater. Sci. Semicond. Process.* **37**, 259–265 (2015).
382. Ran, F. *et al.* In situ polymerization and reduction to fabricate gold nanoparticle-incorporated polyaniline as supercapacitor electrode materials. *Polym. Adv. Technol.* **29**, 1697–1705 (2018).
383. Mikoliunaite, L. *et al.* Development of gold nanoparticle-polypyrrole nanocomposites. *Chemija* **25**,

- 63–69 (2014).
384. Algar, W. R. A brief introduction to traditional bioconjugate chemistry. in *Chemoselective and Bioorthogonal Ligation Reactions* (eds. Algar, W. R., Dawson, P. E. & Medintz, I. L.) 1–36 (Wiley-VCH, 2017). doi:10.1002/9783527683451.ch1.
385. Hermanson, G. T. Chapter 3 - The reactions of bioconjugation. in *Bioconjugate Techniques* (ed. Hermanson, G. T.) 229–258 (Academic Press, 2013). doi:10.1016/b978-0-12-382239-0.00003-0.
386. Hermanson, G. T. Chapter 4 - Zero-length crosslinkers. in *Bioconjugate Techniques* (ed. Hermanson, G. T.) 259–273 (Academic Press, 2013). doi:10.1016/b978-0-12-382239-0.00004-2.
387. Williams, A. & Ibrahim, I. T. A new mechanism involving cyclic tautomers for the reaction with nucleophiles of the water-soluble peptide coupling reagent 1-ethyl-3-(3'-(dimethylamino)propyl)carbodiimide (EDC). *J. Am. Chem. Soc.* **103**, 7090–7095 (1981).
388. Gilles, M. A., Hudson, A. Q. & Borders, C. L. Stability of water-soluble carbodiimides in aqueous solution. *Anal. Biochem.* **184**, 244–248 (1990).
389. Nakajima, N. & Ikada, Y. Mechanism of amide formation by carbodiimide for bioconjugation in aqueous media. *Bioconjug. Chem.* **6**, 123–130 (1995).
390. Madison, S. A. & Carnali, J. O. pH optimization of amidation via carbodiimides. *Ind. Eng. Chem. Res.* **52**, 13547–13555 (2013).
391. Sehgal, D. & Vijay, I. K. A method for the high efficiency of water-soluble carbodiimide-mediated amidation. *Anal. Biochem.* **218**, 87–91 (1994).
392. Staros, J. V. N-hydroxysulfosuccinimide active esters: bis(N-hydroxysulfosuccinimide) esters of two dicarboxylic acids are hydrophilic, membrane-impermeant, protein cross-linkers. *Biochemistry* **21**, 3950–3955 (1982).
393. Staros, J. V., Wright, W. & Swingle, D. M. Enhancement by N-hydroxysulfosuccinimide of water-soluble carbodiimide-mediated coupling reactions. *Anal. Biochem.* **156**, 220–222 (1986).
394. Bartczak, D. & Kanaras, A. G. Preparation of peptide-functionalized gold nanoparticles using one pot EDC/Sulfo-NHS coupling. *Langmuir* **27**, 10119–10123 (2011).
395. Sanchez, C., Belleville, P., Popal, M. & Nicole, L. Applications of advanced hybrid organic–inorganic nanomaterials: from laboratory to market. *Chem. Soc. Rev.* **40**, 696–753 (2011).
396. Das, P. P., Chaudhary, V., Kumar Singh, R., Singh, D. & Aditya Bachchan, A. Advancement in hybrid materials, its applications and future challenges: a review. *Mater. Today Proc.* **47**, 3794–3801 (2021).
397. Lebeau, B. & Innocenzi, P. Hybrid materials for optics and photonics. *Chem. Soc. Rev.* **40**, 886–906 (2011).

398. Zhan, C. *et al.* Conductive polymer nanocomposites: a critical review of modern advanced devices. *J. Mater. Chem. C* **5**, 1569–1585 (2017).
399. Liras, M., Barawi, M. & de la Peña O'Shea, V. A. Hybrid materials based on conjugated polymers and inorganic semiconductors as photocatalysts: from environmental to energy applications. *Chem. Soc. Rev.* **48**, 5454–5487 (2019).
400. Taylor-Pashow, K. M. L., Della Rocca, J., Huxford, R. C. & Lin, W. Hybrid nanomaterials for biomedical applications. *Chem. Commun.* **46**, 5832–5849 (2010).
401. Uddin, M. F. & Sun, C. T. Improved dispersion and mechanical properties of hybrid nanocomposites. *Compos. Sci. Technol.* **70**, 223–230 (2010).
402. Jung, E. D. *et al.* Highly efficient flexible optoelectronic devices using metal nanowire-conducting polymer composite transparent electrode. *Electron. Mater. Lett.* **11**, 906–914 (2015).
403. Riedel, B. *et al.* Tailored highly transparent composite hole-injection layer consisting of Pedot:PSS and SiO₂ nanoparticles for efficient polymer light-emitting diodes. *Adv. Mater.* **23**, 740–745 (2011).
404. Sonar, P., Lim, J. P. F. & Chan, K. L. Organic non-fullerene acceptors for organic photovoltaics. *Energy Environ. Sci.* **4**, 1558–1574 (2011).
405. Mayer, A. C., Scully, S. R., Hardin, B. E., Rowell, M. W. & McGehee, M. D. Polymer-based solar cells. *Mater. Today* **10**, 28–33 (2007).
406. Chuang, M. K. & Chen, F. C. Synergistic plasmonic effects of metal nanoparticle-decorated pegylated graphene oxides in polymer solar cells. *ACS Appl. Mater. Interfaces* **7**, 7397–7405 (2015).
407. Nah, Y. C. *et al.* Enhanced electrochromic absorption in Ag nanoparticle embedded conjugated polymer composite films. *Electrochem. commun.* **9**, 1542–1546 (2007).
408. Namboothiry, M. A. G. *et al.* Electrochromic properties of conducting polymer metal nanoparticles composites. *Synth. Met.* **157**, 580–584 (2007).
409. Srivastava, S., Schaefer, J. L., Yang, Z., Tu, Z. & Archer, L. A. Polymer-particle composites: phase stability and applications in electrochemical energy storage. *Adv. Mater.* **26**, 201–234 (2014).
410. Tang, C., Chen, N. & Hu, X. Conducting polymer nanocomposites: recent developments and future prospects. in *Conducting Polymer Hybrids. Springer Series on Polymer and Composite Materials* (eds. Kumar, V., Kalia, S. & Swart, H. C.) 1–44 (Springer International Publishing, 2017). doi:10.1007/978-3-319-46458-9_1.
411. Cho, S., Kim, M. & Jang, J. Screen-printable and flexible RuO₂ nanoparticle-decorated PEDOT:PSS/graphene nanocomposite with enhanced electrical and electrochemical performances for high-capacity supercapacitor. *ACS Appl. Mater. Interfaces* **7**, 10213–10227 (2015).

-
412. Rybak, A., Boiteux, G., Melis, F. & Seytre, G. Conductive polymer composites based on metallic nanofiller as smart materials for current limiting devices. *Compos. Sci. Technol.* **70**, 410–416 (2010).
413. Amjadi, M., Pichitpajongkit, A., Lee, S., Ryu, S. & Park, I. Highly stretchable and sensitive strain sensor based on silver nanowire-elastomer nanocomposite. *ACS Nano* **8**, 5154–5163 (2014).
414. Lei, W., Si, W., Xu, Y., Gu, Z. & Hao, Q. Conducting polymer composites with graphene for use in chemical sensors and biosensors. *Microchim. Acta* **181**, 707–722 (2014).
415. Putzbach, W. & Ronkainen, N. J. Immobilization techniques in the fabrication of nanomaterial-based electrochemical biosensors: a review. *Sensors* **13**, 4811–4840 (2013).
416. Gerard, M., Chaubey, A. & Malhotra, B. D. Application of conducting polymers to biosensors. *Biosens. Bioelectron.* **17**, 345–359 (2002).
417. Miao, Y., Wu, X., Chen, J., Liu, J. & Qiu, J. Polypyrrole composite nanoparticles and study of their electrocatalytical reduction to oxygen with (without) laccase. *Gold Bull.* **41**, 336–340 (2008).
418. Qiu, J.-D., Shi, L., Liang, R.-P., Wang, G.-C. & Xia, X.-H. Controllable deposition of a platinum nanoparticle ensemble on a polyaniline/graphene hybrid as a novel electrode material for electrochemical sensing. *Chem. Eur. J.* **18**, 7950–7959 (2012).
419. Cummins, G. & Desmulliez, M. P. Y. Inkjet printing of conductive materials: a review. *Circuit World* **38**, 193–213 (2012).
420. Wu, L. Y. L., Kerk, W. T. & Wong, C. C. Transparent conductive film by large area roll-to-roll processing. *Thin Solid Films* **544**, 427–432 (2013).
421. Liu, Z. *et al.* Ultraflexible in-plane micro-supercapacitors by direct printing of solution-processable electrochemically exfoliated graphene. *Adv. Mater.* **28**, 2217–2222 (2016).
422. Min, S.-H., Lee, G.-Y. & Ahn, S.-H. Direct printing of highly sensitive, stretchable, and durable strain sensor based on silver nanoparticles/multi-walled carbon nanotubes composites. *Compos. Part B Eng.* **161**, 395–401 (2019).
423. Backes, I. K. *et al.* Molecular origin of electrical conductivity in gold-polythiophene hybrid particle films. *J. Phys. Chem. Lett.* **11**, 10538–10547 (2020).
424. Chen, S., Yang, M., Hong, S. & Lu, C. Nonionic fluorosurfactant as an ideal candidate for one-step modification of gold nanorods. *Nanoscale* **6**, 3197–3205 (2014).
425. El Kurdi, R. & Patra, D. The role of OH⁻ in the formation of highly selective gold nanowires at extreme pH: multi-fold enhancement in the rate of the catalytic reduction reaction by gold nanowires. *Phys. Chem. Chem. Phys.* **19**, 5077–5090 (2017).
426. Lide, D. R. *CRC Handbook of Chemistry and Physics*. (CRC Press, 2003).

427. Nikoobakht, B., Wang, J. & El-Sayed, M. A. Surface-enhanced Raman scattering of molecules adsorbed on gold nanorods : off-surface plasmon resonance condition. *Chem. Phys. Lett.* **366**, 17–23 (2002).
428. Zhang, Z. & Lin, M. Fast loading of PEG–SH on CTAB-protected gold. *RSC Adv.* **4**, 17760–17767 (2014).
429. Carlini, L. *et al.* Comparison between silver and gold nanoparticles stabilized with negatively charged hydrophilic thiols : SR-XPS and SERS as probes for structural differences and similarities. *Colloids Surfaces A Physicochem. Eng. Asp.* **532**, 183–188 (2017).
430. Chaudhary, V., Pandey, R. K., Prakash, R. & Singh, A. K. Self-assembled H-aggregation induced high performance poly (3-hexylthiophene) Schottky diode. *J. Appl. Phys.* **122**, 225501(1–7) (2017).
431. Veerender, P. *et al.* Probing the annealing induced molecular ordering in bulk heterojunction polymer solar cells using in-situ Raman spectroscopy. *Sol. Energy Mater. Sol. Cells* **120**, 526–535 (2013).
432. Houlton, H. G. & Tartar, H. V. Raman spectra of sodium alkyl sulfonates and sulfinates. *J. Am. Chem. Soc.* **60**, 544–548 (1937).
433. Yi, C. *et al.* Highly electrically conductive polyethylenedioxythiophene thin films for thermoelectric applications. *J. Mater. Chem. A* **4**, 12730–12738 (2016).
434. Yi, C. *et al.* Enhanced thermoelectric properties of poly(3,4-ethylenedioxythiophene):poly(styrenesulfonate) by binary secondary dopants. *ACS Appl. Mater. Interfaces* **7**, 8984–8989 (2015).
435. Pacchioni, G. A not-so-strong bond. *Nat. Rev. Mater.* **4**, 226 (2019).
436. Reimers, J. R., Ford, M. J., Halder, A., Ulstrup, J. & Hush, N. S. Gold surfaces and nanoparticles are protected by Au(0)-thiyl species and are destroyed when Au(I)-thiolates form. *Proc. Natl. Acad. Sci. U. S. A.* **113**, E1424–E1433 (2016).
437. Lavrich, D. J., Wetterer, S. M., Bernasek, S. L. & Scoles, G. Physisorption and chemisorption of alkanethiols and alkyl sulfides on Au(111). *J. Phys. Chem. B* **102**, 3456–3465 (1998).
438. Merche, D. *et al.* One step polymerization of sulfonated polystyrene films in a dielectric barrier discharge. *Plasma Process. Polym.* **7**, 836–845 (2010).
439. Jönsson, S. K. M. *et al.* The effects of solvents on the morphology and sheet resistance in poly(3,4-ethylenedioxythiophene)-polystyrenesulfonic acid (PEDOT–PSS) film. *Synth. Met.* **139**, 1–10 (2003).
440. Buckel, F., Effenberger, F., Yan, C., Götzhäuser, A. & Grunze, M. Influence of aromatic groups incorporated in long-chain alkanethiol self-assembled monolayers on gold. *Adv. Mater.* **12**, 901–

- 905 (2000).
441. Fan, L.-J., Yang, Y.-W. & Tao, Y.-T. Molecular orientation and bonding of terthiophene-thiol self-assembled on Au(111): a combined NEXAFS and XPS study. *J. Electron Spectros. Relat. Phenomena* **144–147**, 433–436 (2005).
442. Castner, D. G., Hinds, K. & Grainger, D. W. X-ray photoelectron spectroscopy sulfur 2p study of organic thiol and disulfide binding interactions with gold surfaces. *Langmuir* **12**, 5083–5086 (1996).
443. Noh, J. *et al.* High-resolution STM and XPS studies of thiophene self-assembled monolayers on Au(111). *J. Phys. Chem. B* **106**, 7139–7141 (2002).
444. Plekan, O. *et al.* Functionalisation and immobilisation of an Au(110) surface via uracil and 2-thiouracil anchored layer. *Phys. Chem. Chem. Phys.* **17**, 15181–15192 (2015).
445. Liu, Y. *et al.* Hydrothermal synthesis of gold polyhedral nanocrystals by varying surfactant concentration and their LSPR and SERS properties. *RSC Adv.* **5**, 68668–68675 (2015).
446. Gai, P. L. & Harmer, M. A. Surface atomic defect structures and growth of gold nanorods. *Nano Lett.* **2**, 771–774 (2002).
447. Gao, H.-M., Liu, H., Qian, H.-J., Jiao, G.-S. & Lu, Z.-Y. Multiscale simulations of ligand adsorption and exchange on gold nanoparticles. *Phys. Chem. Chem. Phys.* **20**, 1381–1394 (2018).
448. Villarreal, E., Li, G. G., Zhang, Q., Fu, X. & Wang, H. Nanoscale surface curvature effects on ligand–nanoparticle interactions: a plasmon-enhanced spectroscopic study of thiolated ligand adsorption, desorption, and exchange on gold nanoparticles. *Nano Lett.* **17**, 4443–4452 (2017).
449. Walker, D. A., Leitsch, E. K., Nap, R. J., Szleifer, I. & Grzybowski, B. A. Geometric curvature controls the chemical patchiness and self-assembly of nanoparticles. *Nat. Nanotechnol.* **8**, 676–681 (2013).
450. Corbierre, M. K., Cameron, N. S. & Lennox, R. B. Polymer-stabilized gold nanoparticles with high grafting densities. *Langmuir* **20**, 2867–2873 (2004).
451. Minari, T. *et al.* Room-temperature printing of organic thin-film transistors with π -junction gold nanoparticles. *Adv. Funct. Mater.* **24**, 4886–4892 (2014).
452. Abe, Y., Kanehara, M. & Kanai, K. Electronic structure of phthalocyanine derivative-protected π -junction Au nanoparticles. *Org. Electron.* **15**, 3465–3470 (2014).
453. Kanehara, M. *et al.* Electroconductive π -junction Au nanoparticles. *Bull. Chem. Soc. Jpn.* **85**, 957–961 (2012).
454. Ha, T. H., Koo, H.-J. & Chung, B. H. Shape-controlled syntheses of gold nanoprisms and nanorods influenced by specific adsorption of halide ions. *J. Phys. Chem. C* **111**, 1123–1130 (2007).

455. Wu, H.-L., Chen, C.-H. & Huang, M. H. Seed-mediated synthesis of branched gold nanocrystals derived from the side growth of pentagonal bipyramids and the formation of gold nanostars. *Chem. Mater.* **21**, 110–114 (2009).
456. Liu, Y., Yang, L. & Shen, Y. Hydrothermal synthesis of gold nanoplates and their structure-dependent LSPR properties. *J. Mater. Res.* **33**, 2671–2679 (2018).
457. Fang, C. *et al.* Facile growth of high-yield gold nanobipyramids induced by chloroplatinic acid for high refractive index sensing properties. *Sci. Rep.* **6**, 36706(1–8) (2016).
458. Wang, Y.-N., Wei, W.-T., Yang, C.-W. & Huang, M. H. Seed-mediated growth of ultralong gold nanorods and nanowires with a wide range of length tunability. *Langmuir* **29**, 10491–10497 (2013).
459. Feng, L. *et al.* Efficient photoinduced charge transfer in chemically-linked organic-metal Ag-P3HT nanocomposites. *Opt. Mater. Express* **6**, 3063(1–12) (2016).
460. Lee, D. & Jang, D. J. Charge-carrier relaxation dynamics of poly(3-hexylthiophene)-coated gold hybrid nanoparticles. *Polymer (Guildf)*. **55**, 5469–5476 (2014).
461. Cui, Y. *et al.* A novel pH neutral self-doped polymer for anode interfacial layer in efficient polymer solar cells. *Macromolecules* **49**, 8126–8133 (2016).
462. Tengstedt, C. *et al.* Fermi-level pinning at conjugated polymer interfaces. *Appl. Phys. Lett.* **88**, 053502(1–3) (2006).
463. Huang, X. & El-Sayed, M. A. Gold nanoparticles : optical properties and implementations in cancer diagnosis and photothermal therapy. *J. Adv. Res.* **1**, 13–28 (2010).
464. Dileseigres, A. S., Prado, Y. & Pluchery, O. How to use localized surface plasmon for monitoring the adsorption of thiol molecules on gold nanoparticles ? *Nanomaterials* **12**, 292(1–15) (2022).
465. Sardar, R., Funston, A. M., Mulvaney, P. & Murray, R. W. Gold nanoparticles: past, present, and future. *Langmuir* **25**, 13840–13851 (2009).
466. Englebienne, P., Van Hoonacker, A. & Verhas, M. High-throughput screening using the surface plasmon resonance effect of colloidal gold nanoparticles. *Analyst* **126**, 1645–1651 (2001).
467. Hoener, B. S. *et al.* Plasmonic sensing and control of single-nanoparticle electrochemistry. *Chem* **4**, 1560–1585 (2018).
468. Novo, C., Funston, A. M., Gooding, A. K. & Mulvaney, P. Electrochemical charging of single gold nanorods. *J. Am. Chem. Soc.* **131**, 14664–14666 (2009).
469. Jo, G., Jung, J. & Chang, M. Controlled self-assembly of conjugated polymers via a solvent vapor pre-treatment for use in organic field-effect transistors. *Polymers (Basel)*. **11**, 332 (1–11) (2019).
470. Aiyar, A. R., Hong, J.-I., Nambiar, R., Collard, D. M. & Reichmanis, E. Tunable crystallinity in regioregular poly(3-hexylthiophene) thin films and its impact on field effect mobility. *Adv. Funct.*

- Mater.* **21**, 2652–2659 (2011).
471. Miller, A. J., Hatton, R. A. & Silva, S. R. P. Water-soluble multiwall-carbon-nanotube-polythiophene composite for bilayer photovoltaics. *Appl. Phys. Lett.* **89**, 131–133 (2006).
 472. Alkilany, A. M. *et al.* Cellular uptake and cytotoxicity of gold nanorods: molecular origin of cytotoxicity and surface effects. *Small* **5**, 701–708 (2009).
 473. Guo, J., Armstrong, M. J., O'Driscoll, C. M., Holmes, J. D. & Rahme, K. Positively charged, surfactant-free gold nanoparticles for nucleic acid delivery. *RSC Adv.* **5**, 17862–17871 (2015).
 474. Joseph, E. & Singhvi, G. Chapter 4 - Multifunctional nanocrystals for cancer therapy: a potential nanocarrier. in *Nanomaterials for Drug Delivery and Therapy* (ed. Grumezescu, A. M.) 91–116 (William Andrew Publishing, 2019). doi:10.1016/B978-0-12-816505-8.00007-2.
 475. Samimi, S., Maghsoudnia, N., Eftekhari, R. B. & Dorkoosh, F. Chapter 3 - Lipid-based nanoparticles for drug delivery systems. in *Characterization and Biology of Nanomaterials for Drug Delivery* (eds. Mohapatra, S. S., Ranjan, S., Dasgupta, N., Mishra, R. K. & Thomas, S.) 47–76 (Elsevier, 2019). doi:10.1016/B978-0-12-814031-4.00003-9.
 476. Freitas, C. & Mu, R. H. Effect of light and temperature on zeta potential and physical stability in solid lipid nanoparticle (SLNTM) dispersions. *Int. J. Pharm.* **168**, 221–229 (1998).
 477. Sreeprasad, T. S., Samal, A. K. & Pradeep, T. One-, two-, and three-dimensional superstructures of gold nanorods induced by dimercaptosuccinic acid. *Langmuir* **24**, 4589–4599 (2008).
 478. Gómez-Graña, S. *et al.* Surfactant (bi)layers on gold nanorods. *Langmuir* **28**, 1453–1459 (2012).
 479. Zhong, L. *et al.* Rational design and SERS properties of side-by-side, end-to-end and end-to-side assemblies of Au nanorods. *J. Mater. Chem.* **21**, 14448–14455 (2011).
 480. Shafiq, A. R., Aziz, A. A. & Mehrdel, B. Nanoparticle optical properties: size dependence of a single gold spherical nanoparticle. *J. Phys. Conf. Ser.* **1083**, 012040 (2018).
 481. Jain, P. K., Eustis, S. & El-Sayed, M. A. Plasmon coupling in nanorod assemblies: Optical absorption, discrete dipole approximation simulation, and exciton-coupling model. *J. Phys. Chem. B* **110**, 18243–18253 (2006).
 482. Jin, R., Wu, G., Li, Z., Mirkin, C. A. & Schatz, G. C. What controls the melting properties of DNA-linked gold nanoparticle assemblies? *J. Am. Chem. Soc.* **125**, 1643–1654 (2003).
 483. Storhoff, J. J., Elghanian, R., Mucic, R. C., Mirkin, C. A. & Letsinger, R. L. One-pot colorimetric differentiation of polynucleotides with single base imperfections using gold nanoparticle probes. *J. Am. Chem. Soc.* **120**, 1959–1964 (1998).
 484. Lin, S., Li, M., Dujardin, E., Girard, C. & Mann, S. One-dimensional plasmon coupling by facile self-assembly of gold nanoparticles into branched chain networks. *Adv. Mater.* **17**, 2553–2559

- (2005).
485. Winkler, R. G., Gold, M. & Reineker, P. Collapse of polyelectrolyte macromolecules by counterion condensation and ion pair formation: a molecular dynamics simulation study. *Phys. Rev. Lett.* **80**, 3731–3734 (1998).
486. Kundagrami, A. & Muthukumar, M. Effective charge and coil-globule transition of a polyelectrolyte chain. *Macromolecules* **43**, 2574–2581 (2010).
487. Loh, P. *et al.* Collapse of linear polyelectrolyte chains in a poor solvent: when does a collapsing polyelectrolyte collect its counterions? *Macromolecules* **41**, 9352–9358 (2008).
488. Reichardt, C. Empirical parameters of solvent polarity. in *Solvents and Solvent Effects in Organic Chemistry* (eds. Reichardt, C. & Welton, T.) 425–508 (Wiley-VCH, 2011). doi:10.1002/3527601791.ch7.
489. Sang Yeon, L. & Boo, B. H. Density functional theory study of vibrational spectra of fluorene. *J. Phys. Chem.* **100**, 8782–8785 (1996).
490. Michaelian, K. H. *et al.* Raman and photoacoustic infrared spectra of fluorene derivatives: experiment and calculations. *Vib. Spectrosc.* **74**, 33–46 (2014).
491. Chua, Y. T. & Stair, P. C. An ultraviolet Raman spectroscopic study of coke formation in methanol to hydrocarbons conversion over zeolite H-MFI. *J. Catal.* **213**, 39–46 (2003).
492. Bree, A. & Zwarich, R. Vibrational assignment of fluorene from the infrared and Raman spectra. *J. Chem. Phys.* **51**, 912–920 (1969).
493. Bürgi, T. Properties of the gold-sulphur interface: from self-assembled monolayers to clusters. *Nanoscale* **7**, 15553–15567 (2015).
494. Tlahuice-Flores, A., Whetten, R. L. & Jose-Yacaman, M. Vibrational normal modes of small thiolate-protected gold clusters. *J. Phys. Chem. C* **117**, 12191–12198 (2013).
495. Varnholt, B. *et al.* Structural information on the Au-S interface of thiolate-protected gold clusters: a Raman spectroscopy study. *J. Phys. Chem. C* **118**, 9604–9611 (2014).
496. Smith, D., Devlin, J. P. & Scott, D. W. Conformational analysis of ethanethiol and 2-propanethiol. *J. Mol. Spectrosc.* **25**, 174–184 (1968).
497. Byler, D. M. & Gerasimowicz, W. V. Normal coordinate analysis of methanethiol and isotopic analogs. *J. Mol. Struct.* **112**, 207–219 (1984).
498. Bazylewski, P., Divigalpitiya, R. & Fanchini, G. In situ Raman spectroscopy distinguishes between reversible and irreversible thiol modifications in L-cysteine. *RSC Adv.* **7**, 2964–2970 (2017).
499. Kieninger, M. & Ventura, O. N. Calculations of the infrared and Raman spectra of simple thiols and thiol-water complexes. *Int. J. Quantum Chem.* **111**, 1843–1857 (2011).

-
500. Wang, R. *et al.* Adsorption, chemical enhancement, and low-lying excited states of p-methylbenzenethiol on silver and gold nanoparticle surfaces: a surface enhanced Raman spectroscopy and density functional theory study. *J. Phys. Chem. C* **123**, 23026–23036 (2019).
501. Madzharova, F., Heiner, Z. & Kneipp, J. Surface-enhanced hyper Raman spectra of aromatic thiols on gold and silver nanoparticles. *J. Phys. Chem. C* **124**, 6233–6241 (2020).
502. Heydari Gharahcheshmeh, M. & Gleason, K. K. Texture and nanostructural engineering of conjugated conducting and semiconducting polymers. *Mater. Today Adv.* **8**, 100086(1–36) (2020).
503. Liu, Y.-C. & Chuang, T. C. Synthesis and characterization of gold/polypyrrole core-shell nanocomposites and elemental gold nanoparticles based on the gold-containing nanocomplexes prepared by electrochemical methods in aqueous solutions. *J. Phys. Chem. B* **107**, 12383–12386 (2003).
504. Berzina, T., Pucci, A., Ruggeri, G., Erokhin, V. & Fontana, M. P. Gold nanoparticles-polyaniline composite material: synthesis, structure and electrical properties. *Synth. Met.* **161**, 1408–1413 (2011).
505. Fadel, M., Fadeel, D. A., Ibrahim, M., Hathout, R. M. & El-Kholy, A. I. One-step synthesis of polypyrrole-coated gold nanoparticles for use as a photothermally active nano-system. *Int. J. Nanomedicine* **15**, 2605–2615 (2020).
506. Zuber, S. N. M. *et al.* Synthesis and characterization of polyaniline coated gold nanocomposites. *AIP Conf. Proc.* **1674**, 020010(1–6) (2015).
507. Hendel, T. *et al.* In situ determination of colloidal gold concentrations with UV-vis spectroscopy: limitations and perspectives. *Anal. Chem.* **86**, 11115–11124 (2014).
508. Li, J. *et al.* Simple and rapid functionalization of gold nanorods with oligonucleotides using an mPEG-SH/Tween 20-assisted approach. *Langmuir* **31**, 7869–7876 (2015).
509. Zhao, Y., Wang, Z., Zhang, W. & Jiang, X. Adsorbed Tween 80 is unique in its ability to improve the stability of gold nanoparticles in solutions of biomolecules. *Nanoscale* **2**, 2114–2119 (2010).
510. Li, J. *et al.* Synergetic approach for simple and rapid conjugation of gold nanoparticles with oligonucleotides. *ACS Appl. Mater. Interfaces* **6**, 16800–16807 (2014).
511. Tevi, T., Saint Birch, S. W., Thomas, S. W. & Takshi, A. Effect of Triton X-100 on the double layer capacitance and conductivity of poly(3,4-ethylenedioxythiophene):poly(styrenesulfonate) (PEDOT:PSS) films. *Synth. Met.* **191**, 59–65 (2014).
512. Yoon, S.-S. & Khang, D.-Y. Roles of nonionic surfactant additives in PEDOT:PSS thin films. *J. Phys. Chem. C* **120**, 29525–29532 (2016).
513. Rughooputh, S. D. D. V., Hotta, S., Heeger, A. J. & Wudl, F. Chromism of soluble polythienylenes.

- J. Polym. Sci. Part B Polym. Phys.* **25**, 1071–1078 (1987).
514. Zhao, K. *et al.* A new method to improve poly(3-hexyl thiophene) (P3HT) crystalline behavior: decreasing chains entanglement to promote order-disorder transformation in solution. *Langmuir* **26**, 471–477 (2010).
515. Ding, Z., Liu, D., Zhao, K. & Han, Y. Optimizing morphology to trade off charge transport and mechanical properties of stretchable conjugated polymer films. *Macromolecules* **54**, 3907–3926 (2021).
516. Köhler, A., Hoffmann, S. T. & Bässler, H. An order-disorder transition in the conjugated polymer MEH-PPV. *J. Am. Chem. Soc.* **134**, 11594–11601 (2012).
517. Jain, P. K., Qian, W. & El-Sayed, M. A. Ultrafast electron relaxation dynamics in coupled metal nanoparticles in aggregates. *J. Phys. Chem. B* **110**, 136–142 (2006).
518. Zhai, L., Pilston, R. L., Zaiger, K. L., Stokes, K. K. & McCullough, R. D. A simple method to generate side-chain derivatives of regioregular polythiophene via the GRIM metathesis and post-polymerization functionalization. *Macromolecules* **36**, 61–64 (2003).
519. Liu, J., Tanaka, T., Sivula, K., Alivisatos, A. P. & Fréchet, J. M. J. Employing end-functional polythiophene to control the morphology of nanocrystal-polymer composites in hybrid solar cells. *J. Am. Chem. Soc.* **126**, 6550–6551 (2004).
520. Martinez, L. *et al.* Improved electronic coupling in hybrid organic-inorganic nanocomposites employing thiol-functionalized P3HT and bismuth sulfide nanocrystals. *Nanoscale* **6**, 10018–10026 (2014).
521. Hammer, B. A. G. *et al.* Reversible, self cross-linking nanowires from thiol-functionalized polythiophene diblock copolymers. *ACS Appl. Mater. Interfaces* **6**, 7705–7711 (2014).
522. Carreon, A. C., Santos, W. L., Matson, J. B. & So, R. C. Cationic polythiophenes as responsive DNA-binding polymers. *Polym. Chem.* **5**, 314–317 (2014).
523. Zhang, C. *et al.* Synthesis of structurally defined cationic polythiophenes for DNA binding and gene delivery. *ACS Appl. Mater. Interfaces* **10**, 4519–4529 (2018).
524. Hermanson, G. T. Chapter 14 - Microparticles and nanoparticles. in *Bioconjugate Techniques* (ed. Hermanson, G. T.) 549–587 (Academic Press, 2013). doi:10.1016/b978-0-12-382239-0.00014-5.
525. Zhang, Q. *et al.* Study of efficiency of coupling peptides with gold nanoparticles. *Chinese J. Anal. Chem.* **45**, 662–667 (2017).
526. Jazayeri, M. H., Amani, H., Pourfatollah, A. A., Pazoki-Toroudi, H. & Sedighimoghaddam, B. Various methods of gold nanoparticles (GNPs) conjugation to antibodies. *Sens. Bio-Sensing Res.* **9**, 17–22 (2016).

-
527. Khashayar, P., Amoabediny, G., Larijani, B., Hosseini, M. & Vanfleteren, J. Fabrication and verification of conjugated AuNP-antibody nanoprobe for sensitivity improvement in electrochemical biosensors. *Sci. Rep.* **7**, 16070 (1–8) (2017).
528. Sabouri, S., Ghourchian, H., Shourian, M. & Boutorabi, M. A gold nanoparticle-based immunosensor for the chemiluminescence detection of the hepatitis B surface antigen. *Anal. Methods* **6**, 5059–5066 (2014).
529. Farrukh, A. *et al.* Bifunctional poly(acrylamide) hydrogels through orthogonal coupling chemistries. *Biomacromolecules* **18**, 906–913 (2017).
530. Zouani, O. F., Kalisky, J., Ibarboure, E. & Durrieu, M. C. Effect of BMP-2 from matrices of different stiffnesses for the modulation of stem cell fate. *Biomaterials* **34**, 2157–2166 (2013).
531. Poltavets, V., Krawczyk, M., Maslak, G., Abraimova, O. & Jönsson-Niedziółka, M. Formation of MnO₂-coated ITO electrodes with high catalytic activity for enzymatic glucose detection. *Dalt. Trans.* **52**, 13769–13780 (2023).
532. Dudkaitė, V., Kairys, V. & Bagdžiūnas, G. Understanding the activity of glucose oxidase after exposure to organic solvents. *J. Mater. Chem. B* **11**, 2409–2416 (2023).
533. Zhang, S., Wang, N., Niu, Y. & Sun, C. Immobilization of glucose oxidase on gold nanoparticles modified Au electrode for the construction of biosensor. *Sensors Actuators B Chem.* **109**, 367–374 (2005).
534. Soni, A. & Jha, S. K. A paper strip based non-invasive glucose biosensor for salivary analysis. *Biosens. Bioelectron.* **67**, 763–768 (2015).
535. Zhang, Y., Lyu, F., Ge, J. & Liu, Z. Ink-jet printing an optimal multi-enzyme system. *Chem. Commun.* **50**, 12919–12922 (2014).
536. Oliveira, K. A., Medrado e Silva, P. B., De Souza, F. R., Martins, F. T. & Coltro, W. K. T. Kinetic study of glucose oxidase on microfluidic toner-based analytical devices for clinical diagnostics with image-based detection. *Anal. Methods* **6**, 4995–5000 (2014).
537. Ferri, S., Kojima, K. & Sode, K. Review of glucose oxidases and glucose dehydrogenases: a bird's eye view of glucose sensing enzymes. *J. Diabetes Sci. Technol.* **5**, 1068–1076 (2011).
538. Riccardi, C. M., Kasi, R. M. & Kumar, C. V. Chapter nineteen - Nanoarmoring of enzymes by interlocking in cellulose fibers with poly(acrylic acid). in *Methods in Enzymology* (ed. Kumar, C. V.) vol. 590 475–500 (Academic Press, 2017).
539. Kumar, S. D., Kulkarni, A. V., Dhaneshwar, R. G. & D'Souza, S. F. Cyclic voltammetric studies at the glucose oxidase enzyme electrode. *J. Electroanal. Chem.* **342**, 153–160 (1992).
540. Nam, J., Won, N., Jin, H., Chung, H. & Kim, S. pH-induced aggregation of gold nanoparticles for

- photothermal cancer therapy. *J. Am. Chem. Soc.* **131**, 13639–13645 (2009).
541. Park, S. *et al.* Reversibly pH-responsive gold nanoparticles and their applications for photothermal cancer therapy. *Sci. Rep.* **9**, 20180(1–9) (2019).
542. Franco-Ulloa, S. *et al.* Dispersion state phase diagram of citrate-coated metallic nanoparticles in saline solutions. *Nat. Commun.* **11**, 5422(1–10) (2020).
543. Pamies, R. *et al.* Aggregation behaviour of gold nanoparticles in saline aqueous media. *J. Nanoparticle Res.* **16**, 2376(1–11) (2014).
544. Barreto, Â. *et al.* Behavior of colloidal gold nanoparticles in different ionic strength media. *J. Nanoparticle Res.* **17**, 493(1–13) (2015).
545. Wickramathilaka, M. P. & Tao, B. Y. Characterization of covalent crosslinking strategies for synthesizing DNA-based bioconjugates. *J. Biol. Eng.* **13**, 63(1–10) (2019).
546. Courjean, O., Gao, F. & Mano, N. Deglycosylation of glucose oxidase for direct and efficient glucose electrooxidation on a glassy carbon electrode. *Angew. Chemie Int. Ed.* **48**, 5897–5899 (2009).
547. PrévotEAU, A., Courjean, O. & Mano, N. Deglycosylation of glucose oxidase to improve biosensors and biofuel cells. *Electrochem. commun.* **12**, 213–215 (2010).
548. Haskell, A. K. *et al.* Glucose oxidase immobilized on magnetic zirconia: controlling catalytic performance and stability. *ACS Omega* **5**, 12329–12338 (2020).
549. Kowalewska, B. & Jakubow, K. The impact of immobilization process on the electrochemical performance, bioactivity and conformation of glucose oxidase enzyme. *Sensors Actuator B Chem.* **238**, 852–861 (2017).
550. Busch, R. T. *et al.* Optimization and structural stability of gold nanoparticle-antibody bioconjugates. *ACS Omega* **4**, 15269–15279 (2019).
551. Lin, A. Y. *et al.* High-density sub-100-nm peptide-gold nanoparticle complexes improve vaccine presentation by dendritic cells in vitro. *Nanoscale Res. Lett.* **8**, 72(1–11) (2013).
552. Dominguez-Medina, S., Blankenburg, J., Olson, J., Landes, C. F. & Link, S. Adsorption of a protein monolayer via hydrophobic interactions prevents nanoparticle aggregation under harsh environmental conditions. *ACS Sustain. Chem. Eng.* **1**, 833–842 (2013).
553. Wu, R., Peng, H., Zhu, J., Jiang, L. & Liu, J. Attaching DNA to gold nanoparticles with a protein corona. *Front. Chem.* **8**, 121(1–9) (2020).
554. Fagúndez, P., Botasini, S., Pablo, J. P. & Eduardo, M. Systematic process evaluation of the conjugation of proteins to gold nanoparticles. *Heliyon* **7**, e07392(1-10) (2021).
555. Rivas-Arancibia, S., Rodríguez-Martínez, E., Badillo-Ramírez, I., López-González, U. & Saniger,

- J. M. Structural changes of amyloid beta in hippocampus of rats exposed to ozone: a Raman spectroscopy study. *Front. Mol. Neurosci.* **10**, 137(1–11) (2017).
556. Rygula, A. *et al.* Raman spectroscopy of proteins: a review. *J. Raman Spectrosc.* **44**, 1061–1076 (2013).
557. Signorelli, S., Cannistraro, S. & Bizzarri, A. R. Raman evidence of p53-DBD disorder decrease upon interaction with the anticancer protein azurin. *Int. J. Mol. Sci.* **20**, 3078(1–14) (2019).
558. Xie, H. *et al.* Peptide cross-linking modulated stability and assembly of peptide-wrapped single-walled carbon nanotubes. *J. Mater. Chem.* **15**, 1734–1741 (2005).
559. Sadat, A. & Joye, I. J. Peak fitting applied to fourier transform infrared and Raman spectroscopic analysis of proteins. *Appl. Sci.* **10**, 5918(1–16) (2020).
560. Catalini, S. *et al.* Hydrogen bonding and solvation of a proline-based peptide model in salt solutions. *Life* **11**, 824(1–13) (2021).
561. Catalini, S., Rossi, B., Foggi, P., Masciovecchio, C. & Bruni, F. Aqueous solvation of glutathione probed by UV resonance Raman spectroscopy. *J. Mol. Liq.* **283**, 537–547 (2019).
562. Li, D., Fang, Z., Duan, H. & Liang, L. Polydopamine-mediated synthesis of core-shell gold@calcium phosphate nanoparticles for enzyme immobilization. *Biomater. Sci.* **7**, 2841–2849 (2019).
563. Nasir, Z., Ali, A., Alam, M. F., Shoeb, M. & Nusrat Jahan, S. Immobilization of GOx enzyme on SiO₂-coated Ni-Co ferrite nanocomposites as magnetic support and their antimicrobial and photocatalytic activities. *ACS Omega* **6**, 33554–33567 (2021).
564. Altun, S., Çakiroğlu, B., Özacar, M. & Özacar, M. A facile and effective immobilization of glucose oxidase on tannic acid modified CoFe₂O₄ magnetic nanoparticles. *Colloids Surfaces B Biointerfaces* **136**, 963–970 (2015).
565. Du, T., Liu, B., Hou, X., Zhang, B. & Du, C. Covalent immobilization of glucose oxidase onto Poly(St-GMA-NaSS) monodisperse microspheres via BSA as spacer arm. *Appl. Surf. Sci.* **255**, 7937–7941 (2009).
566. Li, Z. F., Kang, E. T., Neoh, K. G. & Tan, K. L. Covalent immobilization of glucose oxidase on the surface of polyaniline films graft copolymerized with acrylic acid. *Biomaterials* **19**, 45–53 (1998).
567. Yang, Y. M., Wang, J. W. & Tan, R. X. Immobilization of glucose oxidase on chitosan-SiO₂ gel. *Enzyme Microb. Technol.* **34**, 126–131 (2004).
568. Blandino, A., Macías, M. & Cantero, D. Immobilization of glucose oxidase within calcium alginate gel capsules. *Process Biochem.* **36**, 601–606 (2001).
569. Kumar, S., Krishna Chaitanya, R. & Preedy, V. R. Chapter 20 - Assessment of antioxidant potential

- of dietary components. in *HIV/AIDS* (eds. Preedy, V. R. & Watson, R. R.) 239–253 (Academic Press, 2018). doi:10.1016/B978-0-12-809853-0.00020-1.
570. Brezová, V., Vrecková, Z., Bilík, P., Čaplovičová, M. & Plesch, G. Photoactivity of mechanochemically prepared nanoparticulate titanium dioxide investigated by EPR spectroscopy. *J. Photochem. Photobiol. A Chem.* **206**, 177–187 (2009).
571. Vuolo, M. M., Lima, V. S. & Maróstica Junior, M. R. Chapter 2 - Phenolic Compounds: structure, classification, and antioxidant power. in *Bioactive Compounds* (ed. Campos, M. R. S.) 33–50 (Woodhead Publishing, 2019). doi:10.1016/B978-0-12-814774-0.00002-5.
572. Ilyasov, I. R., Beloborodov, V. L., Selivanova, I. A. & Terekhov, R. P. ABTS/PP decolorization assay of antioxidant capacity reaction pathways. *Int. J. Mol. Sci.* **21**, 1131(1–27) (2020).
573. González, O. & Alonso, R. M. Validation of bioanalytical chromatographic methods for the quantification of drugs in biological fluids. in *Handbook of Analytical Separations* (ed. Hempel, G.) vol. 7 115–134 (Elsevier Science B.V., 2020).
574. Massart, D. L., Dijkstra, A. & Kaufman, L. Chapter 6 Sensitivity and limit of detection. in *Techniques and Instrumentation in Analytical Chemistry* (eds. Massart, D. L., Dijkstra, A. & Kaufman, L.) vol. 1 143–156 (Elsevier, 1978).
575. Gauglitz, G. Analytical evaluation of sensor measurements. *Anal. Bioanal. Chem.* **410**, 5–13 (2018).
576. Armbruster, D. A. & Pry, T. Limit of blank, limit of detection and limit of quantitation. *Clin. Biochem. Rev.* **29 Suppl 1**, S49-52 (2008).
577. Hamilton, R. G. Assay performance parameters. in *Encyclopedia of Medical Immunology* (eds. Mackay, I. R., Rose, N. R., Ledford, D. K. & Lockey, R. F.) 80–84 (Springer New York, 2014). doi:10.1007/978-1-4614-9194-1_308.
578. Neogen/Megazyme. *D-Glucose (GOPOD Format) assay protocol*. https://www.megazyme.com/documents/Assay_Protocol/K-GLUC_DATA.pdf (2023).
579. Megazyme. *D-Fructose and D-Glucose assay procedure*. https://www.megazyme.com/documents/Assay_Protocol/K-FRUGL_DATA.pdf (2018).
580. Megazyme. *D-Glucose (Megaplex-Red) assay procedure*. https://www.megazyme.com/documents/Assay_Protocol/K-MRGLUC_DATA.pdf (2021).
581. McNaugh, A. D. & Wilkinson, A. *IUPAC. Compendium of Chemical Terminology (the 'Gold Book')*. (Blackwell Scientific Publications, 1997).
582. Allegrini, F. & Olivieri, A. C. IUPAC-consistent approach to the limit of detection in partial least-squares calibration. *Anal. Chem.* **86**, 7858–7866 (2014).
583. Demchenko, A. P. Theoretical aspects. in *Introduction to fluorescence sensing* (ed. Demchenko, A.

- P.) 39–68 (Springer International Publishing, Cham., 2015). doi:10.1007/978-3-319-20780-3_2.
584. Liang, H., Sun, S., Zhou, Y. & Liu, Y. In-situ self-assembly of zinc/adenine hybrid nanomaterials for enzyme immobilization. *Catalysts* **7**, 327(1–11) (2017).
585. Abd Rahman, S. *et al.* CdSe/ZnS capped thiolate for application in glucose sensing. *Biosens. J.* **6**, 143(1–5) (2017).
586. Xiong, Y. *et al.* A high-throughput colorimetric assay for glucose detection based on glucose oxidase-catalyzed enlargement of gold nanoparticles. *Nanoscale* **7**, 15584–15588 (2015).
587. Sun, J. *et al.* Multi-enzyme co-embedded organic-inorganic hybrid nanoflowers: synthesis and application as a colorimetric sensor. *Nanoscale* **6**, 255–262 (2014).
588. Luo, X., Xia, J., Jiang, X., Yang, M. & Liu, S. Cellulose-based strips designed based on a sensitive enzyme colorimetric assay for the low concentration of glucose detection. *Anal. Chem.* **91**, 15461–15468 (2019).
589. Kim, M. Il, Shim, J., Li, T., Lee, J. & Park, H. G. Fabrication of nanoporous nanocomposites entrapping Fe₃O₄ magnetic nanoparticles and oxidases for colorimetric biosensing. *Chem. Eur. J.* **17**, 10700–10707 (2011).
590. Chang, Q. & Tang, H. Optical determination of glucose and hydrogen peroxide using a nanocomposite prepared from glucose oxidase and magnetite nanoparticles immobilized on graphene oxide. *Microchim. Acta* **181**, 527–534 (2014).
591. Ponlakheth, K., Amatongchai, M., Sroysee, W., Jarujamrus, P. & Chairam, S. Development of sensitive and selective glucose colorimetric assay using glucose oxidase immobilized on magnetite-gold-folate nanoparticles. *Anal. Methods* **8**, 8288–8298 (2016).
592. Zhang, R., Yan, X. & Fan, K. Nanozymes inspired by natural enzymes. *Accounts Mater. Res.* **2**, 534–547 (2021).
593. Mohamad, N. R., Marzuki, N. H. C., Buang, N. A., Huyop, F. & Wahab, R. A. An overview of technologies for immobilization of enzymes and surface analysis techniques for immobilized enzymes. *Biotechnol. Biotechnol. Equip.* **29**, 205–220 (2015).
594. Maghraby, Y. R., El-Shabasy, R. M., Ibrahim, A. H. & Azzazy, H. M. E.-S. Enzyme immobilization technologies and industrial applications. *ACS Omega* **8**, 5184–5196 (2023).
595. Nguyen, H. H. & Kim, M. An overview of techniques in enzyme immobilization. *Appl. Sci. Conver. Technol.* **26**, 157–163 (2017).
596. Zeng, D. *et al.* Gold nanoparticles-based nanoconjugates for enhanced enzyme cascade and glucose sensing. *Analyst* **137**, 4435–4439 (2012).
597. Yee, Y. C., Hashim, R., Mohd Yahya, A. R. & Bustami, Y. Colorimetric analysis of glucose oxidase-

- magnetic cellulose nanocrystals (CNCs) for glucose detection. *Sensors* **19**, 2511(1–12) (2019).
598. del Barrio, M. *et al.* Glucose oxidase immobilized on magnetic nanoparticles: nanobiosensors for fluorescent glucose monitoring. *Microchim. Acta* **184**, 1325–1333 (2017).
599. Kim, M. Il, Cho, D. & Park, H. G. Colorimetric quantification of glucose and cholesterol in human blood using a nanocomposite entrapping magnetic nanoparticles and oxidases. *J. Nanosci. Nanotechnol.* **15**, 7955–7961 (2015).
600. Lin, C., Du, Y., Wang, S., Wang, L. & Song, Y. Glucose oxidase@Cu-hemin metal-organic framework for colorimetric analysis of glucose. *Mater. Sci. Eng. C* **118**, 111511 (2021).
601. Lee, P.-C., Li, N.-S., Hsu, Y.-P., Peng, C. & Yang, H.-W. Direct glucose detection in whole blood by colorimetric assay based on glucose oxidase-conjugated graphene oxide/MnO₂ nanozymes. *Analyst* **144**, 3038–3044 (2019).
602. Moses Phiri, M., Wingrove Mulder, D., Mason, S. & Christiaan Vorster, B. Facile immobilization of glucose oxidase onto gold nanostars with enhanced binding affinity and optimal function. *R. Soc. Open Sci.* **6**, 190205(1–12) (2019).
603. Lin, X. *et al.* Rapid colorimetric glucose detection via chain reaction amplification of acrylic functionalized Ag@SiO₂ nanoparticles. *RSC Adv.* **8**, 37729–37734 (2018).
604. Mackey, D., Killard, A. J., Ambrosi, A. & Smyth, M. R. Optimizing the ratio of horseradish peroxidase and glucose oxidase on a bienzyme electrode: comparison of a theoretical and experimental approach. *Sensors Actuators B Chem.* **122**, 395–402 (2007).
605. Ciaurriz, P., Bravo, E. & Hamad-Schifferli, K. Effect of architecture on the activity of glucose oxidase/horseradish peroxidase/carbon nanoparticle conjugates. *J. Colloid Interface Sci.* **414**, 73–81 (2014).
606. Johnson, K. A. & Goody, R. S. The original Michaelis constant: translation of the 1913 Michaelis-Menten paper. *Biochemistry* **50**, 8264–8269 (2011).
607. Michaelis, L. & Menten, M. L. Die Kinetik der Invertinwirkung/The kinetics of invertase action. *Biochem. Z.* **49**, 333–369 (1913).
608. Sjöström, S. L., Joensson, H. N. & Svahn, H. A. Multiplex analysis of enzyme kinetics and inhibition by droplet microfluidics using picoinjectors. *Lab Chip* **13**, 1754–1761 (2013).
609. Männel, M. J. *et al.* Catalytically active protein coatings: toward enzymatic cascade reactions at the intercolloidal level. *ACS Catal.* **7**, 1664–1672 (2017).
610. Savin, R. *et al.* Nanohybrid biosensor based on mussel-inspired electro-cross-linking of tannic acid capped gold nanoparticles and enzymes. *Mater. Adv.* **3**, 2222–2233 (2022).
611. Lineweaver, H. & Burk, D. The determination of enzyme dissociation constants. *J. Am. Chem. Soc.*

- 56**, 658–666 (1934).
612. He, P., Greenway, G. & Haswell, S. J. Development of enzyme immobilized monolith micro-reactors integrated with microfluidic electrochemical cell for the evaluation of enzyme kinetics. *Microfluid. Nanofluidics* **8**, 565–573 (2010).
613. Rogers, M. J. & Brandt, K. G. Interaction of D-glucal with aspergillus niger glucose oxidase. *Biochemistry* **10**, 4624–4630 (1971).
614. Nakamura, S., Hayashi, S. & Koga, K. Effect of periodate oxidation on the structure and properties of glucose oxidase. *Biochim. Biophys. Acta - Enzymol.* **445**, 294–308 (1976).
615. Huang, S.-H., Liao, M.-H. & Chen, D.-H. Direct binding and characterization of lipase onto magnetic nanoparticles. *Biotechnol. Prog.* **19**, 1095–1100 (2003).
616. Bastida, A. *et al.* A single step purification, immobilization, and hyperactivation of lipases via interfacial adsorption on strongly hydrophobic supports. *Biotechnol. Bioeng.* **58**, 486–493 (1998).
617. Charusheela, A. & Arvind, L. Enzyme catalyzed hydrolysis of esters using reversibly soluble polymer conjugated lipases. *Enzyme Microb. Technol.* **30**, 19–25 (2002).
618. Wang, H. *et al.* Immobilization of glucose oxidase using CoFe₂O₄/SiO₂ nanoparticles as carrier. *Appl. Surf. Sci.* **257**, 5739–5745 (2011).
619. Lee, H. U., Song, Y. S., Suh, Y. J., Park, C. & Kim, S. W. Synthesis and characterization of glucose oxidase-core/shell magnetic nanoparticle complexes into chitosan bead. *J. Mol. Catal. B Enzym.* **81**, 31–36 (2012).
620. Pandey, P. *et al.* Application of thiolated gold nanoparticles for the enhancement of glucose oxidase activity. *Langmuir* **23**, 3333–3337 (2007).
621. Mislovičová, D., Pätoprstý, V. & Vikartovská, A. Enzymatic oxidation and separation of various saccharides with immobilized glucose oxidase. *Appl. Biochem. Biotechnol.* **162**, 1669–1677 (2010).
622. Pazur, J. H. & Kleppe, K. The oxidation of glucose and related compounds by glucose oxidase from aspergillus niger. *Biochemistry* **3**, 578–583 (1964).
623. Leskovac, V., Trivić, S., Wohlfahrt, G., Kandrač, J. & Peričin, D. Glucose oxidase from aspergillus niger: the mechanism of action with molecular oxygen, quinones, and one-electron acceptors. *Int. J. Biochem. Cell Biol.* **37**, 731–750 (2005).
624. Pezzotti, F. & Therisod, M. Enzymatic synthesis of aldonic acids. *Carbohydr. Res.* **341**, 2290–2292 (2006).
625. Adams, E. C., Mast, R. L. & Free, A. H. Specificity of glucose oxidase. *Arch. Biochem. Biophys.* **91**, 230–234 (1960).
626. Zhou, L. *et al.* Oriented immobilization of glucose oxidase on graphene oxide. *Biochem. Eng. J.* **69**,

- 28–31 (2012).
627. Bai, J. *et al.* Efficient immobilization of glucose oxidase on mesoporous MIL-125 and their catalytic activities. *Results Mater.* **14**, 100267(1–11) (2022).
628. Otadi, M. & Mobayen, S. The survey of kinetic behavior of immobilized glucose oxidase on gum tragacanth carrier. *World Appl. Sci. J.* **14**, 15–19 (2011).
629. Rossi, L. M., Quach, A. D. & Rosenzweig, Z. Glucose oxidase-magnetite nanoparticle bioconjugate for glucose sensing. *Anal. Bioanal. Chem.* **380**, 606–613 (2004).
630. Romeo, A. *et al.* Inkjet printed flexible non-enzymatic glucose sensor for tear fluid analysis. *Appl. Mater. Today* **10**, 133–141 (2018).
631. Moya, A. *et al.* All-inkjet-printed dissolved oxygen sensors on flexible plastic substrates. *Org. Electron.* **39**, 168–176 (2016).
632. Zea, M., Moya, A., Villa, R. & Gabriel, G. Reliable paper surface treatments for the development of inkjet-printed electrochemical sensors. *Adv. Mater. Interfaces* **9**, 2200371(1–13) (2022).
633. Moya, A. *et al.* Inkjet-printed dissolved oxygen and pH sensors on flexible plastic substrates. *Proc. SPIE 10246, Smart Sensors, Actuators, MEMS VIII* **10246**, 102460F(1–7) (2017).
634. Moya, A., Gabriel, G., Villa, R. & del Campo, F. J. Inkjet-printed electrochemical sensors. *Curr. Opin. Electrochem.* **3**, 29–39 (2017).
635. Li, J., Rossignol, F. & Macdonald, J. Inkjet printing for biosensor fabrication: combining chemistry and technology for advanced manufacturing. *Lab Chip* **15**, 2538–2558 (2015).
636. Escudero, A. *et al.* Large-Scale synthesis of hybrid conductive polymer-gold nanoparticles using ‘sacrificial’ weakly binding ligands for printing electronics. *Inorg. Chem.* **60**, 17103–17113 (2021).
637. Reis, N. & Derby, B. Ink jet deposition of ceramic suspensions: modeling and experiments of droplet formation. *MRS Online Proc. Libr.* **625**, 117–122 (2000).
638. Derby, B. Additive manufacture of ceramics components by inkjet printing. *Engineering* **1**, 113–123 (2015).
639. Derby, B. Inkjet printing of functional and structural materials: fluid property requirements, feature stability, and resolution. *Annu. Rev. Mater. Res.* **40**, 395–414 (2010).
640. Soltman, D. & Subramanian, V. Inkjet-printed line morphologies and temperature control of the coffee ring effect. *Langmuir* **24**, 2224–2231 (2008).
641. Helm, I., Jalukse, L. & Leito, I. Measurement uncertainty estimation in amperometric sensors: a tutorial review. *Sensors* **10**, 4430–4455 (2010).
642. McGarraugh, G. The chemistry of commercial continuous glucose monitors. *Diabetes Technol.*

- Ther.* **11**, S17–S24 (2009).
643. Weltin, A., Kieninger, J. & Urban, G. A. Microfabricated, amperometric, enzyme-based biosensors for in vivo applications. *Anal. Bioanal. Chem.* **408**, 4503–4521 (2016).
644. Eggins, B. R. 2.3.3 Chronoamperometry. in *Chemical Sensors and Biosensors* (ed. Eggins, B. R.) 32–34 (John Wiley & Sons, 2002).
645. Grieshaber, D., MacKenzie, R., Vörös, J. & Reimhult, E. Electrochemical biosensors - sensor principles and architectures. *Sensors* **8**, 1400–1458 (2008).
646. Zhang, J. X. J. & Hoshino, K. Chapter 4 - Electrical transducers: electrochemical sensors and semiconductor molecular sensors. in *Molecular Sensors and Nanodevices* (eds. Zhang, J. X. J. & Hoshino, K.) 181–230 (Academic Press, 2019). doi:10.1016/B978-1-4557-7631-3.00004-1.
647. Chaubey, A. & Malhotra, B. D. Mediated biosensors. *Biosens. Bioelectron.* **17**, 441–456 (2002).
648. Yoo, E.-H. & Lee, S.-Y. Glucose biosensors: an overview of use in clinical practice. *Sensors* **10**, 4558–4576 (2010).
649. Turner, A. P. F., Chen, B. & Piletsky, S. A. In vitro diagnostics in diabetes: meeting the challenge. *Clin. Chem.* **45**, 1596–1601 (1999).
650. Stetter, J. R. & Li, J. Amperometric gas sensors - a review. *Chem. Rev.* **108**, 352–366 (2008).
651. Knake, R., Jacquinet, P., Hodgson, A. W. E. & Hauser, P. C. Amperometric sensing in the gas-phase. *Anal. Chim. Acta* **549**, 1–9 (2005).
652. Lucero, D. P. Design of membrane-covered polarographic gas detectors. *Anal. Chem.* **41**, 613–622 (1969).
653. Qiu, J.-D., Zhou, W.-M., Guo, J., Wang, R. & Liang, R. P. Amperometric sensor based on ferrocene-modified multiwalled carbon nanotube nanocomposites as electron mediator for the determination of glucose. *Anal. Biochem.* **385**, 264–269 (2009).
654. Shan, D., Wang, S., He, Y. & Xue, H. Amperometric glucose biosensor based on in situ electropolymerized polyaniline/poly(acrylonitrile-co-acrylic acid) composite film. *Mater. Sci. Eng. C* **28**, 213–217 (2008).
655. Paahan, A., Köytepe, S. & Ekinçi, E. Synthesis, characterization of a new organosoluble polyimide and its application in development of glucose biosensor. *Polym. - Plast. Technol. Eng.* **50**, 1239–1246 (2011).
656. Çetin, M. Z. & Camurlu, P. An amperometric glucose biosensor based on PEDOT nanofibers. *RSC Adv.* **8**, 19724–19731 (2018).
657. Kandimalla, V. B., Tripathi, V. S. & Ju, H. A conductive ormosil encapsulated with ferrocene conjugate and multiwall carbon nanotubes for biosensing application. *Biomaterials* **27**, 1167–1174

- (2006).
658. Qin, Y. *et al.* In situ synthesis of highly loaded and ultrafine Pd nanoparticles-decorated graphene oxide for glucose biosensor application. *J. Mater. Chem.* **22**, 24821–24826 (2012).
659. Zhu, J. *et al.* Planar amperometric glucose sensor based on glucose oxidase immobilized by chitosan film on prussian blue layer. *Sensors* **2**, 127–136 (2002).
660. Demirkiran, N., Ekinici, E. & Asiltürk, M. Immobilization of glucose oxidase in silica sol-gel film for application to biosensor and amperometric determination of glucose. *J. Chil. Chem. Soc.* **57**, 1336–1339 (2012).
661. Bright, H. J. & Appleby, M. The pH dependence of the individual steps in the glucose oxidase reaction. *J. Biol. Chem.* **244**, 3625–3634 (1969).
662. Weibel, M. K. & Bright, H. J. The glucose oxidase mechanism. *J. Biol. Chem.* **246**, 2734–2744 (1971).
663. Chen, X., Jia, J. & Dong, S. Organically modified sol-gel/chitosan composite based glucose biosensor. *Electroanalysis* **15**, 608–612 (2003).
664. Goldstein, L. [70] Water-insoluble derivatives of proteolytic enzymes. in *Methods in Enzymology* (eds. Perlmann, G. E. & Lorand, L.) vol. 19 935–962 (Academic Press, 1970).
665. Crouch, E., Cowell, D. C., Hoskins, S., Pittson, R. W. & Hart, J. P. A novel, disposable, screen-printed amperometric biosensor for glucose in serum fabricated using a water-based carbon ink. *Biosens. Bioelectron.* **21**, 712–718 (2005).
666. Yu, J., Liu, S. & Ju, H. Glucose sensor for flow injection analysis of serum glucose based on immobilization of glucose oxidase in titania sol-gel membrane. *Biosens. Bioelectron.* **19**, 401–409 (2003).
667. Park, S., Chung, T. D. & Kim, H. C. Nonenzymatic glucose detection using mesoporous platinum. *Anal. Chem.* **75**, 3046–3049 (2003).
668. Male, K. B., Hrapovic, S., Liu, Y., Wang, D. & Luong, J. H. T. Electrochemical detection of carbohydrates using copper nanoparticles and carbon nanotubes. *Anal. Chim. Acta* **516**, 35–41 (2004).
669. Zhang, Y. *et al.* A new preparation of Au nanoplates and their application for glucose sensing. *Biosens. Bioelectron.* **28**, 344–348 (2011).
670. Shan, C. *et al.* Graphene/AuNPs/chitosan nanocomposites film for glucose biosensing. *Biosens. Bioelectron.* **25**, 1070–1074 (2010).
671. Zulkifli, Z. A., Ridhuan, N. S., Nor, N. M., Zakaria, N. D. & Razak, K. A. The effect of gold nanoparticles modified electrode on the glucose sensing performance. *AIP Conf. Proc.* **1865**,

- 020015(1–6) (2017).
672. Onay, A. *et al.* Amperometric glucose sensor based on the glucose oxidase enzyme immobilized on graphite rod electrode modified with Fe₃O₄-CS-Au magnetic nanoparticles. *Ionics (Kiel)*. **24**, 4015–4022 (2018).
673. German, N., Ramanavicius, A. & Ramanaviciene, A. Amperometric glucose biosensor based on electrochemically deposited gold nanoparticles covered by polypyrrole. *Electroanalysis* **29**, 1267–1277 (2017).
674. Li, S. J. *et al.* Direct electrochemistry of glucose oxidase on sulfonated graphene/gold nanoparticle hybrid and its application to glucose biosensing. *J. Solid State Electrochem.* **17**, 2487–2494 (2013).
675. Sadak, O. One-pot scalable synthesis of rGO/AuNPs nanocomposite and its application in enzymatic glucose biosensor. *Nanocomposites* **7**, 44–52 (2021).
676. Zhang, H., Meng, Z., Wang, Q. & Zheng, J. A novel glucose biosensor based on direct electrochemistry of glucose oxidase incorporated in biomediated gold nanoparticles-carbon nanotubes composite film. *Sensors Actuators B Chem.* **158**, 23–27 (2011).
677. Sakalauskiene, L., Popov, A., Kausaite-Minkstimiene, A., Ramanavicius, A. & Ramanaviciene, A. The Impact of glucose oxidase immobilization on dendritic gold nanostructures on the performance of glucose biosensors. *Biosensors* **12**, 320(1–14) (2022).
678. Wang, K.-H., Wu, J.-Y., Chen, L.-H. & Lee, Y.-L. Architecture effects of glucose oxidase/Au nanoparticle composite Langmuir-Blodgett films on glucose sensing performance. *Appl. Surf. Sci.* **366**, 202–209 (2016).
679. Ge, Y. *et al.* Glucose oxidase complexed gold-graphene nanocomposite on a dielectric surface for glucose detection: a strategy for gestational diabetes mellitus. *Int. J. Nanomedicine* **14**, 7851–7860 (2019).
680. Li, Z., Gao, F. & Gu, Z. Vertically aligned Pt nanowire array/Au nanoparticle hybrid structure as highly sensitive amperometric biosensors. *Sensors Actuators B Chem.* **243**, 1092–1101 (2017).
681. Liu, Y., Feng, X., Shen, J., Zhu, J.-J. & Hou, W. Fabrication of a novel glucose biosensor based on a highly electroactive polystyrene/polyaniline/Au nanocomposite. *J. Phys. Chem. B* **112**, 9237–9242 (2008).
682. German, N., Ramanaviciene, A. & Ramanavicius, A. Formation and electrochemical evaluation of polyaniline and polypyrrole nanocomposites based on glucose oxidase and gold nanostructures. *Polymers (Basel)*. **12**, 3026(1–20) (2020).
683. Wang, G. *et al.* Non-enzymatic electrochemical sensing of glucose. *Microchim. Acta* **180**, 161–186 (2013).

684. Cho, S. & Kang, C. Nonenzymatic glucose detection with good selectivity against ascorbic acid on a highly porous gold electrode subjected to amalgamation treatment. *Electroanalysis* **19**, 2315–2320 (2007).
685. Xia, Y., Huang, W., Zheng, J., Niu, Z. & Li, Z. Nonenzymatic amperometric response of glucose on a nanoporous gold film electrode fabricated by a rapid and simple electrochemical method. *Biosens. Bioelectron.* **26**, 3555–3561 (2011).
686. Luna Castro, A. M., de Mele, M. F. L. & Ariva, A. J. The electro-oxidation of glucose on microcolumnar gold electrodes in different neutral solutions. *J. Electroanal. Chem.* **323**, 149–162 (1992).
687. Thota, R. & Ganesh, V. Chemically modified flexible strips as electrochemical biosensors. *Analyst* **139**, 4661–4672 (2014).
688. Bacon, N. C. & Hall, E. A. H. A sandwich enzyme electrode giving electrochemical scavenging of interferents. *Electroanalysis* **11**, 749–755 (1999).
689. Wang, J., Liu, J., Chen, L. & Lu, F. Highly selective membrane-free, mediator-free glucose biosensor. *Anal. Chem.* **66**, 3600–3603 (1994).
690. Saidina, D. S., Eawwiboonthanakit, N., Mariatti, M., Fontana, S. & Hérold, C. Recent development of graphene-based ink and other conductive material-based inks for flexible electronics. *J. Electron. Mater.* **48**, 3428–3450 (2019).
691. Nayak, L., Mohanty, S., Nayak, S. K. & Ramadoss, A. A review on inkjet printing of nanoparticle inks for flexible electronics. *J. Mater. Chem. C* **7**, 8771–8795 (2019).
692. Kholghi Eshkalak, S. *et al.* A review on inkjet printing of CNT composites for smart applications. *Appl. Mater. Today* **9**, 372–386 (2017).
693. Wang, P. *et al.* Beyond color: the new carbon ink. *Adv. Mater.* **33**, 2005890(1–30) (2021).
694. Tilmaciu, C.-M. & Morris, M. C. Carbon nanotube biosensors. *Front. Chem.* **3**, 59(1–21) (2015).
695. Wang, Z. & Dai, Z. Carbon nanomaterial-based electrochemical biosensors: an overview. *Nanoscale* **7**, 6420–6431 (2015).
696. Yang, W. *et al.* Carbon nanomaterials in biosensors: should you use nanotubes or graphene. *Angew. Chemie Int. Ed.* **49**, 2114–2138 (2010).
697. Sireesha, M., Jagadeesh Babu, V., Kranthi Kiran, A. S. & Ramakrishna, S. A review on carbon nanotubes in biosensor devices and their applications in medicine. *Nanocomposites* **4**, 36–57 (2018).
698. Moya, A. *et al.* Stable full-inkjet-printed solid-state Ag/AgCl reference electrode. *Anal. Chem.* **91**, 15539–15546 (2019).

-
699. Da Silva, E. T. S. G., Miserere, S., Kubota, L. T. & Merkoçi, A. Simple on-plastic/paper inkjet-printed solid-state Ag/AgCl pseudoreference electrode. *Anal. Chem.* **86**, 10531–10534 (2014).
700. Vagner, J., Qu, H. & Hruby, V. J. Peptidomimetics, a synthetic tool of drug discovery. *Curr. Opin. Chem. Biol.* **12**, 292–296 (2008).
701. Del Gatto, A., Cobb, S. L., Zhang, J. & Zaccaro, L. Editorial: Peptidomimetics: synthetic tools for drug discovery and development. *Front. Chem.* **9**, 802120(1–2) (2021).
702. Li Petri, G., Di Martino, S. & De Rosa, M. Peptidomimetics: an overview of recent medicinal chemistry efforts toward the discovery of novel small molecule inhibitors. *J. Med. Chem.* **65**, 7438–7475 (2022).
703. Farrukh, A. *et al.* Photoactivatable adhesive ligands for light-guided neuronal growth. *ChemBioChem* **19**, 1271–1279 (2018).
704. Li, X. *et al.* Short laminin peptide for improved neural stem cell growth. *Stem Cells Transl. Med.* **3**, 662–670 (2014).
705. Patel, R. *et al.* Ile-Lys-Val-ala-Val (IKVAV) peptide for neuronal tissue engineering. *Polym. Adv. Technol.* **30**, 4–12 (2019).
706. Hersel, U., Dahmen, C. & Kessler, H. RGD modified polymers: biomaterials for stimulated cell adhesion and beyond. *Biomaterials* **24**, 4385–4415 (2003).
707. Ruoslahti, E. RGD and other recognition sequences for integrins. *Annu. Rev. Cell Dev. Biol.* **12**, 697–715 (1996).
708. Ruoslahti, E. & Pierschbacher, M. D. New perspectives in cell adhesion: RGD and integrins. *Science* (80-.). **238**, 491–497 (1987).
709. Pierschbacher, M. D. & Ruoslahti, E. Cell attachment activity of fibronectin can be duplicated by small synthetic fragments of the molecule. *Nature* **309**, 30–33 (1984).
710. Ruoslahti, E. & Pierschbacher, M. D. Arg-Gly-Asp: a versatile cell recognition signal. *Cell* **44**, 517–518 (1986).
711. Jessberger, S., Aimone, J. B. & Gage, F. H. 4.41 - Neurogenesis. in *Learning and Memory: A Comprehensive Reference* (ed. Byrne, J. H.) 839–858 (Academic Press, 2008).
712. Jensen, J. B. & Parmar, M. Strengths and limitations of the neurosphere culture system. *Mol. Neurobiol.* **34**, 153–161 (2006).
713. Monni, E., Congiu, T., Massa, D., Nat, R. & Diana, A. Human neurospheres: from stained sections to three-dimensional assembly. *Transl. Neurosci.* **2**, 43–48 (2011).
714. Thonhoff, J. R., Lou, D. I., Jordan, P. M., Zhao, X. & Wu, P. Compatibility of human fetal neural stem cells with hydrogel biomaterials in vitro. *Brain Res.* **1187**, 42–51 (2008).

715. Wang, G. *et al.* The effect of topology of chitosan biomaterials on the differentiation and proliferation of neural stem cells. *Acta Biomater.* **6**, 3630–3639 (2010).
716. Ren, Y. J. *et al.* Hyaluronic acid/polylysine hydrogel as a transfer system for transplantation of neural stem cells. *J. Bioact. Compat. Polym.* **24**, 56–62 (2009).
717. Liesi, P. Do neurons in the vertebrate CNS migrate on laminin? *EMBO J.* **4**, 1163–1170 (1985).
718. Flanagan, L. A., Rebaza, L. M., Derzic, S., Schwartz, P. H. & Monuki, E. S. Regulation of human neural precursor cells by laminin and integrins. *J. Neurosci. Res.* **83**, 845–856 (2006).
719. Colognato, H. & Yurchenco, P. D. Form and function: the laminin family of heterotrimers. *Dev. Dyn.* **218**, 213–234 (2000).
720. Kleinman, H. K. *et al.* Identification of a 110-kDa nonintegrin cell surface laminin-binding protein which recognizes an a chain neurite-promoting peptide. *Arch. Biochem. Biophys.* **290**, 320–325 (1991).
721. Yamada, M. *et al.* Ile-Lys-Val-Ala-Val (IKVAV)-containing laminin α 1 chain peptides form amyloid-like fibrils. *FEBS Lett.* **530**, 48–52 (2002).
722. Sephel, G. C. *et al.* Laminin a chain synthetic peptide which supports neurite outgrowth. *Biochem. Biophys. Res. Commun.* **162**, 821–829 (1989).
723. Nomizu, M. *et al.* Structure-activity study of a laminin α 1 chain active peptide segment Ile-Lys-Val-Ala-Val (IKVAV). *FEBS Lett.* **365**, 227–231 (1995).
724. Tashiro, K. *et al.* A synthetic peptide containing the IKVAV sequence from the A chain of laminin mediates cell attachment, migration, and neurite outgrowth. *J. Biol. Chem.* **264**, 16174–16182 (1989).
725. Kibbey, M. C., Grant, D. S. & Kleinman, H. K. Role of the SIKVAV site of laminin in promotion of angiogenesis and tumor growth: an in vivo Matrigel model. *J. Natl. Cancer Inst.* **84**, 1633–1638 (1992).
726. Kanemoto, T. *et al.* Identification of an amino acid sequence from the laminin A chain that stimulates metastasis and collagenase IV production. *Proc. Natl. Acad. Sci. U. S. A.* **87**, 2279–2283 (1990).
727. Silva, G. A. *et al.* Selective differentiation of neural progenitor cells by high-epitope density nanofibers. *Science (80-.).* **303**, 1352–1355 (2004).
728. Farrukh, A. *et al.* In situ, light-guided axon growth on biomaterials via photoactivatable laminin peptidomimetic IK(HANBP)VAV. *ACS Appl. Mater. Interfaces* **10**, 41129–41137 (2018).
729. Luo, X.-L., Xu, J.-J., Zhang, Q., Yang, G.-J. & Chen, H.-Y. Electrochemically deposited chitosan hydrogel for horseradish peroxidase immobilization through gold nanoparticles self-assembly. *Biosens. Bioelectron.* **21**, 190–196 (2005).

730. Lei, C.-X., Hu, S.-Q., Gao, N., Shen, G.-L. & Yu, R.-Q. An amperometric hydrogen peroxide biosensor based on immobilizing horseradish peroxidase to a nano-Au monolayer supported by sol-gel derived carbon ceramic electrode. *Bioelectrochemistry* **65**, 33–39 (2004).
731. Jia, J. *et al.* A method to construct a third-generation horseradish peroxidase biosensor: self-assembling gold nanoparticles to three-dimensional sol-gel network. *Anal. Chem.* **74**, 2217–2223 (2002).
732. Li, S. *et al.* Development of a novel method to measure macrophage migration inhibitory factor (MIF) in sera of patients with rheumatoid arthritis by combined electrochemical immunosensor. *Int. Immunopharmacol.* **8**, 859–865 (2008).
733. Tang, L. *et al.* Rapid detection of picloram in agricultural field samples using a disposable immunomembrane-based electrochemical sensor. *Environ. Sci. Technol.* **42**, 1207–1212 (2008).
734. Li, X. *et al.* Amperometric immunosensor based on toluidine blue/nano-Au through electrostatic interaction for determination of carcinoembryonic antigen. *J. Biotechnol.* **123**, 356–366 (2006).
735. Cai, H., Xu, C., He, P. & Fang, Y. Colloid Au-enhanced DNA immobilization for the electrochemical detection of sequence-specific DNA. *J. Electroanal. Chem.* **510**, 78–85 (2001).
736. Kang, J., Li, X., Wu, G., Wang, Z. & Lu, X. A new scheme of hybridization based on the Au_{nano}-DNA modified glassy carbon electrode. *Anal. Biochem.* **364**, 165–170 (2007).
737. Gaur, R. K. Introduction of 5'-terminal amino and thiol groups into synthetic oligonucleotides. *Nucleosides and Nucleotides* **10**, 895–909 (1991).
738. Bischoff, R., Coull, J. M. & Regnier, F. E. Introduction of 5'-terminal functional groups into synthetic oligonucleotides for selective immobilization. *Anal. Biochem.* **164**, 336–344 (1987).
739. Agrawal, S. Functionalization of oligonucleotides with amino groups and attachment of amino specific reporter groups. in *Protocols for Oligonucleotide Conjugates. Methods in Molecular Biology* (ed. Agrawal, S.) vol. 26 93–120 (Humana Press, 1994).
740. Reynolds, R. A., Mirkin, C. A. & Letsinger, R. L. Homogeneous, nanoparticle-based quantitative colorimetric detection of oligonucleotides. *J. Am. Chem. Soc.* **122**, 3795–3796 (2000).
741. Godakhindi, V. S. *et al.* Tuning the gold nanoparticle colorimetric assay by nanoparticle size, concentration, and size combinations for oligonucleotide detection. *ACS Sensors* **2**, 1627–1636 (2017).
742. Zhu, X. *et al.* A sensitive gold nanoparticle-based aptasensor for colorimetric detection of A β ₁₋₄₀ oligomers. *Anal. Methods* **10**, 641–645 (2018).
743. Zhen, Z., Tang, L.-J., Long, H. & Jiang, J.-H. Enzymatic immuno-assembly of gold nanoparticles for visualized activity screening of histone-modifying enzymes. *Anal. Chem.* **84**, 3614–3620

- (2012).
744. Yuan, J. *et al.* A sensitive gold nanoparticle-based colorimetric aptasensor for *Staphylococcus aureus*. *Talanta* **127**, 163–168 (2014).
745. Zhu, R. *et al.* Electrical stimulation affects neural stem cell fate and function in vitro. *Exp. Neurol.* **319**, 112963(1–15) (2019).
746. Chen, C., Bai, X., Ding, Y. & Lee, I.-S. Electrical stimulation as a novel tool for regulating cell behavior in tissue engineering. *Biomater. Res.* **23**, 25(1–12) (2019).
747. Bertucci, C., Koppes, R., Dumont, C. & Koppes, A. Neural responses to electrical stimulation in 2D and 3D in vitro environments. *Brain Res. Bull.* **152**, 265–284 (2019).
748. Cheng, H., Huang, Y., Yue, H. & Fan, Y. Electrical stimulation promotes stem cell neural differentiation in tissue engineering. *Stem Cells Int.* **2021**, 6697574(1–14) (2021).
749. Yao, L., Pandit, A., Yao, S. & McCaig, C. D. Electric field-guided neuron migration: a novel approach in neurogenesis. *Tissue Eng. Part B Rev.* **17**, 143–153 (2011).
750. Yamada, M. *et al.* Electrical stimulation modulates fate determination of differentiating embryonic stem cells. *Stem Cells* **25**, 562–570 (2007).
751. Yuan, X., Arkonac, D. E., Chao, P. G. & Vunjak-Novakovic, G. Electrical stimulation enhances cell migration and integrative repair in the meniscus. *Sci. Rep.* **4**, 3674(1–12) (2015).
752. Yao, L., McCaig, C. D. & Zhao, M. Electrical signals polarize neuronal organelles, direct neuron migration, and orient cell division. *Hippocampus* **19**, 855–868 (2009).
753. Chang, K. A. *et al.* Biphasic electrical currents stimulation promotes both proliferation and differentiation of fetal neural stem cells. *PLoS One* **6**, e18738(1–11) (2011).
754. Park, S. Y. *et al.* Enhanced differentiation of human neural stem cells into neurons on graphene. *Adv. Mater.* **23**, 263–267 (2011).
755. Imaninezhad, M. *et al.* Directed and enhanced neurite outgrowth following exogenous electrical stimulation on carbon nanotube-hydrogel composites. *J. Neural Eng.* **15**, 056034(1–17) (2018).
756. Min, J. H., Patel, M. & Koh, W.-G. Incorporation of conductive materials into hydrogels for tissue engineering applications. *Polymers (Basel)*. **10**, 1078(1–36) (2018).
757. Zhang, L., Stauffer, W. R., Jane, E. P., Sammak, P. J. & Cui, X. T. Enhanced differentiation of embryonic and neural stem cells to neuronal fates on laminin peptides doped polypyrrole. *Macromol. Biosci.* **10**, 1456–1464 (2010).
758. Stauffer, W. R. & Cui, X. T. Polypyrrole doped with 2 peptide sequences from laminin. *Biomaterials* **27**, 2405–2413 (2006).

759. Cui, X., Wiler, J., Dzaman, M., Altschuler, R. A. & Martin, D. C. In vivo studies of polypyrrole/peptide coated neural probes. *Biomaterials* **24**, 777–787 (2003).
760. Lee, J.-W., Serna, F., Nickels, J. & Schmidt, C. E. Carboxylic acid-functionalized conductive polypyrrole as a bioactive platform for cell adhesion. *Biomacromolecules* **7**, 1692–1695 (2006).
761. Tan, J. M. R., Farraj, Y., Kamyshny, A. & Magdassi, S. Fabrication approaches of soft electronics. *ACS Appl. Electron. Mater.* **5**, 1376–1393 (2023).
762. Zhang, S., Li, S., Xia, Z. & Cai, K. A review of electronic skin: soft electronics and sensors for human health. *J. Mater. Chem. B* **8**, 852–862 (2020).
763. Heng, W., Solomon, S. & Gao, W. Flexible electronics and devices as human-machine interfaces for medical robotics. *Adv. Mater.* **34**, 2107902(1–48) (2022).
764. Rao, Z. *et al.* Soft electronics for the skin: from health monitors to human-machine interfaces. *Adv. Mater. Technol.* **5**, 2000233(1–27) (2020).
765. Niu, Y. *et al.* The new generation of soft and wearable electronics for health monitoring in varying environment: from normal to extreme conditions. *Mater. Today* **41**, 219–242 (2020).
766. Pulkkinen, P. *et al.* Poly(ethylene imine) and tetraethylenepentamine as protecting agents for metallic copper nanoparticles. *ACS Appl. Mater. Interfaces* **1**, 519–525 (2009).
767. Jeong, S. *et al.* Controlling the thickness of the surface oxide layer on Cu nanoparticles for the fabrication of conductive structures by ink-jet printing. *Adv. Funct. Mater.* **18**, 679–686 (2008).
768. Kanninen, P., Johans, C., Merta, J. & Kontturi, K. Influence of ligand structure on the stability and oxidation of copper nanoparticles. *J. Colloid Interface Sci.* **318**, 88–95 (2008).
769. Pakiari, A. H. & Jamshidi, Z. Nature and strength of MS bonds (M = Au, Ag, and Cu) in binary alloy gold clusters. *J. Phys. Chem. A* **114**, 9212–9221 (2010).
770. Husson, J., Lakard, S., Monney, S., Buron, C. C. & Lakard, B. Elaboration and characterization of carboxylic acid-functionalized polypyrrole films. *Synth. Met.* **220**, 247–254 (2016).
771. Trechová, M., Jasenská, D., Bláha, M., Prokeš, J. & Stejskal, J. Conducting polyaniline prepared in the solutions of formic acid: does functionalization with carboxyl groups occur? *Spectrochim. Acta Part A Mol. Biomol. Spectrosc.* **235**, 118300(1–11) (2020).
772. Kim, S.-C., Whitten, J., Kumar, J., Bruno, F. F. & Samuelson, L. A. Self-doped carboxylated polyaniline: effect of hydrogen bonding on the doping of polymers. *Macromol. Res.* **17**, 631–637 (2009).
773. Jin, W. *et al.* The influence of CTAB-capped seeds and their aging time on the morphologies of silver nanoparticles. *Nanoscale Res. Lett.* **14**, 81(1–11) (2019).
774. Bernabò, M., Pucci, A., Ramanitra, H. H. & Ruggeri, G. Polymer nanocomposites containing

- anisotropic metal nanostructures as internal strain indicators. *Materials (Basel)*. **3**, 1461–1477 (2010).
775. Biçer, M. & Şişman, I. Controlled synthesis of copper nano/microstructures using ascorbic acid in aqueous CTAB solution. *Powder Technol.* **198**, 279–284 (2010).
776. Wu, S.-H. & Chen, D.-H. Synthesis of high-concentration Cu nanoparticles in aqueous CTAB solutions. *J. Colloid Interface Sci.* **273**, 165–169 (2004).
777. Lin, Z.-W., Tsao, Y.-C., Yang, M.-Y. & Huang, M. H. Seed-mediated growth of silver nanocubes in aqueous solution with tunable size and their conversion to Au nanocages with efficient photothermal property. *Chem. Eur. J.* **22**, 2326–2332 (2016).
778. Wang, J., Guo, X., He, Y., Jiang, M. & Sun, R. The synthesis and tribological characteristics of triangular copper nanoplates as a grease additive. *RSC Adv.* **7**, 40249–40254 (2017).
779. Hegde, H., Santhosh, C. & Sinha, R. K. Seed mediated synthesis of highly stable CTAB capped triangular silver nanoplates for LSPR sensing. *Mater. Res. Express* **6**, 105075(1–9) (2019).
780. Sastry, M. Phase transfer protocols in nanoparticle synthesis. *Curr. Sci.* **85**, 1735–1745 (2003).
781. Kittler, S., Hickey, S. G., Wolff, T. & Eychmüller, A. Easy and fast phase transfer of CTAB stabilised gold nanoparticles from water to organic phase. *Z. Phys. Chem.* **229**, 235–245 (2015).
782. Ten Hove, J. B., Schijven, L. M. I., Wang, J. & Velders, A. H. Size-controlled and water-soluble gold nanoparticles using UV-induced ligand exchange and phase transfer. *Chem. Commun.* **54**, 13355–13358 (2018).
783. Dheyab, M. A. *et al.* Monodisperse gold nanoparticles: a review on synthesis and their application in modern medicine. *Int. J. Mol. Sci.* **23**, 7400(1–34) (2022).
784. Yuk, H. *et al.* 3D printing of conducting polymers. *Nat. Commun.* **11**, 1604(1–8) (2020).
785. Zheng, Y. *et al.* A review of conductive carbon materials for 3D printing: materials, technologies, properties, and applications. *Materials (Basel)*. **14**, 3911(1–24) (2021).
786. Ryan, K. R., Down, M. P., Hurst, N. J., Keefe, E. M. & Banks, C. E. Additive manufacturing (3D printing) of electrically conductive polymers and polymer nanocomposites and their applications. *eScience* **2**, 365–381 (2022).
787. Baker, D. V., Bao, C. & Kim, W. S. Highly conductive 3D printable materials for 3D structural electronics. *ACS Appl. Electron. Mater.* **3**, 2423–2433 (2021).
788. Zhang, D. *et al.* Fabrication of highly conductive graphene flexible circuits by 3D printing. *Synth. Met.* **217**, 79–86 (2016).
789. Chizari, K., Daoud, M. A., Ravindran, A. R. & Therriault, D. 3D Printing of highly conductive nanocomposites for the functional optimization of liquid sensors. *Small* **12**, 6076–6082 (2016).

-
790. Wang, Z. *et al.* 3D-printed graphene/polydimethylsiloxane composites for stretchable and strain-insensitive temperature sensors. *ACS Appl. Mater. Interfaces* **11**, 1344–1352 (2019).
791. Hohimer, C. J., Petrossian, G., Ameli, A., Mo, C. & Pötschke, P. 3D printed conductive thermoplastic polyurethane/carbon nanotube composites for capacitive and piezoresistive sensing in soft pneumatic actuators. *Addit. Manuf.* **34**, 101281(1–14) (2020).
792. Carrico, J. D., Traeden, N. W., Aureli, M. & Leang, K. K. Fused filament 3D printing of ionic polymer-metal composites (IPMCs). *Smart Mater. Struct.* **24**, 125021(1–11) (2015).
793. Maurel, A. *et al.* Highly loaded graphite – polylactic acid composite-based filaments for lithium-ion battery three-dimensional printing. *Chem. Mater.* **30**, 7484–7493 (2018).
794. Sun, C. *et al.* 3D printing nanocomposite gel-based thick electrode enabling both high areal capacity and rate performance for lithium-ion battery. *Chem. Eng. J.* **381**, 122641(1–8) (2020).
795. Wang, Z. *et al.* Three-dimensional printing of polyaniline/reduced graphene oxide composite for high-performance planar supercapacitor. *ACS Appl. Mater. Interfaces* **10**, 10437–10444 (2018).
796. Foo, C. Y., Lim, H. N., Mahdi, M. A., Wahid, M. H. & Huang, N. M. Three-dimensional printed electrode and its novel applications in electronic devices. *Sci. Rep.* **8**, 7399(1–11) (2018).
797. Abshirini, M., Charara, M., Marashizadeh, P., Saha, M. C. & Altan, M. C. Functional nanocomposites for 3D printing of stretchable and wearable sensors. *Appl. Nanosci.* **9**, 2071–2083 (2019).
798. Eutonnat-Diff, P. A. *et al.* Development of flexible and conductive immiscible thermoplastic/elastomer monofilament for smart textiles applications using 3D printing. *Polymers (Basel)*. **12**, 2300(1–31) (2020).
799. Liu, S., Chen, X. & Zhang, Y. Chapter 14 - Hydrogels and hydrogel composites for 3D and 4D printing applications. in *3D and 4D Printing of Polymer Nanocomposite Materials* (eds. Sadasivuni, K. K., Deshmukh, K. & Almaadeed, M. A.) 427–465 (Elsevier, 2020). doi:10.1016/B978-0-12-816805-9.00014-4.
800. Soleymani Eil Bakhtiari, S. *et al.* 3-Dimensional printing of hydrogel-based nanocomposites: a comprehensive review on the technology description, properties, and applications. *Adv. Eng. Mater.* **23**, 2100477(1–21) (2021).
801. Distler, T. & Boccaccini, A. R. 3D printing of electrically conductive hydrogels for tissue engineering and biosensors – a review. *Acta Biomater.* **101**, 1–13 (2020).
802. Yang, R. *et al.* Recent advances in the 3D printing of electrically conductive hydrogels for flexible electronics. *J. Mater. Chem. C* **10**, 5380–5399 (2022).
803. Li, X. *et al.* 3D printing of flexible liquid sensor based on swelling behavior of hydrogel with carbon

- nanotubes. *Adv. Mater. Technol.* **4**, 1800476(1–9) (2019).
804. Deng, Z. *et al.* Stimuli-responsive conductive nanocomposite hydrogels with high stretchability, self-healing, adhesiveness, and 3D printability for human motion sensing. *ACS Appl. Mater. Interfaces* **11**, 6796–6808 (2019).
805. Håkansson, K. M. O. *et al.* Solidification of 3D printed nanofibril hydrogels into functional 3D cellulose structures. *Adv. Mater. Technol.* **1**, 1600096(1–9) (2016).
806. Janarthanan, G., Lee, S. & Noh, I. 3D printing of bioinspired alginate-albumin based instant gel ink with electroconductivity and its expansion to direct four-axis printing of hollow porous tubular constructs without supporting materials. *Adv. Funct. Mater.* **31**, 2104441(1–13) (2021).
807. Yun, X. *et al.* Direct 3D printing of a graphene oxide hydrogel for fabrication of a high areal specific capacitance microsupercapacitor. *RSC Adv.* **9**, 29384–29395 (2019).
808. Chi, K. *et al.* Freestanding graphene paper supported three-dimensional porous graphene-polyaniline nanocomposite synthesized by inkjet printing and in flexible all-solid-state supercapacitor. *ACS Appl. Mater. Interfaces* **6**, 16312–16319 (2014).
809. Afanasenkau, D. *et al.* Rapid prototyping of soft bioelectronic implants for use as neuromuscular interfaces. *Nat. Biomed. Eng.* **4**, 1010–1022 (2020).
810. Xavier Mendes, A. *et al.* Enhanced electroactivity, mechanical properties, and printability through the addition of graphene oxide to photo-cross-linkable gelatin methacryloyl hydrogel. *ACS Biomater. Sci. Eng.* **7**, 2279–2295 (2021).
811. Bergonzi, C. *et al.* Three-dimensional (3D) printed silver nanoparticles/alginate/nanocrystalline cellulose hydrogels: study of the antimicrobial and cytotoxicity efficacy. *Nanomaterials* **10**, 844(1–15) (2020).
812. Zhao, Y. *et al.* Skin-inspired antibacterial conductive hydrogels for epidermal sensors and diabetic foot wound dressings. *Adv. Funct. Mater.* **29**, 1901474(1–12) (2019).
813. Wu, Z. & Hong, Y. Combination of the silver-ethylene interaction and 3D printing to develop antibacterial superporous hydrogels for wound management. *ACS Appl. Mater. Interfaces* **11**, 33734–33747 (2019).
814. Bauhofer, W. & Kovacs, J. Z. A review and analysis of electrical percolation in carbon nanotube polymer composites. *Compos. Sci. Technol.* **69**, 1486–1498 (2009).
815. Marsden, A. J. *et al.* Electrical percolation in graphene-polymer composites. *2D Mater.* **5**, 032003(1–19) (2018).
816. Rahaman, M. *et al.* A new insight in determining the percolation threshold of electrical conductivity for extrinsically conducting polymer composites through different sigmoidal models. *Polymers*

- (*Basel*). **9**, 527(1–17) (2017).
817. Motaghi, A., Hrymak, A. & Motlagh, G. H. Electrical conductivity and percolation threshold of hybrid carbon/polymer composites. *J. Appl. Polym. Sci.* **132**, 41744(1–9) (2015).
818. Choi, H. J., Kim, M. S., Ahn, D., Yeo, S. Y. & Lee, S. Electrical percolation threshold of carbon black in a polymer matrix and its application to antistatic fibre. *Sci. Rep.* **9**, 6338(1–12) (2019).
819. Mohan, V. B., Jayaraman, K. & Bhattacharyya, D. Hybridization of graphene-reinforced two polymer nanocomposites. *Int. J. Smart Nano Mater.* **7**, 179–201 (2016).
820. Coelho, P. H. & Morales, A. R. Electrical conductivity, percolation threshold and dispersion properties of PMMA nanocomposites of hybrid conducting fillers. *14th IEEE Int. Conf. Nanotechnology, Toronto, ON, Canada* 706–710 (2014) doi:10.1109/NANO.2014.6968023.
821. Bauer, G. Section 19 Copper, silver, gold. in *Handbook of Preparative Inorganic Chemistry* (ed. Bauer, G.) vol. 1 1003–1066 (Academic Press, 1963).
822. Tebbe, M., Kuttner, C., Männel, M., Fery, A. & Chanana, M. Colloidally stable and surfactant-free protein-coated gold nanorods in biological media. *ACS Appl. Mater. Interfaces* **7**, 5984–5991 (2015).
823. Zulfajri, M., Huang, W.-J., Huang, G.-G. & Chen, H.-F. Effects of different surfactant charges on the formation of gold nanoparticles by the LASiS method. *Materials (Basel)*. **14**, 2937(1–13) (2021).
824. Lomant, A. J. & Fairbanks, G. Chemical probes of extended biological structures: synthesis and properties of the cleavable protein cross-linking reagent [³⁵S]dithiobis(succinimidyl propionate). *J. Mol. Biol.* **104**, 243–261 (1976).
825. Staros, J. V. Membrane-impermeant crosslinking reagents: probes of the structure and dynamics of membrane proteins. *Acc. Chem. Res.* **21**, 435–441 (1988).
826. Cuatrecasas, P. & Parikh, I. Adsorbents for affinity chromatography. Use of N-hydroxysuccinimide esters of agarose. *Biochemistry* **11**, 2291–2299 (1972).
827. Takeuchi, A. *et al.* Human myelomonocytic cell line THP-1 produces a novel growth-promoting factor with a wide target cell spectrum. *Cancer Res.* **53**, 1871–1876 (1993).
828. Farrukh, A., Paez, J. I. & del Campo, A. 4D Biomaterials for light-guided angiogenesis. *Adv. Funct. Mater.* **29**, 1807734(1–11) (2019).
829. Paez, J. I., Farrukh, A., Valbuena-Mendoza, R., Włodarczyk-Biegun, M. K. & del Campo, A. Thiol-methylsulfone-based hydrogels for 3D cell encapsulation. *ACS Appl. Mater. Interfaces* **12**, 8062–8072 (2020).
830. Zhao, S. Dissertation: Microenvironments to regulate cellular behavior for neural development and

- regeneration. (Saarland University, Technical and Science Faculty, 2018). doi:10.22028/D291-27325.
831. Costa, M. R., Jagasia, R. & Berninger, B. Directed neuronal differentiation of embryonic and adult-derived neurosphere cells. in *Protocols for Neural Cell Culture. Springer Protocols Handbooks* (ed. Doering, L. C.) 29–49 (Humana Press, 2009). doi:10.1007/978-1-60761-292-6.
832. Azari, H., Sharififar, S., Rahman, M., Ansari, S. & Reynolds, B. A. Establishing embryonic mouse neural stem cell culture using the neurosphere assay. *J. Vis. Exp.* **47**, e2457(1-4) (2011).
833. Zhao, S. *et al.* Microenvironments to study migration and somal translocation in cortical neurons. *Biomaterials* **156**, 238–247 (2018).
834. Schindelin, J. *et al.* Fiji: an open-source platform for biological-image analysis. *Nat. Methods* **9**, 676–682 (2012).
835. Shirley, D. A. High-resolution X-Ray photoemission spectrum of the valence bands of gold. *Phys. Rev. B* **5**, 4709–4714 (1972).
836. Yeh, J. J. & Lindau, I. Atomic subshell photoionization cross sections and asymmetry parameters: $1 \leq Z \leq 103$. *At. Data Nucl. Data Tables* **32**, 1–155 (1985).
837. Binnig, G. & Rohrer, H. Scanning tunneling microscopy. *Surf. Sci.* **126**, 236–244 (1983).
838. Binnig, G., Rohrer, H., Gerber, C. & Weibel, E. 7×7 Reconstruction on Si(111) resolved in real space. *Phys. Rev. Lett.* **50**, 120–123 (1983).
839. Tersoff, J. & Hamann, D. R. Theory of scanning tunneling microscope. *Phys. Rev. B* **31**, 805–813 (1985).
840. Tersoff, J. & Hamann, D. R. Theory and application for the scanning tunneling microscope. *Phys. Rev. Lett.* **50**, 1998–2001 (1983).
841. Akerlof, G. Dielectric constants of some organic solvent-water mixtures at various temperatures. *J. Am. Chem. Soc.* **54**, 4125–4139 (1932).
842. Howard, K. S. & McAllister, R. A. The viscosity of acetone-water solutions up to their normal boiling points. *AIChE J.* **4**, 362–366 (1958).
843. Kurtz, S. S. J., Wikingsson, A. E., Camin, D. L. & Thompson, A. R. Refractive index and density of acetone-water solutions. *J. Chem. Eng. Data* **10**, 330–334 (1965).
844. Schiel, J. E. & Hage, D. S. Density measurements of potassium phosphate buffer from 4 to 45°C. *Talanta* **65**, 495–500 (2005).
845. Hoang, V. T. *et al.* Optical properties of buffers and cell culture media for optofluidic and sensing applications. *Appl. Sci.* **9**, 1145(1–11) (2019).

-
846. Diéguez, L. *et al.* Effect of the refractive index of buffer solutions in evanescent optical biosensors. *Sens. Lett.* **7**, 851–855 (2009).
847. Zhao, C. *et al.* Covalent interactions between carbon nanotubes and P3HT by thiol–ene click chemistry towards improved thermoelectric performance. *Mater. Chem. Front.* **4**, 1174–1181 (2020).
848. Karim, M. R. Synthesis and characterizations of poly(3-hexylthiophene) and modified carbon nanotube composites. *J. Nanomater.* **2012**, 174353(1–8) (2012).
849. Alves, A. P. P., Trigueiro, J. P. C., Calado, H. D. R. & Silva, G. G. Poly(3-hexylthiophene)-multi-walled carbon nanotube (1:1) hybrids: structure and electrochemical properties. *Electrochim. Acta* **209**, 111–120 (2016).
850. Gedefaw, D. *et al.* An alternating copolymer of fluorene donor and quinoxaline acceptor versus a terpolymer consisting of fluorene, quinoxaline and benzothiadiazole building units: synthesis and characterization. *Polym. Bull.* **73**, 1167–1183 (2016).
851. Hwang, D.-H. *et al.* Syntheses and light-emitting properties of poly(9,9-di-n-octylfluorenyl-2,7-vinylene) and PPV copolymers. *J. Mater. Chem.* **13**, 1540–1545 (2003).
852. Li, H. *et al.* A high voltage solar cell using a donor–acceptor conjugated polymer based on pyrrolo[3,4-f]-2,1,3-benzothiadiazole-5,7-dione. *J. Mater. Chem. A* **2**, 17925–17933 (2014).
853. Luceño Sánchez, J. A., Peña Capilla, R. & Díez-Pascual, A. M. High-performance PEDOT: PSS/hexamethylene diisocyanate-functionalized graphene oxide nanocomposites: preparation and properties. *Polymers (Basel)*. **10**, 1169(1–19) (2018).
854. Friedel, B. *et al.* Effects of layer thickness and annealing of PEDOT:PSS layers in organic photodetectors. *Macromolecules* **42**, 6741–6747 (2009).
855. Wu, X., Yang, C., Ge, J. & Liu, Z. Polydopamine tethered enzyme/metal–organic framework composites with high stability and reusability. *Nanoscale* **7**, 18883–18886 (2015).
856. Zhao, Z., Huang, Y., Liu, W., Ye, F. & Zhao, S. Immobilized glucose oxidase on boronic acid-functionalized hierarchically porous MOF as an integrated nanozyme for one-step glucose detection. *ACS Sustain. Chem. Eng.* **8**, 4481–4488 (2020).
857. Liu, Y. & Derby, B. Experimental study of the parameters for stable drop-on-demand inkjet performance. *Phys. Fluids* **31**, 032004(1–11) (2019).

Publication list

Journal articles

- Backes, I., González-García, L., Holtsch, A., Müller, F., Jacobs, K. & Kraus, T. Molecular origin of electrical conductivity in gold–polythiophene hybrid particle films. *J. Phys. Chem. Lett.* **11**, 10538-10547 (2020).
- Maurer, J. H. M., González-García, L., Backes, I., Reiser, B., Schlossberg, S. M. & Kraus, T. Direct nanoimprinting of a colloidal self-organizing nanowire ink for flexible, transparent electrodes. *Adv. Mater. Technol.* **2**, 1700034(1-8) (2017).

Patent applications

- *Conductive functionalizable nanocomposites*
Inventors: Backes, I., Hegetschweiler, A., González-García, L., Kraus, T., del Campo A., Farrukh, A. & Thai, T.
Original Assignee: Leibniz-Institut Für Neue Materialien Gemeinnützige GmbH
File reference: DE102019135645A1
Priority date: 2019-12-20

Oral presentations

- Backes, I., Drzic, J., González-García, L. & Kraus, T. The molecular origin of electrical conductivity in hybrid inkjet-printable nanoinks. *MSE - Materials Science and Engineering Congress (Digital Conference)*, September 22-25, 2020, Darmstadt.
- Backes, I., González-García, L., Doblas-Jiménez, D., Müller, F., Jacobs, K. & Kraus, T. Size- and shape-dependent binding of conductive polymer ligands in sintering-free gold nanoparticle hybrid inks for printed electronics. *15th Zsigmondy Colloquium of the German Colloidal Society*, July 10-12, 2019, Dresden.
- Backes, I., Hegetschweiler, A., González-García, L., Doblas-Jiménez, D., Escudero, A., Drzic, J., Strahl, R. & Kraus, T. Inkjet-printable sinter-free inks for electronics: hybrid structure and electrical conductivity. *6th Nano Today Conference*, June 16-20, 2019, Lisbon.
- Backes, I., Reiser, B., González-García, L., Doblas-Jimenez, D. & Kraus, T. Hybrid gold nanoparticles with conductive polymer ligands. *14th Zsigmondy Colloquium of the German Colloidal Society*, April 9-11, 2018, Mainz.

Posters

- Backes, I., Hegetschweiler, A., González-García, L. & Kraus, T. Conductive hybrid inkjet inks with biological functionalities. *Living materials conference*, February 12-14, 2020, Saarbrücken.